



©2022 Universidad EAFIT. All rights reserved.

vicomtech

MEMBER OF BASQUE RESEARCH
& TECHNOLOGY ALLIANCE



UNIVERSIDAD EAFIT

DOCTORAL PUBLICATION

Computational Geometry Contributions Applied to Additive Manufacturing

Dissertation Modality:
Compendium of Publications

Supervisor:
Prof. Dr. Eng. Oscar E. Ruiz Salguero,
Universidad EAFIT, Colombia

Co-supervisor:
Dr. Eng. Jorge Posada Velásquez,
Vicomtech, Spain

Doctoral Student:
Diego Alejandro Montoya Zapata

Examining Committee:
Prof. Dr. Eng. Diego Borro Yagüez,
CEIT, Universidad de Navarra, Spain
Prof. Dr. Eng. Rodrigo Marín Castillo,
Universidad de los Andes, Colombia
Prof. Dr. Math. Carlos Cadavid Moreno,
Universidad EAFIT, Colombia

Dissertation
Submitted as partial fulfillment of the requirements for the degree of Doctor of Philosophy in Engineering
of the College of Applied Sciences and Engineering at the Universidad EAFIT

UNIVERSIDAD EAFIT
COLLEGE OF APPLIED SCIENCES AND ENGINEERING
DOCTORAL PROGRAM IN ENGINEERING
MEDELLÍN, COLOMBIA
NOVEMBER 2022

Dedication

A mis cuatro pilares.

También a los niños de todo el mundo. A todos. Para que algún día todos tengan derecho a soñar.

Acknowledgments

Disclaimer 1: This list is comprehensive but, most likely, not exhaustive. I apologize to those whom I forgot to mention herein.

Disclaimer 2: There is some Spanish text for the people I mention in this list who do not speak English. The English translation of that text is below the original.

No fue difícil decidir quiénes serían los primeros en esta lista: madre, padre, hermano y futura esposa (espero que no se eche para atrás). Ustedes son las personas más importantes en mi vida y las personas son lo más importante en mi vida. Además, a veces parece que yo también soy importante para ustedes. Gracias por todo su apoyo en esta locura (por llamarlo de alguna manera).

It was not hard to realize who had to be on the top of this list: mom, dad, brother, and future wife (I hope she doesn't change her mind). You are the most important people, and people are the essential thing in my life. And, sometimes, it looks like I'm also important to you. Thank you for being so supportive of this experience.

My directors guided me, helped me, and taught me. Thank you, Prof. Oscar Ruiz and Dr. Jorge Posada. Thank you for trusting me. I hope you don't regret it. I also trusted you (it's a mutual relationship), and I'm glad I did. I also thank the institutions that you represent. The Universidad EAFIT and Vicomtech have supported my education since my Master's. I'm grateful for that.

Aitor, you may not read it, but this would've been unbearable without you. You were the best shield for me and my Doctorate. There's not enough *lulos* on earth to pay you back. However, whenever possible, I'll continue being your *lulos* provider.

Thank you, Prof. Juan M. Rodriguez, for all your efforts. You guided me in the world of numerical methods in computational mechanics. I wanted to enter this world at that moment, and your help was incalculable.

Thank you, V0ers. Please take care of such an amazing environment to work in. You all are brilliant, but on top of that, you all are great people. Special mention to Iñigo Barandiaran, the *Kapellmeister*, and to the colleagues in my research line (Virtual Engineering): Ander, Aitor, Daniel, Carlos, Carles (not at V0 anymore, but it was a pleasure to meet you), Puy, Sara, Bruno, Javier, and David.

I'm also grateful to the people of the Laboratory of CAD CAM CAE. I appreciate your help in both technical and administrative duties. I must dedicate a few lines to Camilo Cortés and Juan Camilo Pareja.

Camilo, we met in the lab 6 years ago, and we've been working together since then. But the crucial moment was our first informal conversation (sponsored by a third party). You said a phrase that has helped me throughout my Master's and Doctorate. And then you adopted me when I arrived in Donosti.

Juan Camilo, we also met a long time ago. We collaborated, played football, and shared some beers while discussing politics, art, sports, and so on. All of this to say, I've had a great time.

During my Ph.D. I had to coexist with some machines. Thanks to Igor, Marian, Patxi, Piera, André, Diego (*tocayo*) and the INZU Group as institution. You've made my life close to the machines much easier.

And last but definitively not least, it's time to say thanks to other family members. Thanks to my family in San Sebastián and Barcelona.

林霄 (Lín Xiāo) and 孙懿 (Sūn Yì). Best roomies one may wish. We've had great moments at home (and I can call it home, not only house). We even had a pandemic in the middle and being at home with you helped me a lot. And of course, I'm not going to forget my new friend 林雨竹 (Lín Yǔ Zhú). What a beautiful family you are.

Gracias a mis tías y sus familias por acogerme en sus casas. Gracias por su compañía y su trato tan especial. Isabella, algún día (pronto) volveré pa' atenderte en FIFA, Ubongo o lo que prefieras.

Thanks to my aunts and their families for welcoming me to their homes. Thanks for your company. Isabella, I'll be back soon to beat you again, as always.

Epilogue: Prof. Oscar, you must be proud of yourself. No one takes care better of his students. No one works more than you. I'm sure I'm not the only one who feels this way. Once one learns to deal with your character, one discovers what an excellent professor you are and what an incredible human being. This path called Doctorate has its ups and downs. I can't say if I would do it again, but I already know whom I'd pick as my mentor if I did.

Contents

I	Introduction	1
I.A	— Organization of this Document	2
I.B	— Goal of the Final Examination	3
II	Academic Trajectory	4
II.A	— Academic History	5
II.A.1	Summary	6
II.A.2	List of Publications - Doctoral Period	8
II.A.3	List of Publications - Master Period	12
II.A.4	List of Co-authors	14
II.A.5	Doctoral Courses	16
II.A.5.1	Preparatory Courses	16
II.A.5.2	Qualifying Exams	17
II.A.5.3	Preliminary Exam of Dissertation	17
II.A.6	Personalized Special Trainings	18
II.A.7	Attendance to Specialized Forums - Doctoral Period	19
II.A.7.1	Scientific Conferences - Doctoral Period	19
II.A.7.2	Professional Forums - Doctoral Period	20
II.A.8	Attendance to Specialized Forums - Master Period	21
II.A.8.1	Scientific Conferences - Master Period	21
II.A.8.2	Scientific Trainings - Master Period	21
II.A.9	Special Advisors Provided by the Universidad EAFIT and Vicomtech	22
II.A.10	Industrial Projects Undertaken in the Scope of the Doctoral Internship at Vicomtech	24

III	Research Results	26
III.A	— Summary of Contributions	27
III.B	— Shape Optimization in Lattice Structures	31
III.B.1	Sensitivity Analysis in Shape Optimization using Voxel Density Penalization	32
III.B.1.1	Context	32
III.B.1.2	Introduction	33
III.B.1.3	Literature Review	35
III.B.1.3.1	Structural Optimization and Visual Computing	35
III.B.1.3.2	Structural Optimization for Additive Manufacturing	35
III.B.1.3.3	Effect of the Parameters in Voxel-density Algorithms	35
III.B.1.3.4	Conclusions of the Literature Review	36
III.B.1.4	Methodology.	36
III.B.1.4.1	Tuning of Element Density.	36
III.B.1.4.2	Conversion of the Voxel Density Map to the Design-for-Manufacturing.	37
III.B.1.4.3	Sensitivity Analysis	38
III.B.1.4.4	Case Study	38
III.B.1.4.5	Set-up of Numerical Experiments	40
III.B.1.5	Results and Discussion	40
III.B.1.5.1	Influence of the Penalty Factor in the Geometry, Manufacturability and Mechanical Performance of the Design.	41
III.B.1.5.2	Influence of the Filter Radius in the Geometry, Manufacturability and Mechanical Performance of the Design.	43
III.B.1.5.3	Sensitivity Analysis	45
III.B.1.5.4	Evaluation of the Manufacturability and 3D Printed Pieces	46
III.B.1.6	Conclusions	47
III.B.1.6.1	Limitations	48
III.B.1.6.2	Future Work	48
III.B.2	Density-sensitive Implicit Functions Using Sub-voxel Sampling in Additive Manufacturing	49
III.B.2.1	Context	49
III.B.2.2	Introduction	50
III.B.2.3	Literature Review	52
III.B.2.3.1	Topology Optimization in Additive Manufacturing	52
III.B.2.3.2	Lattice Structures in Additive Manufacturing	53
III.B.2.3.3	Explicit Realization of the Results of Topology Optimization into Surface-based Lattices	53
III.B.2.3.4	Conclusions of the Literature Review	54
III.B.2.4	Methodology.	54
III.B.2.4.1	Formulation of SIMP	54
III.B.2.4.2	Morphology of Schwarz Primitive Lattice Structures	55
III.B.2.4.3	Relation between the Iso-value and the Relative Density of Schwarz Primitive Cells	58

III.B.2.4.4	Lattice Iso-value as Function of the Relative Density	59
III.B.2.4.5	Generation of Variable-density Surface Lattice Structures	60
III.B.2.4.6	Explicit Realization of a Density Field into Variable-density Surface Lattice Structures	62
III.B.2.5	Results	65
III.B.2.5.1	Density Field into Surface Lattice Structures. Applications in Topology Optimization	65
III.B.2.5.2	Physical Realization of the Devised Lattice Structures	68
III.B.2.5.3	Stress Concentration in Variable-density Surface Lattice Structures	70
III.B.2.6	Conclusions	74
III.B.2.7	Abbreviations	74
III.B.2.8	Appendix A. Iso-level Functions	76
III.B.3	Approximation of the Mechanical Response of Large Lattice Domains Using Homogenization and Design of Experiments	77
III.B.3.1	Context	77
III.B.3.2	Introduction	79
III.B.3.3	Literature Review	80
III.B.3.3.1	Lattice Structures and Material Homogenization	80
III.B.3.3.2	Modeling and Simulation of Lattice Structures	80
III.B.3.3.3	Conclusions of the Literature Review	81
III.B.3.4	Methodology	82
III.B.3.4.1	Schwarz Primitive Lattice Structures	82
III.B.3.4.2	Methodology to Estimate the Stress/Strain Response of Lattice Structures	82
III.B.3.4.3	Material Homogenization	84
III.B.3.4.4	Generation of Meta-models using DOE	85
III.B.3.5	Results	88
III.B.3.5.1	Validation of the Proposed Methodology	88
III.B.3.5.2	Application of Our Methodology to Large Lattice Domains	98
III.B.3.6	Conclusions	98
III.B.3.6.1	Future Work	99
III.C	Simulation of Laser Metal Deposition	100
III.C.1	2D Linear Finite Element Simulation of Laser Metal Heating for Digital Twins	101
III.C.1.1	Context	101
III.C.1.2	Introduction	102
III.C.1.3	Literature Review	103
III.C.1.3.1	Numerical Studies of Process Parameters in Additive Manufacturing	103
III.C.1.3.2	Digital Twins in Additive Manufacturing	103
III.C.1.3.3	Conclusions of the Literature Review	104
III.C.1.4	Methodology	104
III.C.1.4.1	Problem Description	104
III.C.1.4.2	Governing Equations	105
III.C.1.4.3	Galerkin Weak Form	106
III.C.1.4.4	Finite Element Discretization	106

III.C.1.4.5	Time Discretization	107
III.C.1.4.6	Modeling of the Heat Provided by the Laser	107
III.C.1.4.7	Finite Element Mesh and Boundary Conditions	109
III.C.1.4.8	Material Properties and Process Parameters for the Numerical Simulation	110
III.C.1.5	Results	111
III.C.1.5.1	Influence of the Laser Intensity Function	111
III.C.1.5.2	Influence of the Laser Radius	114
III.C.1.5.3	Influence of the Process Speed	116
III.C.1.5.4	Comparison with Non-linear Simulations	118
III.C.1.6	Conclusions and Future Work	118
III.C.2	Nonlinear Thermal Simulation of Laser Metal Deposition	120
III.C.2.1	Context	120
III.C.2.2	Introduction	123
III.C.2.3	Literature Review	123
III.C.2.3.1	Simulation of Laser Metal Deposition	123
III.C.2.3.2	Assessment of Temperature Predictions and Computational Resources	124
III.C.2.3.3	Representation of the Bead Geometry	124
III.C.2.3.4	Conclusions of the Literature Review	125
III.C.2.4	Methodology	125
III.C.2.4.1	Problem Description	125
III.C.2.4.2	Governing Equations	126
III.C.2.4.3	Model of the Energy Provided by the Laser	129
III.C.2.4.4	Temperature-Dependent Material Properties	130
III.C.2.4.5	Phase Change	131
III.C.2.4.6	Convection and Radiation Heat Losses	131
III.C.2.4.7	Material Deposition	132
III.C.2.4.8	Remeshing Strategy	133
III.C.2.4.9	Material Properties for the Computational Simulations	137
III.C.2.5	Results	138
III.C.2.5.1	Computational Results	139
III.C.2.5.2	Discussion	142
III.C.2.6	Conclusions	144
III.D	— Process Planning for Laser Metal Deposition	145
III.D.1	Generation of 2.5D Deposition Strategies for LMD-based Additive Manufacturing	146
III.D.1.1	Context	146
III.D.1.2	Introduction	148
III.D.1.3	Literature Review	148
III.D.1.3.1	Path Planning in Laser Metal Deposition	148
III.D.1.3.2	Conclusions of the Literature Review	149

III.D.1.4	Methodology	149
III.D.1.4.1	Workflow of the Generation of Trajectories in 2.5D	149
III.D.1.4.2	2D Infill Generation	151
III.D.1.4.3	CAM Trajectory Generation	152
III.D.1.4.4	Generation of Idle Paths	153
III.D.1.5	Results	154
III.D.1.5.1	CAM Trajectory Generation	154
III.D.1.5.2	Experimental Validation	157
III.D.1.6	Conclusions	158
III.D.2 Cylindrical Transform Slicing of Revolute Parts with Overhangs for Laser Metal Deposition		160
III.D.2.1	Context	160
III.D.2.2	Introduction	161
III.D.2.2.1	Scope	161
III.D.2.3	Literature Review	162
III.D.2.3.1	Conclusions of the Literature Review	162
III.D.2.4	Methodology	162
III.D.2.4.1	Cylindrical-Based Slicing for Overhanging Geometry	165
III.D.2.4.2	Toolpath Generation Using Isometric Parametrization	165
III.D.2.5	Results	166
III.D.2.6	Conclusions	168
III.D.3 Computational Minimization of Over-deposition at Corners of Trajectories in Laser Metal Deposition		169
III.D.3.1	Context	169
III.D.3.2	Introduction	170
III.D.3.3	Literature Review	170
III.D.3.3.1	Conclusions of the Literature Review	171
III.D.3.4	Methodology	171
III.D.3.4.1	Geometry Deposition Model	171
III.D.3.4.2	Minimization of Material Overfill in Corners	171
III.D.3.5	Results	173
III.D.3.6	Conclusions	174
III.D.4 Experimental and Computational Assessment of Minimizing Overfill in Trajectory Corners by Laser Velocity Control of Laser Cladding		177
III.D.4.1	Context	177
III.D.4.2	Introduction	179
III.D.4.2.1	Research target	179
III.D.4.2.2	Context	179
III.D.4.3	Literature review	180
III.D.4.3.1	Minimization of material overfill in trajectory corners	180
III.D.4.3.2	Registration for dimensional inspection	181
III.D.4.3.3	Bead topography models	183

III.D.4.4	Methodology	184
III.D.4.4.1	Material overfill in trajectory corners in LMD	185
III.D.4.4.2	Geometry deposition simulator	186
III.D.4.4.3	Minimization of material overfill at corners in LMD	187
III.D.4.4.4	Materials for the experiments and the 3D scanning	189
III.D.4.4.5	Registration of the experimental corners	190
III.D.4.5	Results	192
III.D.4.5.1	Computational results	192
III.D.4.5.2	Experimental validation	197
III.D.4.5.3	Comparison of the predicted vs. experimental corners	198
III.D.4.5.4	Similarities and differences with other approaches	202
III.D.4.6	Conclusions	203
III.D.5	Synthesis of Reeb Graph and Morse Operators from Level Sets of a Boundary Representation	205
III.D.5.1	Context	205
III.D.5.2	Introduction	206
III.D.5.3	Literature Review	207
III.D.5.3.1	Conclusion of Literature Review	208
III.D.5.4	Methodology	208
III.D.5.4.1	Level sets extraction	209
III.D.5.4.2	Nodes definition	209
III.D.5.4.3	Edges definition	210
III.D.5.5	Results	212
III.D.5.6	Conclusions	212
IV	General Conclusions	215
IV.A	— Contributions	216
IV.B	— Future Directions and Opportunities	218
	Bibliography	220

Part I

Introduction

I.A

Organization of this Document

This document is organized as follows:

- Part I: Introduction. This part states the goal of the Doctoral Final Examination.
- Part II: Academic Trajectory. This part reports the following aspects of the doctoral process:
 - (a) Summary of the student's academic history
 - (b) List of publications and co-authors
 - (c) Doctoral courses and exams
 - (d) Personalized special trainings
 - (e) Attendance to specialized forums
 - (f) Special advisors provided by the Universidad EAFIT and Vicomtech
 - (g) Industrial projects undertaken in the scope of the doctoral internship
- Part III: Research Results. This part reports:
 - (a) An overview of the domains in which the doctoral investigation has been conducted.
 - (b) The compendium of publications generated in each of the investigated domains.
- Part IV: General Conclusions.

I.B

Goal of the Final Examination

Under the regulations of the Doctoral Program in Engineering at the Universidad EAFIT, the purpose of the Final Examination is to assess the thesis work of the doctoral student, which should reflect the capacity of the student to (I) conduct high-quality scientific research, (II) contribute to the state of the art, and (III) articulate in novel manners the existing knowledge to advance in the formulation and solution of theoretical and practical problems in the Engineering domain.

The Final Exam assesses the following aspects:

1. The academic trajectory and opportunities profited by the doctoral student during the doctoral studies, in terms of (a) Doctoral courses, (b) Special trainings, (c) Attendance to specialized forums and industries (d) Equipment, software, accessory materials, (e) Funding proceedings, (f) Special advisors, etc.
2. The thematically connected results of the research of the student and the doctoral team, and the endorsement of the international scientific community to these results, in the form of ranked publications.

The Jury either approves or reproves the thesis work of the doctoral student.

Part II

Academic Trajectory

II.A

Academic History

II.A.1

Summary

Table II.A.1.1: Doctoral student's academic trajectory. Summary.

Date	Academic Status	Comment
July 2016	Undergrad student. Mathematical Engineering	Diego Alejandro Montoya Zapata, the Doctorand, joined the Laboratory of CAD CAM CAE at the Universidad EAFIT, under the supervision of Prof. Dr. Eng. Oscar Ruiz Salguero.
Dec. 2016	Undergrad student. Mathematical Engineering	The Doctorand obtained his bachelor's degree in Mathematical Engineering at the Universidad EAFIT.
Jan. 2017	Master student in Engineering	The Doctorand started his Master in Science studies in Engineering at the Laboratory of CAD CAM CAE, Universidad EAFIT, under the supervision of Prof. Dr. Eng. Oscar Ruiz.
Jan. 2018 - Dec. 2018	Master student in Engineering	The Doctorand undertook a research internship at the Department of Industry and Advanced Manufacturing at Vicomtech, Spain, under the mentoring of Dr. Eng. Jorge Posada (Supervisor) and Dr. Eng. Aitor Moreno (Daily Supervisor).
Dec. 2018	Master student in Engineering	The Doctorand obtained his M.Sc. degree in Engineering at the Universidad EAFIT. Master thesis titled: "Compendium of Publications on: Computational Geometry and Numerical Simulation in Applications of Computational Mechanics".

Continued on next page

Table II.A.1.1 – *Continued from previous page*

Date	Academic Status	Comment
Jan. 2019	Doctoral student in Engineering	The Doctorand started his Doctoral studies in Engineering at the Universidad EAFIT under the mentoring of Prof. Dr. Eng. Oscar Ruiz, Supervisor (Universidad EAFIT, Colombia), Dr. Eng. Jorge Posada, Co-Supervisor (Vicomtech, Spain) and Dr. Eng. Aitor Moreno, Daily Supervisor (Vicomtech, Spain).
Jan. 2019 - Dec. 2022 (projected)	Doctoral student in Engineering	The Doctorand continued his research internship at the Department of Industry and Advanced Manufacturing at Vicomtech (Spain) as part of his Doctoral Thesis.
Jan. 2018 - Dec. 2022 (projected)	Master student in Engineering (2018). Doctoral student in Engineering (2019-2022)	The Doctorand received collaborative funding as part of a joint sponsorship provided by the Universidad EAFIT and Vicomtech for his M.Sc. and Ph.D. studies.

II.A.2

List of Publications - Doctoral Period

In the framework of the collaborative program between the Universidad EAFIT and Vicomtech, the student and his doctoral support team achieved several publications. These publications formalized the doctoral work of the student. The doctoral support team comprises both doctoral supervisors (Prof. Oscar Ruiz Salguero and Dr. Jorge Posada) and several researchers from the Universidad EAFIT and Vicomtech. Tables II.A.2.1 and II.A.2.2 report the journal and conference publications achieved by the student and his support team during the Doctoral period (2019 - 2022).

Table II.A.2.1: List of published and submitted journal articles of the doctoral support team. **Doctoral period.** Inverse chronological order.

Item	Bibliographic Information	Status	Indexing
0	Diego Montoya-Zapata, Aitor Moreno, Igor Ortiz, Jorge Posada, Oscar Ruiz-Salguero. Computer supported toolpath planning for LMD additive manufacturing based on cylindrical slicing. In process of publication.	In process of publication	N/A
1	Diego Montoya-Zapata, Jorge Posada, Piera Alvarez, Carles Creus, Aitor Moreno, Igor Ortiz and Oscar Ruiz-Salguero. Experimental and computational assessment of minimizing overfill in trajectory corners by laser velocity control of laser cladding. <i>International Journal of Advanced Manufacturing Technology</i> . Springer London. ISSN: 0268-3768. e-ISSN: 1433-3015. 2022 , 119(9), pp. 6393-6411, DOI: doi.org/10.1007/s00170-021-08641-8	Published	JCR(Q2), SCOPUS(Q1), Publindex(A1), Scimago(Q1)

Continued on next page

Table II.A.2.1 – *Continued from previous page*

Item	Bibliographic Information	Status	Indexing
2	Diego Montoya-Zapata, Juan M. Rodríguez, Aitor Moreno, Oscar Ruiz-Salguero and Jorge Posada. Nonlinear thermal simulation of Laser Metal Deposition. <i>Australian Journal of Mechanical Engineering</i> . Taylor & Francis. ISSN: 1448-4846. e-ISSN: 2204-2253. 2021 , 19(5), pp. 653–668, DOI: doi.org/10.1080/14484846.2021.1988435	Published	SCOPUS(Q3), JCI(Q3), Publindex(B), Scimago(Q3)
3	Diego Montoya-Zapata, Juan M. Rodríguez, Aitor Moreno, Jorge Posada and Oscar Ruiz-Salguero. 2D linear finite element simulation of laser metal heating for digital twins. <i>International Journal for Simulation and Multidisciplinary Design Optimization</i> . EDP Sciences. eISSN 1779-6288. 2021 , 12, 11, DOI: doi.org/10.1051/smdo/2021011	Published	SCOPUS(Q4), Publindex(C), Scimago(Q4)
4	Diego Montoya-Zapata, Carles Creus, Aitor Moreno, Igor Ortiz, Piera Alvarez, Oscar Ruiz-Salguero and Jorge Posada. Computational minimization of over-deposition at corners of trajectories in Laser Metal Deposition. <i>Manufacturing Letters</i> . Elsevier. ISSN 2213-8463. 2021 , 29, pp. 29-33, DOI: doi.org/10.1016/j.mfglet.2021.05.001	Published	SCOPUS(Q1), JCI(Q2), Publindex(A1), Scimago(Q1)
5	Diego Montoya-Zapata, Diego A. Acosta, Camilo Cortes, Juan Pareja-Corcho, Aitor Moreno, Jorge Posada and Oscar Ruiz-Salguero. Approximation of the mechanical response of large lattice domains using homogenization and design of experiments. <i>Applied Sciences</i> . MDPI. ISSN: 2076-3417. 2020 , 10(11), 3858, DOI: doi.org/10.3390/app10113858	Published	JCR(Q2), SCOPUS(Q2), Publindex(A1), Scimago(Q1)
6	Diego Montoya-Zapata, Aitor Moreno, Juan Pareja-Corcho, Jorge Posada and Oscar Ruiz-Salguero. Density-sensitive implicit functions using sub-voxel sampling in additive manufacturing. <i>Metals</i> . MDPI. ISSN: 2075-4701. 2019 , 9(12), 1293, DOI: doi.org/10.3390/met9121293	Published	JCR(Q1), SCOPUS(Q2), Publindex(A1), Scimago(Q2)

Table II.A.2.2: List of published conference articles of the doctoral support team. **Doctoral period.** Inverse chronological order.

Item	Bibliographic Information	Status	Indexing / Qualification
1	Diego Montoya-Zapata, Aitor Moreno, Igor Ortiz, Oscar Ruiz-Salguero and Jorge Posada. (2022). Cylindrical transform slicing of revolute parts with overhangs for Laser Metal Deposition. In <i>XXXI Spanish Computer Graphics Conference (CEIG 2022)</i> . July 5-8, Vic, Spain. ISBN: 978-3-03868-186-1. DOI: doi.org/10.2312/ceig.20221141.	Published	Eurographics Digital Library
2	Juan Pareja-Corcho, Diego Montoya-Zapata, Carlos Cadavid, Aitor Moreno, Jorge Posada, Ketzare Arenas-Tobon and Oscar Ruiz-Salguero. (2022). Synthesis of Reeb graph and Morse operators from level sets of a boundary representation. In <i>XXXI Spanish Computer Graphics Conference (CEIG 2022)</i> . July 5-8, Vic, Spain. ISBN: 978-3-03868-186-1. DOI: doi.org/10.2312/ceig.20221140.	Published	Eurographics Digital Library
3	Diego Montoya-Zapata, Carles Creus, Igor Ortiz, Piera Alvarez, Aitor Moreno, Jorge Posada, Oscar Ruiz-Salguero. (2020). Generation of 2.5D deposition strategies for LMD-based additive manufacturing. <i>Procedia Computer Science</i> . 180, pp. 280-289. ISSN: 1877-0509. International Conference on Industry 4.0 and Smart Manufacturing (ISM 2020). November 23-25, Hagenberg, Austria. (Virtual attendance). DOI: doi.org/10.1016/j.procs.2021.01.165	Published.	SCOPUS, INSPEC
4	Diego Montoya-Zapata, Diego A. Acosta, Camilo Cortes, Juan Pareja-Corcho, Aitor Moreno, Jorge Posada and Oscar Ruiz-Salguero. (2020). Meta-modeling of lattice mechanical responses via design of experiments. In <i>2nd International Conference on Mathematics and Computers in Science and Engineering (MACISE 2020)</i> . January 18-20, Madrid, Spain. pp. 308-317. DOI: doi.org/10.1109/MACISE49704.2020.00065. ISBN: 978-1-7281-6696-4	Published.	SCOPUS, Web of Science

Continued on next page

Table II.A.2.2 – *Continued from previous page*

Item	Bibliographic Information	Status	Indexing / Qualification
5	Diego Montoya-Zapata, Diego A. Acosta, Aitor Moreno, Jorge Posada and Oscar Ruiz-Salguero. (2019). Sensitivity analysis in shape optimization using voxel density penalization. In <i>XXIX Spanish Computer Graphics Conference (CEIG 2019)</i> . June 26-28, Donostia - San Sebastián, Spain. ISBN: 978-3-03868-093-2. DOI: doi.org/10.2312/ceig.20191201.	Published	Eurographics Digital Library, Web of Science, SCOPUS

II.A.3

List of Publications - Master Period

Tables II.A.3.1 and II.A.3.2 report the journal and conference publications achieved by the student and his support team during the Master period (2017 - 2018).

Table II.A.3.1: List of published journal articles published. **Master period.** Inverse chronological order.

Item	Bibliographic Information	Status	Indexing
1	Diego Montoya-Zapata, Camilo Cortes and Oscar Ruiz-Salguero. FE-simulations with a simplified model for open-cell porous materials: A Kelvin cell approach. <i>Journal of Computational Methods in Sciences and Engineering</i> . IOS Press. ISSN: 1472-7978. e-ISSN: 1875-8983. 2019 , 19(4), p. 989-1000. DOI: doi.org/10.3233/JCM-193669	Published	SCOPUS(Q3), Publindex(A2), Scimago(Q3)
2	Diego Montoya-Zapata, Diego A. Acosta, Oscar Ruiz-Salguero, Jorge Posada and David Sanchez-Londono. A General Meta-graph Strategy for Shape Evolution under Mechanical Stress. <i>Cybernetics and Systems</i> . Taylor & Francis. ISSN: 0196-9722. e-ISSN: 1087-6553. 2019 , 50(1), p. 3-24. DOI: doi.org/10.1080/01969722.2018.1558011	Published	JCR(Q3), SCOPUS(Q2), Publindex(A2), Scimago(Q2)
3	Daniel Mejia-Parra, Diego Montoya-Zapata, Ander Arbelaiz, Aitor Moreno, Jorge Posada and Oscar Ruiz-Salguero. Fast analytic simulation for multi-laser heating of sheet metal in GPU. <i>Materials</i> . MDPI. e-ISSN: 1996-1944. 2018 , 11(11), 2078. DOI: doi.org/10.3390/ma11112078.	Published	JCR(Q2), SCOPUS(Q2), Publindex(A2), Scimago(Q2)

Table II.A.3.2: List of published conference articles. **Master period.** Inverse chronological order.

Item	Bibliographic Information	Status	Indexing / Qualification
1	<p>Juan M. Muñoz-Betancur, Oscar Ruiz-Salguero, Diego Montoya, Camilo Cortes and Carlos Cadavid. (2018). Direct Scalar Field - to - Truss Representation and Stress Simulation of Open Pore Domains. In <i>Smart Tools and Applications in Graphics (STAG 2018)</i>. Eurographics Italian Chapter Annual Event. October 18-19, Brescia, Italy. ISBN: 978-3-03868-075-8. DOI: doi.org/10.2312/stag.20181295.</p>	Published	EUROGRAPHICS Digital Library, SCOPUS
2	<p>Diego Montoya-Zapata, Diego A. Acosta, Oscar Ruiz-Salguero and David Sanchez-Londono. (2018). FEA Structural Optimization Based on Metagraphs. In <i>International Conference on Soft Computing Models in Industrial and Environmental Applications (SOCO 2018)</i>. June 6-8, Donostia - San Sebastián, Spain. ISBN: 978-3-319-94119-6. DOI: doi.org/10.1007/978-3-319-94120-2_20.</p>	Published	SCOPUS, Web of Science
3	<p>Diego Montoya-Zapata, Oscar Ruiz-Salguero, Juan Lalinde-Pulido, Juan Pareja-Corcho and Jorge Posada. (2018). Non-manifold modelling of lattice materials using kinematically constrained FEA. In <i>Proceedings of the 12th International Symposium on Tools and Methods of Competitive Engineering (TMCE 2018)</i>. May 7-11, Las Palmas de Gran Canaria, Spain. ISBN: 978-94-6186-910-4.</p>	Published	

II.A.4

List of Co-authors

The reader may notice the thematic continuity of the Doctoral investigation with respect to the Master's, as shown by the Doctoral and Master publications reported in Tables II.A.2.1–II.A.3.2. Because of this close relationship between the Doctoral and Master research topics, the lists of co-authors of the Doctoral and Master publications are very similar. Table II.A.4.1 reports the names and affiliations of the co-authors of the articles listed in Tables II.A.2.1–II.A.3.2.

Table II.A.4.1: Co-authors of the articles in the Master and Doctoral periods. Tables II.A.2.1–II.A.3.2.

Name	Affiliation
Prof. Dr. Eng. Oscar Ruiz Salguero	Laboratory of CAD CAM CAE, Universidad EAFIT
Dr. Eng. Jorge Posada	Associate Director, Vicomtech
Prof. Dr. Eng. Diego A. Acosta	Grupo de Desarrollo y Diseño de Procesos, Universidad EAFIT
M.Sc. Eng. Piera Alvarez	Ikerkune A.I.E.
Dr. Eng. Ander Arbelaiz	Industry and Advanced Manufacturing, Vicomtech
Eng. Ketzare Arenas Tobon	Laboratory of CAD CAM CAE, Universidad EAFIT
Prof. Dr. Sc. Math. Carlos Cadavid	Mathematics and Applications, Universidad EAFIT
Dr. Eng. Camilo Cortés	Digital Health and Biomedical Technologies, Vicomtech
Dr. Eng. Carles Creus	Industry and Advanced Manufacturing, Vicomtech
Dr. Eng. Juan Guillermo Lalinde Pulido	High Performance Computing Facility APOLO, Universidad EAFIT
Dr. Eng. Daniel Mejía Parra	Laboratory of CAD CAM CAE, Universidad EAFIT
Dr. Eng. Aitor Moreno	Industry and Advanced Manufacturing, Vicomtech
Eng. Juan M. Muñoz Betancur	Laboratory of CAD CAM CAE, Universidad EAFIT

Continued on next page

Table II.A.4.1 – *Continued from previous page*

Name	Affiliation
M.Sc. Eng. Juan Pareja Corcho	Laboratory of CAD CAM CAE, Universidad EAFIT
M.Sc. Eng. Igor Ortiz	Ikerkune A.I.E.
Prof. Dr. Eng. Juan M. Rodríguez	Department of Mechanical Engineering, Universidad EAFIT
M.Sc. Eng. David Sánchez Londoño	Laboratory of CAD CAM CAE, Universidad EAFIT

II.A.5

Doctoral Courses

II.A.5.1 Preparatory Courses

According to the regulations of the Universidad EAFIT, the courses that prepare the student to perform his doctoral thesis are taken during the Master and Doctoral programs. Table II.A.5.1 presents the preparatory courses that the student took:

Table II.A.5.1: Master (2017 to 2018) and Doctoral (2019 to 2021) preparatory courses.

Ph.D. / M.Sc. Course	Semester	Academic Status
IC0692 - Introduction to the Boundary Element Method	2017-1	Master student
IC0682 - Advanced Continuum Mechanics	2017-1	Master student
IM0819 - Underlying Mathematics for CAD CAM	2017-1	Master student
ST0920 - Advanced Data Structures and Algorithms	2017-1	Master student
EI0813 - Research Tools	2017-2	Master student
IC0602 - Introduction to the Finite Element Method	2017-2	Master student
IC0695 - Advanced Mathematics for Engineers	2017-2	Master student
IM0923 - Design Optimization	2017-2	Master student
IM0906 - Computer Aided Geometric Design I	2018-1	Master student
IM0904 - Optimization Techniques	2019-1	Doctoral student
PR0902 - Statistics for Researchers	2019-2	Doctoral student
IM0926 - Non-linear Finite Element Method	2020-1	Doctoral student
IM0912 - Numerical Solutions of Differential Equations	2020-2	Doctoral student
IM0916 - Computational Geometry	2021-1	Doctoral student
IM0929 - Dimensionality Reduction	2021-2	Doctoral student

II.A.5.2 Qualifying Exams

Table II.A.5.2 reports the doctoral qualifying exams that the student took and approved during the first and second years of the doctoral program.

Table II.A.5.2: Qualifying exams.

Subject	Examiner	Result	Date
Design of Experiments and Statistical Methods	Prof. Dr. Eng. Diego Andrés Acosta Maya, Universidad EAFIT	Approved	December 2019
Computational Mechanics	Prof. Dr. Eng. Juan Manuel Rodríguez Prieto, Universidad EAFIT	Approved	July 2020

II.A.5.3 Preliminary Exam of Dissertation

During the third year of the doctoral studies, the student prepared, presented and approved the Preliminary Exam of Dissertation. The Preliminary Examination assessed: (a) the academic trajectory undertaken and opportunities profited by the doctoral student during the first 36 months of the doctoral studies, (b) the thematically connected results of the research of the student and the doctoral team in the form of ranked publications, and (c) the closure research activities and goals of the doctoral student and supporting team for the remaining 12 months (approx.).

On December 15, 2021, the Jury (see Table II.A.5.3) decided to permit the doctoral student to continue the academic and research activities, in order to prepare and perfect the materials, goals, publications, etc. for the Final Examination.

Table II.A.5.3: Preliminary exam of dissertation.

Supervisors	Jury	Result	Date
Prof. Dr. Eng. Oscar E. Ruiz Salguero, Universidad EAFIT	Dr. Eng. Aitor Moreno Guerrero, Vicomtech	Approved	December 15, 2021
Dr. Eng. Jorge L. Posada Velásquez, Vicomtech	Dr. Eng. Daniel Mejía Parra, Vicomtech		

II.A.6

Personalized Special Trainings

Table II.A.6.1 presents the trainings undertaken by the student as part of the doctoral formation:

Table II.A.6.1: Personalized special trainings.

Topic	Entity	Context	Date	Advisor
Process Planning for Laser Metal Deposition	INZU Group (Ikergune, Talens, Etxe-tar, Izadi, Macarbox, and 8 more companies)	Industrial Collaboration Agreement:	Nov. 2019 - Dec. 2022 (projected)	M.Sc. Eng. Igor Ortiz
	(a) Ikergune: R&D unit of the INZU Group	Vicomtech - INZU Group		Dr. Chem. M. Angeles Montealegre
	(b) Talens: Heat and laser applications			Dr. Eng. Alejandro Vioria
	(c) Etxe-tar: Machine tool manufacturing			
	(d) Izadi: Machining, repair and assembly services for industrial equipment			
(e) Macarbox: Cardboard product machining center				

II.A.7

Attendance to Specialized Forums - Doctoral Period

The student attended the following specialized forums during his doctoral formation:

II.A.7.1 Scientific Conferences - Doctoral Period

1. **CEIG 2022 - XXXI Spanish Computer Graphics Conference**, July 2022. Vic, Spain. Presentation and publication of two articles:
 - (a) “Cylindrical transform slicing of revolute parts with overhangs for Laser Metal Deposition; Diego Montoya-Zapata, Aitor Moreno, Igor Ortiz, Oscar Ruiz-Salguero and Jorge Posada”
 - (b) “Synthesis of Reeb graph and Morse operators from level sets of a boundary representation; Juan Pareja-Corcho, Diego Montoya-Zapata, Carlos Cadavid, Aitor Moreno, Jorge Posada, Ketzare Arenas-Tobon and Oscar Ruiz-Salguero”
2. **EUROGRAPHICS 2021 - 42nd Annual Conference of the European Association for Computer Graphics**: Organized by the Research Unit of Computer Graphics at TU Wien. May 3-7, 2021. Virtual attendance.
3. **ISM 2020 - International Conference on Industry 4.0 and Smart Manufacturing**, November 2020. Virtual attendance. Presentation and publication of the article “Generation of 2.5D deposition strategies for LMD-based additive manufacturing; Diego Montoya-Zapata, Carles Creus, Igor Ortiz, Piera Alvarez, Aitor Moreno, Jorge Posada, Oscar Ruiz-Salguero”.
4. **ICONACES 2020 - International Conference on Applications in Computational Engineering & Sciences**, October 2020. Virtual attendance. Presentation of the extended abstract “2D thermal model for laser heating processes: A finite element approach; Diego Montoya-Zapata, Juan M. Rodríguez, Aitor Moreno, Jorge Posada, Oscar Ruiz-Salguero”.
5. **MACISE 2020 - 2nd International Conference on Mathematics and Computers in Science and Engineering**, January 2020. Madrid, Spain. Presentation and publication of the article “Meta-modeling of lattice mechanical responses via design of experiments; Diego

Montoya-Zapata, Diego A. Acosta, Camilo Cortes, Juan Pareja-Corcho, Aitor Moreno, Jorge Posada and Oscar Ruiz-Salguero”.

6. **CEIG 2019 - XXIX Spanish Computer Graphics Conference**, June 2019. San Sebastián, Spain. Presentation and publication of the article “Sensitivity analysis in shape optimization using voxel density penalization; Diego Montoya-Zapata, Diego A. Acosta, Aitor Moreno, Jorge Posada and Oscar Ruiz-Salguero”.

II.A.7.2 Professional Forums - Doctoral Period

1. **Doctoral Internship:** Vicomtech. Industry and Advanced Manufacturing. January 2019 to December 2022 (projected). Donostia - San Sebastián, Spain.
2. **M.Sc. Internship:** Vicomtech. Industry and Advanced Manufacturing. January 2018 to December 2018. Donostia - San Sebastián, Spain.
3. **Additive Talks 2022. Addit3D - International Fair of Additive Manufacturing and 3D Printing. International Machine-Tool Biennial (BIEMH 2022).** Organized by Bilbao Exhibition Centre and ADDIMAT. June 17, 2022. Bilbao, Spain.
4. **PostAdditive 2019: Conferencia sobre Tecnologías de Posprocesado en Fabricación Aditiva (Conference on Postprocessing Technologies for Additive Manufacturing).** Organized by CIDETEC Surface Engineering. November 6-7, 2019. Donostia - San Sebastián, Spain.
5. **CMH 2019: Congreso de Máquina-Herramienta (Conference on Machine-Tool).** Organized by AFM Cluster for Advanced and Digital Manufacturing. October 23-25, 2019. Donostia - San Sebastián, Spain.

II.A.8

Attendance to Specialized Forums - Master Period

The student attended the following specialized forums during his master's formation:

II.A.8.1 Scientific Conferences - Master Period

1. **STAG 2018 - Smart Tools and Applications in Graphics:** Presentation and publication of the article “Direct scalar field-to-truss representation and stress simulation of open pore domains; Juan M. Muñoz-Betancur, Oscar Ruiz-Salguero, Diego Montoya, Camilo Cortes and Carlos Cadavid”. October 2018. Brescia, Italy.
2. **SOCO 2018 - International Conference on Soft Computing Models in Industrial and Environmental Applications:** Presentation and publication of the article “FEA structural optimization based on metagraphs; Diego Montoya-Zapata, Diego A. Acosta, Oscar Ruiz-Salguero and David Sanchez-Londono”. June 2018. San Sebastián, Spain.
3. **TMCE 2018 - Twelfth International Symposium on Tools and Methods of Competitive Engineering:** Presentation and publication of the article “Non-manifold modelling of lattice materials using kinematically constrained FEA; Diego Montoya-Zapata, Oscar Ruiz-Salguero, Juan Lalinde-Pulido, Juan Pareja-Corcho and Jorge Posada”. May 2018. Las Palmas de Gran Canaria, Spain.

II.A.8.2 Scientific Trainings - Master Period

1. **PhD School: International School on Graphics and Geometry Processing for Digital Manufacturing.** Organized by the Italian Chapter of EUROGRAPHICS. October 16-18, 2018. Brescia, Italy.

II.A.9

Special Advisors Provided by the Universidad EAFIT and Vicomtech

Table II.A.9.1 presents the specialists, besides the two Supervisors, from the Universidad EAFIT and Vicomtech who advised the student during his doctoral formation:

Table II.A.9.1: Special advisors, besides the two supervisors, provided by the Universidad EAFIT and Vicomtech.

Name	Role	Entity	Topic
Dr. Eng. Aitor Moreno	(a) Daily Supervisor (b) Scientific coordinator and advisor (c) Head of AdditiCAM and AMGLib	Industry and Advanced Manufacturing, Vicomtech, Spain	Computational geometry. Path planning for Additive Manufacturing.
Prof. Dr. Eng. Diego A. Acosta	Scientific coordinator and advisor	Design and Development of Processes and Products Research Group (DDP), Universidad EAFIT, Colombia	Optimization techniques. Design of experiments.
Prof. Dr. Math. Carlos Cadavid	Scientific coordinator and advisor	Mathematics and Applications, Universidad EAFIT, Colombia	Morse and Reeb theory.
Dr. Eng. Camilo Cortés	(a) Scientific coordinator and advisor (b) Head of MAKBY	Digital Health and Biomedical Technologies, Vicomtech, Spain	Modeling of lattice structures. Computational mechanics.
Dr. Eng. Carles Creus	Advisor	Industry and Advanced Manufacturing, Vicomtech, Spain	Computational geometry. C++ programming.

Continued on next page

Table II.A.9.1 – *Continued from previous page*

Name	Role	Entity	Topic
Prof Dr. Eng. Juan G. Lalinde	Scientific coordinator and advisor	High Performance Computing facility APOLO, EAFIT, Colombia.	Data structures and algorithms.
Dr. Eng. Daniel Mejía	Advisor	Industry and Advanced Manufacturing, Vi-comtech, Spain	Computational geometry. Path planning for Additive Manufacturing.
Prof. Dr. Eng. Juan M. Rodríguez	Scientific coordinator and advisor	Department of Mechanical Engineering, Universidad EAFIT, Colombia.	Computational mechanics. Numerical methods. Nonlinear Finite Element Method.

II.A.10

Industrial Projects Undertaken in the Scope of the Doctoral Internship at Vicomtech

Table II.A.10.1 reports the participation of the student in projects during his internship at Vicomtech. The projects were related to Computational Geometry, CAD CAM CAE, Industry and Manufacturing:

Table II.A.10.1: Industrial projects undertaken in the scope of the Doctoral internship at Vicomtech.

Code	Acronym	Title	Funding entity	Comments
	AdditiCAM	Software CAD/CAM for Additive Manufacturing	Direct industrial contract: INZU Group	<ul style="list-style-type: none"> (a) Cross-platform SDK to support CAD and CAM in Laser Metal Deposition manufacturing. (b) Application of computational geometry and graph algorithms for LMD process planning in 3D geometry. (c) Neutral formats trajectory exporting for customization to the additive manufacturing machine.
KK-2018/00115	Addisend	Cooperación científica en fabricación aditiva para control robusto de la cadena de valor	Basque Government. ELKARTEK program	English title: Scientific cooperation in Additive Manufacturing for the robust control of the value chain

Continued on next page

Table II.A.10.1 – *Continued from previous page*

Code	Acronym	Title	Funding entity	Comments
KK-2018/00071	LangileOK	Tecnologías avanzadas de apoyo a los operarios de la Industria 4.0	Basque Government. ELKARTEK program	English title: Advanced technologies to support the operators in the Industry 4.0
KK-2019/00006	B4H	Investigación fundamental colaborativa para la bioimpresión de constructos cutáneos aplicados al tratamiento de heridas crónicas	Basque Government. ELKARTEK program	English title: Collaborative fundamental research for the bioprinting of cutaneous constructs applied to the treatment of chronic wounds
	AMGLib	Additive Manufacturing Generic Library	Vicomtech. Internal resources	<ul style="list-style-type: none"> (a) Cross-platform SDK focused on additive manufacturing. (b) Geometric operations for the generation of CAM (Computer-Aided Manufacturing) models. (c) Algorithms for the generation of 2D and 3D CAM trajectories.
	MAKBY	Making Bioprinting Easy	Vicomtech. Internal resources. Selected in the competitive post-covid internal call	<ul style="list-style-type: none"> (a) SDK to ease the end-user's configuration for the generation of high-quality models for bioprinting. (b) Configuration of multi-material models. (c) Path-planning optimization to minimize extrusion interruption and material overlapping.

Part III

Research Results

III.A

Summary of Contributions

This thesis presents contributions to the field of Computational Geometry Applied to Additive Manufacturing. Fig. 1 shows an overview of the areas of Computational Geometry addressed in this thesis: (i) Shape Optimization in Lattice Structures, (ii) Simulation of Laser Metal Deposition and (iii) Process Planning for Laser Metal Deposition.

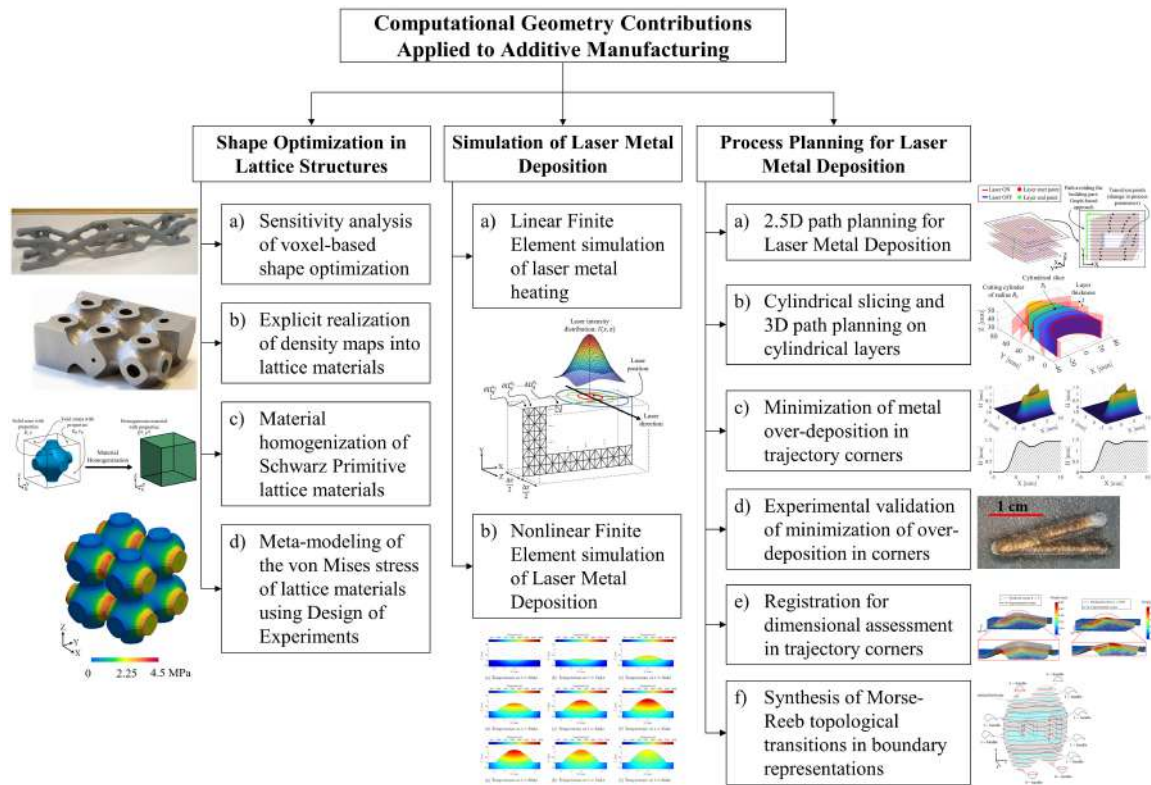


Figure 1: Overview of the contributions of this thesis to Computational Geometry and its applications to Additive Manufacturing.

Table 1 summarizes the contributions to the three areas of Computational Geometry addressed in this thesis: (i) Shape Optimization in Lattice Structures, (ii) Simulation of Laser Metal Deposition and (iii) Process Planning for Laser Metal Deposition.

Table 1: Summary of the contributions of this thesis to Computational Geometry and its applications to Additive Manufacturing.

Applied Domain	Contributions
Shape Optimization in Lattice Structures	<ul style="list-style-type: none"> <li data-bbox="548 411 1352 533">(a) Sensitivity analysis of the Solid Isotropic Material with Penalization (SIMP) strategy for shape optimization. The SIMP method seeks a redistribution of local voxel-densities of a part in order to stand mechanical demands [121]. <li data-bbox="548 558 1352 709">(b) Explicit realization of lattice structures that follow the distribution of non-manufacturable density maps prescribed by shape optimization algorithms (e.g. SIMP). The produced lattice structures are successfully manufactured via Additive Manufacturing (fused deposition modeling, selective laser melting and binder jetting) [127]. <li data-bbox="548 735 1352 827">(c) Material homogenization of Schwarz Primitive lattice materials for efficient Finite Element Analysis of large Schwarz lattice domains [119, 120]. <li data-bbox="548 852 1352 1003">(d) Generation of simplified mathematical functions (meta-models) that relate the stress/strain behavior of the Schwarz lattice domains with the displacements of prismatic domains with <u>diluted</u> material properties. The meta-model generation follows methods of Design of Experiments [120].
Simulation of Laser Metal Deposition	<ul style="list-style-type: none"> <li data-bbox="548 1100 1352 1222">(a) Linear Finite Element simulation of laser heating on a metallic substrate. The analysis is confined to a 2D cross-section of the substrate assuming constant and stable process parameters (tool-head speed and laser power) [130]. <li data-bbox="548 1247 1352 1430">(b) Nonlinear Finite Element simulation of Laser Metal Deposition. The implemented model considers temperature-dependent material properties, phase change and radiation. The analysis is confined to a 2D cross-section of the substrate assuming constant and stable process parameters (tool-head speed, powder deposition rate and laser power) [129].

Continued on next page

Table 1 – *Continued from previous page*

Applied Domain	Contributions
Process Planning for Laser Metal Deposition	<ul style="list-style-type: none"> (a) Implementation of 2.5D path planning for Laser Metal Deposition which includes a graph-based algorithm for 2D region avoidance during the laser repositioning [125]. (b) Implementation of cylindrical slicing and 3D path planning on cylindrical layers for the manufacturing of overhanging features of revolution workpieces via laser metal deposition [126]. (c) Development of a computational minimization module for limiting metal over-deposition in trajectory corners in Laser Metal Deposition [124, 128]. (d) Experimental validation of the computational minimization algorithm for limiting over-deposition in trajectory corners in Laser Metal Deposition [128]. (e) Implementation of datum-based registration for dimensional assessment in trajectory corners in Laser Metal Deposition [128]. (f) Methodology for the generation of the Reeb Graph from discrete level sets (slices) of the boundary representation of a closed 2-manifold \mathcal{M} [138].

Some of the formal scientific concepts relevant to this research are presented in Table 2.

Table 2: Formal scientific concepts relevant to this research.

Mathematical / Computer Science Concept	Area of Application
Coordinate frames	Process Planning for Laser Metal Deposition
Coordinate transformation	Process Planning for Laser Metal Deposition
Delaunay triangulation	Simulation of Laser Metal Deposition
Design of experiments	Shape Optimization in Lattice Structures
Exhaustive search method	Process Planning for Laser Metal Deposition
Graph theory, Dijkstra’s algorithm	Process Planning for Laser Metal Deposition
Linear/Nonlinear Finite Element Method	Simulation of Laser Metal Deposition, Shape Optimization in Lattice Structures
Material homogenization	Shape Optimization in Lattice Structures
Morse theory, Reeb graph	Process Planning for Laser Metal Deposition
Newton-Raphson method	Simulation of Laser Metal Deposition

Continued on next page

Table 2 – *Continued from previous page*

Mathematical / Computer Science Concept	Area of Application
Nonlinear optimization	Shape Optimization in Lattice Structures, Process Planning for Laser Metal Deposition
Numerical integration, Gauss quadrature	Simulation of Laser Metal Deposition, Process Planning for Laser Metal Deposition
Shape optimization	Shape Optimization in Lattice Structures
Surface parametrization	Process Planning for Laser Metal Deposition
Principal component analysis	Process Planning for Laser Metal Deposition

III.B

Shape Optimization in Lattice Structures

III.B.1

Sensitivity Analysis in Shape Optimization using Voxel Density Penalization

Diego Montoya-Zapata^{1,2}, Diego A. Acosta³, Aitor Moreno², Jorge Posada² and Oscar Ruiz-Salguero¹

¹Laboratory of CAD CAM CAE, Universidad EAFIT, Cra 49 no 7-sur-50, Medellín 050022, Colombia

²Vicomtech Foundation, Basque Research and Technology Alliance (BRTA), Mikeletegi 57, Donostia-San Sebastian 20009, Spain

³Grupo de Diseño y Desarrollo de Procesos (DDP), Universidad EAFIT, Cra 49 no 7-sur-50, Medellín 050022, Colombia



III.B.1.1 Context

Diego Montoya-Zapata, Diego A. Acosta, Aitor Moreno, Jorge Posada and Oscar Ruiz-Salguero Sensitivity Analysis in Shape Optimization using Voxel Density Penalization. Spanish Computer Graphics Conference (CEIG 2019). San Sebastian, Spain. 26-29 June 2019. A. Jarabo and D. Casas (Editors). Publisher: The Eurographics Association. ISBN: 978-3-03868-093-2. DOI: <https://doi.org/10.2312/ceig.20191201>. URI: <https://diglib.eg.org/handle/10.2312/ceig20191201>. Proceedings: <https://diglib.eg.org/handle/10.2312/2632793>.

Indexing: SCOPUS, EUROGRAPHICS Digital Library

Abstract

Shape optimization in the context of technical design is the process by which mechanical demands (e.g. loads, stresses) govern a sequence of piece instances, which satisfy the demands, while at the same time evolving towards more attractive geometric features (e.g. lighter, cheaper, etc.). The SIMP (Solid Isotropic Material with Penalization) strategy seeks a redistribution of local densities of a part in order to stand stress / strain demands. Neighborhoods (e.g. voxels) whose density drifts to lower values are considered superfluous and removed, leading to an optimization of the part shape. This manuscript presents a study on how the parameters governing the voxel pruning affect the convergence speed and performance of the attained shape. A stronger penalization factor establishes the criteria by which thin voxels are considered void. In addition, the filter discourages punctured, chessboard pattern regions. The SIMP algorithm produces a forecasted density map on the whole piece voxels. A post-processing is applied to effectively eliminate voxels with low density, to obtain the effective shape. In the literature, mechanical performance finite element analyses are conducted on the full voxel set with diluted densities by linearly weakening each voxel resistance according to its diluted density. Numerical tests show that this approach predicts a more favorable mechanical performance as compared with the one obtained with the shape which actually lacks the voxels with low density. This voxel density - based optimization is particularly convenient for additive manufacturing, as shown with the piece actually produced in this work. Future endeavors include different evolution processes, albeit based on variable density voxel sets, and mechanical tests conducted on the actual sample produced by additive manufacture.

Keywords

Applied computing → Computer-aided manufacturing
Computing methodologies → Modeling and simulation

Glossary

Term	Description	Units
FEA	Finite element analysis	N/A
$\eta \in (0, 1)$	Fraction of mass to be retained in the final design	Adimensional
$p \geq 1$	Penalty factor aimed to polarize element relative densities around 0 and 1	Adimensional
$R \geq 0$	Filter radius used to discourage chessboard voxel patterns	Adimensional
M_0	Initial mass of the domain	g
M	Mass function of the domain	g
c	Compliance function of the domain	μJ

III.B.1.2 Introduction

Shape Optimization usually includes the set up of physical demands (stress, abrasion, vibration, light, heat, temperature, etc.) on the desired object and a domain evolution (reduction, in most

publications). Evolution takes place until some constraint domain is satisfied, both in terms of remaining volume and of responses to the demands.

This paper uses the term *shape optimization* as encompassing both *geometry* and *topology* aspects. The reason for this usage is that when voxel densities in one region vanish (geometry change), a side effect may be the creation of holes or disjoint portions, which are topological changes. Therefore, topological changes derive in natural form from geometry changes. Fig. III.B.1.1 shows an example of the application of shape optimization to a fixed beam subjected to a linear distributed load.

The strategy SIMP (Solid Isotropic Microstructure with Penalization [100, 165]) implies setting up of a goal percentage of domain volume reduction, the decomposition of the domain in finite elements, the load and boundary conditions. For the purpose of the present discussion one may assume that the finite elements are voxels. In each iteration of the algorithm, the density of each voxel is re-considered to minimize the compliance of the piece, always keeping the piece mass (i.e. summation of density times voxel volume) below a certain level.

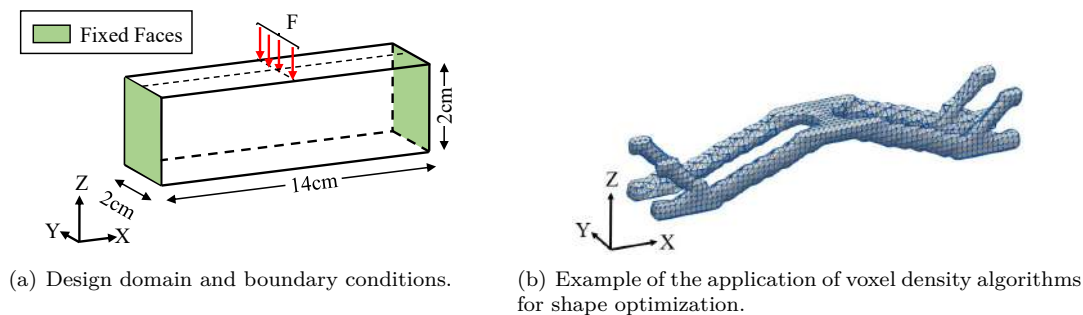


Figure III.B.1.1: Design domain and result of the application of shape optimization.

The voxel density strategy uses a parameter p to polarize the densities of the finite elements towards 0 and 1. It also uses a filter (parameter R) which discourages puncturing or chessboard effects that would produce low and high density voxels mixing in a non-dense pattern. The goal is, therefore, to have voxel - density - homogeneous regions.

This paper studies the influence of the parameters of the density-based algorithm, which is one of the most used structural optimization algorithms in additive manufacturing. For this purpose, a case study in the field of solid mechanics is defined. This paper evaluates the impact of the density-based algorithm parameters, not only in the geometry of the final design, but also in the structural performance and computation time.

The rest of the paper is organized as follows: Section III.B.1.3 provides a review of the related literature. Section III.B.1.4 describes the methodology used for testing the influence of the studied parameters. Section III.B.1.5 presents and discusses the obtained results. Finally, Section III.B.1.6 concludes the work and proposes some potential lines for future research.

III.B.1.3 Literature Review

Section III.B.1.3.1 shows the development of visualization tools to assist manufacturing processes. Subsequently, Section III.B.1.3.2 presents the use of structural optimization for additive manufacturing. Section III.B.1.3.3 introduces the studies on the effects of the optimization parameters in the solution given by the voxel density algorithm. Finally, Section III.B.1.3.4 concludes the literature review and synthesizes the contributions of this work.

III.B.1.3.1 Structural Optimization and Visual Computing

Structural optimization may be traced back to the work in Ref. [12] and has evolved rapidly since the beginning of the 2000's. Applications in aerospace [170], fluid flow [87] and biomedicine [177] show the adoption of structural optimization in different fields. The reader is referred to the works in Refs. [42, 166] for a more detailed review. Section III.B.1.3.2 discusses the use of structural optimization in manufacturing.

In recent years, different tools of visual computing have started to support structural optimization and manufacturing [107, 110, 196], proving that visual computing is a core technology of Industry 4.0 [145]. This paper states the mathematical and algorithmic background for the development of an interactive and intuitive tool to assist the process of structural optimization in additive manufacturing.

III.B.1.3.2 Structural Optimization for Additive Manufacturing

Although structural and shape optimization impact diverse manufacturing methods, additive manufacturing is particularly convenient for materializing voxel scale optimization. In the context of additive manufacturing, optimization is conducted by (a) growing / clipping the shape (i.e. bi-directional evolutionary structural optimization -BESO [122, 181, 182]), (b) tuning the density of spatial neighborhoods ([90, 137, 206]), (c) using level sets to determine infill and shell profiles ([63, 99]), and (d) tuning diameters (proportional topology [29]).

Voxel density as tuning parameter has been used along level sets as supports for shape optimization in the context of additive manufacturing ([98]). Voxel density variations are relevant in various additive manufacturing aspects, such as: (1) minimization of support structures during the material deposition stages, (2) generation of lattice and porous structures for weight reduction, and (3) tailoring part designs for additive manufacturing.

Ref. [90] presents neighborhood density optimization which hosts elimination of deposition stage support structures. Ref. [137] maps density maps onto lattice materials suited for shape optimization. Ref. [206] finds voxel density maps which optimize shape, while at the same time integrates an overhang constraint into the formulation of the shape optimization with additive manufacturing.

III.B.1.3.3 Effect of the Parameters in Voxel-density Algorithms

As shown in the previous section, voxel density algorithms have been used in structural optimization for different and varied applications. However, it is not clear how the parameters associated to the optimization process affect, not only the topology and geometry of the final design, but also other relevant variables, such as the convergence speed, objective function, and structural performance of the obtained design.

The impact of the penalization factor p in the geometry of the final design has been widely studied. It is known that large penalization factors ($p > 3$) tend to produce black-and-white designs [5, 38, 70, 100, 165, 189]. However, the influence of the penalization factor on the behavior of other variables (e.g. compliance and von Mises stress) has not been established.

On the other hand, it is common to use filtering techniques to reduce the checkerboard patterns that result from numerical instabilities of the density-based methods [14]. In this case, a filtering radius R must be included. This parameter defines the area of the neighborhood in which the filter is applied. The larger the filtering radius R , the simpler the geometry of the final shape [67, 70]. However, the impact of this parameter on the compliance, time of convergence and structural performance is not well studied yet.

Ref. [67] studies the effects of the variation of the goal volume/mass fraction in the geometrical complexity of the obtained designs. Refs. [5, 52] state that different designs can be obtained by varying the initial density distribution. Besides, other parameters concerning the finite element analysis (FEA) are also studied. Ref. [38] shows the advantage of quadratic finite elements over the linear ones for avoiding checker-board patterns and Ref. [52] exhibits the mesh density dependency of the geometry of the final solution. However, these analyses mainly focus on the geometry of the final shape, leaving aside the structural and mechanical performance of the piece.

III.B.1.3.4 Conclusions of the Literature Review

The interest of the additive manufacturing community to advance towards structurally optimal designs has been shown. Different structural optimization algorithms (e.g. density-based, level set, evolutionary structural optimization) have been used in the context of additive manufacturing. However, the success of the optimization is highly dependent on the chosen parameters associated to the algorithm.

This paper focuses on getting a better understanding on how the parameters of the voxel density method affect (1) the behavior of the algorithm and, (2) the geometry and structural performance of the obtained design. This literature review has shown that exist few works that tackle this task. Most of the studies limit to evaluate only changes on the final geometry.

This work assess (1) the speed of convergence of the algorithm, (2) the final compliance, (3) the final maximum von Mises stress and, (4) the geometry and manufacturability of the final shape. As opposed to the found in previous works—in which the tested design is the voxel density map—measurements are also taken on the final piece.

III.B.1.4 Methodology

III.B.1.4.1 Tuning of Element Density

The objective of the classical structural optimization algorithms is to minimize the amount of material of a design so that it remains functional. In particular, density-based methods for shape optimization are heuristic strategies that aim to find the optimal distribution of the relative densities (x_i) of the FEA elements along the domain.

In order to avoid FEA elements with intermediate (gray) densities—i.e. densities that are neither close to 0 nor 1—, voxel density methods adopt the heuristic rule in Eq. III.B.1.1:

$$E_i = x_i^p E_0 \tag{III.B.1.1}$$

where p is the penalization power for intermediate densities and, E_i and E_0 are the elastic moduli of the i -th element and the raw material, respectively.

The formulation for the minimization of compliance in Eq. III.B.1.2 ([100, 165]) assumes that the domain is (1) rectangular prismatic, and (2) discretized into N cubic FEA elements (voxels):

$$\begin{aligned} \underset{\mathbf{X}}{\text{minimize}} \quad & c(\mathbf{X}) = \mathbf{U}^T \mathbf{K} \mathbf{U} \\ \text{subject to} \quad & M(\mathbf{X}) \leq \eta M_0, \\ & \mathbf{K} \mathbf{U} = \mathbf{F}, \\ & 0 < x_{\min} \leq x_i \leq 1, i = 1, \dots, N. \end{aligned} \tag{III.B.1.2}$$

where $\mathbf{X} = [x_1, \dots, x_N]^T$ is the vector of relative densities, x_{\min} is the minimum value that the relative density can reach (non-zero to avoid discontinuities that can produce numerical issues), $c(\mathbf{X})$ is the compliance function, \mathbf{U} is the global displacement vector, \mathbf{F} is the global force vector, \mathbf{K} is the global stiffness matrix, M_0 is the mass of the initial design domain, η is the fraction of mass that aims to be retained in the final design and $M(\mathbf{X})$ is the mass function (Eq. III.B.1.3),

$$M(\mathbf{X}) = \frac{M_0}{N} \sum_{i=1}^N x_i. \tag{III.B.1.3}$$

Most of the implementations of the voxel density algorithms also include filtering techniques to avoid checkerboard patterns and, mesh-dependent solutions [165]. One of the most frequently used filters is the *sensitivity filter*, which operates on the derivatives of the compliance function, as shown in Eq. III.B.1.4 [165]:

$$\widetilde{\frac{\partial c}{\partial x_i}} = \frac{\sum_{j \in N_i} H_{ij} \frac{\partial c}{\partial x_j} x_j}{x_j \sum_{j \in N_i} H_{ij}}, \tag{III.B.1.4}$$

where $N_i = \{j : \text{dist}(i, j) \leq R\}$ is the neighborhood of the i -th element and R is the filter radius and, H_{ij} is a weight factor defined in Eq. III.B.1.5:

$$H_{ij} = R - \text{dist}(i, j), \tag{III.B.1.5}$$

where $\text{dist}(i, j)$ is the distance between the centers of the elements i and j (c_i and c_j , respectively), divided by the length l of the FEA elements (Eq. III.B.1.6):

$$\text{dist}(i, j) = \frac{\|c_i - c_j\|}{l}. \tag{III.B.1.6}$$

III.B.1.4.2 Conversion of the Voxel Density Map to the Design-for-Manufacturing

The output of the implemented heuristic algorithm is a density map (Fig. III.B.1.2(a)) in which each voxel i has an associated relative density x_i ($0 \leq x_i \leq 1$). In general, this design cannot be manufactured. In order to select the elements to manufacture, this paper employs the algorithm presented in Ref. [166]. The algorithm finds the minimum density threshold x_T that guarantees the mass constraint for the design-for-manufacturing (also called black-and-white design). The surviving elements are those for which $x_i \geq x_T$. Fig. III.B.1.2 shows an example of the conversion of the voxel density map to the design-to-manufacturing.

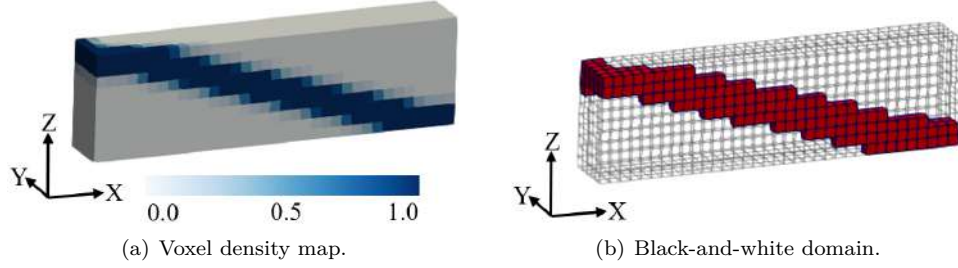


Figure III.B.1.2: Conversion of the voxel density map to the design-to-manufacture.

III.B.1.4.3 Sensitivity Analysis

The formula in Eq. III.B.1.7 allows the numerical analysis of the sensitivity of the function F with respect to the parameter α :

$$S_{\alpha}^F = \frac{\partial \ln F}{\partial \ln \alpha} = \frac{\alpha}{F} \frac{\partial F}{\partial \alpha} \approx \frac{\bar{\alpha}}{\bar{F}} \frac{\Delta F}{\Delta \alpha}, \quad (\text{III.B.1.7})$$

where $\Delta \alpha$ and ΔF denote small changes in the value of α and F ; and $\bar{\alpha} = \alpha + \Delta \alpha / 2$, $\bar{F} = (F_{\alpha} + F_{\alpha + \Delta \alpha}) / 2$.

In this paper, the functions F to analyze are: compliance, maximum von Mises stress and number of iterations. Likewise, the parameters α to study are p and R .

Relative sensitivity allows to study how slight variations in the value of the parameters can affect the mechanical performance of the final piece.

Von Mises stress is used in solid mechanics as a failure criterion and it is desirable to minimize it. Von Mises stress is defined as per Eq. III.B.1.8:

$$\sigma_{VM} = \sqrt{\frac{(\sigma_1 - \sigma_2)^2 + (\sigma_2 - \sigma_3)^2 + (\sigma_3 - \sigma_1)^2}{2}}, \quad (\text{III.B.1.8})$$

where σ_1, σ_2 and σ_3 are the principal stresses.

III.B.1.4.4 Case Study

This paper uses a case study for the analysis of the effects of the algorithm parameters. This section describes: (1) the domain and material used for the simulations and, (2) the configuration of the numerical tests.

III.B.1.4.4.1 Domain of Analysis and Material Characterization

The studied domain is a 3D fixed beam with linearly distributed load applied in the center of the top face (see Fig. III.B.1.1(a)). The beam has size 140.0mm x 20.0mm x 20.0mm and the magnitude of the total applied load is 1.1N. The material employed for the simulations is a PLA filament of a commercial brand. The properties of this material are presented in Table III.B.1.1.

Table III.B.1.1: Properties of the PLA filament used for the simulations.

Property	Value
Young's modulus	1230 MPa [23]
Poisson's ratio	0.33 [59]
Density	1.24 g/cm ³ [23]

The domain in Fig. III.B.1.1(a) is symmetric to the planes depicted in Figs. III.B.1.3(a) and III.B.1.3(b). Therefore, it can be simplified to the domain in Fig. III.B.1.3(c). The equivalent load case is shown in Fig. III.B.1.4.

In order to show the equivalence of the load cases presented in Figs. III.B.1.1(a) and III.B.1.4, a FEA simulation is executed for each domain, using $F = 1.1\text{N}$. Results of the simulations are presented in Fig. III.B.1.5. Notice how the displacements of the two load cases are equivalent. This result allows to execute the simulations of the shape optimization algorithm on the simplified domain.

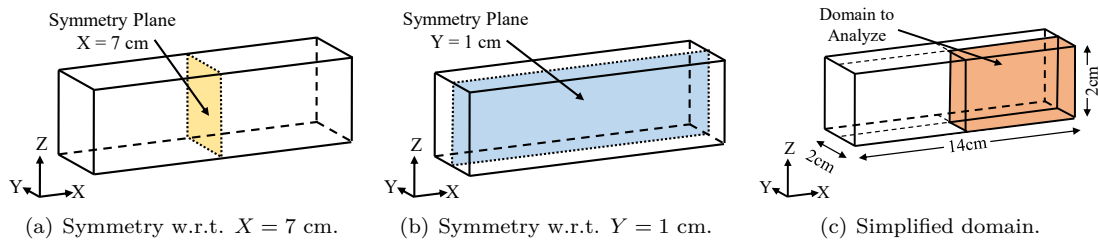


Figure III.B.1.3: Simplification of the domain in Fig. III.B.1.1(a).

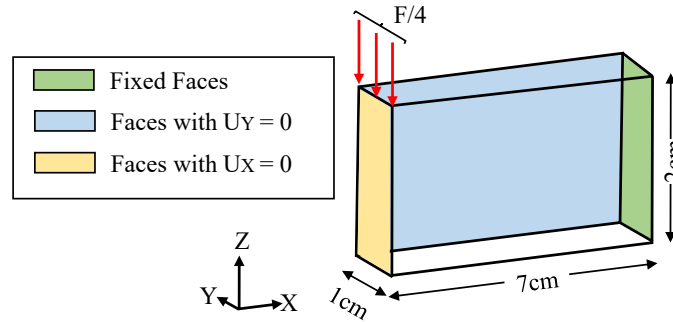


Figure III.B.1.4: Design domain and boundary conditions. Simplified domain.

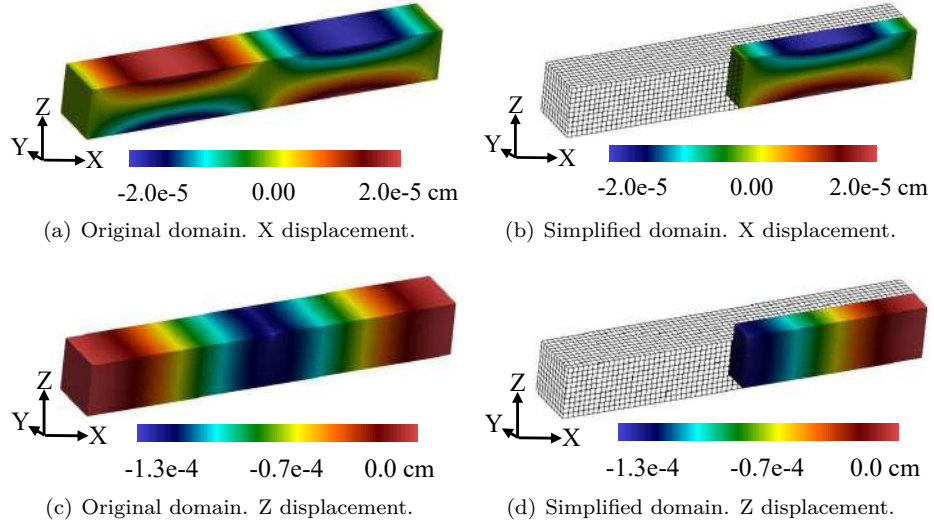


Figure III.B.1.5: Comparison of the X and Z displacements for the original and simplified domain.

III.B.1.4.5 Set-up of Numerical Experiments

This paper conducts studies of the effects of p (density polarization) and R (region homogenization) parameters upon the piece geometry and mechanical performance, in the scenario of voxel density optimization methods. Table III.B.1.2 presents the set of different simulations used for the study of each parameter. The measured variables for each simulation are: (1) compliance, (2) maximum von Mises stress and, (3) convergence speed, measured by the number of iterations. The authors implemented the heuristic voxel density optimization method in C++. The implementation uses the optimality criteria for updating the variables within the optimizer [13].

To execute the FEA simulations, the domain in Fig. III.B.1.4 is discretized into 1750 voxels ($35 \times 5 \times 10$). Subsequently, the FEA mesh is obtained by converting every voxel into a regular hexahedral (cubic) FEA element.

III.B.1.5 Results and Discussion

Sections III.B.1.5.1 and III.B.1.5.2 discuss the influence of the penalty factor p and the filter radius R in the manufacturability, compliance and maximum von Mises stress of the final design, so as the convergence speed of the algorithm. Measurements are executed on both the voxel density map and the black-and-white design. Subsequently, Section III.B.1.5.3 presents a sensitivity analysis of the studied variables with respect to p and R . Finally, Section III.B.1.5.4 shows some of the specimens generated using different parameter configurations.

III.B.1.5.1 Influence of the Penalty Factor in the Geometry, Manufacturability and Mechanical Performance of the Design

To evaluate the influence of the penalty factor p in the geometry and structural performance of the final design, 14 simulations were executed varying the value of p between 1.0 and 7.5, as shown in Table III.B.1.2. Figs. III.B.1.6(a), III.B.1.6(b) and III.B.1.6(c) show the resultant density field for $p = 1.0$ (no penalty), $p = 3.0$ and, $p = 7.0$. Histograms in Figs. III.B.1.6(d), III.B.1.6(e) and III.B.1.6(f) depict the frequency distribution of the density values. Notice that for $p = 1.0$, density distribution is concentrated in the interval $(0.0, 0.2)$. On the other hand, for $p = 3.0$ and $p = 7.0$, the largest bars are for $x_i = 0.0$ and $x_i = 1.0$. These density distributions show the action of the penalty factor to eliminate the intermediate densities.

Table III.B.1.2: Values of the parameters used for the numerical simulations.

Analyzed parameter	Parameter value			
	p	R	η	M_0
p	{1.0, 1.5, ..., 7.5}	1.0	0.1	17.4 g
R	3.0	{0, 1, ..., 5}	0.1	17.4 g

Figs. III.B.1.6(g), III.B.1.6(h) and III.B.1.6(i) display the black-and-white design for $p = 1.0$, $p = 3.0$ and, $p = 7.0$. The design for $p = 1.0$ is composed by multiple non-connected parts and cannot be manufactured. The differences in the designs for $p = 3.0$ and $p = 7.0$ show that larger values of p tend to produce simpler geometries.

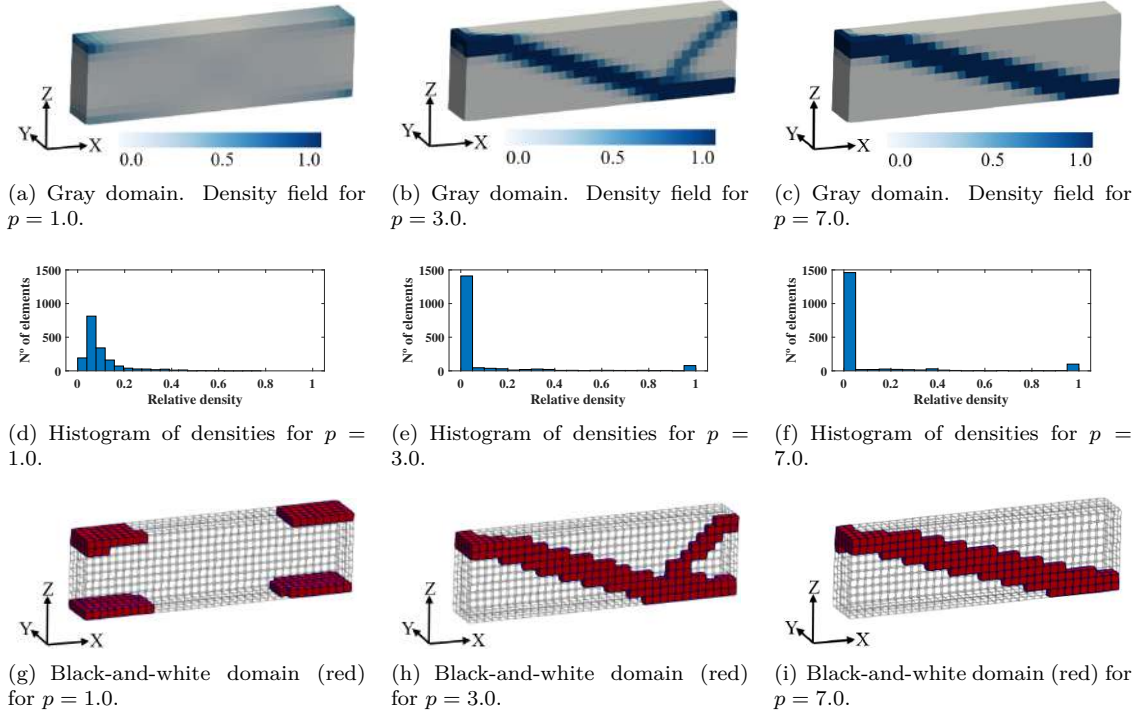


Figure III.B.1.6: Impact of the penalty factor in the geometry and manufacturability.

Fig. III.B.1.7(a) shows the compliance of the gray and black-and-white designs of the 14 simulations varying p . For $p = 1.0$ and $p = 1.5$, the black-and-white domains are not connected and, therefore, compliance is not reported. Notice that for the gray domain, compliance tends to increase as p increases. However, for the black-and-white design, compliance converges to a value close to $4.0 \mu\text{J}$.

Fig. III.B.1.7(b) displays the maximum von Mises stress for the gray and black-and-white domains. So as in the case of compliance, maximum von Mises stress has a different behavior for the gray and black-and-white designs. In the case of the gray domain, maximum von Mises stress tends to increase, even for $p \geq 2.0$. On the other hand, for the black-and-white domain, maximum von Mises stress oscillates around 100 kPa.

For the studied gray domains, the compliance and maximum von Mises stress attain their lowest values when $p = 1.0$ and $p = 1.5$. However, for these values of p , the respective black-and-white domains cannot be manufacture. It exhibits that the results for the black-and-white domain are not necessarily in concordance with the results for the gray domain. It demonstrates the importance of analyzing the black-and-white domain, which is the one to be manufactured.

In Fig. III.B.1.7(c) can be seen the number of iterations that the algorithm needed to converge for every value of p . The reader can see that, for the domains that can be manufactured ($p > 2.5$), large values of p tend to accelerate the convergence of the algorithm.

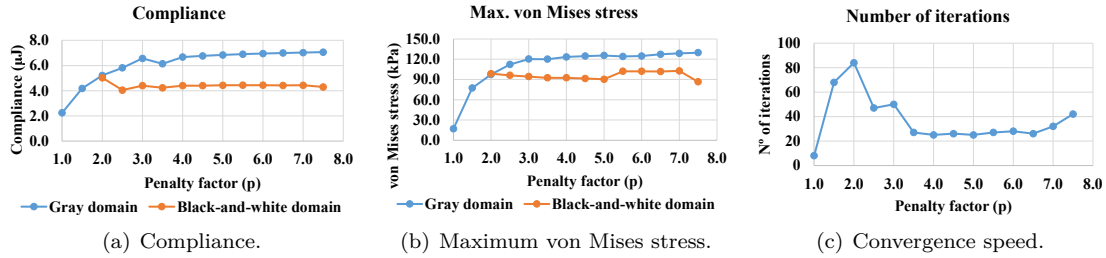


Figure III.B.1.7: Impact of the penalty factor in the convergence speed and mechanical performance.

III.B.1.5.2 Influence of the Filter Radius in the Geometry, Manufacturability and Mechanical Performance of the Design

To study the influence of the filter radius R , it was varied between 0.0 and 6.0. Figs. III.B.1.8(a), III.B.1.8(b) and III.B.1.8(c) show the resultant density field for $R = 0.0$ (no filtering), $R = 1.0$ and, $R = 3.0$. Figs. III.B.1.8(d), III.B.1.8(e) and III.B.1.8(f) show the corresponding histograms of the density maps: when R increases, the density is distributed more evenly along the domain and, therefore, more intermediate densities appear.

The black-and-white domains for $R = 0.0$, $R = 1.0$ and, $R = 3.0$ are displayed in Figs. III.B.1.8(g), III.B.1.8(h) and III.B.1.8(i). Complex and detailed geometries are attained for small values of R . However, the geometrical complexity stimulates the appearance of non-manufacturable sub-domains. Fig. III.B.1.12(c) show that for $R = 0.0$ appear voxels that are connected by a single edge, which impedes the correct manufacturing (even using additive manufacturing technologies) of the piece. The occurrence of these chessboard patterns are associated to numerical errors that may be caused by the voxel discretization and the type of FEA element used for the simulations [144].

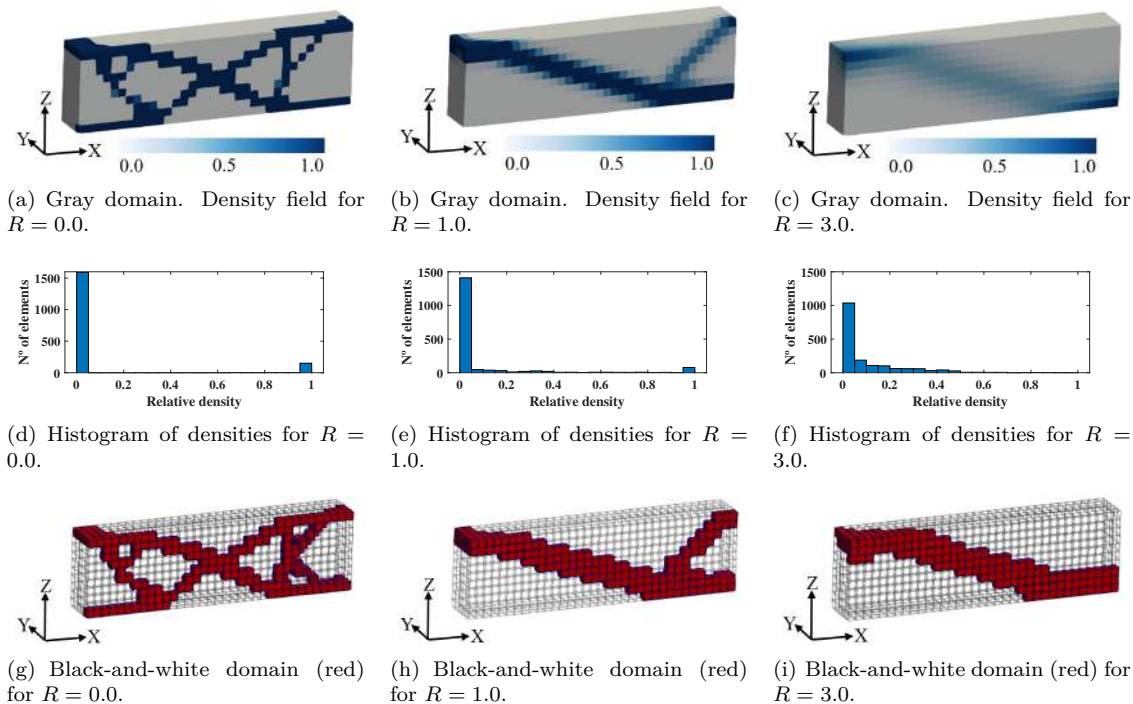


Figure III.B.1.8: Impact of the radius filter in the geometry and manufacturability.

The compliance and maximum von Mises stress are shown in Figs. III.B.1.9(a) and III.B.1.9(b). For $R = 5.0$, compliance and maximum von Mises stress are not reported for the black-and-white domain because the domain is not connected. The increase of the compliance for the gray domain (Fig. III.B.1.9(a)) for increments in R is noticeable. However, the value of R does not affect the compliance of the black-and-white domain.

So as in the previous section, the behavior of the compliance and maximum von Mises stress is different for the black-and-white and gray domains. The mechanical performance of the gray domain is merely illustrative and does not represent a real piece. Therefore, it is necessary to check the performance of the piece for manufacturing. This finding shows the relevance of a stage of validation in the pipeline of structural optimization.

Fig. III.B.1.9(b) shows that larger values of R produce structures with larger maximum von Mises stress for the black-and-white domain. This result agrees with the result for the gray domain when $R \leq 3.0$. However, for $R \geq 4.0$, the maximum von Mises stress of the gray domain decays. It is related to the more even distribution of the relative densities in the volume.

Fig. III.B.1.9(c) shows the convergence speed of the algorithm depending on the value of R . No filtering and large filter radii contribute to a faster convergence. However, the final design may not be manufacturable. Therefore, intermediate values of R should be selected.

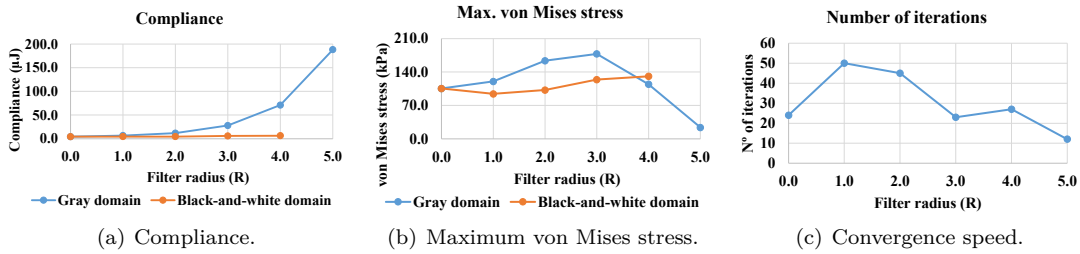


Figure III.B.1.9: Impact of the filter radius in the convergence speed and mechanical performance.

III.B.1.5.3 Sensitivity Analysis

Fig. III.B.1.10 presents the relative sensitivity of the compliance, maximum von Mises stress and number of iterations with respect to the parameter p . To calculate these values, R was fixed to 1.0. It is noticeable that for $p > 4.0$, the compliance and the maximum von Mises stress are not affected by the value of p . On the other hand, the convergence speed of the algorithm is very sensitive to the value of p .

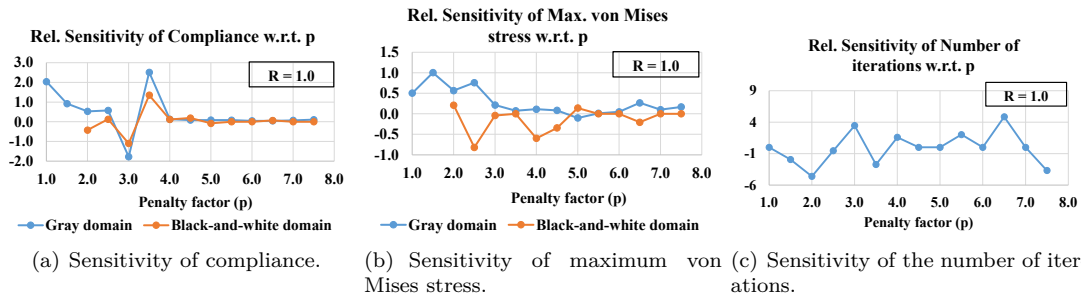


Figure III.B.1.10: Relative sensitivity of the compliance, maximum von Mises stress and convergence speed w.r.t. p .

Fig. III.B.1.11 displays the sensitivity analysis of the parameter R for the studied variables: compliance, maximum von Mises stress and convergence speed. From Figs. III.B.1.11(a) and III.B.1.11(b) can be inferred that R does not have much influence on the compliance and maximum von Mises stress of the final design. However, R does impact the mechanical performance of the voxel density map, specially for larger values of R . Convergence speed is also affected when $R \geq 2.0$.

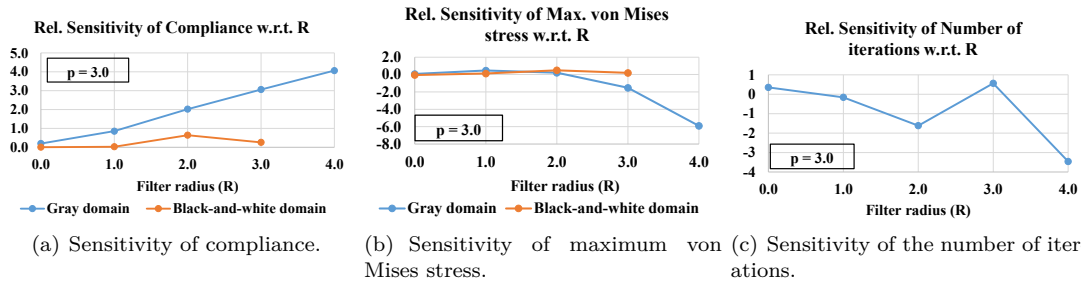


Figure III.B.1.11: Relative sensitivity of the compliance, maximum von Mises stress and convergence speed w.r.t. R .

III.B.1.5.4 Evaluation of the Manufacturability and 3D Printed Pieces

Additive manufacturing allows the production of complicated geometries that cannot be manufactured using other technologies. To evaluate the feasibility of the designs produced by the voxel density algorithm, three resultant domains of Sections III.B.1.5.1 and III.B.1.5.2 were selected. Figs. III.B.1.12(a)–III.B.1.12(c) show the corresponding STL model of each design. The domain in Fig. III.B.1.12(c) has neighborhoods in which the voxels are connected only by an edge, which compromises the manufacturability of the piece.

Figs. III.B.1.12(d)–III.B.1.12(f) show the 3D printed pieces obtained from the STL models in Figs. III.B.1.12(a)–III.B.1.12(c). Notice that for the first two domains, the geometry of the shape can be reproduced accurately. However, due to the single edge’s connections in the third design, some sub-domains disconnect when support material is removed. In order to improve the manufacturability of the final piece, different solutions for suppressing these punctured or chessboard-looking regions have been proposed. Filtering techniques (as the implemented in this work), the use of higher-order FEA elements and the deletion of single-edge or single vertex connections [144] are some of the plausible solutions. Other possible solution is to smooth the voxel design. This work uses the Marching Cubes algorithm to smooth the surface associated to the voxel domain. Figs.III.B.1.13 show the obtained STL models after smoothing the domains in Fig. III.B.1.12 and the corresponding 3D-printed pieces.

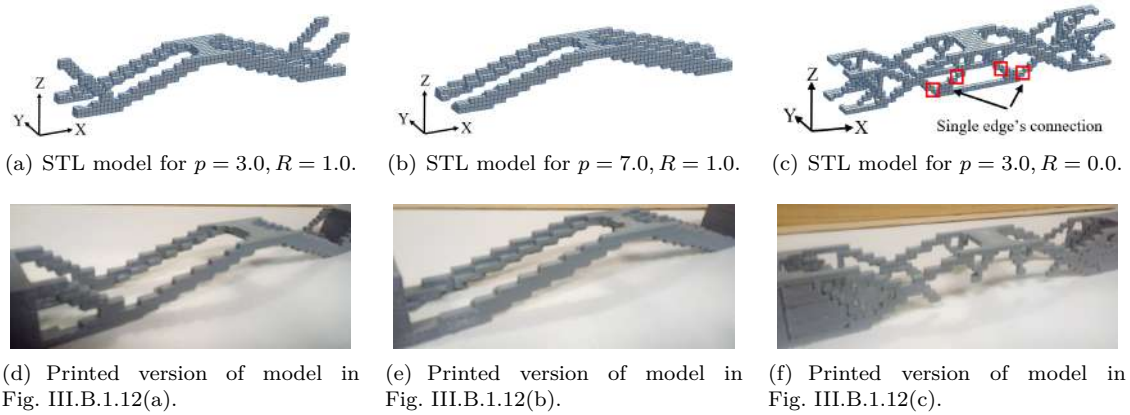


Figure III.B.1.12: 3D printed designs obtained using the voxel density algorithm.

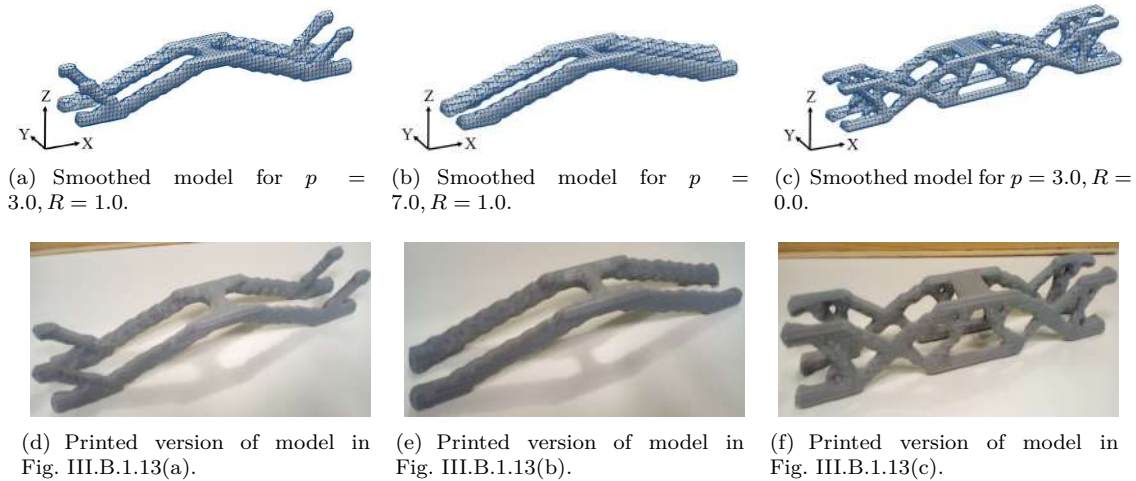


Figure III.B.1.13: Smoothed designs using Marching Cubes algorithm and the corresponding 3D printed pieces.

III.B.1.6 Conclusions

This paper presents analysis of the effects of the parameters of the heuristic voxel density algorithms in (1) the geometry and structural performance of the final design and, (2) the convergence speed of the algorithm. For the study, the authors use one set-up, therefore conclusions on the detailed behavior of the parameters may not be drawn. However, results show that (a) extreme values of the parameters may affect the manufacturability and mechanical performance of the designs and (b) mechanical analyses must be executed on the domain-to-manufacture and not in the *optimal* voxel density map given by the algorithm.

Shape optimization is an intermediate step in the work-flow of the design-to-manufacturing. In this realm, it is important to understand how the shape optimization algorithms work and how their parameters affect the obtained design. This work can be a worthy tool for many designers and engineers that use commercial software that implements density-based methods.

III.B.1.6.1 Limitations

This work studies the effects of the penalty power p and the filter radius R independently. It may be interesting to understand the interaction between these two parameters. Future research should address the analysis of simultaneous changes in the values of p and R . Moreover, other parameters (e.g. mass fraction η) can be investigated. Physical experimentation is also required for testing the correctness and exactitude of the numerical results.

III.B.1.6.2 Future Work

The authors look forward to generate an interactive tool to assist the design process in additive manufacturing. The tool would allow designers to visualize different different pieces and their mechanical performance. It has to be capable of generating different configurations for the domain, loads, constraints and parameter configurations for shape optimization.

It is necessary to validate the conclusions drawn in this work. In that sense, there are three lines of research that are open for further work: (1) the simulation of other domains with different load cases, (2) the analysis of interactions between p and R and (3) physical tests to confirm numerical results.

III.B.2

Density-sensitive Implicit Functions Using Sub-voxel Sampling in Additive Manufacturing

Diego Montoya-Zapata^{1,2}, Aitor Moreno², Juan Pareja-Corcho¹, Jorge Posada² and Oscar Ruiz-Salguero¹

¹Laboratory of CAD CAM CAE, Universidad EAFIT, Cra 49 no 7-sur-50, Medellín 050022, Colombia

²Vicomtech Foundation, Basque Research and Technology Alliance (BRTA), Mikeletegi 57, Donostia-San Sebastian 20009, Spain



metals

an Open Access Journal by MDPI



Modeling Metal 3D Printing Processes

III.B.2.1 Context

Density-Sensitive Implicit Functions Using Sub-Voxel Sampling in Additive Manufacturing. Diego Montoya-Zapata, Aitor Moreno, Juan Pareja-Corcho, Jorge Posada, Oscar Ruiz-Salguero. Journal Metals, ISSN 2075-4701, volume 9, number 12, Publisher MDPI. Special Issue Modeling Metal 3D Printing Processes, url= <https://www.mdpi.com/2075-4701/9/12/1293>, doi= <https://doi.org/10.3390/met9121293> Received: 30 October 2019; Accepted: 27 November 2019; Published: 30 November 2019

Indexing: JCR(Q1), SCOPUS(Q2), Publindex(A1)

Abstract

In the context of lattice-based design and manufacturing, the problem of physical realization of density maps into lattices of a particular family is central. Density maps are prescribed by design optimization algorithms, which seek to fulfill structural demands on a workpiece, while saving material. These density maps cannot be directly manufactured since local graded densities cannot be achieved using the bulk solid material. Because of this reason, existing topology optimization approaches bias the local voxel relative density to either 0 (void) or 1 (filled). Additive manufacturing and 3D printing open possibilities to produce graded density individuals belonging to different lattice families. However, voxel-level sampled boundary representations of the individuals produce rough and possibly disconnected shells. In response to this limitation, this article uses a sub-voxel sampling (largely unexploited in the literature) to generate lattices of graded densities. This sub-voxel sampling eliminates the risk of shell disconnections and renders better surface continuity. The manuscript devises the function to produce Schwarz cells that materializes a given relative density. This article illustrates a correlation of continuity against stress concentration by simulating C^0 and C^1 inter-lattice continuity. The implemented algorithm produces implicit functions and thus lattice designs which are suitable for metal additive manufacturing and able to achieve the target material savings. Additional work is required in the modeling of the mechanical response (stress/strain/deformation) response of large lattice sets (with arbitrary geometry and topology) under working loads.

Keywords

3D printing; topology optimization; Schwarz Primitive; lattice structure

III.B.2.2 Introduction

Additive manufacturing (also called 3D printing) makes feasible the production of complex and intricate geometric features. However, the high production costs limit the application range of this technology. In this context, topology optimization plays a major role in the production of lightweight parts that reduce material usage and, consequently, production costs. Existing topology optimization algorithms deliver density maps as the result of the optimization. These density maps cannot be directly manufactured since the density of a bulk solid material cannot be locally graded. In order to overcome this limitation, additive manufacturing takes advantage of its geometrical freedom to enable the physical realization of these density maps into real pieces, using lattice structures.

Lattice structures are families of repetitive architectures whose distribution of void/filled sections can be controlled. Moreover, the attractiveness of lattice structures lies on its ability to retain good mechanical properties (e.g. high strength-to-weight ratio, energy absorption) while saving material. Current works aim to use surface lattice materials for converting density maps into manufacturable workpieces. Surface lattices are a particular family of lattice structures that can be generated as isosurfaces of an implicit function that controls the shape of the structure. However, the materialization of density maps into surface lattice structures poses different challenges: (a) a procedure to control the density of surface lattice structures must be established, (b) the mass of the given density map must be preserved, and (c) stress concentration in terms of inter-lattice

continuity is to be considered.

Initially, the paper presents how to generate surface lattice structures of variable density from a general perspective. Then, the paper addresses, in a formal and intuitive manner, the problem of controlling the density of the variable-density surface lattices, so that the arrangement of the void/filled regions of the lattice structure resembles the given density map. This is achieved by deriving the relationship between the iso-value (necessary to produce the isosurface) used to generate the surface lattice and its corresponding density for the family of Schwarz lattices. The produced structures are effectively manufactured via three processes of additive manufacturing: fused deposition modeling, binder jetting and selective laser melting.

With the aim of guiding the reader through the paper, the basic terminology is graphically presented here. Figure III.B.2.1(a) shows the initial or rectangular prismatic design domain (Ω), of width w , depth d and height h . The domain Ω is partitioned into two different sets. One corresponds to the finite element mesh, built by cubic finite elements or voxels (Fig. III.B.2.1(b)). On the other hand, the domain is also divided into cubic lattices that are larger than voxels. In this sense, a lattice is composed by an array of $k \times k \times k$ voxels (Fig. III.B.2.1(c)). Finally, the space occupied by a cubic lattice becomes a Schwarz Primitive cell. So, the final surface lattice domain can be seen as the union of all the produced Schwarz Primitive cells (Fig. III.B.2.1(d)). It is important to clarify that (a) Fig. III.B.2.1(c) is merely illustrative and, in reality, it is usual that $k \geq 10$, and (b) the triangular mesh or full boundary representation (B-Rep) for the domain is generated by devising an overall piecewise implicit Schwarz family function and then by making the mesh explicit using a Marching Cubes algorithm.

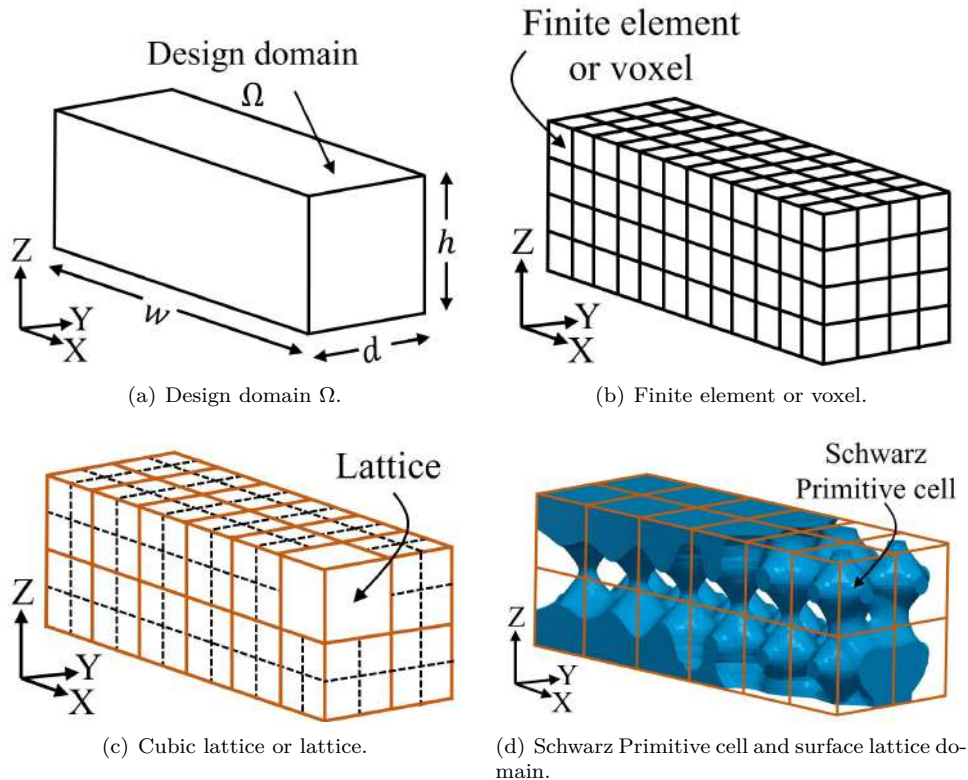


Figure III.B.2.1: Geometric entities.

The remainder of this article is organized as follows: Section III.B.2.3 provides a review of the relevant related work. Section III.B.2.4 describes the methodology to generate surface lattice structures and presents the algorithm to convert density maps into lattice materials with controlled density. Section III.B.2.5 presents and evaluates the results obtained following the presented approach. Advantages and limitations of the implemented algorithm are discussed. Section III.B.2.6 concludes the manuscript and presents potential research lines to extend this work.

III.B.2.3 Literature Review

III.B.2.3.1 Topology Optimization in Additive Manufacturing

Additive manufacturing offers more geometrical freedom than traditional subtractive manufacturing techniques. This geometrical flexibility gives to additive manufacturing/3D printing the capacity to exploit and materialize the complex results of topology optimization [65, 97].

There are three mainly used topology optimization algorithms used in additive manufacturing applications [98]. The first is Solid Isotropic Material with Penalization (SIMP) or density-based topology optimization, which iteratively adjusts the density of localized neighborhoods [121, 165]. The second strategy acts by removing and adding material in different locations of the domain. It

is called bi-directional evolutionary structural optimization [122, 182]. Finally, the third approach only modifies the boundary of the domain, which is represented by level set functions [99].

Topology optimization in additive manufacturing seeks to (1) design of light-weight and functional pieces [121, 122], (2) suppress or minimize the amount of support structures needed during the manufacturing stage [90, 188], and (3) define optimal infill strategies for existing designs [137, 196].

III.B.2.3.2 Lattice Structures in Additive Manufacturing

Besides being lightweight and keeping a high strength-to-weight ratio, lattice structures possess important characteristics which make them appropriate in engineering. Among these properties are: energy absorption [79], heat transfer [105], and vibration and acoustic damping [203]. Authors also evaluate specific mechanical characteristics. References [91, 123] study the elastic properties of surface-based and Kelvin lattices, respectively. Reference [56] analyzes the feasibility of surface-based lattices for acoustic isolation by obtaining their vibration bandgaps. Applications of lattice structures can be found in bioengineering, automotive, aeronautic, and aerospace [78].

Regarding additive manufacturing, lattice structures are beneficial because they save material and time, reduce material wasting on supports and diminish energy expenses during manufacturing [78]. In particular, surface-based lattices serve in biomedical [8, 113] or industrial applications [94, 137]. Surface-based structures are also employed as supports during the building process [173]. Research also focuses on the characterization of surface-based lattice structures fabricated via additive manufacturing. Reference [1] investigate the elastic and plastic deformation under compression of polymer surface-based lattices. Besides, Ref. [201] assesses manufacturability and mechanical performance of metal surface-based lattices.

III.B.2.3.3 Explicit Realization of the Results of Topology Optimization into Surface-based Lattices

As stated before, density-based topology optimization is commonly used in additive manufacturing applications. The outcome of this kind of algorithms is a density map onto the finite element mesh. The drawback then is that this density map does not have a direct physical realization, due to the density of a material cannot be graded. Since the filled-void proportion of lattices can be manipulated, lattices have emerged as a plausible alternative to solve this issue.

In order to adapt the results of topology optimization into a lattice domain, the related literature relies in the concept of controlling the density (filled-void relation) of the lattice structure, so that it resembles the density map of topology optimization. In this realm, Refs. [24, 168, 208] propose solutions using different 2D lattice structures and Ref. [4] introduces a density mapping using 3D trusses. Likewise, surface lattices are also adopted for this task. References [94, 102, 137, 160, 208] employ surface lattices to materialize the results of topology optimization. Nevertheless, these works have some limitations: (1) the lack of a formal definition of the problem of mapping the densities of topology optimization into surface lattices, (2) the size of the finite elements affects the geometrical quality of the obtained surface (except for Ref. [208]), and (3) the mass of the produced lattice structure differs from the mass determined by the given density map.

III.B.2.3.4 Conclusions of the Literature Review

The literature review has shown that the development of topology optimization is one of the key points for the progress of additive manufacturing. Different topology optimization techniques (namely SIMP, evolutionary structural, and level set-based) are used to exploit the geometrical versatility brought by additive manufacturing. However, the problem of materializing the output of topology optimization into a manufacturable (printable) model is still an open research question.

In order to solve this problem, different authors propose to convert the results of the SIMP optimization algorithm into lattice domains, particularly surface-based lattices. However, there are three aspects that need to be revised: (1) the formalization of the problem of mapping the densities of topology optimization into surface lattices, (2) the generation of surface lattice domains whose quality is not restricted by the mesh used for the optimization, and (3) the preservation of the mass dictated in the optimization stage.

This paper focuses on the formalization of the problem in an accurate and intuitive manner. The proposed solution to the stated problem detaches the geometrical resolution of the generated surface lattice from the initial mesh used for the optimization. Likewise, this paper proposes a solution for the problem of mass preservation by considering the characteristics of the surface lattices during the optimization stage.

III.B.2.4 Methodology

III.B.2.4.1 Formulation of SIMP

Structural optimization aims to minimize the amount of material of a design while keeping its functionality. SIMP-based (also called density-based) methodology seeks the optimal distribution of the relative density (x_i) along the domain.

The classic formulation of density-based topology optimization methods targets the minimization of the compliance $c(\mathbf{X})$, which is a measure of the total strain energy. SIMP relies on finite element analysis (FEA) to perform the simulations. Equation III.B.2.1 presents the problem of compliance minimization for a rectangular prismatic domain Ω , meshed with N cubic FEA elements (also called voxels) [100, 165]:

$$\begin{aligned} & \underset{\mathbf{X}}{\text{minimize}} && c(\mathbf{X}) = \mathbf{U}^T \mathbf{K} \mathbf{U} = \mathbf{U}^T \mathbf{F} \\ & \text{subject to} && V(\mathbf{X}) \leq \eta V_0, \\ & && \mathbf{K} \mathbf{U} = \mathbf{F}, \\ & && 0 < x_i \leq 1, i = 1, \dots, N. \end{aligned} \tag{III.B.2.1}$$

where $\mathbf{X} = [x_1, \dots, x_N]^T$ are the relative densities associated to the FEA elements, \mathbf{U} is the global displacement vector, \mathbf{F} is the global force vector, \mathbf{K} is the global stiffness matrix, V_0 is the initial domain volume, η is the maximum proportion of volume of the optimal design and $V(\mathbf{X})$ is the domain volume, calculated as per Eq. III.B.2.2,

$$V(\mathbf{X}) = \frac{V_0}{N} \sum_{i=1}^N x_i. \tag{III.B.2.2}$$

The formulation of density-based topology optimization adopts the rule in Eq. III.B.2.3:

$$E_i = x_i^p E_0 \quad (\text{III.B.2.3})$$

where E_i and E_0 are the elastic moduli of the i -th element and the raw material, respectively, and p is a penalization parameter that makes x_i tends to either 0 or 1.

The outcome of density-based topology optimization is a density (x_i) map onto the FEA elements, with $0 \leq x_i \leq 1$. Intuitively, $x_i = 1$ represents the presence and $x_i = 0$ the absence of material. However, intermediate densities—i.e. densities that are not 0 or 1—do not have a physical meaning and cannot be manufactured. In this realm, the junction of additive manufacturing and lattice materials offers a practical solution: the relative density (occupied volume) of the lattice structure can be adjusted to tailor the density map obtained from topology optimization.

This paper assesses, formulates and describes the process of explicitly realizing the density map given by topology optimization into variable-density surface lattice structures. Therefore, this paper does not need to correct intermediate densities and chooses $p = 1.0$ (no penalization).

III.B.2.4.2 Morphology of Schwarz Primitive Lattice Structures

Schwarz Primitive cells are an instance of surface-based lattice structures that have been used in engineering applications [137]. One of the main advantages of Schwarz Primitive cells is that they are stiffer [108] than other surface-based lattices (e.g. gyroid). Uniform-density Schwarz Primitive lattice structures are generated as isosurfaces of the function shown in Eq. III.B.2.4, in which L denotes the length of the cell [192]. This article studies two types of Schwarz Primitive lattices: network-phase and matrix-phase cells (Fig. III.B.2.2). The volume enclosed by the surface associated to the iso-value t (inequality in Eq. III.B.2.5) produces network-phase cells. On the other hand, the volume between the isosurfaces $-t$ and t (inequality in Eq. III.B.2.6) delivers matrix-phase cells. Figures III.B.2.2(a) and III.B.2.2(b) show Schwarz Primitive network-phase cells for $t = 0.6$ (S_1) and $t = -0.6$ (S_2). Figure III.B.2.2(c) shows the matrix-cell associated to $t = 0.6$ (S_3). From Fig. III.B.2.2, the reader may notice that S_3 is the result of the Boolean difference between S_1 and S_2 ($S_3 = S_1 \setminus S_2$).

$$F(x, y, z) = \cos\left(\frac{2\pi}{L}x\right) + \cos\left(\frac{2\pi}{L}y\right) + \cos\left(\frac{2\pi}{L}z\right) \quad (\text{III.B.2.4})$$

$$F(x, y, z) \leq t, \quad -3 \leq t \leq 3 \quad (\text{III.B.2.5})$$

$$-t \leq F(x, y, z) \leq t, \quad 0 \leq t \leq 3 \quad (\text{III.B.2.6})$$

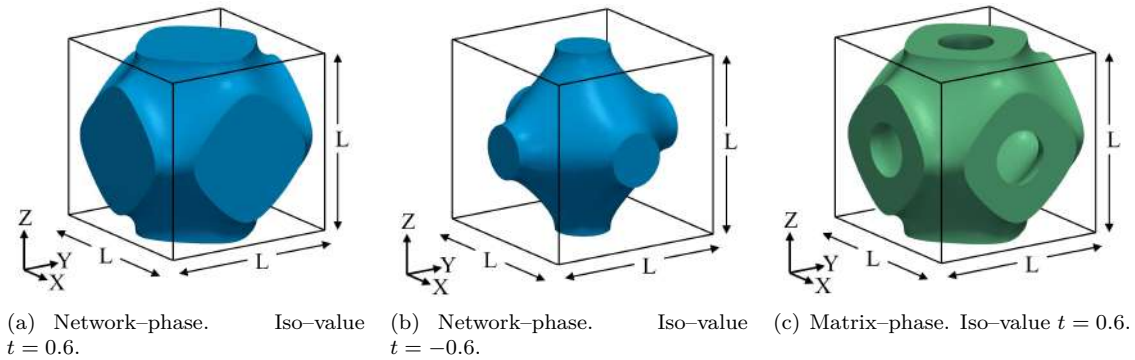


Figure III.B.2.2: Geometry of Schwarz Primitive triply periodic surface.

The relative density ρ (or volume fraction) of a lattice cell is the ratio of its volume and the volume of the lattice (L^3). Figure III.B.2.3 shows five samples of network-phase Schwarz Primitive cells. Each sample is associated to a different iso-value t , reported in the figure. Notice that the larger the value of t , the higher the relative density. The cell corresponding to $t = -1.2$ (Fig. III.B.2.3(a)) is totally contained within the depicted cube and would not have connections with neighbor cells. Therefore, it cannot be used for the explicit realization of density maps into surface lattice structures. This phenomenon appears when the iso-value is lower than -1 ($t < -1.0$), which corresponds to a relative density $\rho = 0.21$.

Figure III.B.2.4 reproduces five examples of matrix-phase cells. As in the case of network-phase cells, a larger t produces cells with larger relative density. On the other hand, for every $t > 0$, there is a region of the cell that allows the connectivity with their neighbors. In this case, the manufacturing technique and its capacity to produce fine details dictate the minimum value of t suitable for manufacturing. However, when $t > 1.0$ (Figs. III.B.2.4(d) and III.B.2.4(e)) appears an internal cavity in the cell. This cavities would trap the raw material in processes as powder bed fusion, but do not represent an issue in processes where the raw material is deposited, such as directed energy deposition or fused deposition modeling.

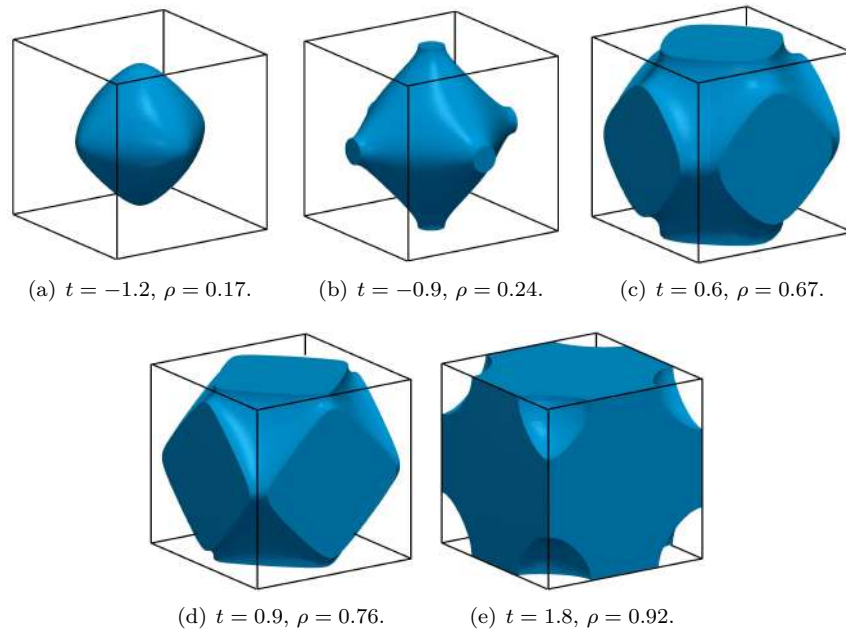


Figure III.B.2.3: Geometry of Schwarz Primitive network-phase cells.

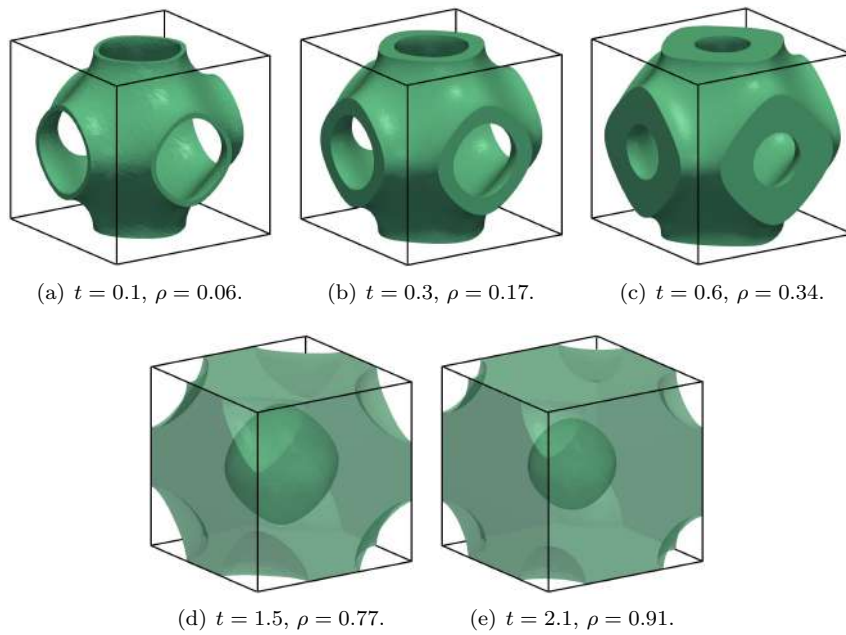


Figure III.B.2.4: Geometry of Schwarz Primitive matrix-phase cells.

III.B.2.4.3 Relation between the Iso-value and the Relative Density of Schwarz Primitive Cells

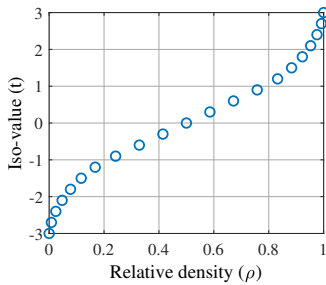
In order to control the relative density of the generated surface lattice domain, it is necessary to express the iso-value t as a function of the relative density ρ . This section addresses this task for the network and matrix-phase Schwarz Primitive cells.

III.B.2.4.3.1 Network-phase Cells

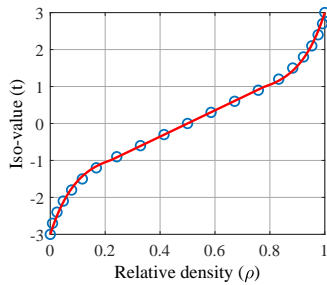
Network-phase Schwarz Primitive cells are generated using an iso-value $t \in [-3, 3]$. To determine the relationship between t and ρ , the interval $[-3, 3]$ may be discretized (sampled) and the relative density associated to each value of t must be inspected. In this paper, the selected size of the sample was 19. That is, 19 network-phase cells were generated using different values of t in Eq. III.B.2.5. The iso-values were $t = -2.7, -2.4, \dots, 0.0, \dots, 2.4, 2.7$. The corresponding relative density ρ of each cell was measured. The results are shown in Fig. III.B.2.5(a). Moreover, for $\rho = 0.0, t = -3.0$ and for $\rho = 1.0, t = 3.0$.

The reader may observe that (1) there is a linear behavior for $t \in [-1, 1]$ and a non-linear behavior out of this range, (2) for $\rho = 0.5, t = 0.0$, and (3) the graph is symmetric with respect to the point $(\rho = 0.5, t = 0.0)$. Considering these findings and the relationship between t and ρ for the studied specimens, a function is adjusted to the data. The function has the form of Eq. III.B.2.7, with a linear zone and two non-linear portions. The values of the parameters $\{a, b, c, d\}$ are listed in Table III.B.2.1. Figure III.B.2.5(b) compares the experimental data and the fitted curve. Notice that the obtained function $t_N(\rho)$ has two properties that are indispensable for the current application: (1) it is continuous, and (2) it is monotonically increasing.

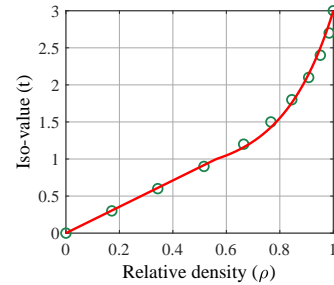
$$t_N(\rho) = \begin{cases} -be^{-c[\rho-(1-d)]} - (1-b) & , 0.0 \leq \rho \leq (1-d) \\ a\rho - \frac{a}{2} & , (1-d) < \rho \leq d \\ be^{c(\rho-d)} + (1-b) & , d < \rho \leq 1.0 \end{cases} \quad (\text{III.B.2.7})$$



(a) Network-phase Schwarz Primitive cells. Iso-value t vs. relative density ρ .



(b) Network-phase Schwarz Primitive cells. Fitted curve.



(c) Matrix-phase Schwarz Primitive cells. Fitted curve.

Figure III.B.2.5: Establishment of the relation between the iso-value t vs. and the relative density ρ for Schwarz Primitive cells.

Table III.B.2.1: Parameters of the fitted functions in Eqs. III.B.2.7 and III.B.2.9.

Parameter	Value
a	3.5549
b	0.2225
c	10.5214
d	$\frac{a+2}{2a} \approx 0.7813$

III.B.2.4.3.2 Matrix-phase Cells

Matrix-phase cells can be generated with the Boolean difference among two network-phase cells. Therefore, the relative density ρ_M of a matrix-phase cell associated to the iso-value t may be written in terms of the relative density of two network-phase cells (ρ_N), as follows:

$$\rho_M(t) = \rho_N(t) - \rho_N(-t) \quad (\text{III.B.2.8})$$

The relationship stated in Eq. III.B.2.8 and the function fitted for the network-phase cells (Eq. III.B.2.7) are used to construct a function that associates t with ρ for the matrix-phase Schwarz Primitive cells. The function t_M in Eq. III.B.2.9 shows the obtained result. Figure III.B.2.5(c) shows the concordance between the fitted function and the experimental relative density measured for some samples of matrix-phase cells.

$$t_M(\rho) = \begin{cases} \frac{a}{2}\rho & , 0.0 \leq \rho \leq (2d-1) \\ be^{\frac{a}{2}[\rho-(2d-1)]} + (1-b) & , (2d-1) < \rho \leq 1.0 \end{cases} \quad (\text{III.B.2.9})$$

The two function in Eqs. III.B.2.7 and III.B.2.9 allow to retrieve the iso-value that produces a Schwarz Primitive cell with a prescribed relative density $0 \leq \rho \leq 1$. The reader may refer to Section III.B.2.4.4 to find a more detailed explanation on how t_N and t_M were inferred.

III.B.2.4.4 Lattice Iso-value as Function of the Relative Density

To establish the relationship between the iso-value t and the relative density ρ of Schwarz Primitive cells, it was necessary to fit the functions t_N and t_M (Eqs. III.B.2.7 and III.B.2.9). The following sections give more insights on how these functions were constructed.

III.B.2.4.4.1 Network-phase Cells

For the network-phase Schwarz Primitive cells, a sample of 19 specimens was generated. Every specimen was associated to a different value of $t \in [-3, 3]$ (see Fig. III.B.2.5(b)). According to the experimental results, the fitted function t_N had to fulfill the following criteria: (1) linearity for $t \in [-1, 1]$ and non-linearity for $t \in [-3, -1) \cup (1, 3]$, (2) symmetry with respect to the point $(\rho = 0.5, t = 0.0)$, (3) $t_N(0.5) = 0.0$, and (4) $t_N(0.0) \approx -3.0$ and $t_N(1.0) \approx 3.0$.

Considering criteria (2) and (3), Eq. III.B.2.10 was deduced. Moreover, using the symmetry stated in criterion (2), only the relationship for $t \in [0, 3]$ was analyzed.

$$t(\rho) = -t(1 - \rho), \quad 0 \leq \rho \leq 1 \quad (\text{III.B.2.10})$$

Criteria (1) and (4) were used to obtain the piece-wise continuous function $t(\rho)$ ($0.5 \leq \rho \leq 1$), shown in Eq. III.B.2.11. The values of the parameters $\{a, b, c, d\}$ are listed in Table III.B.2.1.

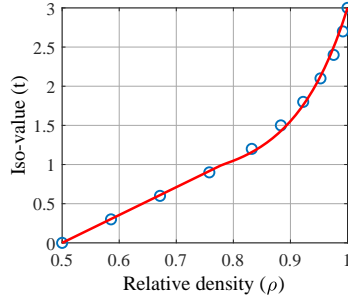


Figure III.B.2.6: Fitting of the iso-value t as a function of ρ ($0.5 \leq \rho \leq 1$) for the network-phase Schwarz Primitive cell.

Figure III.B.2.6 compares the experimental data and the fitted curve. Notice that, for the obtained function: (1) $t(0.5) = 0$, (2) $t(1.0) \approx 3.0$, (3) it is continuous, and (4) it is monotonically increasing.

The reader may notice that the functions t_N and t are equal for $0.5 \leq \rho \leq 1$ (Equations III.B.2.7 and III.B.2.11). Moreover, the left piece of t_N for $0 \leq \rho < 0.5$ was obtained using Equations III.B.2.10 and III.B.2.11, by replacing $\rho \rightarrow 1 - \rho$ and then multiplying by -1 .

$$t(\rho) = \begin{cases} a\rho - \frac{a}{2} & , 0.5 \leq \rho \leq d \\ be^{c(\rho-d)} + (1-b) & , d < \rho \leq 1.0 \end{cases} \quad (\text{III.B.2.11})$$

III.B.2.4.4.2 Matrix-phase Cells

Since the matrix-phase cell with iso-value t can be generated as the Boolean difference between the network-phase cells of iso-values t and $-t$, the relative density ρ_M of a matrix-phase cell is given by the difference of the relative densities of the network-phase cells (Eq. III.B.2.12), where $\rho_M(t) = t_M^{-1}(\rho)$ and $\rho_N(t) = t_N^{-1}(\rho)$.

$$\rho_M(t) = \rho_N(t) - \rho_N(-t) \quad (\text{III.B.2.12})$$

On the other hand, it can be shown that $\rho_N(-t) = 1 - \rho_N(t)$. Hence, Eq. III.B.2.12 may be written as per Eq III.B.2.13,

$$\rho_M(t) = 2\rho_N(t) - 1, \quad (\text{III.B.2.13})$$

which is equivalent to Eq. III.B.2.14.

$$\rho_N(t) = \frac{\rho_M(t) + 1}{2} \quad (\text{III.B.2.14})$$

Hence, the function t_M (Eq. III.B.2.9) was obtained by replacing $\rho \rightarrow (\rho+1)/2$ into Eq. III.B.2.11.

III.B.2.4.5 Generation of Variable-density Surface Lattice Structures

The paper has discussed how to generate surface lattice structures (such as Schwarz Primitive) of uniform density. This section introduces how to develop variable-density Schwarz Primitive lattice

structures. This procedure can be applied to several types of surface lattice structures (e.g. Schwarz Primitive or gyroid) that are approximated with implicit functions, as the one in Eq. III.B.2.4.

In order to generate surface lattice structures with variable density, let

$$G(x, y, z) = F(x, y, z) - T(x, y, z), \quad (\text{III.B.2.15})$$

where $F(x, y, z)$ is a function that defines the shape of the lattice structure (as the given in Eq. III.B.2.4) and $T(x, y, z)$ is an iso-level function that fulfills $-3 \leq T(x, y, z) \leq 3$. The function T is the one that determines the relative density of the structure.

Figure III.B.2.7 depicts a diagram to describe the generation of variable-density surface lattice structures in network-phase for a prismatic rectangular domain Ω . The process is divided into three steps:

1. **Generation of the point grid:** the first step is to sample Ω , given its dimensions and the grid sampling rate in which Ω must be sampled. The output of this step is a point grid.
2. **Evaluation of the function $G(x, y, z)$:** the function G is evaluated in the point grid obtained in the previous step. Apart from the point grid, it is necessary to provide (1) the size of the cell (L in Eq. III.B.2.4), and (2) the iso-level function T . The outcome of this step is the scalar field $G(x, y, z)$.
3. **Extraction of the isosurface $G(x, y, z) = 0$:** the final step is to retrieve the isosurface $G = 0$ from the scalar field generated in step 2 using Marching Cubes algorithm. This algorithm returns a triangular mesh that approximates the required isosurface.

To generate matrix-phase cells, the process must be performed twice, using the functions $G_1(x, y, z) = F(x, y, z) - T(x, y, z)$ and $G_2(x, y, z) = F(x, y, z) + T(x, y, z)$. Additionally, T must be non-negative, that is, $0 \leq T(x, y, z) \leq 3$.

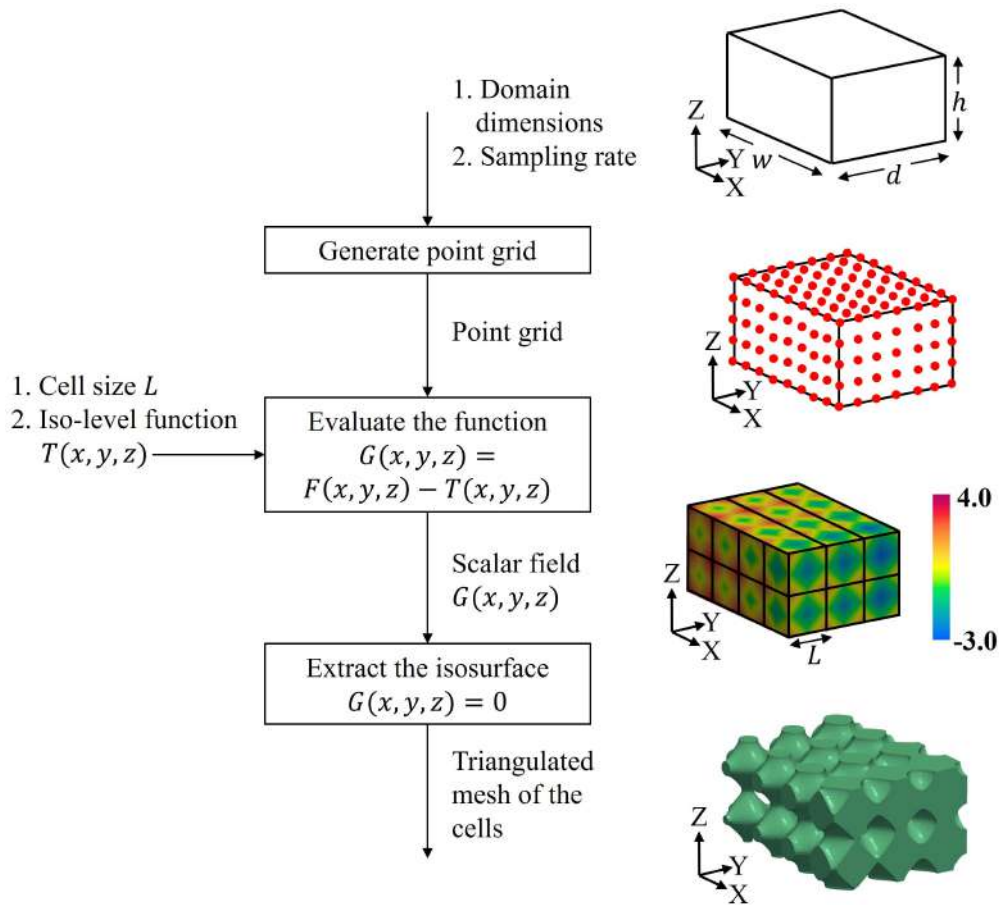


Figure III.B.2.7: Work-flow for the generation of variable-density surface lattices. Images are merely illustrative. The surface lattice was generated with a denser point grid.

III.B.2.4.6 Explicit Realization of a Density Field into Variable-density Surface Lattice Structures

The previous section described how to generate variable-density Schwarz Primitive cells. However, it has not been yet shown how to transform a given density field (as the obtained with topology optimization) into a surface lattice structure. Intuitively, and using the knowledge acquired in Section III.B.2.4.5, this section shows how to construct an iso-level function T that resembles a given density map. The key point is to generate a function T that serves as the input of the second step of the procedure to create variable-density surface lattice domains. The problem is stated using the following *Given/Goal* scheme:

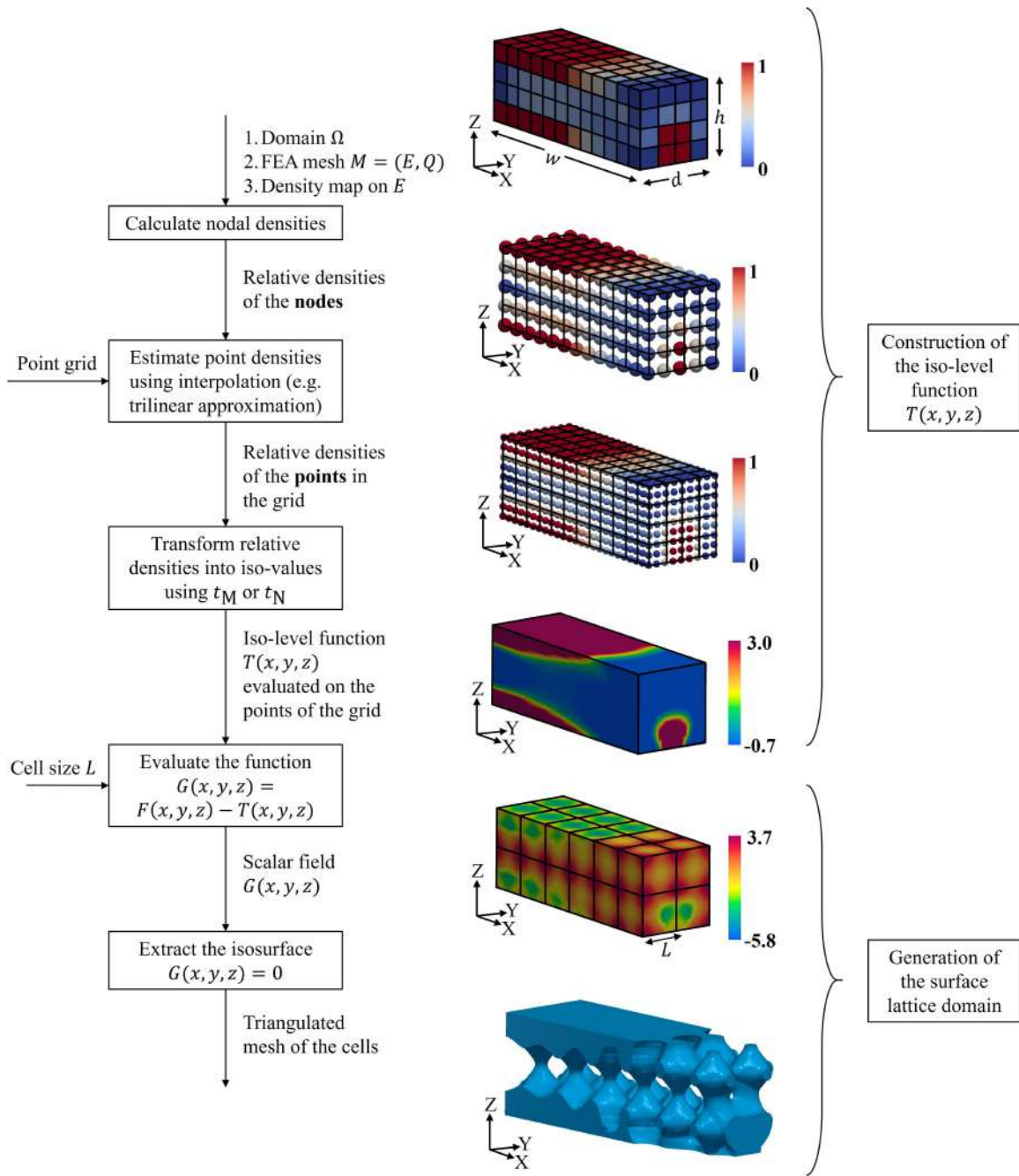


Figure III.B.2.8: Work-flow for the explicit realization of density maps into surface lattice structures. Images are merely illustrative. The generated surface lattice structure correspond to a denser FEA mesh and a denser point grid.

Given

1. A prismatic rectangular domain $\Omega \subset \mathbb{R}^3$.
2. An FEA mesh $M = (E, Q)$ that discretizes Ω , where Q is the set of nodes and E is the set of cubic elements.
3. A density map ρ_E defined on E . Let $E = \{e_1, e_2, \dots, e_N\}$, then $\rho_E : E \rightarrow [0, 1]$, where $\rho_E(e_i)$ represents the relative density of the i -th element.

Goal

1. To generate a surface lattice structure over Ω , whose density mimics the density map ρ_E . That is, to find the iso-level function $T : \mathbb{R}^3 \rightarrow \mathbb{R}$ such that for each point $p \in \Omega$, if $p \in e_i$ and $t_p = T(p)$, then $\rho(t_p) \approx \rho_E(e_i)$, where $\rho(t)$ ($\rho : \mathbb{R} \rightarrow [0, 1]$) denotes the relative density of a uniform-density Schwarz Primitive cell generated with the iso-value t .

This paper proposes a procedure for constructing the iso-level function T using the known functions t_N and t_M (Eqs. III.B.2.7 and III.B.2.9). The proposed method is divided into two main phases: (I) the construction of the iso-level function T and (II) to use to generate a variable-density surface lattice structure. Figure III.B.2.8 summarizes the steps of the whole process.

The first phase of the proposed method has three stages. The output of this phase is an iso-level function T that enables the generation of a surface lattice structure of variable and controlled density. A detailed explanation of each stage follows.

1. **Calculation of the nodal densities:** in this step, the densities of the nodes of the mesh are computed. Let $n \in Q$ be a node of the mesh that belongs to the elements $\{e_1^{(n)}, e_2^{(n)}, \dots, e_q^{(n)}\}$. The density ρ_Q of n is defined in Eq. III.B.2.16.

$$\rho_Q(n) = \frac{1}{q} \sum_{i=1}^q \rho_E(e_i^{(n)}) \quad (\text{III.B.2.16})$$

2. **Estimation of the densities of the points in the grid:** once the nodal densities are calculated, these can be used to estimate the density of every point $p \in \Omega$. Assuming (1) $\{n_1^{(i)}, n_2^{(i)}, \dots, n_8^{(i)}\}$ are the nodes of element e_i , (2) $\{\lambda_1^{(i)}, \dots, \lambda_8^{(i)}\}$ are the nodal densities and (3) $p \in e_i$, the relative density of the point p is given by $\rho_i(p) = H(p; \lambda_1^{(i)}, \dots, \lambda_8^{(i)})$, ($\rho_i : e_i \rightarrow \mathbb{R}$), where H is an interpolation function. This paper uses trilinear interpolation for the simulations.
3. **Transformation of the relative densities into iso-values:** the relative density of each point of the grid must be transformed into its corresponding iso-value. The function t_N (or t_M) in Eq. III.B.2.7 (or Eq. III.B.2.9) is used for this task. Therefore, the iso-level function of element e_i is $T_i(p) = t_N(\rho_i(p))$. The obtained iso-level function T is:

$$T(p) = \begin{cases} T_1(p), & p \in e_1 \\ \vdots \\ T_N(p), & p \in e_N \end{cases} \quad (\text{III.B.2.17})$$

It is important to remark that the function in Eq. III.B.2.17 is a piece-wise continuous function.

The second phase of the process is to use the provided function T (phase I) to generate a variable-density surface lattice structure, following the procedure described in Section III.B.2.4.5 to generate the isosurface $G = 0$ and obtain a triangulated mesh of the surface lattice domain.

III.B.2.5 Results

III.B.2.5.1 Density Field into Surface Lattice Structures. Applications in Topology Optimization

A rectangular prismatic domain Ω of size 12cm x 4cm x 4cm was used to test the algorithm described in Section III.B.2.4.6 for the explicit realization of density maps into surface lattice structures of variable density. The generated density maps correspond to the results of topology optimization on Ω . The domain Ω was discretized into the mesh M , composed by 60x20x20 cubic elements and 61x21x21 nodes. The size of each element was 0.2cm x 0.2cm x 0.2cm.

First, the SIMP algorithm was applied to optimize Ω under the loads in Fig. III.B.2.9(a). The selected volume fraction to run SIMP was $\eta = 0.5$, therefore, the target volume of the optimized domain was 96cm³. Since the key point was to test the performance of the algorithm for converting a density map into surface lattice structures, it was not necessary to force the SIMP algorithm to produce relative densities close to 0 or 1. Therefore, the value of the penalization factor was set to $p = 1.0$, which means that no penalization was imposed on the intermediate densities. The retrieved density map with the optimal density distribution dictated by the SIMP algorithm is shown in Fig. III.B.2.9(b). Notice that this density map is defined over the densities of Ω and, therefore, it is not continuous.

After SIMP delivered the density map over the elements of M , it was necessary to construct the iso-level function T to generate the equivalent surface lattice domain, using the algorithm in Section III.B.2.4.6. Therefore, a grid of 121x41x41 points was generated. Then, the element densities were converted into nodal densities and tri-linear interpolation was used to obtain the density associated to each point of the grid. The outcome of this stage is shown in Fig. III.B.2.9(c). In this figure can be seen that, in contrast with the element densities, the point densities generate a continuous variation of the density along the domain.

The density of each point of the grid was converted into the corresponding iso-value using the function t_N (Eq. III.B.2.7). In this sense, the iso-level function T was generated. Due to the limitation of network-phase Schwarz Primitive cells to deal with small densities, all point densities below 0.3 were set to this value. The resultant iso-level function T is depicted in Fig. III.B.2.9(d). Then, using the result of the previous step and the characteristic function F of Schwarz Primitive cells (Eq. III.B.2.4), the scalar field $G = F - T$ was produced. The size of the cells was defined as $L = 2.0$ cm. In Fig. III.B.2.9(e) can be seen the scalar field G . Finally, the isosurface $G = 0$ was generated using ParaView [2]. The resultant network-phase domain is depicted in Fig. III.B.2.9(f).

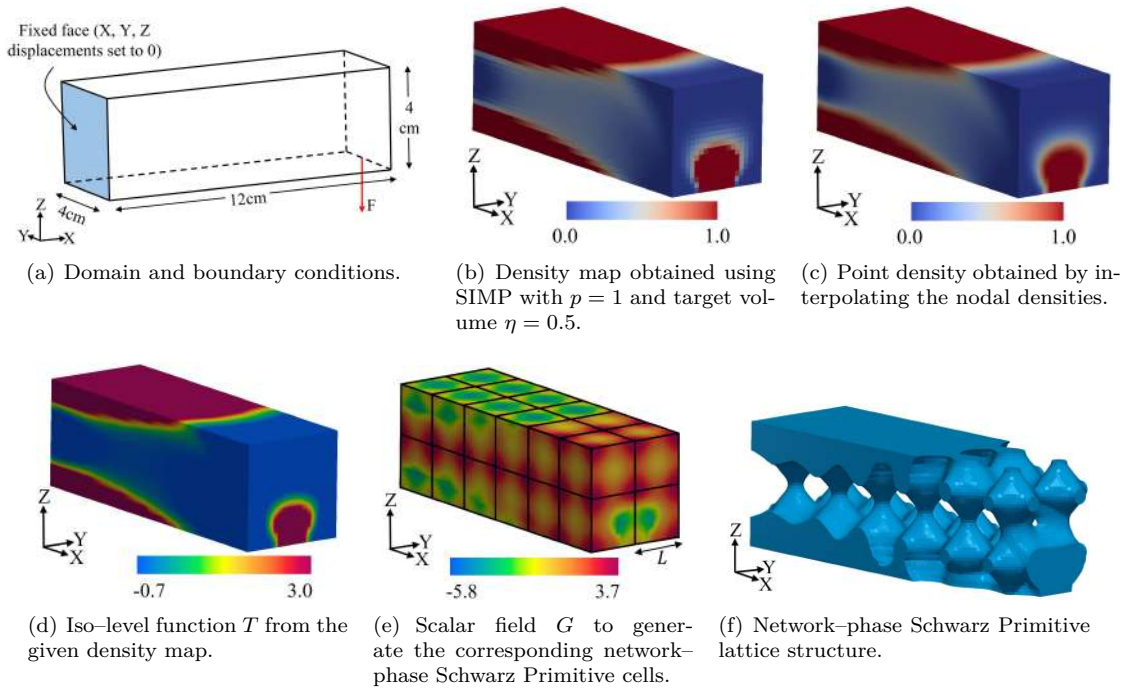


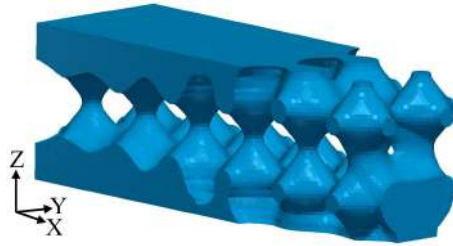
Figure III.B.2.9: Explicit realization of the results of topology optimization into surface lattice structures. The procedure was applied over a point grid of $121 \times 41 \times 41$ points.

Following a similar procedure, the density map given by SIMP in Fig. III.B.2.9(b) was used to generate other two Schwarz-modified lattice structures. Figure III.B.2.10 shows the three lattice structures generated from the density map in Fig. III.B.2.9(b). In contrast to the network-phase lattice in Fig. III.B.2.10(a), the lattice structure in Fig. III.B.2.10(b) was generated using a grid of $61 \times 21 \times 21$ points, which coincide with the nodes of the mesh M . It can be seen that the surface generated with the denser point grid is smoother, that is, surface in Fig. III.B.2.10(a) is smoother than surface in Fig. III.B.2.10(b). It shows the advantage of implementing an algorithm that allows the presence of points in the grid that do not coincide with the FEA nodes (i.e. sub-voxel sampling). It represents a main difference with most of the algorithms found in the literature, where the nodes of M are used as the point grid to generate the surface lattice domain.

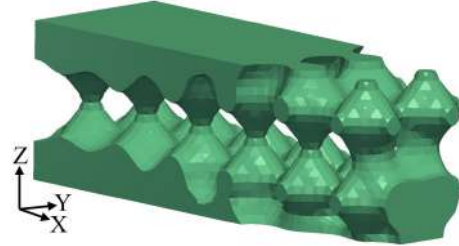
On the other hand, Fig. III.B.2.10(c) displays a matrix-phase lattice structure that resembles the density map in Fig. III.B.2.9(b). Despite matrix-phase Schwarz cells are well-suited for mapping low density values, in order to avoid numerical issues when computing the corresponding isosurface, densities below 0.05 were set to this value. Table III.B.2.2 lists the volume of the three lattice domains. It can be seen that the volume of the two network-phase domains exceeded in more than 13% the target volume. This behavior was principally caused by the threshold of 0.3 imposed to the low densities.

Table III.B.2.2: Volumes of the generated surface lattice domains.

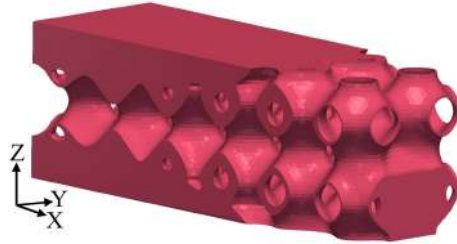
Domain	Figure number	Volume (cm ³)	Percentage of over volume (%)
Network-phase from original SIMP	III.B.2.10(a)	108.8	13.33%
Network-phase from original SIMP and point grid of 61x21x21	III.B.2.10(b)	108.8	13.33%
Matrix-phase from original SIMP	III.B.2.10(c)	97.2	1.25%
Network-phase from modified SIMP with $x_{\min} = 0.3$	III.B.2.11(b)	100.8	5.00%
Matrix-phase from modified SIMP with $x_{\min} = 0.3$	III.B.2.11(c)	96.8	0.83%



(a) Network-phase domain obtained with a grid point of 121 x 41 x 41 points.



(b) Network-phase domain obtained with a grid point of 61 x 21 x 21 points.



(c) Matrix-phase domain obtained with a grid point of 121 x 41 x 41 points.

Figure III.B.2.10: Schwarz-modified Primitive domains obtained from density map in Fig. III.B.2.9(b).

It is common in the literature [137, 208] the use of arbitrary thresholds for suppressing small values of densities produced by SIMP (as the previously used 0.3). Nevertheless, results have shown that this approach generates surface lattice domains with volumes much larger than the target volume. For this reason, this paper evaluated a simple approach in which the thresholds for low densities are included directly in the optimization stage. In this sense, the topology optimization

algorithm generates a density field that does not contain small density values.

In order to produce density maps without densities below 0.3, the formulation of SIMP was modified, so that the range of x_i in Eq. III.B.2.1 is $[x_{\min}, 1]$ (instead of $(0, 1]$), where $x_{\min} > 0$ is the minimum permitted value of density. Figure III.B.2.11(a) shows the resultant density field when $x_{\min} = 0.3$. In comparison with the results produced by the non-modified SIMP algorithm, it can be seen that the density distribution is similar but small densities ($x_i < 0.3$) disappeared.

The new density map was used to generate the lattice domains in Figure III.B.2.11. Figures III.B.2.11(b) and III.B.2.11(c) exhibit the resultant network and matrix versions of Schwarz Primitive lattice domains, respectively. In Table III.B.2.2 can be seen the volume of these two surface lattice domains. The volumes of the network and matrix-phase domains are 5% and 1% larger than the target domain. These small discrepancies between the target volume and the volume of the surface lattices may be due to (1) the fitting process of t_N and t_M , and (2) numerical issues when computing the isosurfaces.

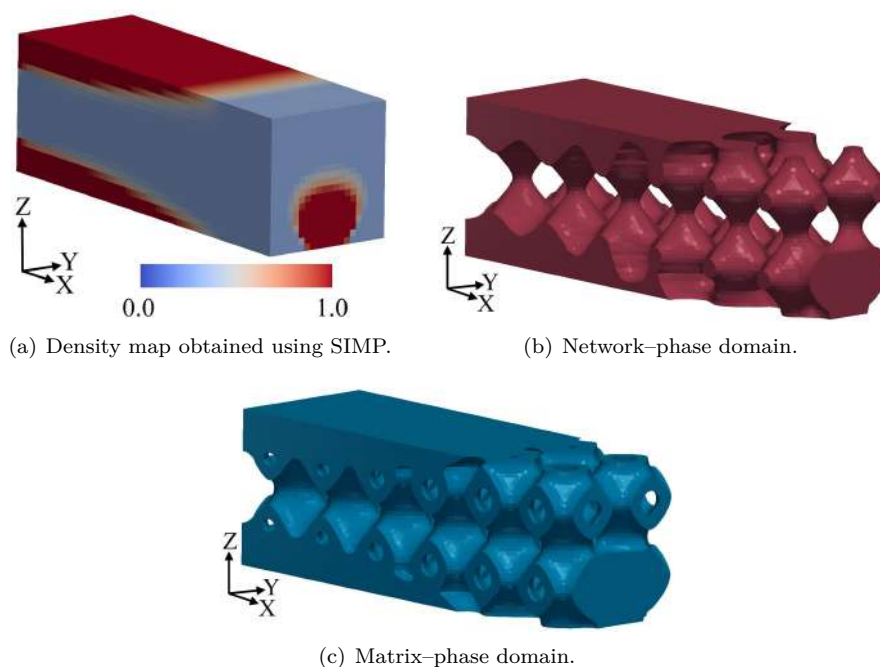


Figure III.B.2.11: Schwarz-modified Primitive domains obtained from density map in Fig. III.B.2.11(a), which has minimum density of $x_{\min} = 0.3$.

III.B.2.5.2 Physical Realization of the Devised Lattice Structures

The manufacturing of an overall domain of our implicit Schwarz-modified continuous B-Rep (Fig. III.B.2.11) would be unfeasible using traditional subtractive techniques (e.g. CNC machining). However, this domain is natural in additive manufacturing. As proof of manufacturability, our full lattice domains (Fig. III.B.2.11) were 3D-printed using Fused Deposition Modeling. Two lattice types were printed: (a) network-phase (without cavities), and (b) matrix-phase (with

cavities). In addition, partial lattice domain B-Reps (Fig. III.B.2.13(a)) were additively manufactured using Binder Jetting (Figs. III.B.2.13(b) and III.B.2.13(d)), and Selective Laser Melting (Figs. III.B.2.13(c) and III.B.2.13(e)).

Table III.B.2.3: Experimental set-up for additive manufacturing (3D printing) tests.

Domain	Figures	Size (cm x cm x cm)	Technology	Bulk material
Network-phase domain in Fig. III.B.2.11(b) (without cavities)	Fig. III.B.2.12(a)	12 x 4 x 4	Fused Deposition Modeling	PLA (Polylactic acid)
Matrix-phase domain in Fig. III.B.2.11(c) (with cavities)	Fig. III.B.2.12(b)	12 x 4 x 4	Fused Deposition Modeling	PLA (Polylactic acid)
Portion of the matrix-phase domain in Fig. III.B.2.13(a)	Figs. III.B.2.13(b) and III.B.2.13(d)	6 x 2 x 2	Binder Jetting	17-4PH stainless steel
Portion of the matrix-phase domain in Fig. III.B.2.13(a)	Figs. III.B.2.13(c) and III.B.2.13(e)	6 x 2 x 2	Selective Laser Melting	SS316L stainless steel

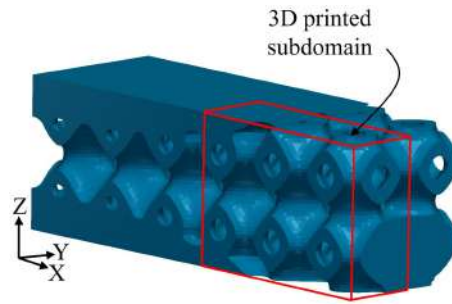


(a) Network-phase domain (without cavities).

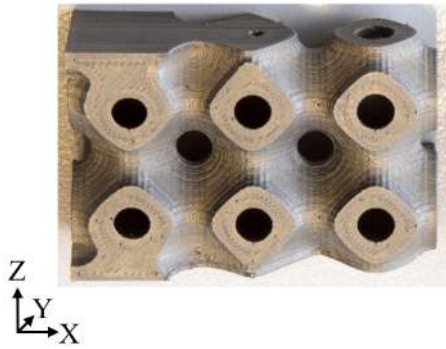


(b) Matrix-phase domain (with cavities).

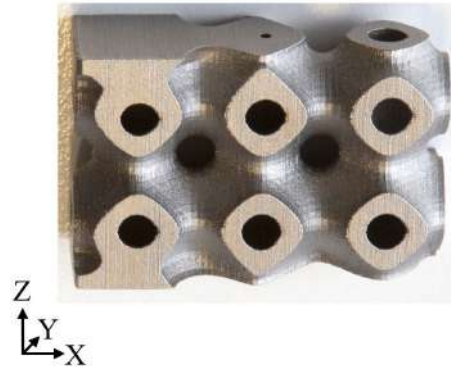
Figure III.B.2.12: Explicit realization of the results of topology optimization. 3D printed Schwarz Primitive domains using Fused Deposition Modeling.



(a) 3D printed subdomain.



(b) Binder jetting. View 1.



(c) Selective laser melting. View 1.



(d) Binder jetting. View 2.



(e) Selective laser melting. View 2.

Figure III.B.2.13: Metal additive manufacturing of the matrix-phase Schwarz-modified structures produced from topology optimization.

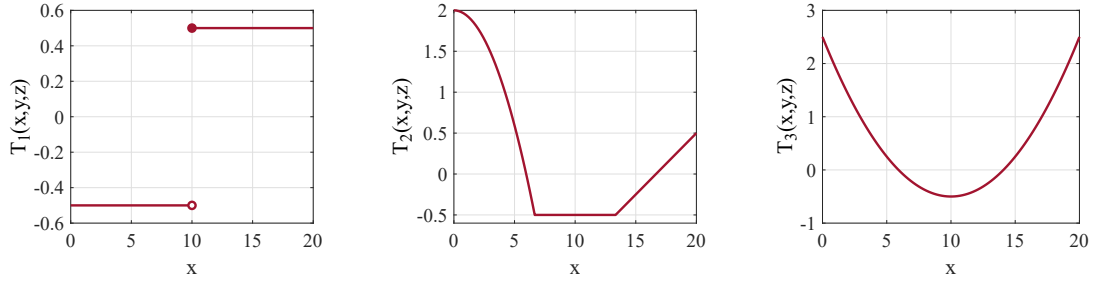
III.B.2.5.3 Stress Concentration in Variable-density Surface Lattice Structures

Previous Sections III.B.2.5.1 and III.B.2.5.2 have shown how discrete density maps can become physical objects using surface lattice functions. The first phase of this process involves the gener-

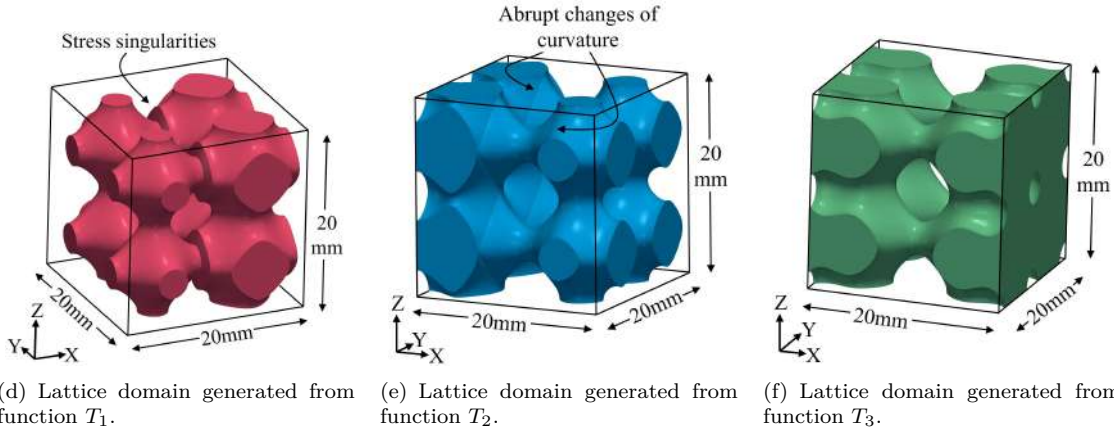
ation of a *continuous* iso-level function T from the given *discontinuous* density map. Herein, this article shows the importance of producing a continuous iso-level function. Three surface lattice structures were generated using a (1) discontinuous (T_1), (2) C^0 continuous (T_2), and (3) C^1 smooth (T_3) iso-level function. The corresponding surface lattice domains and the respective iso-level functions can be seen in Fig. III.B.2.14. The size of the domain was 20mm x 20mm x 20mm and the cell size was $L = 10$ mm.

The only difference in the generation of the three lattice domains was the iso-level function T used for each one. The reader may notice that the iso-level function not only determines the density distribution, but also establishes the characteristics of continuity and smoothness of the obtained surface lattice domain. In Fig. III.B.2.14(f) can be seen that the the smooth function T_3 generated a smooth surface. Likewise, Fig. III.B.2.14(e) shows that the continuous and non-smooth function T_2 generated a continuous domain where some abrupt changes of curvature in the points where the partial derivatives of T_2 are not continuous. On the other hand, sharp corners appeared in the lattice domain generated with the discontinuous function T_1 (Fig. III.B.2.14(d)) at $x = 10$, that coincides with the discontinuity of T_1 .

The sharp corners in the domain generated with T_3 tend to concentrate the mechanical stress and favor material failure. In order to analyze the effect of the sharp corners, the simulation shown in Fig. III.B.2.15(a) was executed. All domains were subjected to a tension load in x direction of 12kN. The material for the simulations was Ti-6Al-4V of Young's modulus $E = 114$ GPa and Poisson's ratio 0.33.



(a) Non-continuous iso-level function T_1 . (b) Continuous and non-smooth iso-level function T_2 . (c) Smooth iso-level function T_3 .



(d) Lattice domain generated from function T_1 . (e) Lattice domain generated from function T_2 . (f) Lattice domain generated from function T_3 .

Figure III.B.2.14: Variable-density Schwarz Primitive domains generated from different analytic iso-level functions.

Figures III.B.2.15(b), III.B.2.15(c) and III.B.2.15(d) show the stress in x direction for the three domains. In all cases, the maximum stress is reached at $x = 10$. Moreover, the three domains have the same cross-sectional area, since $T_1 = T_2 = T_3 = 0.5$ at $x = 10$. The maximum stress for the domains generated with continuous functions T_2 and T_3 is 480MPa. On the other hand, the maximum stress for the domain generated with the discontinuous function is 980MPa, which doubles the stress of the other two domains. It is noticeable that the stress is completely concentrated in the sharp corners. This results show the relevance of using

As stated in Section III.B.2.4.6, the iso-level function that generates the algorithm proposed in this article is continuous. However, its partial derivatives are not continuous in the intersection of the FEA elements. Therefore, its behavior is analogous to the behavior of T_2 . The executed experiments have not shown any effects on the mechanical stress of the non-smooth transitions of the generated lattice domains. However, numerical and physical tests should be done in the future to test the mechanical response of the surface lattice structures generated with the proposed methodology.

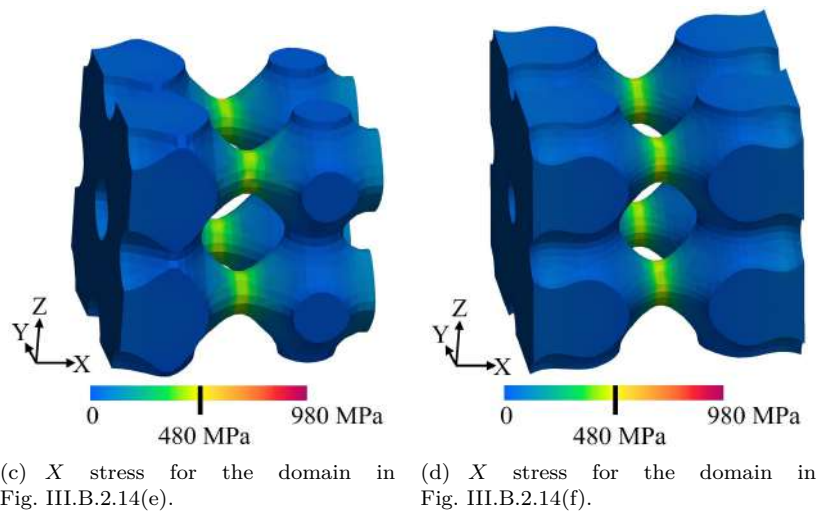
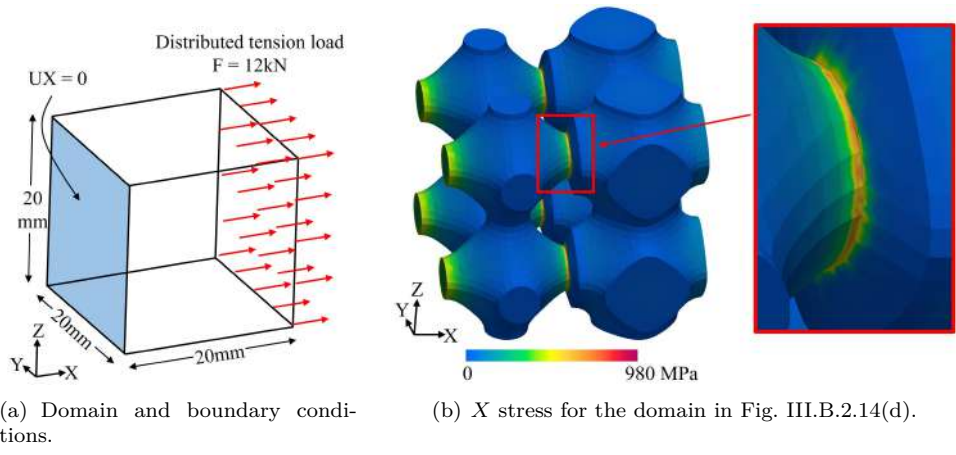


Figure III.B.2.15: FEA analysis and stress concentration in variable-density Schwarz Primitive domains.

III.B.2.6 Conclusions

This paper presents a procedure to effectively transform density maps (as generated by topology optimization algorithms) into manufacturable surface lattice structures, such as Schwarz Primitive architectures. The results show that the generated surface lattice domains (1) effectively resemble the given density map and (2) can be fabricated using additive manufacturing/3D printing techniques. The results also reveal that the network-phase (architecture without internal cavities) lattice structures have limitations to map small density values, due to the generation of disconnections in the boundary of the cells. On the other hand, matrix-phase (architecture with internal cavities) structures have the capacity to map along the range of densities $(0, 1]$. In this case, the minimum density that can be represented is dictated by the manufacturing technology and the limitations associated to the machine (minimum detail that can be accurately reproduced).

Our implementation removes the limitation of the SIMP algorithm which polarizes the FEA relative densities to either 0 or 1 by allowing a real number in the interval $(0, 1]$. These intermediate densities are achievable by using the sub-voxel implicit functions used in our implementation. The smoothness in the spatial element density field is important because abrupt changes of density may lead to high stress concentrations.

This study also contributes the derivation of a function that expresses the Schwarz Primitive iso-value as a function of the relative density. This function allows to control the relative density of the Schwarz Primitive domain and may be used in future applications of Schwarz Primitive cells.

Future research is needed in the modeling of mechanical response (stress/strain/deformation) of large sets of lattices under working loads, with arbitrary topology and geometry of the lattice-based workpiece. Likewise, further efforts are required in the mechanical characterization of physical surface lattice samples produced by additive manufacturing techniques.

Author Contributions: D.M-Z., A.M. and O.R-S. conceptualized the algorithm. D.M-Z. and J.P-C. carried out and validated the simulations A.M., J.P. and O.R-S. supervised the Computational Geometry and Manufacturing aspects and applications of this research. All the authors contributed to the writing of the article.

Funding: This research received no external funding.

Conflicts of Interest: The authors declare no conflict of interest.

III.B.2.7 Abbreviations

FEA:	Finite element analysis.
SIMP:	Solid isotropic material with penalization, which is a topology optimization algorithm.
c :	$c(\mathbf{X})$, $c : \mathbb{R}^n \rightarrow \mathbb{R}$, denotes the compliance or total strain energy of a domain with vector of relative densities \mathbf{X} (J).
$p \geq 1$:	Penalty factor aimed to polarize element relative densities around 0 and 1.
$\eta \in (0, 1)$:	Fraction of volume to be retained (or target volume) in the final design.

V :	$V(\mathbf{X})$, $V : \mathbb{R}^n \rightarrow \mathbb{R}$, denotes the volume of a domain with vector of relative densities \mathbf{X} (mm^3 or cm^3).
V_0 :	Volume of the design domain Ω (mm^3 or cm^3).
E_0 :	Young's modulus of the bulk material (Pa).
E_i :	Young's modulus of the i -th element of the mesh (Pa).
L :	Length of the surface lattice cell (mm or cm).
$0 \leq \rho \leq 1$:	Relative density or volume fraction of a Schwarz Primitive cell of uniform density (mm or cm).
$\rho(t)$:	The function $\rho : \mathbb{R} \rightarrow [0, 1]$ returns the relative density of a Schwarz Primitive cell generated with an iso-value t .
$\rho_N(t)$ (or $\rho_M(t)$):	The function $\rho_N : \mathbb{R} \rightarrow [0, 1]$ (or $\rho_M : \mathbb{R} \rightarrow [0, 1]$) returns the relative density of a network-phase (or matrix-phase) Schwarz Primitive cell generated with an iso-value t .
$\rho_E(e)$ (or $\rho_P(n)$):	The function $\rho_E : E \rightarrow [0, 1]$ (or $\rho_n : P \rightarrow [0, 1]$) gives the relative density of an element $e \in E$ (or node $n \in P$) of the mesh.
$t \in \mathbb{R}$:	Iso-value to generate a Schwarz Primitive cell of uniform density.
$t(\rho)$:	The function $t : [0, 1] \rightarrow \mathbb{R}$ returns the iso-value that generates a Schwarz Primitive cell of relative density ρ .
$t_N(\rho)$ (or $t_M(\rho)$):	The function $t_N : [0, 1] \rightarrow \mathbb{R}$ (or $t_M : [0, 1] \rightarrow \mathbb{R}$) returns the iso-value that generates a network-phase (or matrix-phase) Schwarz Primitive cell of relative density ρ .
$F(x, y, z)$:	$F : \mathbb{R}^3 \rightarrow \mathbb{R}$ is the implicit function that characterizes the Schwarz Primitive surfaces.
$T(x, y, z)$:	The iso-level function ($T : \mathbb{R}^3 \rightarrow \mathbb{R}$) used to produce variable-density surface lattice structures. The function T is the generalization of the value t .
$G = F + T$:	Scalar field $G : \mathbb{R}^3 \rightarrow \mathbb{R}$ that is evaluated to generate variable-density surface lattice structures.
$\Omega \subset \mathbb{R}^3$:	Rectangular prismatic subset of \mathbb{R}^3 , which represents the design domain.
w, d, h :	Width, depth and height of Ω (mm or cm).
$M = (E, V)$:	Finite element mesh associated to the design domain, that is, a discretization of Ω . The set $E = \{e_1, e_2, \dots, e_N\}$ denotes the elements of the mesh and the set $P = \{n_1, n_2, \dots, n_l\} \subset \mathbb{R}^3$ denotes the nodes of the mesh.
H :	Interpolation function. In this paper $H(p; \lambda_1, \dots, \lambda_8)$ refers to tri-linear interpolation of point p given the values $\lambda_1, \dots, \lambda_8$.
$X = [x_1, \dots, x_n]$:	Vector of relative densities of the N elements of the mesh M .

III.B.2.8 Appendix A. Iso-level Functions

The iso-levels functions used in Section III.B.2.5.3 are presented in Table III.B.2.4. The explicit version of the function is associated to the corresponding figures where it is employed. The value of the cell size is $L = 10\text{mm}$.

Table III.B.2.4: Iso-level functions used in Section III.B.2.5.3.

Figure numbers	Iso-level function
III.B.2.14(a) and III.B.2.14(d)	$T_1(x, y, z) = \begin{cases} -0.5 & , 0 \leq x \leq L \\ 0.5 & , L < x \leq 2L \end{cases}$
III.B.2.14(b) and III.B.2.14(e)	$T_2(x, y, z) = \begin{cases} -\frac{5}{2} \left(\frac{3x}{2L}\right)^2 + 2 & , 0 \leq x \leq \frac{2L}{3} \\ \frac{39}{20L}x - \frac{9}{5} & , \frac{2L}{3} < x \leq \frac{4L}{3} \\ -\frac{99}{20L}x + \frac{37}{5} & , \frac{4L}{3} < x \leq 2L \end{cases}$
III.B.2.14(c) and III.B.2.14(f)	$T_3(x, y, z) = 3 \left(\frac{x}{L} - 1\right)^2 - \frac{1}{2}, 0 \leq x \leq 2L$

III.B.3

Approximation of the Mechanical Response of Large Lattice Domains Using Homogenization and Design of Experiments

Diego Montoya-Zapata^{1,2}, Diego A. Acosta³, Camilo Cortés², Juan Pareja-Corcho^{1,2}, Aitor Moreno², Jorge Posada² and Oscar Ruiz-Salguero¹

¹Laboratory of CAD CAM CAE, Universidad EAFIT, Cra 49 no 7-sur-50, Medellín 050022, Colombia

²Vicomtech Foundation, Basque Research and Technology Alliance (BRTA), Mikeletegi 57, Donostia-San Sebastian 20009, Spain

³Grupo de Diseño y Desarrollo de Procesos (DDP), Universidad EAFIT, Cra 49 no 7-sur-50, Medellín 050022, Colombia

III.B.3.1 Context

III.B.3.1.1 Manuscript in International Conference



Diego Montoya-Zapata, Diego A. Acosta, Camilo Cortes, Juan Pareja-Corcho, Aitor Moreno, Jorge Posada, Oscar Ruiz-Salguero. Meta-modeling of Lattice Mechanical Responses via Design of Experiments. *MACISE - 2020 - 2nd Intl. Conf, on Mathematics and Computers in Science and Engineering*. January 18-20, 2020. Madrid, Spain. Pages: 308-317. DOI: <https://doi.org/10.1109/MACISE49704.2020.00065>, URL: <https://ieeexplore.ieee.org/document/9195607>, e-ISBN: 978-1-7281-6695-7, ISBN: 978-1-7281-6696-4, Publisher: IEEE.

Indexing: SCOPUS, Web of Science

III.B.3.1.2 Extended Follow-up Published in International Journal



applied sciences



an Open Access Journal by MDPI

Diego Montoya-Zapata, Diego A. Acosta, Camilo Cortes, Juan Pareja-Corcho, Aitor Moreno, Jorge Posada, Oscar Ruiz-Salguero. Approximation of the Mechanical Response of Large Lattice Domains Using Homogenization and Design of Experiments. *Journal Applied Sciences*, (ISSN 2076-3417; CODEN: ASPCC7), 2020, 10(11), 3858; (This article belongs to the Special Issue Computational and Mathematical Methods in Engineering and Information Science). url= <https://www.mdpi.com/2076-3417/10/11/3858>, doi= <https://doi.org/10.3390/app10113858>, Published online: 1 June 2020.

Indexing: JCR(Q2), SCOPUS(Q1), Publindex(A1)

Abstract

Lattice-based workpieces contain patterned repetition of individuals of a basic topology (Schwarz, ortho-walls, gyroid, etc.) with each individual having distinct geometric grading. In the context of the design, analysis and manufacturing of lattice workpieces, the problem of rapidly assessing the mechanical behavior of large domains is relevant for pre-evaluation of designs. In this realm, two approaches can be identified: (1) numerical simulations which usually bring accuracy but limit the size of the domains that can be studied due to intractable data sizes, and (2) material homogenization strategies that sacrifice precision to favor efficiency and allow the simulation of large domains. Material homogenization synthesizes diluted material properties in a lattice, according to the volume occupancy factor of such a lattice. Preliminary publications show that material

homogenization is reasonable in predicting displacements, but is not in predicting stresses (highly sensitive to local geometry). As a response to such shortcomings, this paper presents a methodology that systematically uses Design of Experiments (DOE) to produce simple mathematical expressions (meta-models) that relate the stress/strain behavior of the lattice domain and the displacements of the homogeneous domain. The implementation in this paper estimates the von Mises stress in large Schwarz Primitive lattice domains under compressive loads. The results of our experiments show that (1) material homogenization can approximate efficiently and accurately the displacements field even in complex lattice domains and (2) material homogenization and DOE can produce rough estimations of the von Mises stress in large domains (more than 100 cells). The errors in the von Mises stress estimations reach 42% for domains of up to 24 cells. This result means that *coarse* stress / strain estimations may be possible in lattice domains by combining DOE and homogenized material properties. This option is not suitable for *precise* stress prediction in sensitive contexts where high accuracy is needed. Future work is required to refine the meta-models to improve the accuracy of the estimations.

Keywords: Design of Experiments, Lattice Structures, Homogenization, Schwarz Primitive, Mechanical Characterization, Modeling and Simulation.

Glossary

AM:	Additive manufacturing.
CCF:	Central composite face-centered design.
DOE:	Design of experiments.
FEA:	Finite element analysis.
Ω, Ω^Q :	Subsets of \mathbb{R}^3 that represents the lattice domain and the equivalent homogeneous domain, respectively ($\Omega, \Omega^Q \subset \mathbb{R}^3$).
E, E^Q :	Young's moduli of the bulk and equivalent material, respectively (Pa).
ν, ν^Q :	Poisson's ratio of the bulk and equivalent material, respectively.
σ_{VM} :	Von Mises stress (Pa).
L :	Length of the Schwarz Primitive cell ($L > 0$).
ρ :	Relative density or volume fraction of a Schwarz Primitive cell ($0 \leq \rho \leq 1$).
t :	Iso-value used to generate the Schwarz Primitive cell ($t \in [-3, 3]$).

III.B.3.2 Introduction

New emerging technologies in the context of Industry 4.0 such as digital twins pose new challenges in the design and simulation in the industrial and biomedical ecosystems. The interactive nature of the processes of Industry 4.0 requires fast simulation methods that enable real-time decision making and digital twin's continuous update with the physical world [145].

Lattice materials have multiple applications in engineering (e.g. energy absorption) and biomedicine (e.g. implants and scaffolds) [78]. However, the simulation of large lattice domains is in many cases unfeasible because: (1) the meshing of these domains is a time consuming process that involves

human intervention and (2) the size of the produced meshes is intractable due to the geometric complexity associated to these domains [36, 184].

This manuscript implements a methodology that combines material homogenization and design of experiments (DOE) to estimate the stress/strain response in large lattice domains. The main advantage of this methodology is its inferior computational expense in comparison to finite element analysis (FEA). We apply this approach to approximate the von Mises stress in lattice structures of the type Schwarz Primitive. This manuscript is an extension of the work in [119] which presents a methodology to develop the meta-models using DOE but does not integrate them with material homogenization to produce stress/strain estimations in large lattice domains.

The remainder of this article is organized as follows: Section III.B.3.3 provides a review of the relevant related work. Section III.B.3.4 describes the proposed methodology to estimate the stress/strain response in lattice domains using material homogenization and DOE. Section III.B.3.5 presents and evaluates the results of the implementation of our methodology. Section III.B.3.6 concludes the manuscript and suggests future extensions of the article.

III.B.3.3 Literature Review

III.B.3.3.1 Lattice Structures and Material Homogenization

Lattice structures are generally composed by replicas of a unit cell that are continuous, uniformly distributed and fill the space. The reason why lattice structures attract the attention of engineers is its ability to retain a good mechanical performance while reducing material usage and weight. For this reason, lattice structures are used for energy absorption, heat transfer and vibration damping applications [78]. Additive manufacturing (AM) has also widen the application range of lattice structures. The manufacturing freedom of AM has promoted the use of lattice structures for materializing the results of structural optimization [94, 127, 137, 197] and for biomedical applications in orthopedics and tissue engineering [8, 113].

Material homogenization seeks the equivalent Young's modulus and Poisson's ratio to produce a homogeneous structure that resembles the displacements field of the lattice domain. Material homogenization suppresses the geometrical complexity associated to lattice domains. Therefore, lighter FEA meshes are obtained and, consequently, the computational cost and time of FEA simulations are reduced [29, 94].

Apart of predicting macro-mechanical properties (Young's and Poisson's moduli), material homogenization has allowed the study of periodic strut-like lattice structures built via AM, considering the defects caused during the manufacturing with AM and the stiffening in the joints of the structure [101, 139]. These studies are however limited to strut-like lattice structures. Material homogenization has also been successfully integrated with topology optimization to produce optimal designs of lattice structures suitable for AM [29, 94]. However, since the homogeneous and lattice domains have notorious geometrical differences and stresses/strains depend on the geometry, the stress/strain behavior of the homogeneous domain does not resemble the one of the lattice domain.

III.B.3.3.2 Modeling and Simulation of Lattice Structures

The numerical analysis of the mechanical behavior of large lattice structures is challenging due to the high computing (memory and time) requirements [184]. Large lattice structures demand heavy FEA meshes formed by solid elements. Sometimes solid FEA meshes can be simplified using

simpler and lighter FEA elements (beams or shells). This approach has allowed the simulation of relatively large domains of a few hundred of cells [21, 92, 123, 184]. However, this technique cannot be applied to surface-type lattice structures like Schwarz Primitive lattices, since this kind of architecture cannot be synthesized into long struts or thin plates.

Regarding the joint use of FEA and DOE, we found that they have been combined in several applications in non-lattice structures. The current work can be divided in three groups: (i) material or mechanical properties evaluation, including metallic [187], resins [86] and composite materials [136], (ii) shape optimization on mechanical parts, including medical devices [141] and automobile parts [161], and (iii) generation of meta-models to estimate the stress-strain response in small lattice domains using DOE [119]. However, the produced meta-models are not used for any further analysis with large lattice domains. To the best of our knowledge, the works in the literature do not implement a methodology that integrates systematically material homogenization and DOE for stress/strain estimation in the field of lattice materials.

Monte Carlo methods [103, 114] use random samples in the domains of input variables for an experiment. The experiment is run under the prescribed combination of input variables, and the resulting output values recorded. The model mathematical model for the system or cause/effect is computed on the basis of maximal likeness. In our case, the expenses of running each test are significant since each test requires the preparation and setup of the FEA experiment, the execution itself and its post-processing, along with the analysis of results. This high cost is common to almost all experiments, and leads to choose a minimal (and as possible orthogonal) set of samples of the input set, leading to DOE. This DOE, more economical than the Monte Carlo trials, was chosen for the present work.

III.B.3.3.3 Conclusions of the Literature Review

In our literature survey, we found that the geometry of lattice structures implies the use of small FEA elements which produces intractable FEA meshes. Consequently, the numerical analysis of large lattice structures is a complex (sometimes unfeasible) process, limited by its elevated computational cost.

To alleviate the computational burden of the simulation of lattice structures, material homogenization is applied to produce regular domains that mimic the lattice domain. Following this approach, one can obtain fast and accurate approximations of the displacements field of the lattice domain. However, the stress/strain response cannot be directly obtained due to the geometric dissimilarities between the lattice and the homogeneous domains.

Our goal with this paper is to contribute to the problem of the estimation of the stress/strain response in large lattice domains. For this purpose, we propose a methodology that integrates material homogenization and DOE. We use the DOE-based methodology in [119] to devise simple mathematical expressions (meta-models) to characterize the stress/strain of Schwarz Primitive lattice domains. The inputs of the produced meta-models are displacement-based features that can be efficiently calculated using material homogenization instead of full FEA simulations. The meta-models developed in this article are not intended to be suitable in high precision contexts, but to produce rough and efficient estimations of the von Mises stress that allow fast pre-evaluation of designs.

Particularly, we apply our methodology to estimate the von Mises stress under compressive loads for large (more than 100 cells) Schwarz Primitive lattice structures. The meta-models use the strains of the boundary of the lattice cell to relate the displacement field of the homogeneous

domain with the von Mises stress of the lattice domain.

III.B.3.4 Methodology

III.B.3.4.1 Schwarz Primitive Lattice Structures

Schwarz Primitive lattice structures are obtained by calculating isosurfaces of the real valued function $F : \mathbb{R}^3 \rightarrow \mathbb{R}$ in Eq. III.B.3.1:

$$F(x, y, z) = \cos\left(\frac{2\pi}{L}x\right) + \cos\left(\frac{2\pi}{L}y\right) + \cos\left(\frac{2\pi}{L}z\right), \quad (\text{III.B.3.1})$$

where L is the desired length of the cell [192].

Schwarz Primitive lattice structures are employed in topology optimization for AM. The result of some common methods in topology optimization is a density map that is impossible to manufacture. The problem of converting that density map into a manufacturable domain does not have an exact solution. The mathematical structure of Schwarz Primitive lattice allow to find approximate solutions to that problem, providing manufacturable designs with smooth transitions in the connections of multiple cells, preventing stress concentration [127]. Moreover, Schwarz Primitive lattice structures are stiffer than other lattice structures (such as the gyroid) [108]. These properties make Schwarz Primitive structures attractive for engineering and biomedical applications [108, 127, 137].

In order to show the geometry of the Schwarz Primitive cell, we obtained the isosurfaces for the isovalues $t = -0.87, 0.0, 0.87$, that is, we found the surfaces that solved the equation $F = t$. The corresponding relative density ρ (i.e. the ratio of the volume of the cell and L^3) of each cell was $\rho = 0.25, 0.5, 0.75$, respectively. Figure III.B.3.1 displays the cells along with their corresponding isovalues and relative densities.

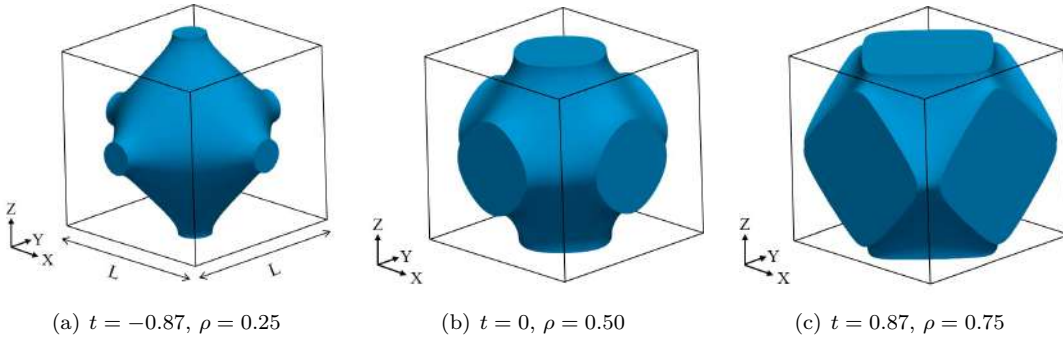


Figure III.B.3.1: Geometry and relative density of Schwarz Primitive cells for different isovalues.

III.B.3.4.2 Methodology to Estimate the Stress/Strain Response of Lattice Structures

In this paper, we propose a methodology for the efficient estimation of the stress/strain response of large lattice structures. The proposed algorithm relies on two main concepts: material homogeniza-

tion and DOE. The algorithm is divided into four stages: (1) material homogenization of the lattice structure, (2) numerical simulation of the load case using the homogeneous domain, (3) extraction of displacement-based features, and (4) the application of meta-models to estimate the response variable based on the features extracted in (3). Below, we describe every step of our algorithm. Figure III.B.3.2 presents a graphical summary of the proposed methodology, with the inputs and outputs of each phase of the process.

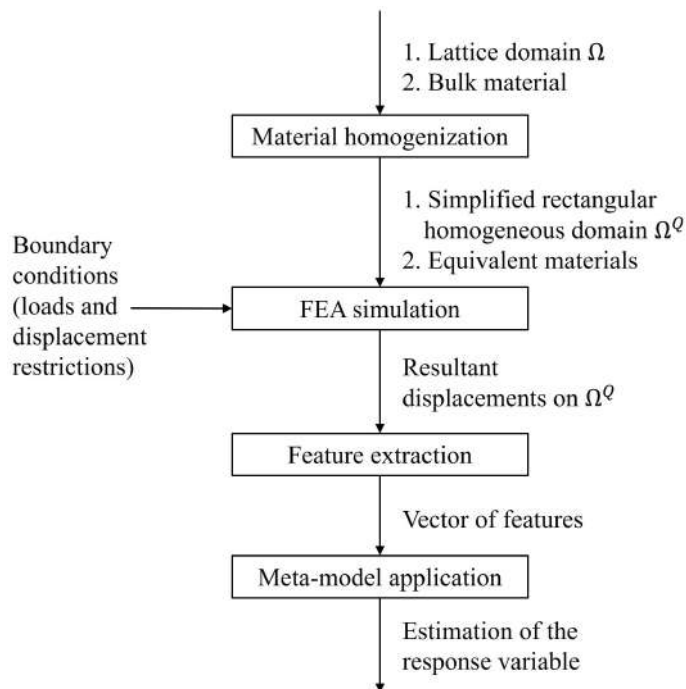


Figure III.B.3.2: Work-flow for the estimation of the mechanical response of lattice domains using material homogenization and DOE.

III.B.3.4.2.1 Material Homogenization

This process seeks to obtain a simplified regular (homogeneous) domain Ω^Q that approximates the heterogeneous lattice structure Ω . The goal is to find an equivalent material (E^Q, ν^Q) so that the regular domain equipped with the equivalent material (E^Q, ν^Q) resembles the displacement field of the original lattice domain. We implemented the numerical homogenization method presented in [172], which has been applied in the context of lattice structures in [29, 94]. In Section III.B.3.4.3, the reader can find more details on the foundations of material homogenization.

III.B.3.4.2.2 FEA Simulation of the Homogeneous Domain

At this stage, the load case is simulated on the homogeneous domain Ω^Q using analogous boundary conditions. The result of this stage is the displacement field on Ω^Q , which is an approximation of the displacement field on the lattice domain Ω .

III.B.3.4.2.3 Feature Extraction

Characteristic features of every cell of the lattice domain Ω are extracted using the displacement field over the homogeneous domain Ω^Q obtained in the previous step. These displacement-based features extracted at this stage are used as inputs of the meta-models to estimate the stress/strain response of every cell. The definition of these features is central to obtain reliable meta-models and is highly dependent to the expertise of the modeler.

The extracted features condense (or characterize) the deformation of the cell and must provide information about the variable of interest. In this work, we use as features the average normal strain at the flat faces of the boundary of the Schwarz Primitive cells, which can be obtained directly from the displacements on the homogeneous domain Ω^Q . A discussion on how to generate the meta-models using DOE is presented in Section III.B.3.4.4.

III.B.3.4.2.4 Meta-model Execution

A meta-model is a simple mathematical expression (i.e. function) that relates the features extracted in the previous stage and the response variable. In other words, the features extracted in the previous stage (denoted by $\mathbf{X} = [x_1, \dots, x_n]^T$) are used to feed a function $f : \mathbb{R}^n \rightarrow \mathbb{R}$ that gives an estimation of the response variable for every cell of the lattice domain. In this article, the meta-models are developed using DOE techniques (see Section III.B.3.4.4).

III.B.3.4.3 Material Homogenization

Material homogenization seeks to represent a heterogeneous material with a simple *homogeneous* material. In the case of lattice structures, a lattice unit cell can be treated as a composite material formed by solid (with bulk properties E and ν) and void (with properties E_0 and ν_0) zones [29, 94]. Material homogenization aims to find the material properties (E^Q and ν^Q) that make a filled cube behaves like the unit lattice cell (see Fig. III.B.3.3).

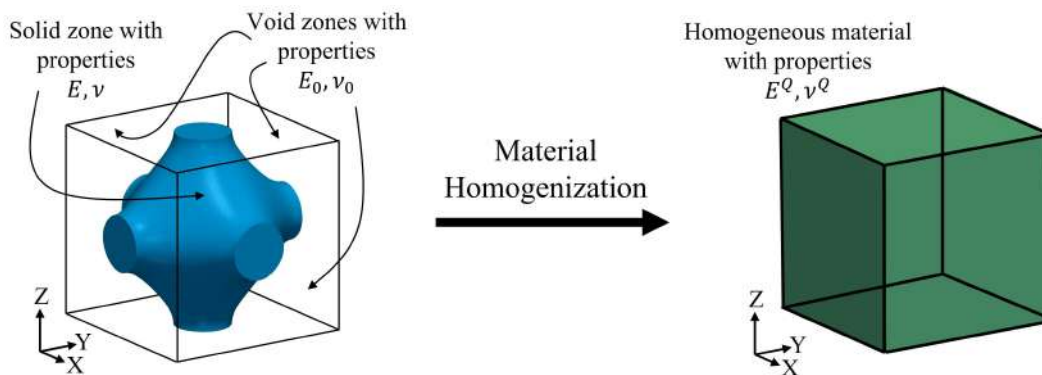


Figure III.B.3.3: Graphical representation of material homogenization.

We implemented the numerical homogenization method proposed in [172]. This method finds the elasticity matrix \mathbf{C}^Q :

$$\mathbf{C}^Q = \begin{bmatrix} c_1 & c_2 & c_2 & 0 & 0 & 0 \\ c_2 & c_1 & c_2 & 0 & 0 & 0 \\ c_2 & c_2 & c_1 & 0 & 0 & 0 \\ 0 & 0 & 0 & c_3 & 0 & 0 \\ 0 & 0 & 0 & 0 & c_3 & 0 \\ 0 & 0 & 0 & 0 & 0 & c_3 \end{bmatrix}, \quad (\text{III.B.3.2})$$

that relates stresses and strains in the homogeneous material as $\boldsymbol{\sigma} = \mathbf{C}^Q \boldsymbol{\varepsilon}$. The corresponding Young E^Q and Poisson ν^Q moduli are provided by the following equations:

$$E^Q = \frac{c_1^2 + c_1 c_2 - 2c_2^2}{c_1 + c_2}, \quad (\text{III.B.3.3})$$

$$\nu^Q = \frac{c_2}{c_1 + c_2}. \quad (\text{III.B.3.4})$$

In this work, we selected the Titanium alloy *Ti-6Al-4V* as bulk material with properties: Young's modulus $E = 114$ GPa and Poisson's ratio $\nu = 0.33$. We applied the homogenization procedure to obtain the diluted properties of Schwarz Primitive cells for the relative densities $\rho \in \{0.25, 0.3, 0.4, 0.5, 0.6, 0.7, 0.8, 0.9\}$. Table III.B.3.2 displays the results obtained. Table III.B.3.2 also includes the case in which the density is $\rho = 1.0$. Notice that the properties of the homogeneous domain coincide with the bulk properties (as expected). When needed, the properties of intermediate densities were obtained via linear interpolation.

Table III.B.3.2: Results of numerical homogenization of Schwarz Primitive cells: Young's modulus and Poisson's ratio.

Relative density (ρ)	Equivalent Young's modulus (E^Q)	Equivalent Poisson's ratio (ν^Q)
0.25	7.5 GPa	0.05
0.3	14.0 GPa	0.09
0.4	24.0 GPa	0.13
0.5	35.0 GPa	0.17
0.6	48.0 GPa	0.21
0.7	61.0 GPa	0.23
0.8	81.0 GPa	0.27
0.9	97.0 GPa	0.29
1.0	114 GPa	0.33

III.B.3.4.4 Generation of Meta-models using DOE

DOE is a traditional and effective methodology based on statistical techniques that supports the analysis of complex processes and systems. DOE allows to establish in a systematic way how changes in the parameters of a system or function affect their outcome, minimizing the uncertainty and the number of required experiments to complete such characterization. DOE covers the whole spectrum, from the planing of the experiments to the statistical analysis of the results [22, 134]. We

used DOE techniques to develop meta-models to estimate the von Mises stress in Schwarz Primitive lattice structures.

The von Mises stress σ_{VM} is a material failure criterion used in the design and analysis of lattice structures in various works (e.g. [151, 153, 205]). The von Mises stress is defined as per Eq. III.B.3.5:

$$\sigma_{VM} = \sqrt{\sigma_1^2 + \sigma_2^2 + \sigma_3^2 - (\sigma_1\sigma_2 + \sigma_1\sigma_3 + \sigma_2\sigma_3)}, \quad (\text{III.B.3.5})$$

where $\sigma_1, \sigma_2, \sigma_3$ are the principal stresses. The criterion states that, for preventing failure, the von Mises stress must be below the tensile strength of the material. However, failure in lattice materials is also governed by buckling instabilities that occur before material failure [101]. For the sake of demonstration of the methodology, this work is limited to the estimation of the von Mises stress, although a more complete failure criterion for lattice structures should consider buckling phenomena.

The procedure to devise meta-models using DOE is summarized into three phases: (1) identification of potential features (also called factors) that may affect the variable of interest, (2) selection of the most influential (main) factors, and (3) development of simple mathematical expressions (meta-models) that relates the main factors and the response variable.

We applied DOE to develop meta-models for the von Mises stress in Schwarz Primitive lattice structures of different relative densities. In an ideal case, we should have attained a meta-model for each relative density $\rho \in (0, 1)$. This computing resource demand makes this option unfeasible. Since we were only seeking approximations of the von Mises stress, we found meta-models for the relative densities $\rho = 0.25, 0.50, 0.75, 1.0$. To find the four meta-models, we used lattice domains formed by a single unit cell of the mentioned relative densities. Below, we describe in detail every stage of the procedure.

III.B.3.4.4.1 Factors Identification

The goal at this stage was to detect features (or factors) $F_V = \{f_1, f_2, \dots, f_n\}$ that (1) were related to the von Mises stress and (2) could be controlled. Additionally, the features had to be based on the displacements over the lattice, so that they could be retrieved from the FEA simulation over the homogeneous domain Ω^Q .

Our set of factors were initially the strains at the flat faces (extreme faces) of the boundary of each unit cell of the Schwarz Primitive lattice domain. For convenience, the flat faces of the boundary were denoted as $\{X, -X, Y, -Y, Z, -Z\}$. $\{-X, -Y, -Z\}$ were the flat faces at $x = 0, y = 0, z = 0$. $\{X, Y, Z\}$ were the flat faces at $x = L, y = L, z = L$. We defined the strains at the flat faces as:

$$\varepsilon_{ij} = \text{sgn}(i) \cdot \frac{U_{ij} - U_{-jj}}{L}, \quad (\text{III.B.3.6})$$

$$i = \pm X, \pm Y, \pm Z, \quad j = x, y, z,$$

where U_{ij} represented the average displacement in j direction of the face i . For instance, U_{-Xx} was the displacement in x direction of the flat face at $x = 0$. The normal strains at the flat faces corresponded to $\{\varepsilon_{-Xx}, \varepsilon_{Xx}, \varepsilon_{-Yy}, \varepsilon_{Yy}, \varepsilon_{-Zz}, \varepsilon_{Zz}\}$. However, from Eq. III.B.3.6, $\varepsilon_{-Xx} = \varepsilon_{-Yy} = \varepsilon_{-Zz} = 0$, which prevented the introduction of false strains due to pure translation of the Schwarz Primitive cell.

In Eq. III.B.3.5 we can see that the von Mises stress depends on the shear stress and, therefore, it is influenced by the shear strain. We conducted preliminary tests considering shear strains at the flat faces of the cell but our results overestimated the von Mises stress by a large factor. We found that the shear strain interaction is not fully understood at the level of DOE. Consequently, our set of factors was reduced to the normal strains at the flat faces of the cell $\{\varepsilon_{Xx}, \varepsilon_{Yy}, \varepsilon_{Zz}\}$.

III.B.3.4.4.2 Factors Selection

In the context of DOE, the goal at this stage is to reduce the number of considered factors, selecting those factors that affect the most the response variable. Mature techniques do exist for this task, such as full or fractional factorial or Plackett-Burman designs [22, 134]. However, we considered only 3 factors, so we decided to develop the meta-models using all of them.

III.B.3.4.4.3 Meta-model Development

The goal at this stage was to develop efficient and simple mathematical expressions that expressed the von Mises stress in Schwarz Primitive lattice domains in terms of $\{\varepsilon_{Xx}, \varepsilon_{Yy}, \varepsilon_{Zz}\}$.

We used Response Surface methodologies, specifically central composite face-centered design (CCF), to efficiently devise the meta-models. The shape of the devised meta-models for Schwarz Primitive cells of relative densities $\rho \in \{0.25, 0.5, 0.75\}$ was

$$\hat{y} = \left(\beta_0 + \sum_{i \leq j} \beta_{ij} \varepsilon_{ii} \varepsilon_{jj} \right)^2, \quad (\text{III.B.3.7})$$

and the shape of the meta-model for $\rho = 1.0$ was

$$\hat{y} = \sqrt{\beta_0 \left(\sum_i \varepsilon_{ii}^2 - \sum_{i < j} \varepsilon_{ii} \varepsilon_{jj} \right)}. \quad (\text{III.B.3.8})$$

We used R [147] to perform the regression analysis to estimate the coefficients (β_i, β_{ij}) of the meta-models (see Table III.B.3.3).

To evaluate the meta-models, we ran 100 random simulations for each of the four domains and compared the experimental (result of FEA) and predicted (result of the meta-model) von Mises stress. The values of the Young's modulus and Poisson's ratio used for the simulations with the homogeneous domains were the ones reported in Table III.B.3.2. For the cell of density $\rho = 0.75$, we used $E^Q = 71.0$ GPa and $\nu^Q = 0.25$, which resulted by interpolating the corresponding moduli of the cells of densities $\rho = 0.7$ and $\rho = 0.8$. We used the displacements on the homogeneous domains to calculate the normal strains at the flat faces ε_{ij} and used them as inputs for the meta-models in Eqs. III.B.3.7 and III.B.3.8.

The boundary conditions imposed on the four domains were prescribed displacements in the normal direction of the flat faces of the domains. The size of the cell used was $L = 1.0$ cm, so that the imposed displacements were equivalent to normal strains at the flat faces (ε_{ij}).

Our analysis was limited to the elastic zone of the material. The range of the variables was $\varepsilon_{ij} \in 10^{-5} \times [-1.0, 1.0]$. The value of the variables was coded in the range $[-1, 1]$ to be in concordance with the procedures found in the literature [134]. To ensure that the strains in the flat faces were in the working range ($\varepsilon_{ij} \in 10^{-5} \times [-1.0, 1.0]$) and to explore it evenly, the values of the

Table III.B.3.3: Values of the coefficients β in the fitted meta-models. Average and maximum relative errors between FEA and our approach for 100 random simulations.

Relative density	β_0	β_{12}	β_{13}	β_{23}	β_{11}	β_{22}	β_{33}	Average relative error	Max. relative error
0.25	0.0438	0.0010	0.0013	0.0005	0.0089	0.0075	0.0067	19%	370%
0.50	0.0369	0.0019	0.0021	0.0019	0.0076	0.0073	0.0074	20%	298%
0.75	0.0419	0.0041	0.0039	0.0036	0.0089	0.0098	0.0091	21%	255%
1.0	0.4036	N/A	N/A	N/A	N/A	N/A	N/A	0%	0%

imposed normal strains at the flat faces were generated from a uniform distribution in the interval $(-1.0 \times 10^{-5}, 1.0 \times 10^{-5})$.

Figure III.B.3.4 displays the aforementioned comparison for each cell. We can see that the meta-models for the densities $\rho \in \{0.25, 0.50, 0.75\}$ tend to overestimate the von Mises stress at low stress conditions. This is due to the term β_0 in Eq. III.B.3.7, which impedes the meta-model to predict small values of von Mises stress. Table III.B.3.3 gives the average and maximum relative error of the predicted vs. the experimental von Mises stress. The maximum relative errors are associated to low stress conditions, mainly influenced by the value of β_0 in Eq. III.B.3.7 (as previously discussed). It is clear that the meta-models are not well-suited for low stress conditions. The average and maximum relative errors in the estimations show that this methodology is not applicable in very sensitive processes where high accuracy is required.

III.B.3.5 Results

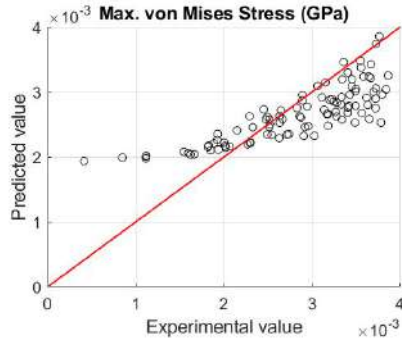
III.B.3.5.1 Validation of the Proposed Methodology

To evaluate our methodology, we compared the results of the FEA simulation and our methodology for six Schwarz Primitive lattice domains. Three of the six domains (Figs. III.B.3.5(a)–III.B.3.5(c)) were formed by 8 unit cells of uniform density $\rho = 0.25, 0.50, 0.75$, respectively. The other three domains were formed by unit cells of graded density, that is, the isovalue t was not a constant but a function $t : \mathbb{R}^3 \rightarrow \mathbb{R}$. The resultant surfaces are the solutions to the equation $F(x, y, z) = t(x, y, z)$ (see Eq. III.B.3.1). The domain of 24 unit cells in Fig. III.B.3.5(f) was taken from Ref. [127] and corresponded to the result of mapping the results of topology onto Schwarz Primitive cells [127]. The domains of 8 cells displayed in Figs. III.B.3.5(d)–III.B.3.5(e) were also taken from [127]. The isovalue functions associated with these two domains are:

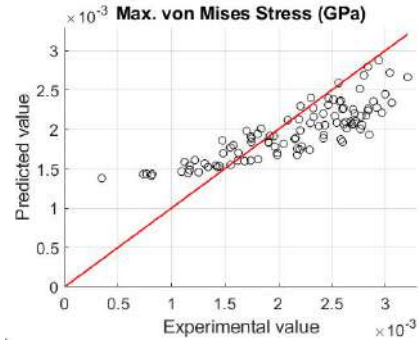
$$t(x, y, z) = \begin{cases} -\frac{5}{2} \left(\frac{3x}{2L}\right)^2 + 2 & , 0 \leq x \leq \frac{2L}{3}, y, z \in \mathbb{R} \\ -\frac{1}{2} & , \frac{2L}{3} < x \leq \frac{4L}{3}, y, z \in \mathbb{R} \\ \frac{3}{2L}x - \frac{5}{2} & , \frac{4L}{3} < x \leq 2L, y, z \in \mathbb{R} \end{cases} \quad (\text{III.B.3.9})$$

$$t(x, y, z) = 3 \left(\frac{x}{L} - 1\right)^2 - \frac{1}{2}, \quad 0 \leq x \leq 2L, y, z \in \mathbb{R} \quad (\text{III.B.3.10})$$

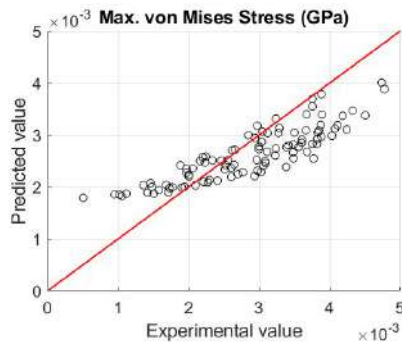
The six domains were subjected to uniaxial compression (see Fig. III.B.3.5). The magnitude of the load was such that the resultant strains in the flat faces of the boundary of the cells lied



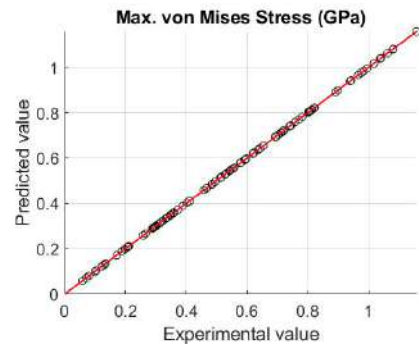
(a) Relative density $\rho = 0.25$.



(b) Relative density $\rho = 0.50$.



(c) Relative density $\rho = 0.75$.



(d) Relative density $\rho = 1.0$.

Figure III.B.3.4: Evaluation of the meta-models to estimate the von Mises stress in Schwarz Primitive lattices. Fitted values vs. Experimental values.

in the range of analysis $\varepsilon_{ij} \in 10^{-5} \times [-1.0, 1.0]$. First, we compared the displacements field of the lattice and homogeneous domain (Section III.B.3.5.1.1). Secondly, we applied our DOE-based methodology using the displacement results from the homogeneous domain to get the maximum von Mises stress in every cell. Finally, we compared the maximum von Mises stress obtained via (1) direct FEA of the lattice domain and (2) our proposed methodology (Section III.B.3.5.1.2).

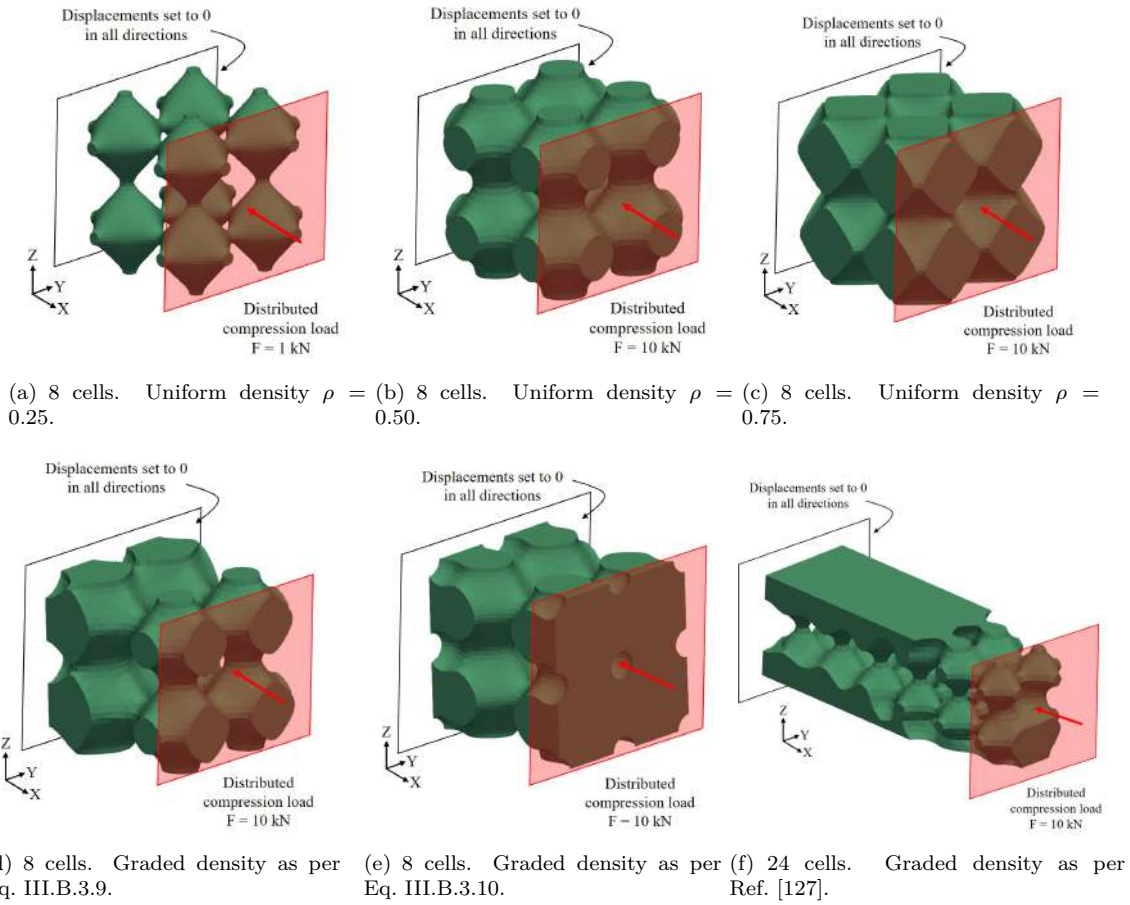


Figure III.B.3.5: Studied domains and boundary conditions. Schwarz Primitive lattice structures of uniform and non-uniform (graded) density.

III.B.3.5.1.1 Material Homogenization in Schwarz Primitive Lattice Structures

The FEA simulations of the lattice and homogeneous domains were executed in ANSYS. The lattice models were meshed in ANSYS using tetrahedral elements (SOLID285). The material properties of the lattice models correspond to the bulk material properties ($\rho = 1.0$ in Table III.B.3.2). On the other hand, given the regular shape of the homogeneous domains, we used cubic elements (SOLID185) for the respective meshes. Each cubic sub-domain was isotropic and its material properties were assigned according to its relative density and the properties reported in Table III.B.3.2. The homogeneous domain was then a regular 3D array of isotropic cubic sub-domains. Since the properties of each sub-domain could be different, the homogeneous domain resulted to be anisotropic.

FEA simulations were executed using different hardware settings and different operative systems, therefore, it was not possible to compare execution times between different simulations in

equal conditions. To overcome this difficulty, we used the number of elements in the mesh as a measurement of computational expense in each domain. The number of elements required for each lattice and homogeneous domain are reported in Fig. III.B.3.6 and Table. III.B.3.4. It is noticeable that the FEA meshes of lattice domains required more elements than the homogeneous domains. Another important aspect to highlight is that the number of elements of the homogeneous domain only depend on the number of cells (particularly, we chose a mesh of $10 \times 10 \times 10$ elements per unit cell). On the other hand, the number of elements for the lattice domains does not completely depend on the number of cells. Notice that 5 out of the 6 domains are conformed by 8 unit cells. However, the number of elements (Fig. III.B.3.6 and Table. III.B.3.4) is different for each domain. These variations are mainly influenced by the shape of the domain, which affects the corresponding meshing algorithms of the FEA software (ANSYS).

After conducting the FEA simulations, we proceeded to compare the resultant displacements of the lattice and homogeneous domains. Figure III.B.3.8 (1) contrasts the nodal displacement in the load direction X for the six load cases and (2) shows the absolute difference between the X displacement predicted by the lattice and homogeneous approaches. The reader may observe the similarity in both the distribution and magnitude of the displacements field of the lattice and homogeneous domains. Figure III.B.3.8 also shows that the maximum value of the absolute error is in all cases approximately 10 times smaller than the maximum displacement. From these results we conclude that material homogenization is an accurate tool to estimate the displacements in lattice structures and its efficiency allow its application in large lattice domains.

III.B.3.5.1.2 Comparison between FEA and Our Methodology

We used the displacements on the homogeneous domains obtained in the previous stage to extract the inputs of our meta-models: the normal strains on the boundary of each cell. Then, we used the meta-models presented in Section III.B.3.4.4 to estimate the maximum von Mises stress in

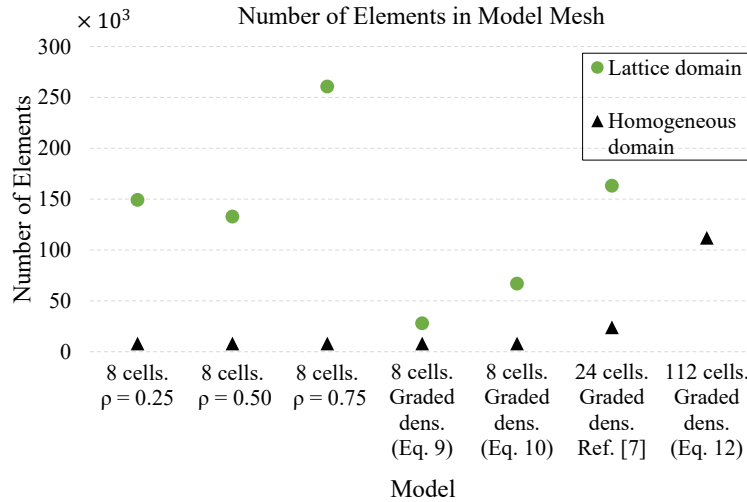


Figure III.B.3.6: Number of elements in the FE meshes of lattice and simplified homogeneous domains.

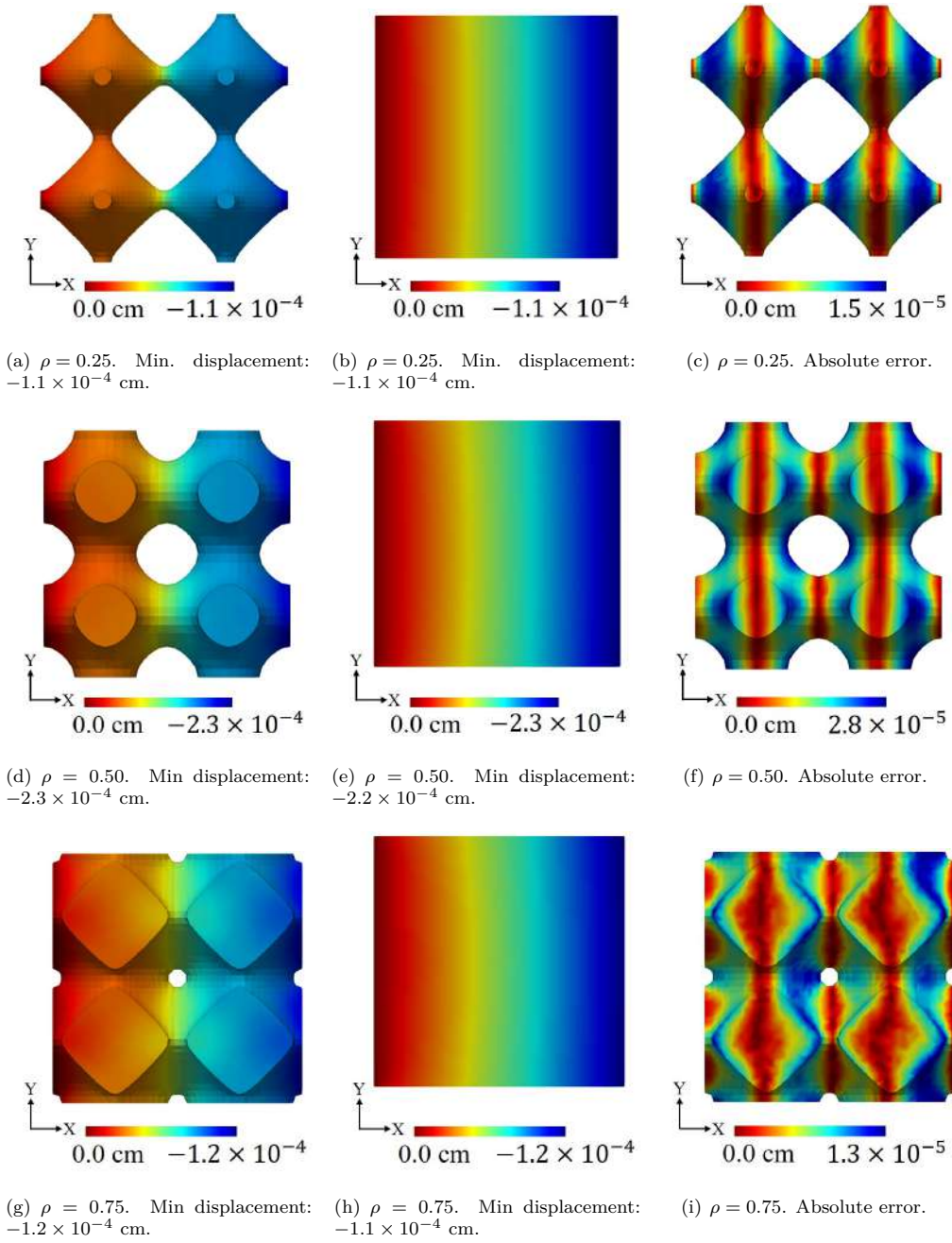
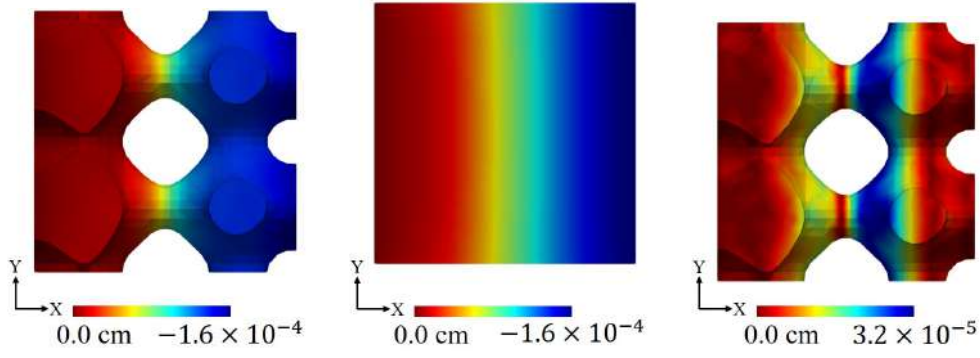
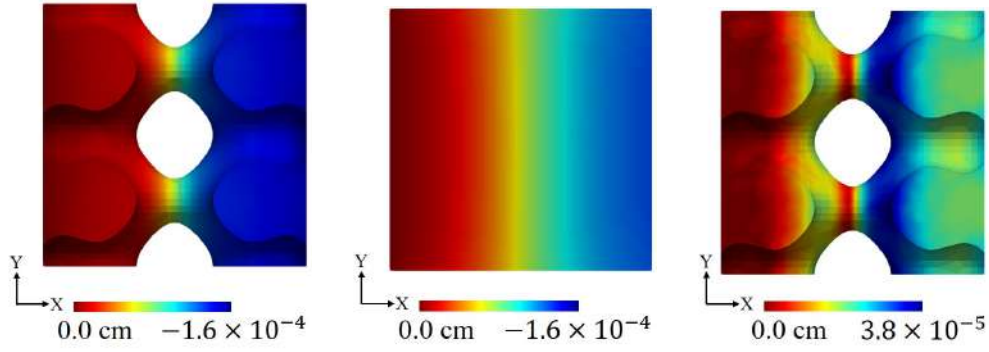


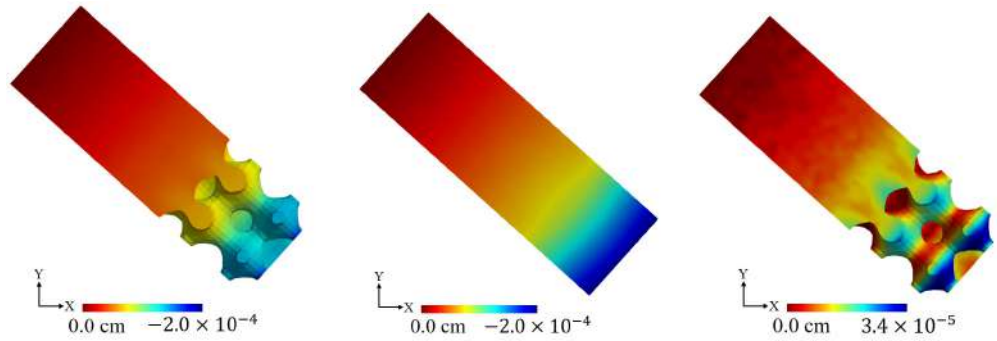
Figure III.B.3.7: *Cont.*



(j) Graded density Eq. III.B.3.9. Min displacement: -1.6×10^{-4} cm. (k) Graded density Eq. III.B.3.9. Min displacement: -1.6×10^{-4} cm. (l) Graded density Eq. III.B.3.9. Absolute error.



(m) Graded density Eq. III.B.3.10. Min. displacement: -1.6×10^{-4} cm. (n) Graded density Eq. III.B.3.10. Min. displacement: -1.3×10^{-4} cm. (o) Graded density Eq. III.B.3.10. Absolute error.



(p) Graded density Ref. [127]. Min displacement: -1.8×10^{-4} cm. (q) Graded density Ref [127]. Min displacement: -2.0×10^{-4} cm. (r) Graded density Ref [127]. Absolute error.

Figure III.B.3.8: Results of X compression test. X displacement. Comparison of lattice ((a), (d), (g), (j), (m), (p)) vs. homogeneous ((b), (e), (h), (k), (n), (q)) domains. Absolute error distribution ((c), (f), (i), (l), (o), (r)). Domains of 8 cells (a)-(o). Domain of 24 cells (p)-(r).

Table III.B.3.4: Number of elements in FE meshes of lattice and simplified homogeneous domains.

Domain	Figure number	No. of elements in Lattice domain	No. of elements in Homogeneous domain
8 cells. Uniform density with $\rho = 0.25$	Fig. III.B.3.5(a)	149090	8000
8 cells. Uniform density with $\rho = 0.50$	Fig. III.B.3.5(b)	132710	8000
8 cells. Uniform density with $\rho = 0.75$	Fig. III.B.3.5(c)	260610	8000
8 cells. Graded density as per Eq. III.B.3.9	Fig. III.B.3.5(d)	27863	8000
8 cells. Graded density as per Eq. III.B.3.10	Fig. III.B.3.5(e)	66890	8000
24 cells. Graded density as per Ref. [127]	Fig. III.B.3.5(f)	163080	24000
112 cells. Graded density as per Eq. III.B.3.12	Fig. III.B.3.11(a)	N/A	112000

each cell. To apply the meta-models, we calculated the average relative density of each cell of the non-uniform (graded) density domains. Since we had only meta-models for the relative densities $\rho \in \{0.25, 0.50, 0.75, 1.0\}$, we used linear interpolation to do the approximations for the intermediate values of density ρ . For instance, $\left(\sigma_{VM}^{(0.4)}\right)$, the von Mises stress for a relative density $\rho = 0.4$ is approximated as

$$\sigma_{VM}^{(0.4)} = \frac{2}{5}\sigma_{VM}^{(0.25)} + \frac{3}{5}\sigma_{VM}^{(0.5)}, \quad (\text{III.B.3.11})$$

where $\sigma_{VM}^{(0.25)}$ and $\sigma_{VM}^{(0.50)}$ denote the von Mises stresses for the cells of densities $\rho = 0.25$ and $\rho = 0.50$. $\sigma_{VM}^{(0.25)}$ and $\sigma_{VM}^{(0.50)}$ are retrieved using Eq. III.B.3.7 with the corresponding coefficients of Table III.B.3.3.

Figures III.B.3.9 and III.B.3.10 show (i) the von Mises stress of the FEA simulation, (ii) the maximum von Mises stress of every cell retrieved from the FEA simulation of the lattice domain, and (iii) the maximum von Mises stress of every cell calculated with our methodology. In addition, Table III.B.3.5 lists, for each domain, the global maximum von Mises stress using (a) FEA simulation of the lattice domain and (b) our methodology. We measured the relative error of our methodology with respect to the FEA simulation of the lattice domain. These results are reported also in Table III.B.3.5.

In Figures III.B.3.9 and III.B.3.10, we can see that the maximum von Mises stress given by our methodology (third column of the figures) is very uniform along all the cells. When compared with the maximum von Mises stress of the FEA methodology (second column of the figures), it is clear that our methodology is not able to capture all the variation of the maximum von Mises stress per cell (see Figs. III.B.3.10(h) and III.B.3.10(i)). However, we can see the correspondence between the most stressed zones using FEA simulation and our methodology. Note that our implementation often predicts the most stressed cell.

In terms of the accuracy of our methodology, we can see in Table III.B.3.5 that (1) the error in the estimations with our methodology is between 16% and 42% and (2) our methodology tends to underestimate the maximum von Mises stress. These results show that our methodology can only do rough estimations (with errors above 20%) of the maximum von Mises stress in Schwarz lattice structures.

We have identified three critical aspects that can improve the accuracy of our methodology:

1. To consider more displacement-based features located inside the cell, not only on the boundary of the cell.

2. To develop meta-models for more relative densities. Currently, it is limited to meta-models of density $\rho \in \{0.25, 0.50, 0.75, 1.0\}$.
3. To enlarge the range of analysis of the displacement-based features, since in a single load case, the magnitude of the deformation of the lattice domain varies in every zone. Currently, the allowed normal strains are currently limited to the interval $10^{-5} \times [-1.0, 1.0]$.

Table III.B.3.5: Maximum von Mises stress values of direct FEA of the lattice domain vs. our methodology.

Domain	Figure number	Max. σ_{VM} : FEA (MPa)	Max. σ_{VM} : our method (MPa)	Rel. error
8 cells. Uniform density with $\rho = 0.25$	Fig. III.B.3.5(a)	3.6	2.4	33%
8 cells. Uniform density with $\rho = 0.50$	Fig. III.B.3.5(b)	4.5	3.6	20%
8 cells. Uniform density with $\rho = 0.75$	Fig. III.B.3.5(c)	3.4	2.4	29%
8 cells. Graded density as per Eq. III.B.3.9	Fig. III.B.3.5(d)	3.1	3.6	16%
8 cells. Graded density as per Eq. III.B.3.10	Fig. III.B.3.5(e)	3.4	2.8	17%
24 cells. Graded density as per Ref. [127]	Fig. III.B.3.5(f)	3.1	1.8	42%

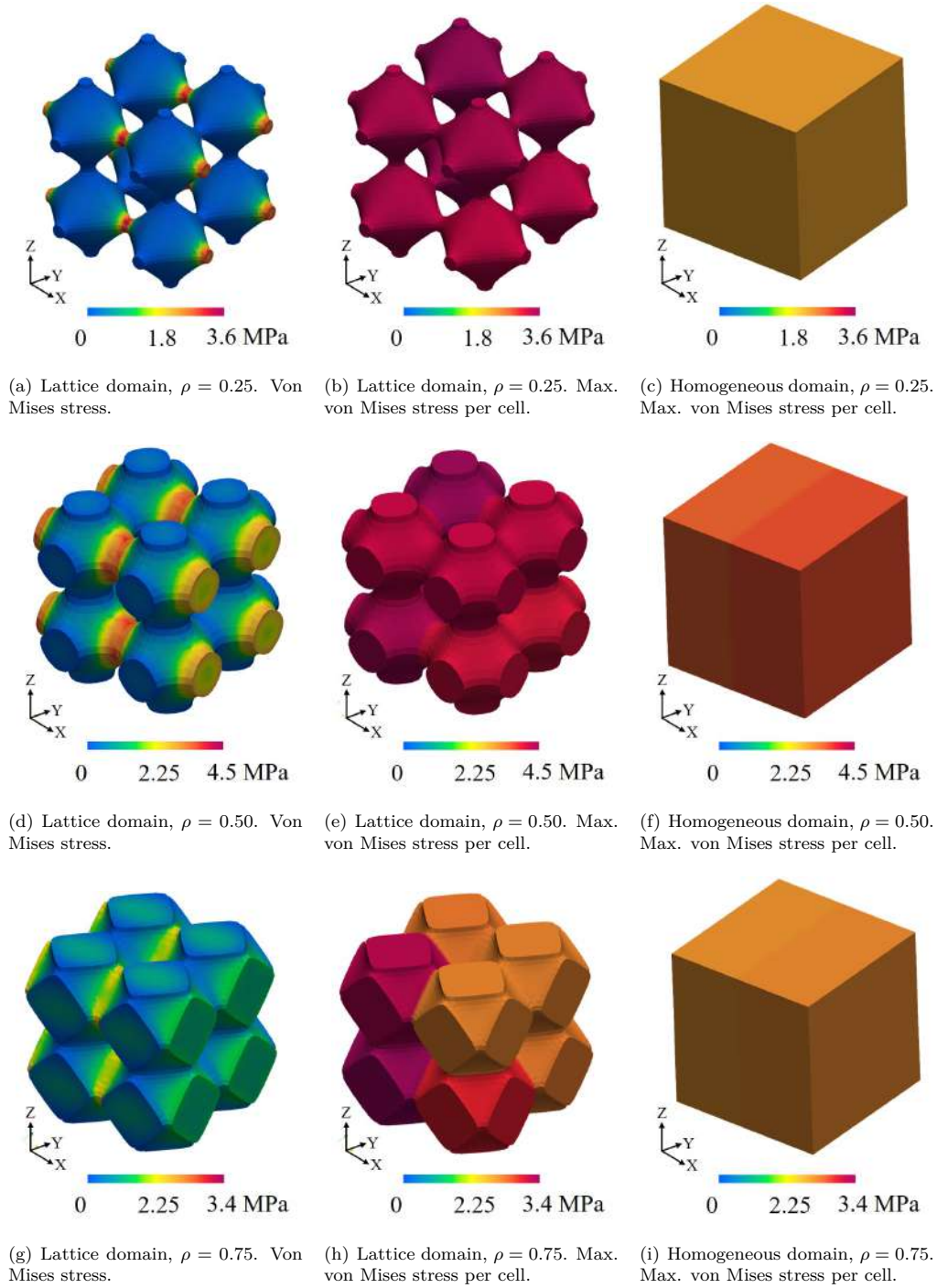


Figure III.B.3.9: Comparison of the maximum von Mises stress in direct FEA (lattice) and our methodology for Schwarz Primitive structures. 8 cells domains of uniform density. Detailed results in Table III.B.3.5.

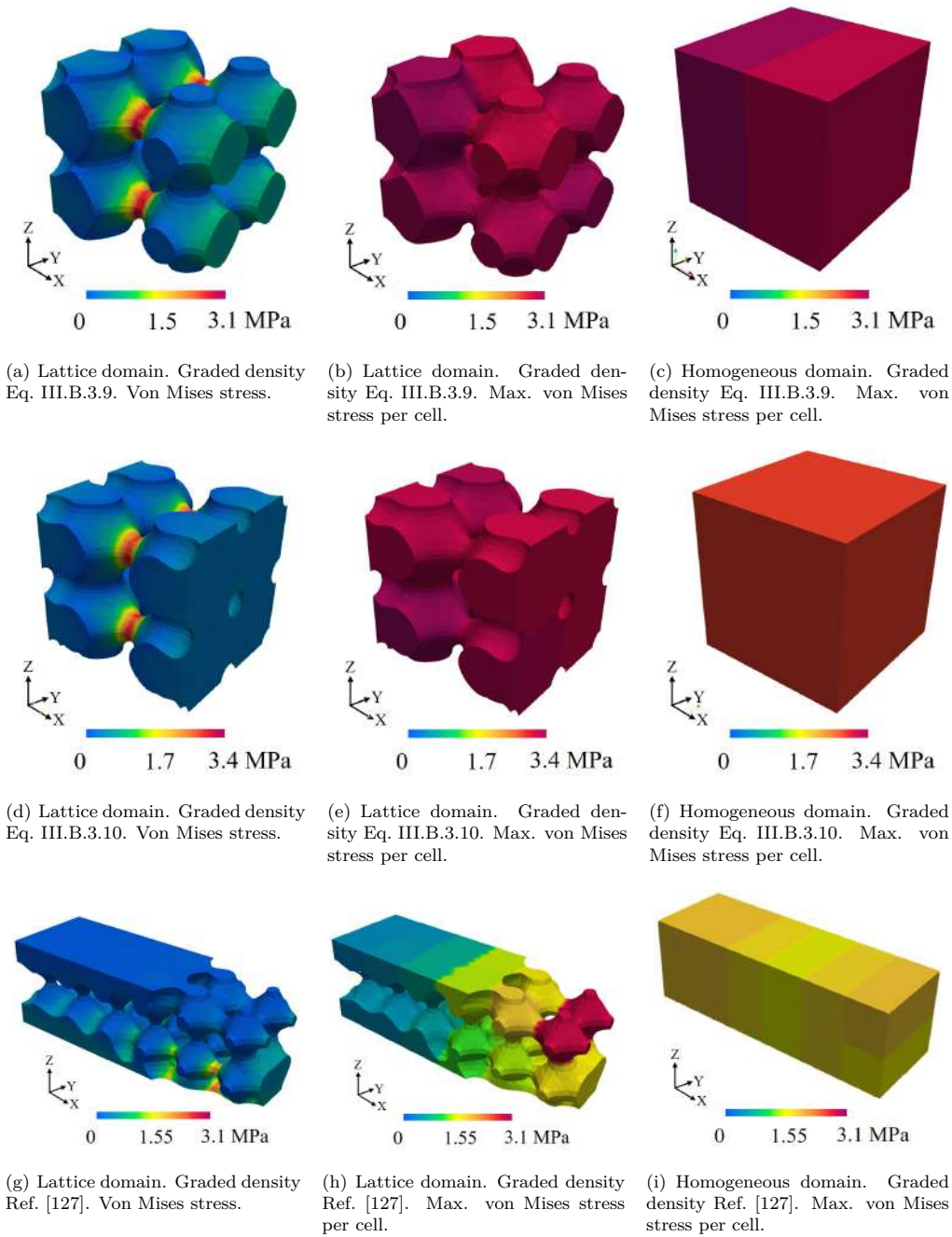


Figure III.B.3.10: Comparison of the maximum von Mises stress in direct FEA (lattice) and Our Methodology (homogeneous) for Schwarz Primitive domains of graded density. Domains of 8 cells (a)-(f). Domain of 24 cells (g)-(i). Detailed results in Table III.B.3.5.

III.B.3.5.2 Application of Our Methodology to Large Lattice Domains

To demonstrate the potential of our methodology to be applied in the rough estimation of the von Mises stress in larger lattice structures, we generated a domain of 112 ($7 \times 4 \times 4$) cells of graded density. We tested it under uniaxial compression in X direction (Fig.III.B.3.11(a)). The isovalue function associated to this domain is:

$$t(x, y, z) = 2.5 - \frac{0.3}{L}(x + y). \quad (\text{III.B.3.12})$$

First, we produced the homogeneous domain and conducted the FEA simulation. The number of elements of the mesh was 112000 ($10 \times 10 \times 10$ elements per cell). Secondly, using the displacements field (Fig. III.B.3.11(b)), we extracted the normal strains on the boundary of each of the 112 cells. Finally, we used the meta-models of Section III.B.3.4.4 along with linear interpolation to estimate the maximum von Mises stress in each cell. The results of this estimation are shown in Fig. III.B.3.11(c).

Due to the large number of cells (117), the FEA directly on the lattice domain was unfeasible. However, it is possible to show the computational efficiency of our approach: to mesh a lattice domain of 24 cells, 160k elements were required (6.6k elements per cell), while for the homogeneous domain of 112 cells, 112k elements were used (1.0k elements per cell). This example has shown the computational efficiency of our approach in comparison with direct FEA simulation. It shows that our approach has the potential to be employed in the estimation of the stress/strain response of large lattice domains.

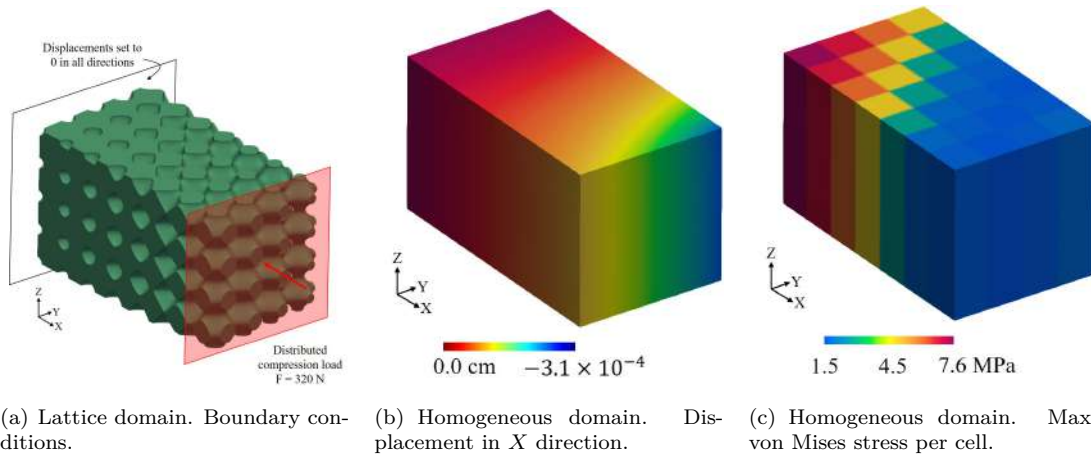


Figure III.B.3.11: Application of our methodology to a large Schwarz Primitive domain of 112 cells of graded density as per Eq. III.B.3.12.

III.B.3.6 Conclusions

In this article we present a methodology that integrates material homogenization and design of experiments (DOE) to estimate the stress/strain response in large lattice domains reducing the

computational cost with respect to direct FEA simulation. On the one hand, material homogenization is used to efficiently approximate the displacements on the lattice domains. On the other hand, DOE is applied to produce simple mathematical expressions to express the stresses in the lattice as functions of the displacements obtained through homogenization. In comparison with related approaches, this methodology is easy to implement, can be applied with different families of lattices (strut or surface based) and offers an efficient alternative to retrieve the stress/strain response of complex lattice domains. However, it is less accurate and produces only rough estimations.

We implemented the proposed methodology to estimate the von Mises stress in Schwarz Primitive lattice structures. Material homogenization proved its suitability for the approximation of the displacements in large lattice domains. Results have also shown that the proposed methodology is an efficient tool with potential applications in the *coarse* estimation of the von Mises stress in large lattice domains. The average errors in the estimations are between 20% and 40%, which *are not acceptable* in sensitive processes where high accuracy is required. However, these results are encouraging when it is considered that we estimated meta-models for only four densities ($\rho \in \{0.25, 0.50, 0.75, 1.0\}$) for a narrow range of strains on the boundary of the cells $10^{-5} \times [-1.0, 1.0]$. Our methodology has shown potential for the pre-evaluation of designs, where less precision is needed.

The methodology presented in this paper can be applied to other types of lattice structures (different to the Schwarz Primitive). It would be necessary to develop meta-models for the lattice structure of interest and, consequently, to perform material homogenization to obtain the Young's and Poisson's moduli associated to the relative density.

III.B.3.6.1 Future Work

Future work is needed to improve the accuracy of the estimations of the von Mises stress. Efforts should be focused on the fitting of more robust meta-models that use more information from the displacements field obtained via material homogenization.

This paper considers the von Mises stress as a failure criterion for lattice domains. However, lattice structures at low densities experience buckling instabilities. This phenomenon should be considered to analyze failure in lattice structures.

Author Contributions: D.M-Z., D.A.A. and O.R-S. conceptualized and designed the algorithm. D.M-Z. and J.P-C. implemented the algorithm and executed the simulations. D.A.A. and A.M. supervised the Design of Experiments and Statistical aspects of this research. C.C., J.P and O.R.-S. supervised the Computational Geometry and Computational Mechanics aspects of this research. All the authors contributed to the writing of the article.

Funding: This research received no external funding.

Conflicts of Interest: The authors declare no conflict of interest.

III.C

Simulation of Laser Metal Deposition

III.C.1

2D Linear Finite Element Simulation of Laser Metal Heating for Digital Twins

Diego Montoya-Zapata^{1,2}, Juan M. Rodríguez³, Aitor Moreno², Jorge Posada², Oscar Ruiz-Salguero¹

¹Laboratory of CAD CAM CAE, Universidad EAFIT, Cra 49 no 7-sur-50, Medellín 050022, Colombia

²Vicomtech Foundation, Basque Research and Technology Alliance (BRTA), Mikeletegi 57, Donostia-San Sebastian 20009, Spain

³Department of Mechanical Engineering, Universidad EAFIT, Cra 49 no 7-sur-50, Medellín 050022, Colombia



III.C.1.1 Context

Diego Montoya-Zapata, Juan M. Rodríguez, Aitor Moreno, Jorge Posada and Oscar Ruiz-Salguero. 2D linear finite element simulation of laser metal heating for digital twins. International Journal for Simulation and Multidisciplinary Design Optimization, EDP Sciences, (eISSN 1779-6288), 2021, 12(11), 11; (This article belongs to the Special Issue Computation Challenges for engineering prob-

lems). url= https://www.ijsmdo.org/articles/smdo/full_html/2021/01/smdo210017, doi= <https://doi.org/10.1051/smdo/2021011>, Published online: 22 July 2021.

Indexing: SCOPUS(Q4), Publindex(C)

Abstract

In the context of laser-based additive manufacturing, the thermal behavior of the substrate is relevant to define process parameters vis-à-vis piece quality. The existing literature focuses on two process variables: (a) lumped laser power and (b) process speed. However, this literature does not consider other variables, such as those related to the laser power distribution. To fill this vacuum, this manuscript includes the laser power spatial distributions (Gaussian, uniform circular and uniform rectangular) in addition to (a) and (b) above in 2D linear substrate heating simulations. The laser energy is modeled as a time dependent heat flux boundary condition on top of the domain. The total laser delivered power was identical for all spatial distributions. The results show that the laser intensity spatial distribution strongly affects the maximum temperature, and the depth and width of the heat affected zone. These 2D finite element simulations prove to be good options for digital twin based design environments, due to their simplicity and reasonable temperature error, compared to non-linear analysis (considered as ground truth for this case). Future publications address non-linear finite element simulations of the laser heating process (including convection and radiation and temperature dependent substrate properties).

Keywords: numerical simulation, heat transfer, finite element method.

Glossary

AM	Additive manufacturing.
HAZ	Heat affected zone.
LMD	Laser metal deposition.
$\Omega \subset \mathbb{R}^2$	Studied domain with boundary $\partial\Omega$
$\mathbf{x} \in \Omega$	Coordinates to represent the position of Ω [m]
$T(\mathbf{x}, t)$	Temperature at $\mathbf{x} \in \Omega$ in the instant t [K]
$\mathbf{q}(\mathbf{x}, t)$	Heat flux into or out of the medium at $\mathbf{x} \in \Omega$ at time t [W / m ²]
$s(\mathbf{x}, t)$	Volumetric heat sources at $\mathbf{x} \in \Omega$ in the instant t [W / m ³]
$\mathbf{n}(\mathbf{x})$	Outward unit normal to the boundary at $\mathbf{x} \in \Omega$
ρ	Density of the material [kg / m ³]
C_p	Specific heat capacity of the material [J / (kg K)]
κ	Thermal conductivity of the material [W / (m K)]

III.C.1.2 Introduction

Metal Additive Manufacturing (AM) has enabled the fabrication of complex geometries that could not be build using traditional manufacturing techniques [45]. Laser-based AM has also grown up because of its applications in repair, reconditioning, coating and remanufacturing of high-valued

industrial pieces [93]. However, the characterization of the laser-based AM is still a matter of research.

In this manuscript, we present an analysis of the influence of the laser intensity distribution, laser radius and process speed on the thermal behavior of the substrate. The analysis is carried out via numerical simulations of a 2D thermal model using the finite element method. The energy contributions of the laser into the substrate are modeled as time dependent heat flux (or Neumann) boundary conditions. We study the effects of three types of laser intensity distributions: Gaussian, uniform circular and uniform rectangular. In our simulations, we do not consider the addition of material, the phase change nor non-linear phenomena.

The remainder of this article is organized as follows: Section III.C.1.3 provides a review of the relevant related work. Section III.C.1.4 describes the governing equations, numerical scheme, and the materials used for the simulations. Section III.C.1.5 presents and discusses the results obtained. Section III.C.1.6 concludes the manuscript and makes suggestions for future work.

III.C.1.3 Literature Review

III.C.1.3.1 Numerical Studies of Process Parameters in Additive Manufacturing

In recent years, there has been an increasing amount of literature on the study of laser-based AM. Several studies have shown that the temperature history has a significant impact in the quality and mechanical properties of the parts manufactured via laser-based AM [28, 37, 77, 149].

Physical experimental studies have been executed to assess the influence of the process parameters on the geometry of parts produced by laser metal deposition (LMD). Most of the research has focused on these three parameters: laser power, process speed and material feeding rate. References [35, 72, 186, 200] analyzed the effects of the process speed, laser power and material feeding rate on the geometry of the melt-pool (width, depth and burn-in shape) and on the dilution ratio. References [34, 200] studied the impact of these three process parameters in the clad geometry (width, height and angle of repose).

Numerical models have also been developed for this purpose. Pure thermal [35, 200] and thermal-fluid [6, 186] were implemented to model the influence of the laser power, process speed and material feeding rate on the geometry and thermal history of the melt-pool and the clad bead. In all of these works, the power intensity distribution of the laser beam was modeled using a Gaussian function. However, other beam spots shapes have been used in physical contexts (e.g. rectangular beam spot [96]).

III.C.1.3.2 Digital Twins in Additive Manufacturing

In the context of Industry 4.0, the concept of *digital twin* is key in the manufacturing environment [145]. In few words, a digital twin is a virtual representation of a real system. This virtual representation resembles as much as possible the real system, allowing the knowledge transfer between the real and cyber-physical worlds [68]. Therefore, simulation over the virtual entity plays a major role, since the gained information can be fed into the real system.

Digital twins for AM are still at early stages of development. Some research has focused on the identification of the main features that should be included in the cyber-physical world (e.g. thermal behavior, melt-pool dynamics, distortions, geometry prediction) [43, 64]. However, one of the major

limitations of the current models is the large amount of computational resources associated to their use, which make them impractical for real-time or interactive applications [43].

Reference [202] presented an approach that integrated real data obtained by sensors and theoretical results in the context of smart manufacturing. Reference [64] used the prior approach to develop a model for AM that used numerical simulations and real data to detect manufacturing defects and deviations. Reference [85] presented a digital twin for AM that integrated some main features related to resemble the real process (e.g. obtained geometry, temperature history, cooling rates, microstructure). The main contribution was the assembly of those features, which are commonly studied independently. A further review on the related works on digital twins for AM can be found in [207].

III.C.1.3.3 Conclusions of the Literature Review

In the currently existing literature, metal laser heating is addressed by considering, in addition to the material properties, lumped laser power input at the material boundary and laser speed. The spatial distribution of the laser power follows a Gaussian profile. This manuscript addresses the role of the laser power spatial distribution on the temperature field at the metal substrate. This temperature distribution is located at the substrate cross section normal to the laser trajectory. Our linear 2D initiative is obviously less precise than the 2D non-linear counterparts. However, we contend that it has value for approximate simplified purposes, e.g. digital twin applications, which require a reasonable appraisal of the substrate temperatures, at early design-stages.

III.C.1.4 Methodology

III.C.1.4.1 Problem Description

Laser Metal Deposition (LMD) is a manufacturing process in which a high-power laser beam is used to melt a metallic material while it is being deposited on the surface of a metallic substrate.

In this work, we aim to analyze the thermal behavior of an LMD process consisting of several parallel linear deposition tracks (see Fig. III.C.1.1). Along each track, we assume that the laser speed, laser power and material feeding rate are constant. Given these conditions, the process can be considered stable for points *far enough* of the start/end of the tracks. Therefore, we follow the approach presented in [200], in which the domain Ω for the thermal analysis is a 2D cross-section of the substrate with thickness Δz . The considered cross-section is perpendicular to the deposition tracks.

Despite the previous assumptions (constant speed, power and feeding rate), the process is still complex to model since it is affected by the properties of the laser beam, the properties of the deposited material and the substrate and the thermal conditions in which the process is executed. Therefore, we make the following simplifications:

1. The addition of material and the phase change (melting) are not taken into account. The analysis is limited to the thermal history of the substrate for temperatures below the melting point.
2. Heat loss is not considered. The following phenomena are not considered: convection between the air and the substrate, thermal radiation, conduction between the substrate and its supporting floor.

3. The properties of the substrate (specific heat, density and thermal conductivity) are assumed to be constant.
4. Heat phenomena in Z direction are neglected, including the conduction produced when the laser heats a neighborhood close to Ω in Z (see Fig. III.C.1.1).

The process studied in this paper can be applied to other laser-aided processes, such as powder-bed laser additive manufacturing.

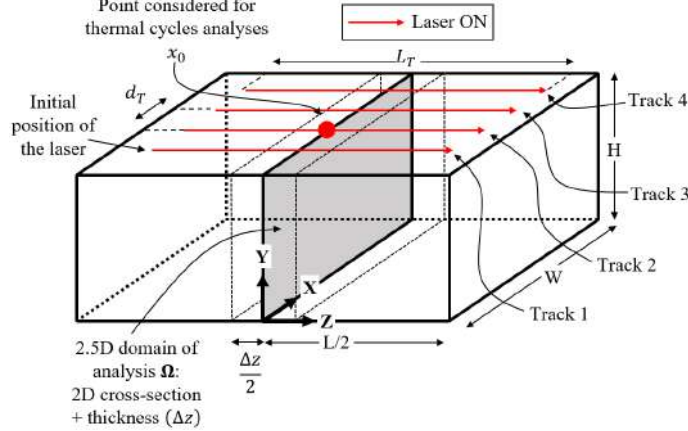


Figure III.C.1.1: Simulation of the deposition of four parallel deposition tracks (Track 1, ..., Track 4). Graphical representation of the domain, reference frame and parameters involved.

III.C.1.4.2 Governing Equations

Let Ω denote our 2D domain of analysis (see Fig. III.C.1.1). Let $T = T(\mathbf{x}, t)$ denote the temperature at position $\mathbf{x} \in \Omega$ at time t . The temperature function satisfies the partial differential equation

$$\rho C_p \frac{\partial T}{\partial t} + \nabla \cdot \mathbf{q} = s \quad \text{in } \Omega \times [0, t_{\max}] \quad (\text{III.C.1.1})$$

where ρ and C_p are the density and specific heat capacity of the material, $\mathbf{q} = \mathbf{q}(\mathbf{x}, t)$ is the heat flux and $s = s(\mathbf{x}, t)$ is the body heat source. The heat flux \mathbf{q} satisfies the following constitutive relation given by Fourier law

$$\mathbf{q} = -\kappa \nabla T \quad (\text{III.C.1.2})$$

where κ is the thermal conductivity of the material. In general, the thermal conductivity κ is a second-order tensor. However, we assume that the material is isotropic and, therefore, treat κ as a scalar.

To complete the mathematical formulation of the thermal problem, it is still necessary to define the initial and the boundary conditions. The initial temperature field is given by

$$T(\mathbf{x}, 0) = T_0(\mathbf{x}) \quad (\text{III.C.1.3})$$

where $T_0(\mathbf{x}) = 300$ K is the prescribed temperature at time $t = 0$. Temperature (Dirichlet) and flux (Neumann) conditions are imposed on the boundary of Ω as

$$T(\mathbf{x}, t) = \bar{T}(\mathbf{x}, t), \quad \mathbf{x} \in \partial\Omega_T \quad (\text{III.C.1.4})$$

$$\mathbf{q}(\mathbf{x}, t) \cdot \mathbf{n}(\mathbf{x}) = \bar{q}(\mathbf{x}, t), \quad \mathbf{x} \in \partial\Omega_q \quad (\text{III.C.1.5})$$

where $\bar{T}(\mathbf{x}, t)$ and $\bar{q}(\mathbf{x}, t)$ are known scalar functions, $\mathbf{n}(\mathbf{x})$ is the unitary outward normal to the boundary at \mathbf{x} . In addition, $\partial\Omega_T \cap \partial\Omega_q = \emptyset$ and $\partial\Omega_T \cup \partial\Omega_q = \partial\Omega$, where $\partial\Omega$ denotes the boundary of Ω . The initial and boundary conditions we imposed are detailed in Section III.C.1.4.7.

III.C.1.4.3 Galerkin Weak Form

Given the constitutive relation in Eq. III.C.1.2, the boundary conditions in Eqs. III.C.1.4 and III.C.1.5, and applying the Galerkin method on Eq. III.C.1.1, the problem is stated as follows [80]:

Find $T^h \in \mathcal{S}^h \subset \mathcal{H}^1(\Omega)$ such that for all $w^h \in \mathcal{V}^h \subset \mathcal{H}^1(\Omega)$:

$$\int_{\Omega} w^h \rho C_p \frac{\partial T^h}{\partial t} dV + \int_{\Omega} \nabla w^h \cdot (\kappa \nabla T^h) dV = \int_{\Omega} w^h s dV - \int_{\partial\Omega_q} w^h \bar{q} dA \quad (\text{III.C.1.6})$$

where

$$\mathcal{S}^h = \{T^h : T^h(\mathbf{x}, t) = \bar{T}(\mathbf{x}, t), \mathbf{x} \in \partial\Omega_T\} \quad (\text{III.C.1.7})$$

$$\mathcal{V}^h = \{w^h : w^h(\mathbf{x}, t) = 0, \mathbf{x} \in \partial\Omega_T\} \quad (\text{III.C.1.8})$$

and, if Δz is the thickness of Ω , the differential elements of volume and area in Eq. III.C.1.6 become $dV = \Delta z dA$ when integrating over Ω and $dA = \Delta z dL$ when integrating over $\partial\Omega_q$.

The function T^h aims to approximate the exact solution T and w^h is a weighting function. Notice that T^h satisfies the Dirichlet boundary conditions and w^h vanishes where Dirichlet boundary conditions are applied.

III.C.1.4.4 Finite Element Discretization

The domain Ω is partitioned in finite elements Ω^e such that

$$\bar{\Omega} = \bigcup_e \bar{\Omega}^e \quad (\text{III.C.1.9})$$

where $\bar{\Omega}$ denotes the closure of Ω . After using an isoparametric formulation, we obtain the semi-discrete form of Eq. III.C.1.6:

$$\mathbf{M}\dot{\mathbf{T}} + \mathbf{K}\mathbf{T} = \mathbf{f} \quad (\text{III.C.1.10})$$

where $\mathbf{T}(t)$ is the vector of the nodal temperatures at time t , $\dot{\mathbf{T}}(t)$ is the vector of the nodal derivatives of the temperature w.r.t. time: $\dot{T}_a = \partial T_a / \partial t$, \mathbf{M} and \mathbf{K} denote the global mass and conductivity matrices, and \mathbf{f} is the global force vector. The components of the corresponding element (local) mass and conductivity matrices are

$$M_{ab}^e = \int_{\Omega^e} \rho C_p N_a N_b \Delta z dA \quad (\text{III.C.1.11})$$

$$K_{ab}^e = \int_{\Omega^e} \nabla N_a \cdot (\kappa \nabla N_b) \Delta z dA \quad (\text{III.C.1.12})$$

where M_{ab}^e and K_{ab}^e are the components of the mass and conductivity matrices that relate nodes a and b in the finite element e , and $\{N_a\}$ are the shape functions. We use 3-node linear triangular finite elements, therefore the functions $\{N_a\}$, $a = 1, 2, 3$ are linear.

The components of the element force vector are given by

$$f_a^e = \int_{\Omega^e} N_a s \Delta z dA - \int_{\partial\Omega_q^e} N_a \bar{q} \Delta z dL - \sum_{b \in \mathcal{B}_T} \left[M_{ab}^e \dot{\bar{T}}_b - K_{ab}^e \bar{T}_b \right] \quad (\text{III.C.1.13})$$

where f_a^e is the component associated to the node a of the force in the element e and $\mathcal{B}_T = \{b : \mathbf{x}_b^e \in \partial\Omega_T^e\}$ represents the nodes in the element e with Dirichlet boundary conditions. The symbol \mathbf{x}_b^e denotes the coordinates of the node b in element e .

The reader may notice that in Eq. III.C.1.10, the vectors \mathbf{T} and $\dot{\mathbf{T}}$ are continuous functions with respect to time. To complete the numerical scheme it is still necessary to perform the time discretization.

III.C.1.4.5 Time Discretization

To execute the time discretization, the time interval $[0, t_{\max}]$ is divided into N sub-intervals of length Δt : $[t_0, t_1], [t_1, t_2], \dots, [t_{N-1}, t_N]$, such that $t_N - t_{N-1} = \Delta t$, $t_0 = 0$ and $t_N = t_{\max}$. The goal in this section is to obtain the solution at time t_{s+1} given the solution at time t_s .

Let ${}^s\mathbf{T} = \mathbf{T}(t_s)$ and ${}^s\dot{\mathbf{T}} = \dot{\mathbf{T}}(t_s)$ for $s = 0, 1, 2, \dots, N$. We approximate the time derivative $\dot{\mathbf{T}}$ at $s + 1$ using the backward Euler method, as follows [80]:

$${}^{s+1}\dot{\mathbf{T}} = \frac{{}^{s+1}\mathbf{T} - {}^s\mathbf{T}}{\Delta t} \quad (\text{III.C.1.14})$$

Assuming that \mathbf{M} , \mathbf{K} and \mathbf{f} are time-independent quantities, Eq. III.C.1.14 is replaced into Eq. III.C.1.10 to obtain

$$\mathbf{M} \left(\frac{{}^{s+1}\mathbf{T} - {}^s\mathbf{T}}{\Delta t} \right) + \mathbf{K} {}^{s+1}\mathbf{T} = \mathbf{f} \quad (\text{III.C.1.15})$$

From Eq. III.C.1.15 can be obtained an expression for ${}^{s+1}\mathbf{T}$:

$${}^{s+1}\mathbf{T} = (\mathbf{M} + \Delta t \mathbf{K})^{-1} (\Delta t \mathbf{f} + \mathbf{M} {}^s\mathbf{T}) \quad (\text{III.C.1.16})$$

III.C.1.4.6 Modeling of the Heat Provided by the Laser

The energy provided by the laser is modeled as a time dependent heat flux boundary condition. At every time step, we calculate the total influx through the boundary of each element on top (i.e. maximum Y direction) of the domain Ω .

Assume the elements on top of the domain are e_1, e_2, \dots, e_L . Let $\partial\Omega_q^{e_i}$ be the edge of the element e_i , $i = 1, 2, \dots, L$ that lies on top of the domain. To calculate the influx energy on each of the $\partial\Omega_q^{e_i}$ we measure the total power provided by the laser in a region $R_q^{e_i}$ which is the result of extruding the edge $\partial\Omega_q^{e_i}$ half of the thickness in $+Z$ and $-Z$ directions (see Fig. III.C.1.2), as shown in the following equation:

$$P^{e_i} = \int_{R_q^{e_i}} I(x, z) dA \quad (\text{III.C.1.17})$$

where $I(x, z)$ is the function that describes the laser intensity distribution and P^{e_i} is the total power acting on the edge $\partial\Omega_q^{e_i}$. Since the integration region is restricted to $R_q^{e_i}$, only the power that acts on the 2D domain is considered.

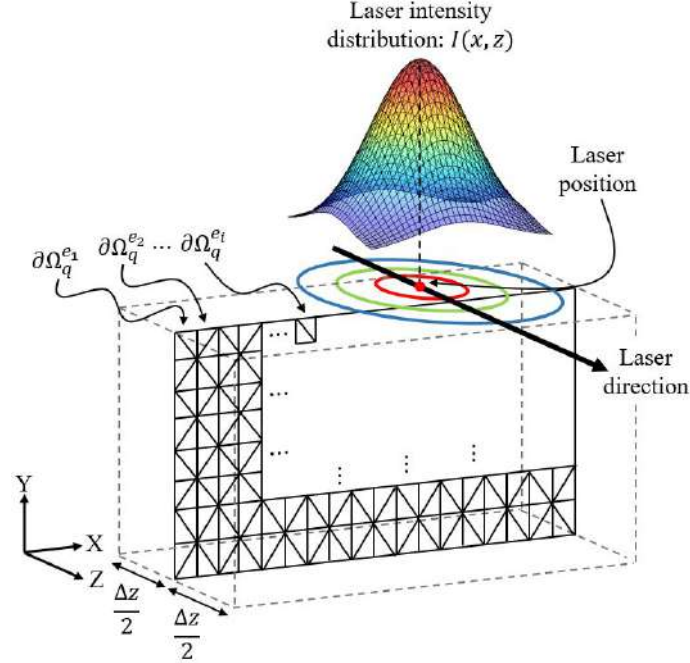


Figure III.C.1.2: Calculation of the inner heat flux provided by the laser at every finite element. Only the laser power that lies inside Ω (dotted lines) is considered.

Hence, to find the heat flux q^{e_i} at $\partial\Omega_q^{e_i}$ due to the action of the laser, we divide P^{e_i} by the area of the integration region, as shown below:

$$q^{e_i} = \frac{1}{\Delta z} \frac{P^{e_i}}{|\partial\Omega_q^{e_i}|} \quad (\text{III.C.1.18})$$

where $|\partial\Omega_q^{e_i}|$ denotes the length of the segment. Fig. III.C.1.2 shows a scheme of the process and the entities involved in it. In this figure, a Gaussian intensity function is depicted, but other intensity functions can be considered.

Since the laser is moving, the function $I(x(t), z(t))$ is also a function of time. Therefore, the previous procedure must be repeated at every time step of the simulation. Fig. III.C.1.3 shows an example of the heat fluxes q^{e_i} calculated for the elements on top of the domain Ω , considering a Gaussian intensity function for the time sequence $t_1, \dots, t_i, t_{i+1}, \dots, t_N$.

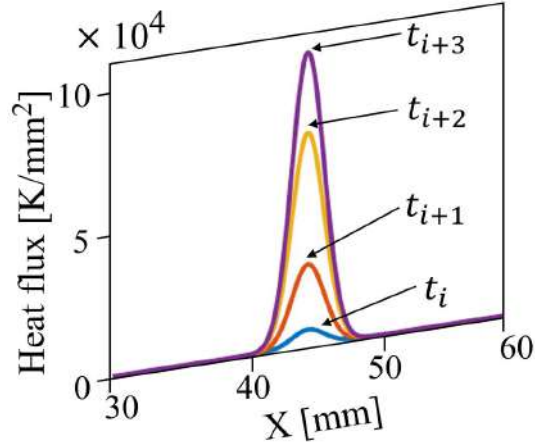


Figure III.C.1.3: Curves of the inner heat flux through the top side of Ω for the time sequence $t_1, t_2, \dots, t_i, t_{i+1}, \dots, t_N$.

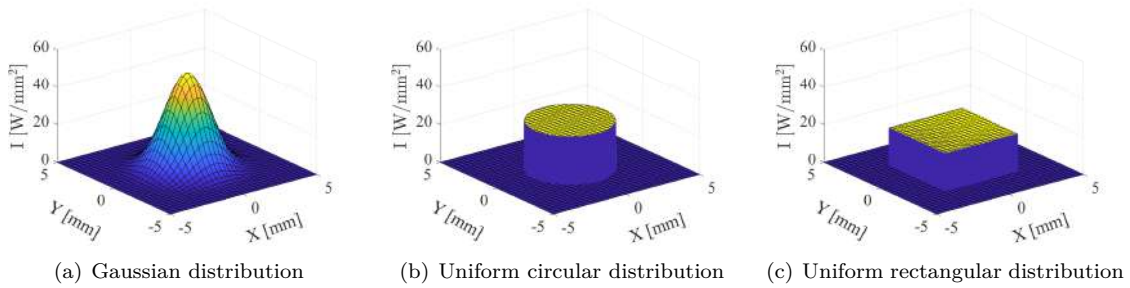


Figure III.C.1.4: Surfaces that describe the laser power distributions for (a) Gaussian, (b) uniform circular and (c) uniform rectangular beams. Laser power $P = 500$ W and laser radius $R = 2.5$ mm.

III.C.1.4.7 Finite Element Mesh and Boundary Conditions

Fig. III.C.1.5 presents the initial and boundary conditions imposed on our 2D domain for the thermal analysis. The initial temperature was 300 K over all the domain. We set constant ambient temperature of 300 K on the left and right hand sides of our domain. The bottom boundary was subjected to an adiabatic boundary condition, i.e. the heat flux was zero. Regarding the top boundary, as mentioned in Section III.C.1.4.6, the laser energy input was model as a heat flux (Neumann) boundary condition. Therefore, those elements that interacted with the laser were subjected to a non-zero flux boundary condition. On the other hand, the elements that did not interact with the laser were under adiabatic boundary conditions (zero flux).

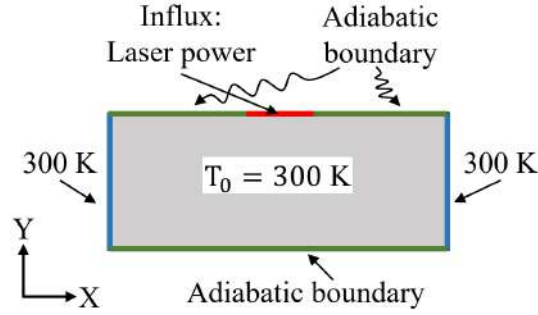


Figure III.C.1.5: Initial and boundary conditions for the simulations.

Fig. III.C.1.6 shows the finite element mesh used for the simulations. The mesh was formed by 3671 linear triangular elements and 1922 nodes. The mesh was refined at the center of the top boundary, since it was the zone that interacted directly with the laser beam. The changes in the temperature obtained with a finer mesh or a smaller time step were negligible for the analysis performed in this work.

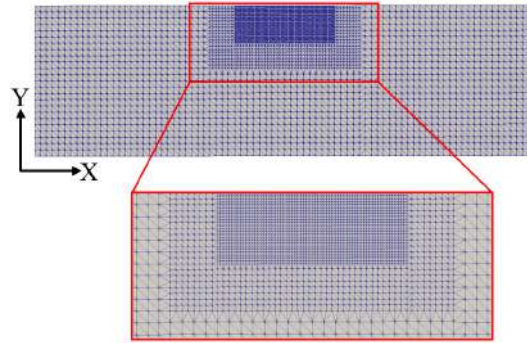


Figure III.C.1.6: Finite element mesh used for the simulations. Mesh refined at neighborhood of laser spot.

III.C.1.4.8 Material Properties and Process Parameters for the Numerical Simulation

For the numerical simulations, we used the *AISI 4140* steel. The material properties (thermal conductivity, density, specific heat and melting point) are given in Table III.C.1.1 [200].

Table III.C.1.1: Material properties of the *AISI 4140* steel used in the numerical simulations [200].

Property	Value
Thermal conductivity (κ)	45 W/(m K)
Density (ρ)	7800 kg/m ³
Specific heat (C_p)	500 J/(kg K)
Melting point	1689 K

Table III.C.1.2: Domain size and process parameters used for the numerical simulations.

Parameter	Value
Width (size in X) of the domain (W in Fig. III.C.1.1)	100 mm
Height (size in Z) of the domain (H in Fig. III.C.1.1)	30 mm
Thickness of the domain (Δz in Fig. III.C.1.1)	5 mm
Length of the tracks (L_T in Fig. III.C.1.1)	100 mm
Separation distance between tracks (d_T in Fig. III.C.1.1)	3.5 mm
Laser power (P)	500 W
Laser radius (R)	2.5 mm (except in Sec. III.C.1.5.2)
Laser speed (v)	13 mm/s (except in Sec. III.C.1.5.3)
Laser intensity distribution	Gaussian (except in Sec. III.C.1.5.1)
Transition time between tracks	2 s
Total simulated time	34 s
Time step (Δt)	0.0769 s
Initial position of the laser	[44.75, 30, -6]

We executed seven numerical simulations in which we studied the influence of different laser intensity distributions, laser radii and process speeds. The simulations aimed to represent the deposition of four parallel tracks (as shown in Fig. III.C.1.1). The domain configuration and process parameters used for the simulations are listed in Table III.C.1.2. For a graphical representation of these parameters, we refer the reader to Fig. III.C.1.1.

III.C.1.5 Results

III.C.1.5.1 Influence of the Laser Intensity Function

We executed three simulations to study the influence of the laser intensity distribution function on the thermal behavior of the substrate. The intensity distributions used were (1) Gaussian in Eq. III.C.1.19, (2) uniform circular in Eq. III.C.1.20 and (3) uniform rectangular in Eq. III.C.1.21. Fig. III.C.1.4 shows the corresponding laser intensity distributions to a laser power $P = 500$ W and

a laser radius $R = 2.5$ mm.

$$I_{Gauss}(x, y) = \frac{2P}{\pi R^2} \exp\left(\frac{-2(x^2 + y^2)}{R^2}\right) \quad (\text{III.C.1.19})$$

$$I_{Circ}(x, y) = \begin{cases} \frac{P}{\pi R^2}, & x^2 + y^2 \leq R^2 \\ 0, & \text{otherwise} \end{cases} \quad (\text{III.C.1.20})$$

$$I_{Sq}(x, y) = \begin{cases} \frac{P}{(2R)^2}, & -R \leq x, y \leq R \\ 0, & \text{otherwise} \end{cases} \quad (\text{III.C.1.21})$$

Fig. III.C.1.7 shows a comparison of the temperature distribution of the Gaussian intensity distribution (on the left) vs. the uniform circular intensity distribution (on the right). The figure presents the temperature at time $t = 8\Delta t$ for the region of the substrate most affected by the laser. We can see that the temperature values and the shapes of the heat affected zone (HAZ) are similar. However, the maximum temperature in the case of the Gaussian distribution is 1210 K while in the case of the uniform circular distribution is 1141 K. This temperature difference is caused by the peak that we can observe in the Gaussian distribution (Fig III.C.1.4) which causes an energy concentration on the center of the HAZ.

Fig. III.C.1.8 presents the comparison of the temperature distributions between the Gaussian (on the left) and the uniform rectangular (on the right) intensity distributions. It is noticeable that the HAZ of the uniform rectangular laser has a larger width and a smaller depth. Likewise, the maximum temperature in the case of the uniform rectangular intensity distribution is 1014 K, almost 200 K less than for the Gaussian intensity distribution.

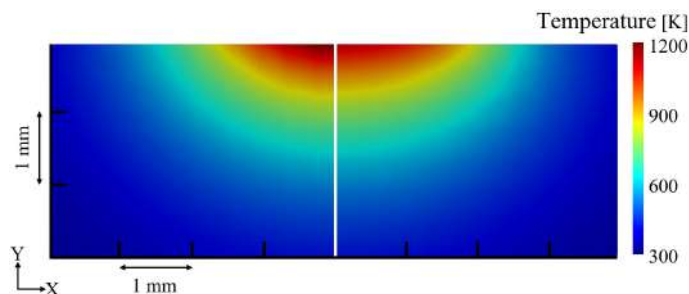


Figure III.C.1.7: Substrate temperature. (i) Gaussian (left) vs. (ii) uniform circular (right) laser power distributions. $t = 8\Delta t$.

To obtain a measure of the energy that goes into the domain along the points of the X axis, we calculated the power per unit of length (I_L) corresponding to each laser intensity function, as given by Eq. III.C.1.22.

$$I_L(x) = \int_{-\infty}^{\infty} I(x, z) dz \quad (\text{III.C.1.22})$$

The resulting functions are shown in Fig. III.C.1.9. It is noticeable the relation between the temperature distributions in Figs. III.C.1.7, III.C.1.8, and III.C.1.9. The peak of the Gaussian distribution for I_L is reflected in the large value for the maximum temperature. Likewise, the larger width in the HAZ corresponding to the rectangular laser beam is explained by the larger

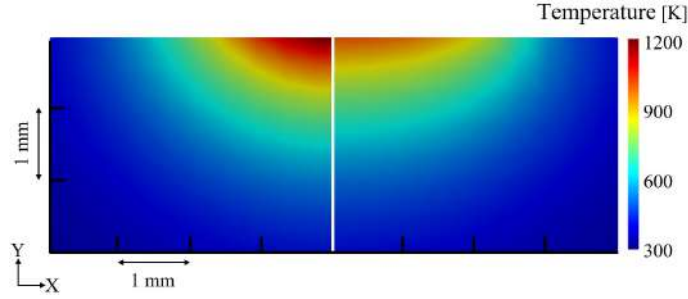


Figure III.C.1.8: Substrate temperature. (i) Gaussian (left) vs. (ii) uniform rectangular (right) laser power distributions. $t = 8\Delta t$.

width of its corresponding I_L . It is important to remark that the areas under the three curves in Fig. III.C.1.9 are equal to the total power of the laser ($P = 500$ W).

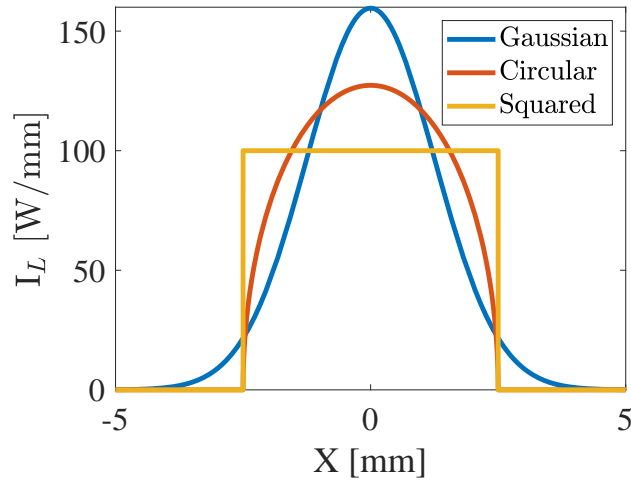


Figure III.C.1.9: Comparison of the functions of laser power per unit of length I_L for the (i) Gaussian, (ii) uniform circular and (iii) uniform rectangular laser power distributions. Laser power (area under the curve) $P = 500$ W and laser radius $R = 2.5$ mm.

Fig. III.C.1.10 shows the thermal history of the point at the top of the domain along the second track (see Fig. III.C.1.1) for the three simulations executed with different laser intensity distributions. In this figure, we can observe that the maximum temperatures are reached when the laser describes the trajectory of the second track. We can see that the maximum temperature corresponds to the simulation performed with the Gaussian intensity distribution. However, before and after the temperature peak, the resulting temperatures for the three laser intensity distributions are very similar. This can be explained by the fact that during these phases, the thermal behavior is determined by the material properties.

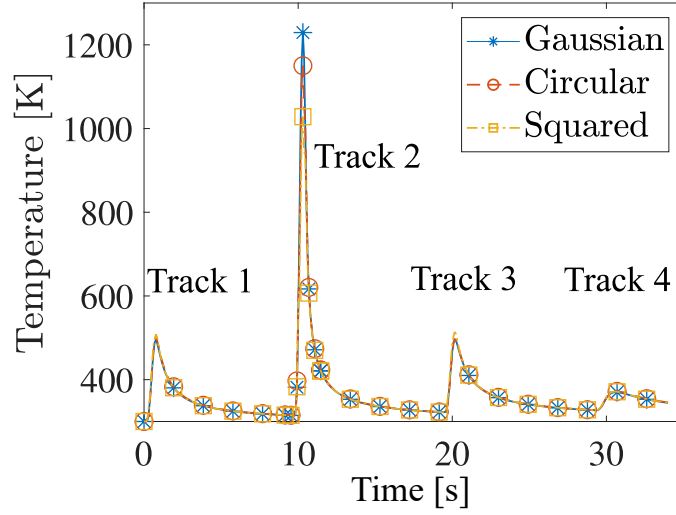


Figure III.C.1.10: Temperature history at x_0 (Fig. III.C.1.1). (i) Gaussian, (ii) uniform circular and (iii) uniform rectangular laser power distributions.

III.C.1.5.2 Influence of the Laser Radius

To study the influence of the laser radius, we performed three simulations using a Gaussian intensity distribution with laser radii $R = 2.0$ mm, $R = 2.5$ mm and $R = 3.0$ mm. Fig. III.C.1.11 compares the temperature distributions between the simulations with $R = 2.5$ mm (left) and $R = 2.0$ mm (right). On the other hand, Fig. III.C.1.12 compares the temperature distributions between the simulations with $R = 2.5$ mm (left) and $R = 3.0$ mm (right). The two figures present the temperature at time $t = 8\Delta t$ for the region of the substrate most affected by the laser. In both figures, we can observe that the simulation with the smallest laser radius produces the largest temperature and depth of the HAZ. Since the delivered power of the laser is kept constant, a smaller radius means that the power is more concentrated at the center of the beam. This power concentration provokes the temperature differences.

We also calculated the amount of power per unit of length (I_L) along the points on the X axis (Eq. III.C.1.22). The resulting functions are depicted in Fig. III.C.1.13. It is noticeable how the peak of the function at the center of the laser beam ($X = 0$) increases while the laser radius decreases.

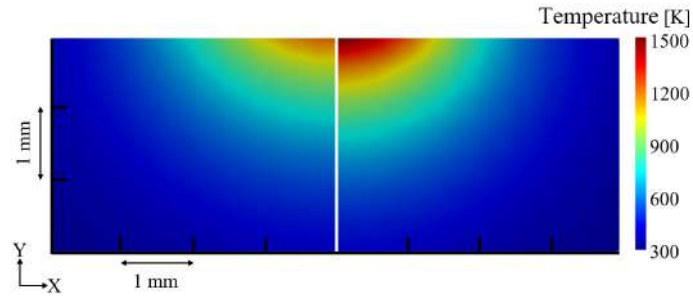


Figure III.C.1.11: Substrate temperature. Gaussian laser power distribution. (a) $R = 2.5$ mm (left), (b) $R = 2.0$ mm (right). $t = 8\Delta t$.

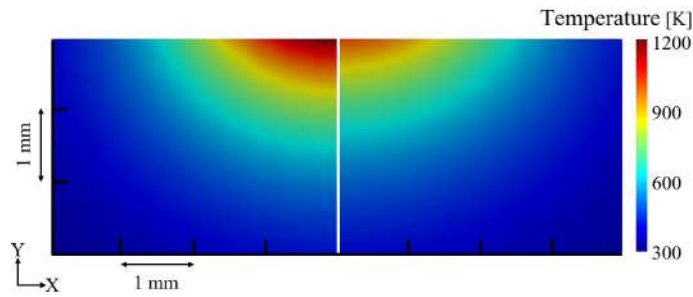


Figure III.C.1.12: Substrate temperature. Gaussian laser power distribution. (a) $R = 2.5$ mm (left), (b) $R = 3.0$ mm (right). $t = 8\Delta t$.

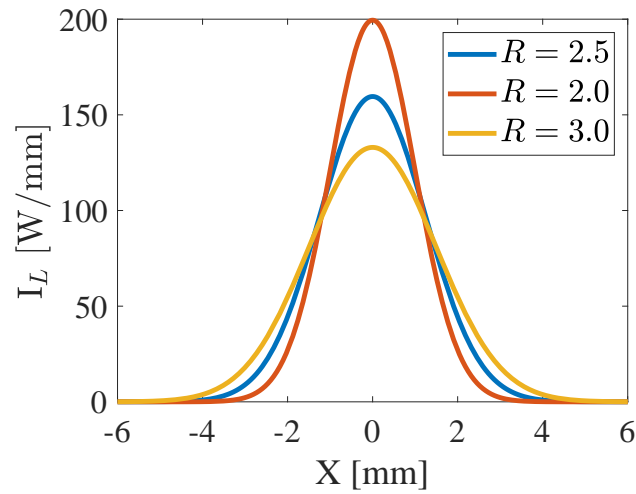


Figure III.C.1.13: Gaussian laser power distribution. Power per unit length I_L . (i) $R = 2.0$ mm, (ii) $R = 2.5$ mm and (iii) $R = 3.0$ mm. Laser power (area under the curve) $P = 500$ W.

Fig. III.C.1.14 shows the thermal history of the point at the top of the domain along the second track (see Fig. III.C.1.1) for the simulations performed with different laser radii. The behavior is similar to the observed in our previous analysis of the impact of the laser intensity distribution: when the laser beam is close to the studied point, temperature differences are noticeable. However, when the laser beam is not close, the thermal behavior is determined by the material properties and the temperatures obtained for the three simulations become very similar.

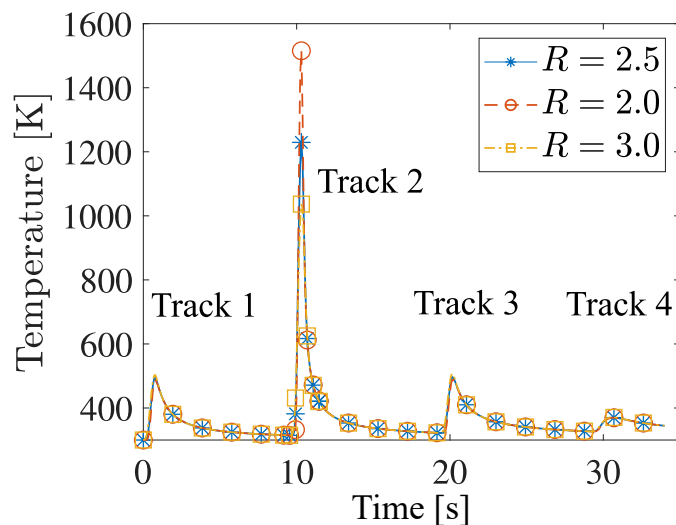


Figure III.C.1.14: Temperature history at x_0 (Fig. III.C.1.1). Gaussian laser power distribution. (i) $R = 2.0$ mm, (ii) $R = 2.5$ mm, (iii) $R = 3.0$ mm.

III.C.1.5.3 Influence of the Process Speed

To study the influence of the process speed, we executed three simulations using a Gaussian intensity distribution with process speed $v = 13.0$ mm/s, $v = 10.4$ mm/s and $R = 15.6$ mm/s.

Fig. III.C.1.15 presents the temperature distribution of the simulations with $v = 13$ mm/s (left) at time $t = 8\Delta t$ and $v = 10.4$ mm/s (right) at time $t = 10\Delta t$. The figures show the configurations with maximum temperature on the first track. First, notice that, since the initial point of the laser was the same (see Table III.C.1.2), the maximum temperature for the simulation with $v = 13$ mm/s was reached before than the one in the case of $v = 10.4$ mm/s ($t = 8\Delta$ vs. $t = 10\Delta t$).

Fig. III.C.1.16 compares the temperature distributions between the simulations with $v = 13$ mm/s (left) at time $t = 8\Delta t$ and $v = 15.6$ mm/s (right) at time $t = 7\Delta t$. As in the previous case, those images correspond to the configuration of maximum temperature for the first track.

In Figs. III.C.1.15 and III.C.1.16, the maximum temperatures of the simulations with $v = 10.4$ mm/s, $v = 13$ mm/s and $v = 15.6$ mm/s were 1276 K, 1210 K and 1160 K, respectively. When the process speed is lower, the interaction time between the laser beam and the domain is larger. Therefore, the energy delivered by the laser (heat influx through the top boundary) is larger for lower process speeds. Consequently, larger temperatures and depths of the HAZs are obtained for lower process speeds.

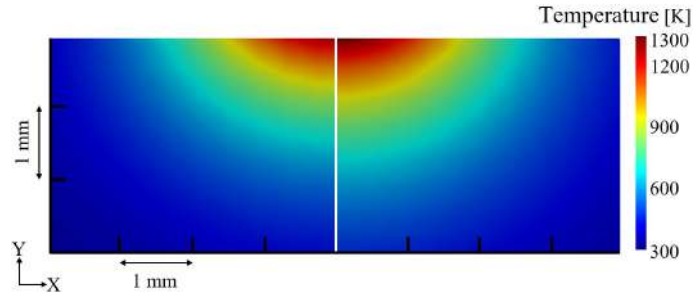


Figure III.C.1.15: Substrate temperature. Gaussian laser power distribution. Laser speed: (i) $v = 13.0$ mm/s (left), (ii) $v = 10.4$ mm/s (right).

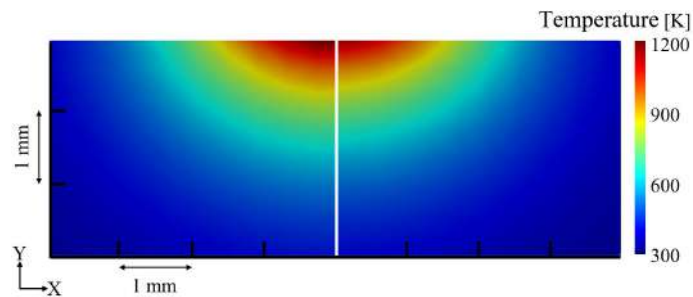


Figure III.C.1.16: Substrate temperature. Gaussian laser power distribution. Laser speed: (i) $v = 13.0$ mm/s (left), (ii) $v = 15.6$ mm/s (right).

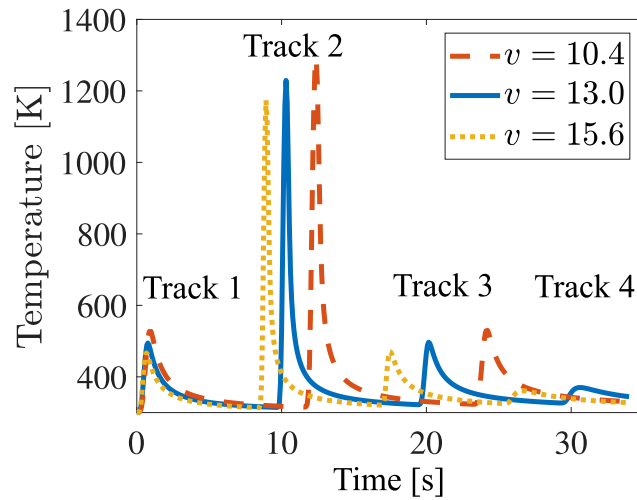


Figure III.C.1.17: Temperature history at x_0 (Fig. III.C.1.1). Gaussian laser power distribution. (i) $v = 10.4$ mm/s, (ii) $v = 13.0$ mm/s, (iii) $v = 15.6$ mm/s.

Fig. III.C.1.17 shows the thermal history of the point at the top of the domain along the second track (see Fig. III.C.1.1) for the simulations performed with different process speeds. The observed peaks of maximum temperature coincide with the previous analysis: lower process speed generates larger maximum temperatures. On the other hand, since the starting point of the laser is the same in the three simulations, we observe that the peaks of maximum temperature occur at different time. It occurs because the point of analysis is reached by the laser at different times, as a consequence of the process speed. The reader may notice that the larger the process speed, the faster the appearance of the temperature peak.

III.C.1.5.4 Comparison with Non-linear Simulations

In order to assess the suitability of the linear model in digital twin environments, we compared the simulations with a non-linear model that included radiation (Eq. III.C.1.24) and natural convection ((Eq. III.C.1.23)) heat losses:

$$q_{\text{conv}} = h_c (T - T_\infty). \quad (\text{III.C.1.23})$$

$$q_{\text{rad}} = \varepsilon \sigma (T^4 - T_\infty^4) \quad (\text{III.C.1.24})$$

where h_c is the natural convection coefficient, ε is the thermal emissivity, $\sigma \approx 5.67 \times 10^{-8} \text{ W m}^{-2} \text{ K}^{-4}$ is the Stefan-Boltzmann constant and T_∞ is the ambient temperature. These two processes were included as Neumann boundary conditions on the top boundary (red boundary in Fig. III.C.1.5). The details of the implementation of the non-linear model are out of the scope of this manuscript.

We executed the same simulations that in Section III.C.1.5.1 with the Gaussian, circular and rectangular laser intensity distributions, but including convection and radiation. The value of the parameters for the simulations are reported in Tables III.C.1.1–III.C.1.3. Since the non-linear model includes heat losses, the temperature calculated are consistently lower than for the linear model. The temperature difference at every time step was below 5% in all cases, using the non-linear model as *ground truth*.

Table III.C.1.3: Thermal properties for the non-linear simulations [110].

Property	Value
Convection coefficient (h_c)	20 W/(m ² K)
Emissivity (ε)	1.0
Ambient temperature (T_∞)	300 K

III.C.1.6 Conclusions and Future Work

This manuscript presents an analysis of the influence of the laser intensity distribution, the laser spot radius and the process speed on the thermal history of a substrate that is heated by the action of the laser. For the analysis, we implemented a 2D linear transient thermal model using the finite element method. The energy provided by the laser was represented as a time/space dependent heat influx (Neumann) boundary condition.

We executed simulations with three types of intensity distribution functions, namely Gaussian, uniform circular and uniform rectangular. Likewise, we performed simulations with laser radius

$R = 2.0$ mm, $R = 2.5$ mm and $R = 3.0$ mm. In all the simulations, the total laser delivered power was identical and equal to $P = 500$ W. Results showed that these two parameters (the type of the intensity distribution function and the laser radius) strongly affect the shape (width and depth) of the HAZ and the maximum temperature.

The comparison of the linear and non-linear models proved that the linear simulations are good options for digital twin based design environments, due to their simplicity and reasonable temperature error. Apart of convection and radiation, further work is required to include important aspects to resemble the real process such as phase change and temperature dependent material properties.

Implications and Influences

In the context of laser-based additive manufacturing, the thermal behavior of the substrate is relevant to define process parameters vis-à-vis piece quality. This manuscript studies the laser power spatial distributions (Gaussian, uniform circular and uniform rectangular) in addition to the laser power and process speed in 2D linear substrate heating simulations. The laser energy is modeled as a time dependent heat flux boundary condition on top of the domain. The results show that the laser intensity spatial distribution strongly affects the maximum temperature and the depth and width of the heat affected zone. These 2D finite element simulations prove to be good options for digital twin based design environments, due to their simplicity and reasonable temperature error, compared to non-linear FEA (considered as ground truth for this case). Future efforts must address non-linear finite element simulations of the laser heating process.

Funding

This work has received funding from the Eusko Jauriaritza/Basque Government under the grants KK-2018/00115 (ADDISEND) and KK-2018/00071 (LANGILEOK).

III.C.2

Nonlinear Thermal Simulation of Laser Metal Deposition

Diego Montoya-Zapata^{1,2}, Juan M. Rodríguez³, Aitor Moreno¹, Oscar Ruiz-Salguero², Jorge Posada¹

¹Vicomtech Foundation, Basque Research and Technology Alliance (BRTA), Mikeletegi 57, Donostia-San Sebastian 20009, Spain

²Laboratory of CAD CAM CAE, Universidad EAFIT, Cra 49 no 7-sur-50, Medellín 050022, Colombia

³Department of Mechanical Engineering, Universidad EAFIT, Cra 49 no 7-sur-50, Medellín 050022, Colombia



III.C.2.1 Context

Diego Montoya-Zapata, Juan M. Rodríguez, Aitor Moreno, Oscar Ruiz-Salguero, Jorge Posada. Nonlinear thermal simulation of Laser Metal Deposition. Australian Journal of Mechanical Engineering, Taylor & Francis, (ISSN: 1448-4846, eISSN: 2204-2253), 2021, 19(5), pp. 653-668. url: <https://doi.org/10.1080/14484846.2021.1988435>, doi: 10.1080/14484846.2021.1988435, Published online: 03 Feb 2022.

Indexing: SCOPUS(Q3), JCI(Q3), Publindex(B)

Abstract

Simulation of Laser Metal Deposition (LMD) is central to the planning of Additive Manufacturing processes. This manuscript presents the computational implementation of a 2D-plus-thickness nonlinear thermal simulation of LMD, which considers: (i) temperature-dependent material properties, (ii) heat losses due to convection and radiation, (iii) geometrical update during material deposition, (iv) phase change and (v) the interaction between the laser and the substrate. The implementation computes the history of the temperature field at a cross-cut normal to the laser trajectory and the history of the bead accumulation. The material deposition model is based on the spatial distribution of the delivered powder. This manuscript presents the mathematical and numerical foundations to execute an efficient local re-meshing of the growing bead. The numerical estimation of the bead geometry is compared with experimental results found in the existing literature. The present model shows reasonable accuracy to predict the bead width (15% error) and bead height (22% error). This implementation is an in-house one, which allows for the inclusion of additional physical effects. Additional work is needed to account for the particle (thermo) dynamics over the substrate, responsible for a significant material and energy waste, which in turn leads to the actual temperature and molten depth being over-estimated in the executed simulations.

Keywords: laser metal deposition, additive manufacturing, nonlinear finite element method.

Glossary

AM	Additive manufacturing.
FEA	Finite element analysis.
FEM	Finite element method.
LMD	Laser metal deposition.
PL	Piecewise linear.
$\Omega \subset \mathbb{R}^2$	2D-plus-thickness FEA domain.
$\partial\Omega$	1D border of domain Ω .
$M = (V, T)$	FEA triangular mesh defined by the set of nodes V and the set of triangles T .
$\Delta z \in \mathbb{R}$	Thickness of the domain Ω [mm]
$\Delta t \in \mathbb{R}$	Time increment for the FEM simulation [s]
$T(\mathbf{x}, t) : \mathbb{R}^2 \times \mathbb{R} \rightarrow \mathbb{R}$	Temperature at $\mathbf{x} \in \Omega$ in the instant t [K]
$T^h(\mathbf{x}, t) : \mathbb{R}^2 \times \mathbb{R} \rightarrow \mathbb{R}$	Approximated temperature function at $\mathbf{x} \in \Omega$ in the instant t [K]. It is the result given by the finite element method.
$\boldsymbol{\theta}(t) : \mathbb{R} \rightarrow \mathbb{R}^{N_{nodes}}$	Global vector of nodal temperatures at time t [K].
$\boldsymbol{\theta}^s \in \mathbb{R}^{N_{nodes}}$	Global vector of nodal temperatures at time t^s [K].
$\boldsymbol{\theta}^{s,k} \in \mathbb{R}^{N_{nodes}}$	Global vector of nodal temperatures at time t^s and iteration k in the Newton-Raphson scheme [K].
$\mathbf{M}(\mathbf{x}, t) : \mathbb{R}^2 \times \mathbb{R} \rightarrow \mathbb{R}^{N_{nodes}} \times \mathbb{R}^{N_{nodes}}$	Global mass matrix in the FEM formulation [J/K].
$\mathbf{M}^s(\mathbf{x}, t) : \mathbb{R}^2 \times \mathbb{R} \rightarrow \mathbb{R}^{N_{nodes}} \times \mathbb{R}^{N_{nodes}}$	Global mass matrix at time t^s [J/K].

$\mathbf{K}(\mathbf{x}, t) : \mathbb{R}^2 \times \mathbb{R} \rightarrow \mathbb{R}^{N_{nodes}} \times \mathbb{R}^{N_{nodes}}$	Global conductivity matrix in the FEM formulation [W/K].
$\mathbf{K}^s(\mathbf{x}, t) : \mathbb{R}^2 \times \mathbb{R} \rightarrow \mathbb{R}^{N_{nodes}} \times \mathbb{R}^{N_{nodes}}$	Global conductivity matrix at time t^s [J/K].
$\mathbf{f}(\mathbf{x}, t) : \mathbb{R}^2 \times \mathbb{R} \rightarrow \mathbb{R}^{N_{nodes}}$	Global force vector in the FEM formulation [W].
$\mathbf{f}^s(\mathbf{x}, t) : \mathbb{R}^2 \times \mathbb{R} \rightarrow \mathbb{R}^{N_{nodes}}$	Global force vector at time t^s [W].
$T^0(\mathbf{x}) : \mathbb{R}^2 \rightarrow \mathbb{R}$	Initial (at $t = 0$) temperature at \mathbf{x} [K]
$T(\mathbf{x}, t) : \mathbb{R}^2 \times \mathbb{R} \rightarrow \mathbb{R}$	Temperature function at the region with Dirichlet boundary conditions [K]
$\bar{q}(\mathbf{x}, t) : \mathbb{R}^2 \times \mathbb{R} \rightarrow \mathbb{R}$	Heat flux function at the region with Neumann boundary conditions [W/m ²]
\mathbf{R}	System of nonlinear equations associated to the semi-discrete FEM formulation.
$\mathbf{q}(\mathbf{x}, t) : \mathbb{R}^2 \times \mathbb{R} \rightarrow \mathbb{R}^2$	Heat flux into or out of the medium at $\mathbf{x} \in \Omega$ at time t [W/m ²]
$s(\mathbf{x}, t) : \mathbb{R}^2 \times \mathbb{R} \rightarrow \mathbb{R}$	Volumetric heat sources at $\mathbf{x} \in \Omega$ in the instant t [W/m ³]
$\mathbf{n}(\mathbf{x}) : \mathbb{R}^2 \rightarrow \mathbb{R}^2$	Outward unit normal to the boundary at $\mathbf{x} \in \Omega$
$\rho(T) : \mathbb{R} \rightarrow \mathbb{R}$	Density of the material [kg/m ³] as a function of the temperature.
$\kappa(T) : \mathbb{R} \rightarrow \mathbb{R}$	Thermal conductivity of the material [W/(m K)] as a function of the temperature.
$C(T) : \mathbb{R} \rightarrow \mathbb{R}$	Specific heat capacity of the material [J/(kg K)] as function of the temperature.
$C_{eq}(T) : \mathbb{R} \rightarrow \mathbb{R}$	Equivalent specific heat capacity of the material [J/(kg K)], used to incorporate phase change into the simulation.
$N_1(\xi, \eta), N_2(\xi, \eta), N_3(\xi, \eta) : \mathbb{R}^2 \rightarrow \mathbb{R}$	Shape functions in the FEM formulation for 3-node triangular elements. Interpolation functions inside the triangular elements.
$N_1^q(\xi), N_2^q(\xi) : \mathbb{R} \rightarrow \mathbb{R}$	Shape functions in the FEM formulation for the edges of 3-node triangular elements. Interpolation functions along the edges with Neumann boundary conditions.
$I(x, z, t) : \mathbb{R}^2 \times \mathbb{R} \rightarrow \mathbb{R}$	Laser energy intensity distribution [W/mm ²]
$P_L \in \mathbb{R}$	Laser nominal power [W]
$R_L \in \mathbb{R}$	Laser beam radius [W]
$[T_s, T_l] \subset \mathbb{R}$	Melting range of the material [K].
$\mu \in \mathbb{R}$	Material flow rate [kg/s]
$f(x, z, t) : \mathbb{R}^2 \times \mathbb{R} \rightarrow \mathbb{R}$	Powder particle distribution projected by the nozzle onto the substrate at time t [kg/(mm ² s)].
$H(x, z, t) : \mathbb{R}^2 \times \mathbb{R} \rightarrow \mathbb{R}$	Height of the bead at time t [mm].
$L \in \mathbb{R}$	Latent heat of fusion [J/kg].
$h_c \in \mathbb{R}$	Convection coefficient [W/(m ² K)].
$\varepsilon \in \mathbb{R}$	Material thermal emissivity.
$\sigma \in \mathbb{R}$	Stefan-Boltzmann constant [W/(m ² K ⁴)].
$T_\infty \in \mathbb{R}$	Ambient temperature [K].

III.C.2.2 Introduction

Laser Metal Deposition (LMD) is an additive manufacturing process in which metal powder is delivered on top of a substrate while a laser melts the added material to produce a new layer. LMD has gained importance during the last several years because of its applications in the repair, coating and manufacturing of high-valued industrial parts [93].

This manuscript presents the implementation of a nonlinear 2D-plus-thickness thermal model for the simulation of LMD. The simplification is justified under the assumption of process stability along the direction of movement of the tool head. The laser energy source is modeled as a flux boundary condition. The present implementation considers the following aspects: (1) the variation of the material properties with respect to the temperature, (2) convection and radiation heat losses and (3) the dynamic evolution of the domain due to material deposition.

This manuscript reports the implementation of the Finite Element Method (FEM) for 2D triangular elements. This manuscript discusses the corresponding FEM matrices of the considered phenomena (heat equation, temperature-dependent material properties, radiation, and convection). A model for the representation of the material addition based on the spatial distribution of the delivered powder is formulated. Its theoretical foundations and its integration into the Finite Element Analysis (FEA) analysis pipeline are also presented in this manuscript.

The remainder of this article is organized as follows: Section III.C.2.3 provides a review of the previous works. Section III.C.2.4 presents the governing equations, numerical schemes and the methods to model material deposition. Section III.C.2.5 presents and discusses the results of the implementation. Section III.C.2.6 concludes the manuscript and suggests potential future work.

III.C.2.3 Literature Review

III.C.2.3.1 Simulation of Laser Metal Deposition

Within LMD, recent studies [34, 55, 72, 133, 135] have employed physical experimentation and statistical techniques (e.g. design of experiments and ANOVA) to devise empirical models that link the process parameters with the final bead geometry. These studies have focused on the influence of the laser power, tool-head speed and mass feed rate on the height, width and dilution ratio of the final bead.

In LMD, the substrate and bead thermal histories are relevant because they allow the prediction of the mechanical properties, the microstructure and residual stresses of the workpiece [28, 37, 77, 115, 130, 149]. Authors have relied on numerical simulation to represent complex phenomena involved in the modeling of LMD. Pure thermal models [35, 115, 200] have allowed the prediction of the thermal history of the melt-pool during deposition. Ref. [200] presents a 2D thermal model that considers convection, radiation and phase change. The model is fed with the powder efficiency to estimate the final bead geometry and thermal history during deposition. The research in [115] confirms the importance of considering convection and radiation heat losses to obtain accurate temperature estimations. Thermal models have also been used to study the impact of the process parameters on the resulting workpiece. In this regard, Ref. [35] uses a 2D thermal model to study the influence of the material flow rate, nozzle speed and laser power on the melting depth in the substrate.

Thermo-fluid models [6, 106, 186] have incorporated fluid flow effects into the thermal simula-

tions to study the dynamics of the melt-pool. Apart from the temperature, thermo-fluid models predict the velocity field in the melt-pool. Models in Refs. [6, 106] include Marangoni and capillary effects, which produce more accurate temperature predictions than pure thermal models. Ref. [186] uses a 2D thermal-fluid model to study the effects of the material flow rate and the laser power on the shape of the melt-pool.

Thermo-mechanical approaches [25, 60, 171] have calculated residual stresses and distortions by estimating the temperature and displacements during deposition. Refs. [60, 171] consider the same phenomena as pure thermal models: radiation, convection, temperature-dependent properties and phase change phenomena. However, they include the effects of thermal expansion to execute solid mechanics analysis via the estimation of the displacement field. Ref. [60] studies the residual stress in several contiguous single-layer tracks. Ref. [171] analyzes the residual stress and distortion of multi-layer cylindrical geometries.

Most of the approaches mentioned above have been executed on commercial software and the implementation has not been discussed. More comprehensive literature reviews on the simulation of LMD can be found in [143, 180].

III.C.2.3.2 Assessment of Temperature Predictions and Computational Resources

The experimental measurement of the temperature in the LMD process is a very challenging task. The high-temperature conditions of LMD make unfeasible the temperature measurement within the melt-pool. Researchers have used non-contact devices (e.g. infrared cameras and pyrometers) to gather temperature data of the melt-pool surface. The accuracy of the measurements of non-contact devices is affected by several conditions, such as (i) the interference of the laser and the powder metal, (ii) non-constant (unknown) thermal emissivity of the melt-pool and (iii) the calibration of the sensing devices [30, 183]. As an alternative, other authors have used metallography as an indirect method to infer the temperature history in the LMD process [6, 25, 35, 186]. Metallography is a destructive technique, which requires the cross-sectioning of the workpiece.

The authors in Refs. [6, 25, 35, 171, 186, 200] do not report the execution times of the numerical simulation. The lack of this data is related to the use of commercial software. Commercial software does not inform the execution time of each sub-process of the simulation (e.g. remeshing, powder metal and laser interaction, and thermal/fluid/mechanical FEM solution). Ref. [115] informs the execution time of the simulation. However, the scope of the simulation and the mathematical models are different in each work. It is, therefore, unfeasible to compare the execution time of the simulation or its sub-process with other related studies.

III.C.2.3.3 Representation of the Bead Geometry

One of the main tasks in the numerical simulation of LMD is the representation of the deposited material. In the literature, two approaches can be identified. The first one pre-defines the cross-section of the final bead geometry. Several functions are used: circular and elliptical [55, 133, 135, 210], sinusoidal [25, 133, 135] and parabolic [186, 200]. This approach does not represent the intermediate states of the bead geometry during the deposition.

In the second approach, the bead geometry is induced by the spatial (3D) distribution of the delivered metal powder delivered on top of the substrate. The powder metal distribution is modeled as a function of the process parameters (powder spatial flow rate profile and nozzle velocity) and

material properties (density). Authors have used two functions: Gaussian [6, 55, 130, 178, 179] and circular [55]. These models give a complete description of the amount and distribution of material on top of the substrate, which can be used to describe the evolution of the bead geometry during the deposition.

III.C.2.3.4 Conclusions of the Literature Review

This literature survey has identified the following numerical approaches to calculate the thermal history during the deposition in LMD: pure thermal, thermo-fluid and thermo-mechanical models. These approaches exploit the capabilities of numerical simulation to include complex phenomena, such as melt-pool dynamics, phase change, variation of the material properties with respect to the temperature, and radiation/convection/conduction heat losses. Many of these publications report the use of commercial software. Therefore, the discussion of the numerical implementation of the mathematical models is missing.

This manuscript presents an in-house implementation of a 2D-plus-thickness nonlinear simulation of LMD. Since no commercial FEA software is used, (i) it is flexible and extensible, (ii) it is particularized to LMD and (iii) the mathematical models are thoroughly presented and discussed. This manuscript reports a thermal model which considers: (i) temperature-dependent material properties, (ii) convection and radiation heat losses, (iii) material deposition and (iv) phase change. The energy input to the system is modeled as a boundary condition of the type flux. This flux occurs at the upper border of the FEA mesh, which contains both substrate and bead elements. This manuscript thus discusses the interaction among physical, mathematical, and numerical considerations in LMD simulation.

This manuscript also reports the remeshing strategy used between time frames. The addition of material causes a (constrained Delaunay) remeshing, which is confined to the bead domain alone. This strategy saves resources both for geometry and temperature field re-computing at successive time steps.

The implemented method does not model (i) laser and metal powder flight interaction, (ii) powder evaporation (c) powder scattering away from bead due to the gas jet dynamics, (d) fluid dynamics within the molten material.

III.C.2.4 Methodology

III.C.2.4.1 Problem Description

This work aims to study the geometry and temperature evolution of a linear track of the Laser Metal Deposition process, as shown in Fig. III.C.2.1. This work considers that the process parameters (tool-head cruise speed, powder deposition rate and laser power) remain constant throughout the deposition. This study is limited to a 2D cross-section (plus thickness Δz). Features of the computer simulations follow.

1. Material deposition is considered. As a result, the bead cross cut and its FE mesh evolve as the time domain increases. This manuscript discusses the theoretical and numerical aspects of the material deposition model.
2. The energy delivered by the laser is modeled as a flux boundary condition that acts on the top of the domain.

3. The physical properties (density, specific heat and conductivity) of the substrate and the cladding materials are functions of the temperature. The simulation also contemplates the phase-change (from solid to liquid and vice-versa) of the substrate and cladding materials.
4. Heat loss due to radiation and convection is included.
5. The Newton-Raphson method is used to execute the nonlinear computation of temperature-dependent material properties, radiation / convection / conduction heat migration, and phase change.
6. This work does not consider molten metal fluid dynamics nor energy attenuation due to the interaction between the laser beam and the powder.

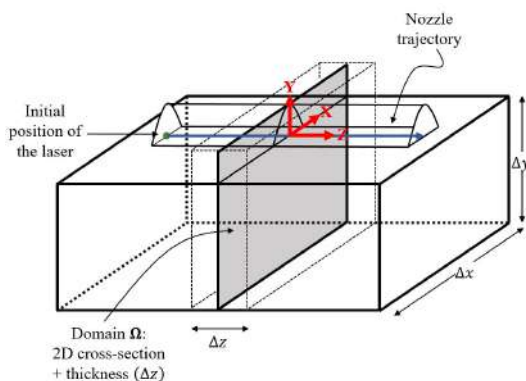


Figure III.C.2.1: Simulation of the deposition of LMD. Graphical representation of the domain, reference frame and parameters involved.

III.C.2.4.2 Governing Equations

The present work uses the heat equation to describe the temperature distribution $T(\mathbf{x}, t)$ in the 2D domain Ω :

$$\rho C \frac{\partial T}{\partial t} - \nabla \cdot (\kappa \nabla T) = s \quad (\text{III.C.2.1})$$

where ρ, C and κ denote the density, specific heat and thermal conductivity, respectively. This work considers that the material properties depend on the temperature. The function $s = s(\mathbf{x}, t)$ represents the heat source (which in this case is equal to 0).

At the beginning of the simulation, the domain is at room temperature (300 K):

$$T(\mathbf{x}, 0) = T^0(\mathbf{x}) = 300 \quad (\text{III.C.2.2})$$

Temperature (Dirichlet) and flux (Neumann) conditions may be imposed on the boundary of Ω ($\partial\Omega$). The regions of $\partial\Omega$ with imposed Dirichlet and Neumann boundary conditions are denoted as $\partial\Omega_T$ and $\partial\Omega_q$, respectively. They fulfill the following conditions:

$$\partial\Omega_T \cup \partial\Omega_q = \partial\Omega; \quad \partial\Omega_T \cap \partial\Omega_q = \emptyset \quad (\text{III.C.2.3})$$

The boundary conditions are formally stated as follows:

$$T(\mathbf{x}, t) = \bar{T}(\mathbf{x}, t), \quad \mathbf{x} \in \partial\Omega_T; \quad \mathbf{q}(\mathbf{x}, t) \cdot \mathbf{n}(\mathbf{x}) = \bar{q}(\mathbf{x}, t), \quad \mathbf{x} \in \partial\Omega_q \quad (\text{III.C.2.4})$$

where \bar{T} and \bar{q} are known scalar functions, and \mathbf{n} is the normal vector that points outwards. The heat flux \mathbf{q} satisfies the Fourier law $\mathbf{q} = -\kappa\nabla T$.

III.C.2.4.2.1 Weak Form and Finite Element Discretization

The weak form of the problem stated in Eqs. III.C.2.1-III.C.2.4 is given by:

$$\int_{\Omega} w \rho C \frac{\partial T}{\partial t} dV + \int_{\Omega} \nabla w \cdot (\kappa \nabla T) dV = \int_{\Omega} w s dV - \int_{\partial\Omega_q} w \bar{q} dA \quad (\text{III.C.2.5})$$

where w is a weighting function. The differential elements of volume and area in Eq. III.C.2.5 become $dV = \Delta z dA$ and $dA = \Delta z dL$ where Δz is the thickness of Ω .

To find an approximate solution of the temperature field T , the domain Ω is partitioned into (3-node) triangular finite elements Ω^e . Say T^h is the approximated solution for T . The interpolation of T^h in the triangular element Ω^e is given by:

$$T^h(\mathbf{x}, t) = \sum_{a=1}^3 N_a(\mathbf{x})^e \theta_a(t), \quad \mathbf{x} \in \Omega^e \quad (\text{III.C.2.6})$$

where ${}^e\theta_a(t)$ is the temperature at node a of the element Ω^e . The functions N_1, N_2 and N_3 are the shape functions for the triangular FEA elements. They also define the mapping between a reference triangle Ω^ξ with vertices $\{(0, 0), (1, 0), (0, 1)\}$ and any element Ω^e in the FEA mesh (see Fig III.C.2.2(a)):

$$N_1(\xi, \eta) = 1 - \xi - \eta; \quad N_2(\xi, \eta) = \xi; \quad N_3(\xi, \eta) = \eta; \quad \xi, \eta \in [0, 1] \quad (\text{III.C.2.7})$$

After the spatial discretization, the semi-discrete (discrete in space and continuous in time) formulation for Eq. III.C.2.5 is obtained:

$$\mathbf{M}\dot{\boldsymbol{\theta}} + \mathbf{K}\boldsymbol{\theta} - \mathbf{f} = 0 \quad (\text{III.C.2.8})$$

where the vector of nodal temperatures $\boldsymbol{\theta}(t)$ is a continuous function of time. The components of the mass and conductivity matrices, $\mathbf{M}(t)$ and $\mathbf{K}(t)$, are:

$${}^e\mathbb{M}_{ab} = \int_{\Omega^e} \rho C N_a N_b \Delta z dA; \quad a, b = 1, 2, 3 \quad (\text{III.C.2.9})$$

$${}^e\mathbb{K}_{ab} = \int_{\Omega^e} \nabla N_a \cdot (\kappa \nabla N_b) \Delta z dA; \quad a, b = 1, 2, 3 \quad (\text{III.C.2.10})$$

Let $\partial\Omega_q^e$ be the edge of the element Ω^e that is subjected to flux boundary conditions. The interpolation for the temperature along the edge $T^h(\mathbf{x}, t)$ is given by:

$$T^h(\mathbf{x}, t) = \sum_{a=1}^2 N_a^q(\mathbf{x})^e \theta_a(t); \quad \mathbf{x} \in \partial\Omega^e \quad (\text{III.C.2.11})$$

The functions N_1^q and N_2^q are the shape functions for the mapping between a reference segment $\partial\Omega^\xi$ with vertices $\{(0,0), (1,0)\}$ and any triangle segment $\partial\Omega_q^e$ in the FEA mesh (see Fig III.C.2.2(b)):

$$N_1^q(\xi) = 1 - \xi; \quad N_2^q(\xi) = \xi \quad (\text{III.C.2.12})$$

The components of the local force vector ${}^e\mathbf{f}(t)$ are:

$${}^e f_a = \int_{\Omega^e} N_a s \Delta z dA - \int_{\partial\Omega_q^e} N_a^q \bar{q} \Delta z dL; \quad a = 1, 2 \quad (\text{III.C.2.13})$$

The simulations in the present work does not consider heat sources ($s = 0$). The function $\bar{q} : \bar{q}(\mathbf{x}, t)$ accounts for the flux boundary conditions that are consider: the energy input of the laser \bar{q}_l , radiation \bar{q}_{rad} and convection \bar{q}_{conv} . The corresponding functions associated to each flux boundary condition are described in detail in the following sections.

Temperature (Dirichlet) boundary conditions are applied at the bottom of the domain. The temperature in this region is set to $\bar{T} = 300$ K during all the simulation.

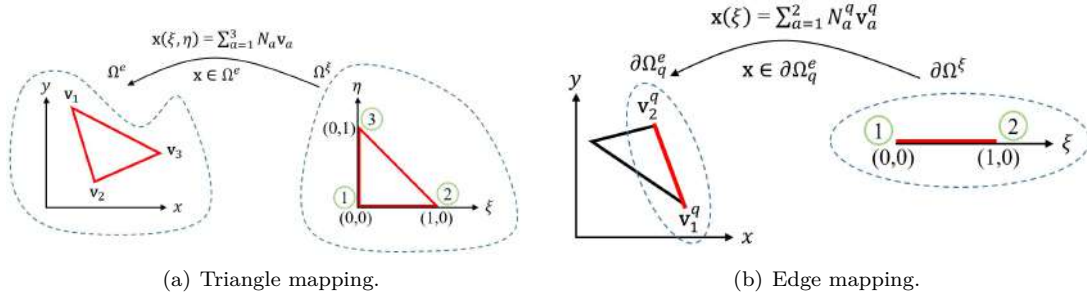


Figure III.C.2.2: Mapping between the reference entities (triangle/edge) and the ones in the FEA mesh.

III.C.2.4.2.2 Time Discretization and Newton-Raphson Scheme

To obtain the fully discrete formulation of Eq. III.C.2.8 it is still necessary to execute the time discretization. The simulation time interval $[0, t_{\text{max}}]$ is divided into N sub-intervals: $[t^0, t^1], [t^1, t^2], \dots, [t^{N-1}, t^N]$, such that $t^0 = 0$ and $t^N = t_{\text{max}}$.

The vector $\boldsymbol{\theta}^s = \boldsymbol{\theta}(t^s)$ denotes the nodal temperatures at t^s . The backward Euler method is used for the time discretization by approximating the time derivative $\dot{\boldsymbol{\theta}}^s$ as follows [80]:

$$\dot{\boldsymbol{\theta}}^s \approx \frac{\boldsymbol{\theta}^s - \boldsymbol{\theta}^{s-1}}{\Delta t} \quad (\text{III.C.2.14})$$

Eq. III.C.2.14 is inserted into Eq. III.C.2.8. The reader may notice that, since ρ, C, κ and \bar{q} depend on the temperature, $\mathbf{M}^s, \mathbf{K}^s$ and \mathbf{f}^s are functions of the temperature (see Eqs. III.C.2.9, III.C.2.10 and III.C.2.13). Therefore, at every instant t^s , one obtains a system of nonlinear equations \mathbf{R} in which the variables are the nodal temperatures $\boldsymbol{\theta}^s$:

$$\mathbf{R}(\boldsymbol{\theta}^s) = \mathbf{M}^s (\boldsymbol{\theta}^s - \boldsymbol{\theta}^{s-1}) + \Delta t \mathbf{K}^s \boldsymbol{\theta}^s - \Delta t \mathbf{f}^s = 0 \quad (\text{III.C.2.15})$$

The Newton-Raphson scheme is used to solve this system of equations. The characteristics of this method requires several iterations to solve for $\boldsymbol{\theta}^s$ at every time instant t^s . Let $\boldsymbol{\theta}^{s,k}$ be the nodal temperature at iteration k . The Newton-Raphson updating rule for iteration k is given by

$$\boldsymbol{\theta}^{s,k} = \boldsymbol{\theta}^{s,k-1} + \mathbf{u}; \quad \mathbf{u} = - \left. \frac{d\mathbf{R}}{d\boldsymbol{\theta}^s} \right|_{\boldsymbol{\theta}^{s,k}} \mathbf{R}(\boldsymbol{\theta}^{s,k}) \quad (\text{III.C.2.16})$$

The matrix $\frac{d\mathbf{R}}{d\boldsymbol{\theta}^s}$ is known as the tangent matrix. It is equal to:

$$\frac{d\mathbf{R}}{d\boldsymbol{\theta}^s} = \frac{d\mathbf{h}^s}{d\boldsymbol{\theta}^s} - \Delta t \frac{d\mathbf{f}^s}{d\boldsymbol{\theta}^s} \quad (\text{III.C.2.17})$$

where \mathbf{h}^s is the following vector:

$$\mathbf{h}^s = \mathbf{M}^s (\boldsymbol{\theta}^s - \boldsymbol{\theta}^{s-1}) + \Delta t \mathbf{K}^s \boldsymbol{\theta}^s \quad (\text{III.C.2.18})$$

In the following sections, the components of the matrix $\frac{d\mathbf{R}}{d\boldsymbol{\theta}^s}$ are discussed.

III.C.2.4.3 Model of the Energy Provided by the Laser

The energy of the laser is modeled as a flux (or Neumann) boundary condition that acts on the top boundary of the domain Ω . This work uses the approach in Ref. [25] to calculate the corresponding heat flux. The function $I(x, z)$ [W/mm²] describes the energy distribution of the laser on the plane XZ , parallel to the substrate surface.

Let Ω^e be an FE element whose edge $\partial\Omega^e$ is at the top boundary. Let $\partial\Omega_{\text{proj}}^e$ be the projection of $\partial\Omega^e$ onto the plane XZ . Let R^e be the extrusion in direction Z , with thickness Δz , of $\partial\Omega_{\text{proj}}^e$ (see Fig. III.C.2.3). The input power P^e [W] and the corresponding heat flux \bar{q}_l^e [W/mm²] at $\partial\Omega^e$ are

$$P^e = \int_{R^e} I(x, z) dA; \quad \bar{q}_l^e = \frac{1}{\Delta z} \frac{P^e}{|\partial\Omega_{\text{proj}}^e|}. \quad (\text{III.C.2.19})$$

Since the laser moves in Z direction, the laser intensity function I is also a function of time. Therefore, the heat flux over each edge must be calculated at every time step of the simulation.

The present work uses a Gaussian laser energy distribution:

$$I(x, z, t) = \frac{2\lambda P_L}{\pi R_L^2} \exp\left(-\frac{-2((x - P_x(t))^2 + (z - P_z(t))^2)}{R_L^2}\right) \quad (\text{III.C.2.20})$$

where P_L is the laser power, λ is the laser absorption efficiency, R_L is the laser beam radius and $\mathbf{P} = (P_x, P_y)$ is the laser position. Fig. III.C.2.3 shows a graphical representation of the process to compute the input heat flux associated to the energy provided by the laser.

Recalling Eqs. III.C.2.9 and III.C.2.10:

$$\begin{aligned} \frac{\partial^e h_a^s}{\partial^e \theta_c^s} &= {}^e \mathbb{M}_{ac}^s + \sum_{b=1}^3 \left(\int_{\Omega^e} \frac{\partial(\rho C)}{\partial^e \theta_c^s} N_a N_b \Delta z dA \right) ({}^e \theta_b^s - {}^e \theta_b^{s-1}) + \\ &\quad \Delta t \left({}^e \mathbb{K}_{ac}^s + \sum_{b=1}^3 \left(\int_{\Omega^e} \sum_{i=1}^2 \frac{\partial N_a}{\partial x_i} \frac{\partial \kappa}{\partial^e \theta_c^s} \frac{\partial N_b}{\partial x_i} \Delta z dA \right) {}^e \theta_b^s \right) \end{aligned} \quad (\text{III.C.2.23})$$

$$\begin{aligned} &= {}^e \mathbb{M}_{ac}^s + \sum_{b=1}^3 \left(\int_{\Omega^e} \left(\rho \frac{\partial C}{\partial T} + C \frac{\partial \rho}{\partial T} \right) N_a N_b N_c \Delta z dA \right) ({}^e \theta_b^s - {}^e \theta_b^{s-1}) + \\ &\quad \Delta t \left({}^e \mathbb{K}_{ac}^s + \sum_{b=1}^3 \left(\int_{\Omega^e} \sum_{i=1}^2 \frac{\partial N_a}{\partial x_i} \frac{\partial \kappa}{\partial T} N_c \frac{\partial N_b}{\partial x_i} \Delta z dA \right) {}^e \theta_b^s \right) \end{aligned} \quad (\text{III.C.2.24})$$

The present work uses numerical integration (Gauss quadrature) to evaluate the integrals described above.

III.C.2.4.5 Phase Change

The present work uses the equivalent specific heat method [15] to model the change of state (from solid to liquid and vice-versa). In this approach, the phase change is modeled by modifying the specific heat of the material C . The new function is called the *equivalent* specific heat C_{eq} and it must add the energy of the latent heat of fusion L [J/kg] into the specific heat of the material in the temperature range $T \in [T_s, T_l]$ where the phase change occurs.

This work uses the following equivalent specific heat C_{eq} [109] function:

$$C_{eq}(T) = C(T) + \frac{2L}{\sqrt{\pi} \Delta T} \exp \left(- \left(\frac{T - T_m}{\Delta T / 2} \right)^2 \right) \quad (\text{III.C.2.25})$$

where $T_m = (T_s + T_l)/2$ and $\Delta T = T_l - T_s$

III.C.2.4.6 Convection and Radiation Heat Losses

This work considers heat losses due to convection and radiation during the cladding process. Both radiation and convection are included into the model as flux (Neumann) boundary conditions. The regions of the domain subjected to heat loss considerations are the top, left- and right-hand sides of the domain.

Given the convection coefficient h_c and the ambient temperature T_∞ , the convection heat loss is accounted as $\bar{q}_{conv} = h_c (T - T_\infty)$. Using the interpolation of the temperature (Eq. III.C.2.11) along the edge with flux boundary condition:

$$\bar{q}_{conv} = h_c \left(\sum_{b=1}^2 N_b^q(\mathbf{x}) {}^e \theta_b(t) - T_\infty \right), \quad (\text{III.C.2.26})$$

Given the thermal emissivity ε and the Stefan-Boltzmann constant $\sigma \approx 5.67 \times 10^{-8}$ [W/(m² K⁴)], the radiation heat loss is represented by $\bar{q}_{rad} = \varepsilon \sigma (T^4 - T_\infty^4)$. Applying Eq. III.C.2.11 for the

temperature interpolation:

$$\bar{q}_{\text{rad}} = \varepsilon\sigma \left(\left(\sum_{b=1}^2 N_b^q(\mathbf{x})^e \theta_b(t) \right)^4 - T_\infty^4 \right), \quad (\text{III.C.2.27})$$

To ease the readability of the Eqs. III.C.2.28-III.C.2.31, one may drop the indices e and s of the components of the vector of nodal temperatures ${}^e\boldsymbol{\theta}^s = [\theta_1, \theta_2]^T$ of the edge $\partial\Omega_q^e$ subjected to radiation and convection.

Eq. III.C.2.13 is applied to calculate the local force vector associated to the convection and radiation boundary conditions:

$${}^e\mathbf{f}_{\text{conv}}^s = \frac{\Delta z |\partial\Omega_q^e| h_c}{6} \begin{bmatrix} 2 & 1 \\ 1 & 2 \end{bmatrix} \begin{bmatrix} \theta_1 \\ \theta_2 \end{bmatrix} - \frac{\Delta z |\partial\Omega_q^e| h_c}{2} \begin{bmatrix} T_\infty \\ T_\infty \end{bmatrix} \quad (\text{III.C.2.28})$$

$${}^e\mathbf{f}_{\text{rad}}^s = \frac{\Delta z |\partial\Omega_q^e| \varepsilon\sigma}{30} \begin{bmatrix} 5 & 4 & 3 & 2 & 1 \\ 1 & 2 & 3 & 4 & 5 \end{bmatrix} \begin{bmatrix} \theta_1^4 \\ \theta_1^3\theta_2 \\ \theta_1^2\theta_2^2 \\ \theta_1\theta_2^3 \\ \theta_2^4 \end{bmatrix} - \frac{\Delta z |\partial\Omega_q^e| h_c}{2} \begin{bmatrix} T_\infty^4 \\ T_\infty^4 \end{bmatrix} \quad (\text{III.C.2.29})$$

The contributions of the radiation and convection to the local tangent matrix are:

$$\frac{d{}^e\mathbf{f}_{\text{conv}}^s}{d{}^e\boldsymbol{\theta}^s} = \frac{\Delta z |\partial\Omega_q^e| h_c}{6} \begin{bmatrix} 2 & 1 \\ 1 & 2 \end{bmatrix} \quad (\text{III.C.2.30})$$

$$\frac{d{}^e\mathbf{f}_{\text{rad}}^s}{d{}^e\boldsymbol{\theta}^s} = \frac{\Delta z |\partial\Omega_q^e| \varepsilon\sigma}{30} \begin{bmatrix} 5 & 4 & 3 & 2 & 1 \\ 1 & 2 & 3 & 4 & 5 \end{bmatrix} \begin{bmatrix} 4\theta_1^3 & 0 \\ 3\theta_1^2\theta_2 & \theta_1^3 \\ 2\theta_1\theta_2^2 & 2\theta_1^2\theta_2 \\ \theta_2^3 & 3\theta_1\theta_2^2 \\ 0 & 4\theta_2^3 \end{bmatrix} \quad (\text{III.C.2.31})$$

where $|\partial\Omega_q^e|$ is the length of the edge.

III.C.2.4.7 Material Deposition

During the deposition stage, the shape of the bead is induced by the distribution of powder particles delivered by the nozzle. The function $f(x, z, t)$ [kg/(mm² s)] represents the powder particle density projected by the nozzle on top of the substrate. The present model assumes f follows a Gaussian distribution:

$$f(x, z, t) = \frac{2\mu}{\pi R_L^2} \exp \left(\frac{-2 \left((x - P_x(t))^2 + (z - P_z(t))^2 \right)}{R_L^2} \right) \quad (\text{III.C.2.32})$$

where μ is the material flow rate [kg/s] and $\mathbf{P}(t) = (P_x(t), P_z(t))$ is the laser position at time t .

The height H [mm] at time t is given by:

$$H(x, z, t) = \frac{1}{\rho_p} \int_0^t f(x, z, \xi) d\xi. \quad (\text{III.C.2.33})$$

where ρ_p is the density of the cladding material

Given Eq. III.C.2.33, the height grow rate is obtained:

$$\frac{\partial H(x, z, t)}{\partial t} = \frac{1}{\rho_p} f(x, z, t) \quad (\text{III.C.2.34})$$

Eq. III.C.2.34 approximates the height change ΔH for the given time increment Δt . Material is added if the temperature on the top boundary is higher than the melting point of the deposited material.

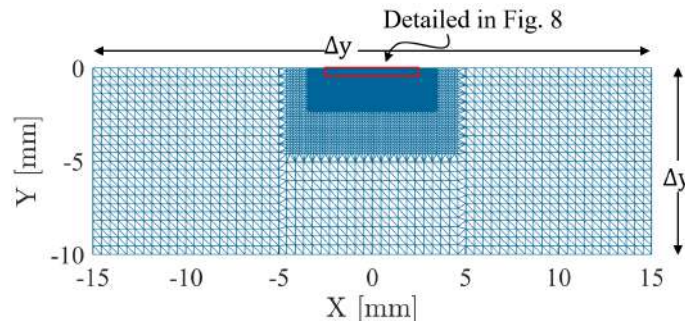


Figure III.C.2.4: FEA mesh of the substrate.

III.C.2.4.8 Remeshing Strategy

In the implementation reported, there are two meshes: substrate mesh and bead mesh. The substrate mesh remains constant with respect to the time evolution. However, the substrate mesh varies with respect to the space. The mesh is finer in the neighborhoods of the laser impact point (Fig. III.C.2.4).

The bead mesh, on the other hand, must be updated at every time step. Fig. III.C.2.5 shows the proposed procedure to conduct the bead remeshing. A description of this procedure follows:

1. **Calculation of the bead grow:** Let $\mathbf{X}^{\text{top}} = \{x^1, x^2, \dots, x^T\}$, $x^k \in \mathbb{R}$, be the x-coordinates of the FEA nodes on top of the substrate (see Fig. III.C.2.6(a)). Eq. III.C.2.34 is used to calculate the height grow ΔH at $z = 0$ for every x^k ($k = 1, \dots, T$). The information required to execute this step is: (i) the nozzle position $\mathbf{P} = (P_x, P_z)$, (ii) the material feed rate μ [kg/s], (iii) the powder particle distribution function $f(x, z, t)$ [kg/(m² s)], (iv) the density of the powder material ρ_p [kg/m³] and (v) the time increment Δt [s].
2. **Calculation of the top boundary of the bead:** Let $M_i = (V_i, T_i)$, with V_i as the set of nodes and T_i as the set of triangles, be the bead mesh at time step i . Given the mesh M_i and the height grow ΔH , the piecewise linear (PL) curve $\mathbf{B} = [\mathbf{b}^1, \mathbf{b}^2, \dots, \mathbf{b}^M]$, $\mathbf{b}^k \in \mathbb{R}^2$, that describes the top boundary of the new mesh is calculated. The x-coordinate of every vertex $\mathbf{b}^k = (b_x^k, b_y^k) \in \mathbf{B}$ belongs to \mathbf{X}^{top} ($b_x^k \in \mathbf{X}^{\text{top}}$). Fig. III.C.2.6(b) shows an example of the resulting PL curve \mathbf{B} .

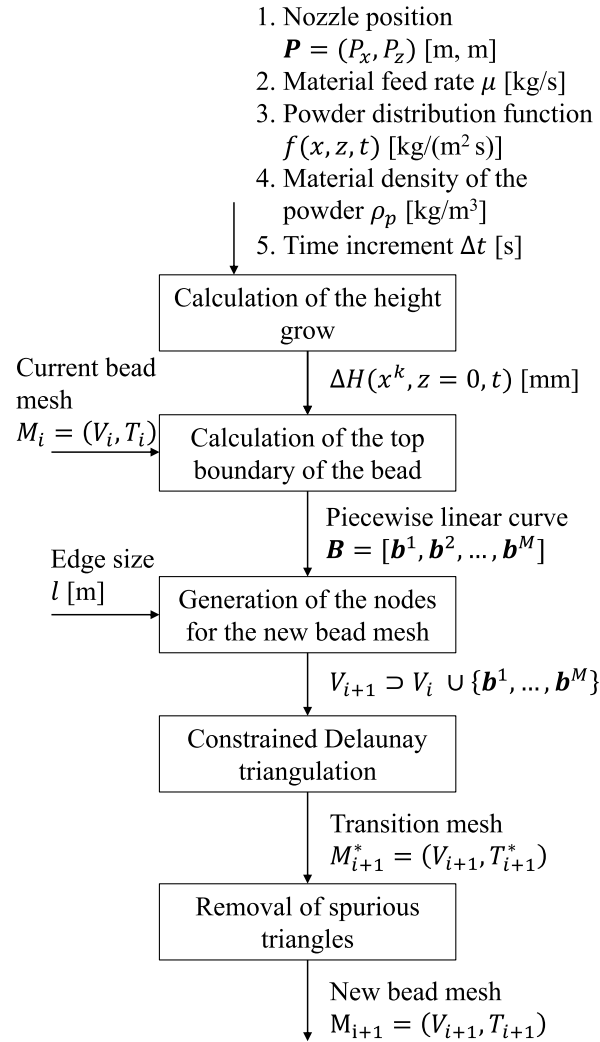


Figure III.C.2.5: Remeshing strategy. Workflow for the generation of the bead mesh at every time step.

3. **Generation of the FEA nodes:** Let V_{i+1} denote the set of nodes of the bead mesh at time step $i + 1$. Firstly, V_{i+1} contains the nodes of the previous mesh V_i and the vertices of \mathbf{B} :

$$V_{i+1} \supset V_i \cup \{\mathbf{b}^1, \dots, \mathbf{b}^M\}. \quad (\text{III.C.2.35})$$

Given the goal edge length l [m], new nodes are added to V_{i+1} when: (i) the height grow is large ($\Delta H(x^k, z = 0) > l$) and (ii) the segments of \mathbf{B} are long ($\|\mathbf{b}^{k+1} - \mathbf{b}^k\| > l$), as shown in Fig. III.C.2.6(b).

4. **Mesh generation:** A mesh $M_{i+1}^* = (V_{i+1}, T_{i+1}^*)$ is generated using constrained Delaunay triangulation [26, 154]. The constraints of the triangulation are given by the edges of the bead boundary \mathbf{B} . The triangulation may contain spurious triangles that do not belong to the bead (see Fig. III.C.2.6(c)). These spurious triangles are removed to produce the bead mesh for time step $i + 1$: $M_{i+1} = (V_{i+1}, T_{i+1})$, $T_{i+1} \subset T_{i+1}^*$, as shown in Fig. III.C.2.6(d).

In this work, triangular elements are preferred over other topologies (e.g. quadrilateral) because they straightforwardly adapt to the geometry of the growing bead. The quadrangular elements present singularities when 2 nodes coincide, which is unavoidable in corners whose geometry –topology is triangular.

III.C.2.4.8.1 Evaluation of the Remeshing Strategy

The time complexity of the proposed remeshing method is dictated by the time complexity of the Delaunay triangulation. The time complexity of the Delaunay triangulation is $\mathcal{O}(N \log N)$ [57, 163], where N is the number of nodes in the triangulation. In this case, N corresponds to the number of nodes in the bead mesh. Table III.C.2.1 presents the time complexity of other relevant methods used for 2D FEA remeshing: (i) advancing-front methods, (ii) Delaunay-based methods, (iii) Laplacian smoothing and (iv) spring-based smoothing. Methods (i)-(ii) are pure meshing procedures while methods (iii)-(iv) are smoothing procedures used in the context of remeshing.

The proposed remeshing method has the same time complexity ($\mathcal{O}(N \log N)$) as the other two pure meshing methods. Smoothing methods, on the other hand, have lower time complexity ($\mathcal{O}(N)$) but produce lower quality meshes [57].

The proposed approach avoids nodes removal or node repositioning. It is advantageous compared to other remeshing approaches because (i) it is confined to the bead domain alone and (ii) the temperature field must not be re-computed when the bead mesh is updated. Since nodes are not repositioned, the representation of the deposited material requires additional nodes. Therefore, the number of nodes in the bead mesh increases at every time step, which leads to higher simulation time at every time step.

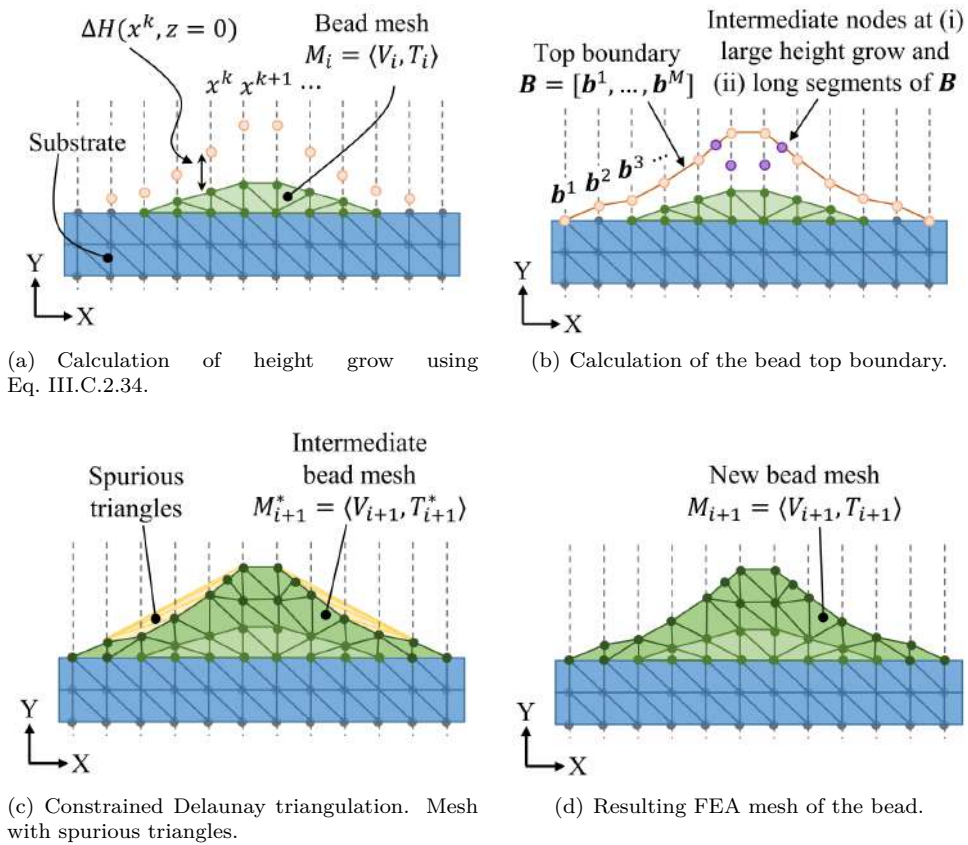


Figure III.C.2.6: Graphical description of the stages of the remeshing strategy.

Table III.C.2.1: Meshing and remeshing methods. Time complexity.

Method	Time complexity	Advantages	Limitations
Proposed method	$\mathcal{O}(N \log N)$ [57, 163]	(i) Good mesh quality and (ii) avoids temperature re-computing	High computational cost
Advancing-front method	$\mathcal{O}(N \log N)$ [57]	Very good mesh quality	Requires temperature re-computing
Delaunay-based method	$\mathcal{O}(N \log N)$ [57]	Very good mesh quality	Requires temperature re-computing
Laplacian smoothing method	$\mathcal{O}(N)$ [169]	Computational efficient	(i) Mesh quality is compromised and (ii) requires temperature re-computing
Spring-based smoothing method	$\mathcal{O}(N)$ [9]	Computational efficient	(i) Mesh quality is compromised and (ii) requires temperature re-computing

III.C.2.4.9 Material Properties for the Computational Simulations

Ref. [35] executed several LMD experiments with an *IPG Photonics YLS-6000* fiber laser of wavelength 900 nm. Ref. [35] used *S355* carbon steel as substrate and *AISI 316L* stainless steel as cladding material. These same materials were used for the numerical simulations. The physical properties of *S355* and *AISI 316L* are listed in Table III.C.2.2. The thermal conductivity κ and specific heat C are considered as functions of the temperature [117, 211], as shown in Figs. III.C.2.7(a) and III.C.2.7(b). The equivalent specific heat is calculated using Eq. III.C.2.25. The resulting functions are shown in Fig. III.C.2.7(c). In order to compare the numerical results with the experimental results in Ref. [35], the simulations use the same domain size and process parameters reported in [35].

Table III.C.2.2: Material properties of the substrate material (*S355*) [211] and cladding material (*AISI 316L*) [117] used in the numerical simulations.

Property	<i>S355</i>	<i>AISI 316L</i>
Density ρ	7840 kg/m ³	7950 kg/m ³
Thermal conductivity κ	See Fig. III.C.2.7(a)	See Fig. III.C.2.7(a)
Specific heat C_p	See Fig. III.C.2.7(b)	See Fig. III.C.2.7(b)
Latent heat of fusion L	2.7×10^4 J/K	2.7×10^4 J/K
Solidus temperature T_s	1673 K	1658 K
Liquidus temperature T_l	1778 K	1723 K
Melting point T_m	1725.5 K	1690.5 K

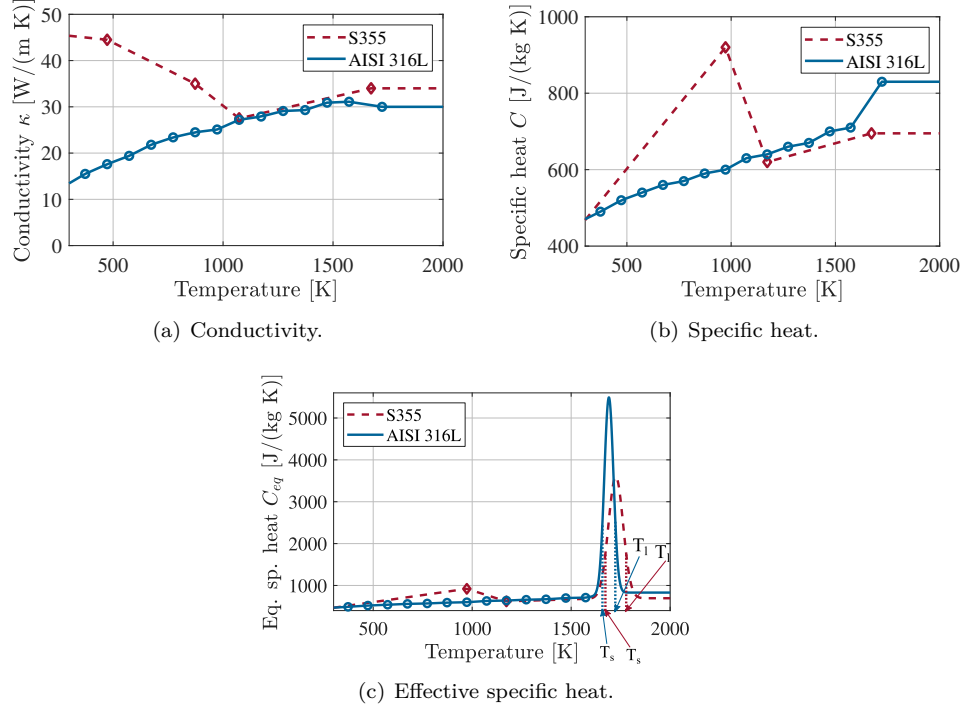


Figure III.C.2.7: Material properties of the substrate material (*S355*) and cladding material (*AISI 316L*). Figures built using the data in References [117, 211].

III.C.2.5 Results

Regarding LMD simulation, the present implementation computes the time history of bead geometry and temperature field as well as the substrate temperature field. These computations are carried out in a substrate cross cut $\Delta x \times \Delta y$ (with thickness Δz) which is normal to the laser velocity (v_z). The powder feed μ , laser power P_L and laser cruise speed v_z are constant during the simulation. The parameters used in the numerical simulation are listed in Table III.C.2.3. The time increment Δt between time steps was constant during the simulation. This parameter was empirically set to guarantee the convergence of the Newton-Raphson method, and to avoid abrupt changes in the geometry and temperature of the domain.

Table III.C.2.3: Domain size and process parameters used for the numerical simulations.

Parameter	Value
Width (size in X) of the substrate Δx	30 mm
Height (size in Y) of the substrate Δy	10 mm
Thickness of the domain Δz	4.6 mm
Laser power P_L	2800 W
Laser absorption efficiency λ	0.6
Laser radius R_L	2.3 mm
Laser speed v_z	10 mm/s
Powder flow rate μ	0.3×10^{-3} kg/s
Initial position of the laser	$[0, 0, -4.6]$
Ambient temperature T_∞	300 K
Convection coefficient h_c	20 W/(m ² K)
Emissivity ε	0.5
Total simulation time	2.44 s
Number of time steps	90
Time increment (Δt)	0.027 s

Fig. III.C.2.4 displays the FEA mesh of the substrate domain, which remained constant along the time-axis simulation. The mesh presents increased levels of detail in the neighborhoods receiving the metal powder and the laser impact. Preliminary simulations without considering material addition were conducted to determine the size of the FEA elements. The substrate mesh used for LMD simulation shown in Fig. III.C.2.4 has 17213 triangular elements. The average edge length in the most detailed zone is 0.05 mm, which is in concordance with the values reported in the literature [186, 200]. The aspect ratio is lower than 2 for 98% of the triangles, and lower than 3 for 100% of the triangles. Thus, this substrate mesh presents very good quality.

III.C.2.5.1 Computational Results

The implementation of the FEM, Newton-Raphson and material deposition model was executed in MATLAB. Figs. III.C.2.8(a)-III.C.2.8(f) show the evolution of the bead geometry in the time interval that the laser spot requires to engage, to heat and to leave behind the relevant cross section. In this simulation, the deposition takes place from the time in which the substrate reaches the material melting point (circa $t = 12\Delta$).

Fig. III.C.2.8(f) depicts the final shape of the domain. The FEA mesh of the final domain has 21862 triangular elements. Almost all the triangles in the FEA mesh had aspect ratio lower than 3 at all times in the simulation. In particular, in the final mesh 98.20% and 99.97% of the triangles have aspect ratio lower than 2 and 3, respectively.

Fig. III.C.2.8(f) shows that the final bead height and width are 1.22 mm and 3.68 mm, respectively. For a physical experiment with the same materials and conditions of this simulation, Ref. [35] reported a bead height of 1.067 mm and a bead width of 4.697 mm. Fig. III.C.2.9 shows a graphical scheme of the geometrical involved in the comparison between the numerical and experimental results in [35]. The relative errors between the simulated and the experimental [35] bead height and width are 14.4% and 21.7%, respectively.

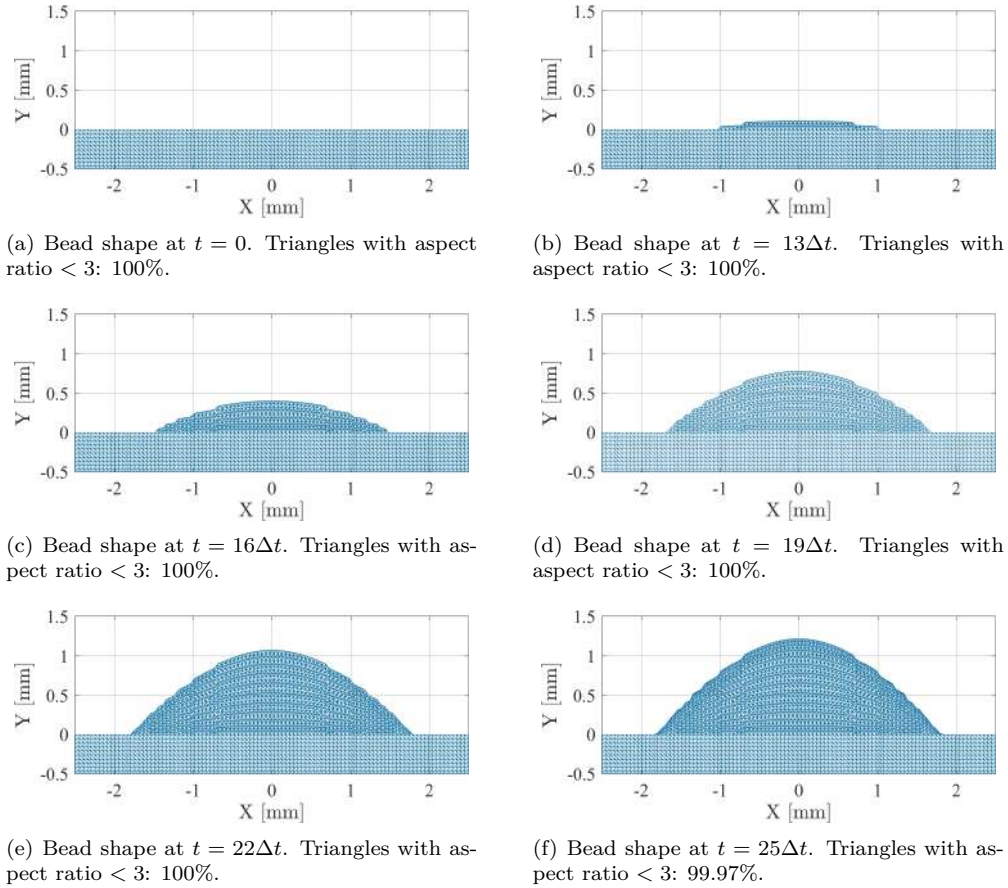


Figure III.C.2.8: Evolution of the shape of the bead during deposition. Finer mesh resolution in the deposition region.

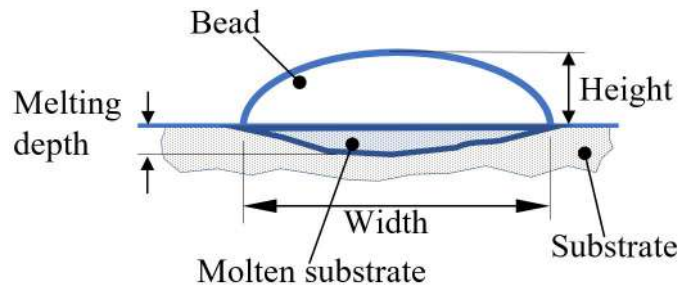


Figure III.C.2.9: Sketch on the semantics of the geometrical parameters in Ref. [35]. (Contains typical names used in the related literature).

Figs. III.C.2.10(a)-III.C.2.10(i) depict the substrate and bead temperature fields. While the laser

energy is being delivered at this particular cross section, the highest temperature appears at the top of the bead. This trend is expected, as this neighborhood directly receives the molten metal and the laser energy. Figs. III.C.2.10(f)-III.C.2.10(i) correspond to the metal dispenser nozzle no longer delivering energy or material at this particular cross section. Between $t = 25\Delta t$ (Fig. III.C.2.10(f)) and $t = 34\Delta t$ (Fig. III.C.2.10(i)), the temperature of the bead decreases whereas the temperature in the substrate does not suffer large variations.

Fig. III.C.2.11 displays the temperature history at four locations: (1) the top point of the bead, (2) the top of the substrate, (3) 0.3 mm depth in the substrate and (4) 0.6 mm depth in the substrate. The top of the bead and the top of the substrate coincide until the start of the deposition. The temperature of the substrate increases rapidly while it interacts directly with the laser. It stabilizes during the deposition stage and decreases once the bead cools down. The results of the simulation show that 0.6 mm is the largest depth at which the substrate melts. Experimentally, Ref. [12] reports a melting depth of 0.36 mm. This discrepancy is discussed in Section III.C.2.5.2.

The temperature of the top of the bead increases in the presence of the laser and quickly decreases in the absence of it. The heat in the bead dissipates due to (1) conduction to the substrate, and (2) radiation and convection. The temperature plateau registered at the top of the bead around $T_m = 1690.5$ K corresponds to a phase change. An amount of energy is released by the system due to the solidification of the powder while temperature remains constant. The maximum temperature is close to 4000 K. Other numerical simulations report similar temperature values for stainless steel under comparable ratios of power per powder deposition rate [200].

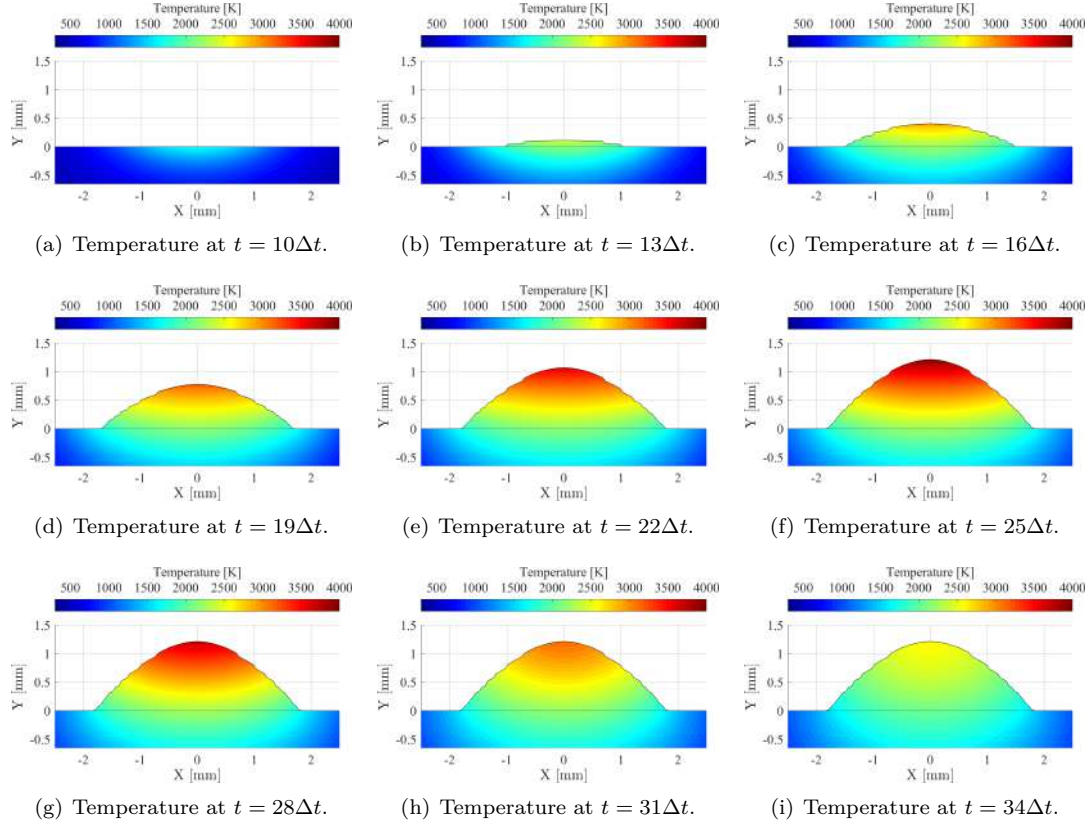


Figure III.C.2.10: Temperature field of the cladding zone during deposition.

III.C.2.5.2 Discussion

This section discusses the discrepancies between the numerical predictions of the non-linear 2.5D implementation reported here and experimental work by other investigators. The comparison is carried out with respect to Ref. [35]. It represents, with this manuscript, two prongs of a common initiative.

An important remark about experimental measurements in LMD is that direct temperature measurement is not feasible within the bead and substrate and very difficult on the bead surface at the melting time. Experimental investigations resort to the after-process cross-sectioning of the bead and substrate and indirect inference of the temperatures reached by observation of the metal micro-structures [30, 183].

There are several experimental effects that are not accounted for in the in-house non-linear FEA implementation:

1. An important portion (near 50%) of the powder metal delivered by the nozzle and heated by the laser does not reach the bead and deforms the space distribution of the powder and

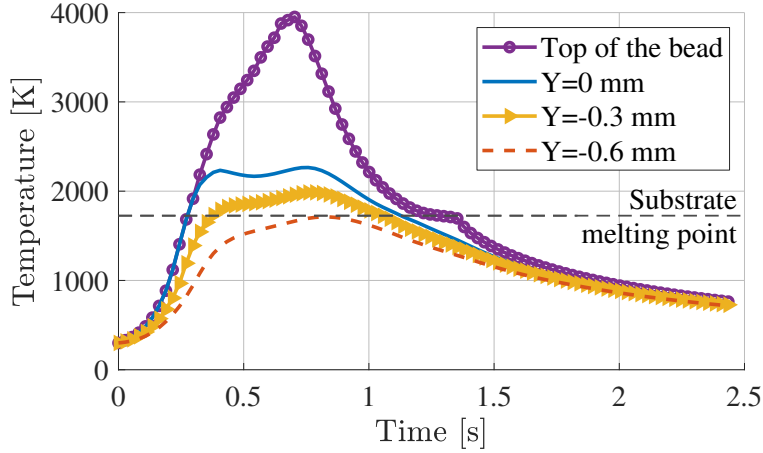


Figure III.C.2.11: Temperature history at the top of the bead and substrate depths 0 mm, 0.3 mm and 0.6 mm.

power input [143, 200]. The present implementation does not consider this effect, therefore over-estimating the power input in the energy balance. A consequence of this neglect is the over-estimation of molten depth (67% error) and bead temperature.

2. A significant portion of the laser power is lost to the environment by direct radiation, convection, and reflection by the powder.
3. Metal powder vaporization produces mass and energy losses. Proposals have been published [11, 73, 167] to account for such losses in LMD and AM (e.g. powder bed fusion). Required parameters include vaporization rate, boiling point and latent heat of vaporization.
4. Molten powder fluid dynamics transforms part of the thermal energy in fluid friction. Parameters required include molten metal viscosity and surface tension.

The present implementation uses two 2D radial Gaussian distributions, mathematically defined in a plane (x, z) parallel to the substrate surface: (i) laser power and (ii) metal powder distribution. The experiments show that the Gaussian distributions incorrectly emphasize power and powder deliver at the laser axis, thus predicting a sharper deposition (i.e. smaller spot). In reality, the bead height is lower and the bead extent is wider than in the prediction. This result is also influenced by effect (1) above.

The absorption coefficient (λ) in the literature [6, 171, 186] expresses the portion of the laser power actually delivered to the bead-substrate domain. This parameters must be calibrated via experimentation. Likewise, all of the effects mentioned above imply the use of new experimentally calibrated parameters. This manuscript does not intend to contribute in this realm.

Table III.C.2.4 summarizes the numerical and experimental results for the bead height, bead width and melting depth. The relative error in Table III.C.2.4 measures the deviation of the numerical result with respect to the experimental result. The error in the estimation of the melting depth is related to an over-estimation of the temperature field during simulation. The causes for the temperature over-estimation and bead width under-estimation are the ones discussed above.

Table III.C.2.4: Comparison between the numerical simulation and the experimental results reported in Ref. [35].

Parameter	Numerical result	Experimental result	Relative error
Bead height	1.22 mm	3.68 mm	14.4%
Bead width	1.067 mm	4.697 mm	21.7%
Melting depth	0.6 mm	0.36 mm	66.7%

III.C.2.6 Conclusions

This manuscript presents the implementation of a nonlinear thermal simulation to model the Laser Metal Deposition (LMD) process. The implementation considers temperature-dependent material properties, phase change, radiation and convection. The energy of the laser is represented as an energy flux boundary condition. The manuscript details the mathematical derivation of the FEM implementation. The nonlinear iterations inherent to each particular time step are executed using the Newton-Raphson method. The nonlinear FEM implementation is written for triangular 2D-plus-thickness elements. The LMD model is dictated by the delivery rate of powder (feed rate μ [kg/s]) and its associated Gaussian function of the radii from the nozzle axis. The model does not assume a particular geometry (parabolic, circular, sinusoidal, etc.) for the bead cross-section, as some previous works do.

Computer simulations are conducted using material and process parameters whose experimental counterpart is already reported in Ref. [35]. The results show reasonable accuracy to predict bead geometry (width error 15%, height error 22%). The model over-estimates the temperature at the domain and the maximal depth, in the substrate, at which melting occurs. The absorption coefficient (λ), which expresses the portion of the laser power input to the bead-substrate domain requires further investigation. It is affected by phenomena not yet understood or even identified. It is not the intention or capacity of this manuscript to contribute in this realm. Future work is also needed to account for the particle (thermo) dynamics over the substrate, responsible for a significant material and energy waste.

Funding

This work has received funding from the Eusko Jauriaritza/Basque Government under the grants KK-2018/00115 (ADDISEND) and KK-2018/00071 (LANGILEOK).

III.D

Process Planning for Laser Metal Deposition

III.D.1

Generation of 2.5D Deposition Strategies for LMD-based Additive Manufacturing

Diego Montoya-Zapata^{1,2}, Carles Creus², Igor Ortiz³, Piera Alvarez³, Aitor Moreno², Jorge Posada² and Oscar Ruiz-Salguero¹

¹Laboratory of CAD CAM CAE, Universidad EAFIT, Cra 49 no 7-sur-50, Medellín 050022, Colombia

²Vicomtech Foundation, Basque Research and Technology Alliance (BRTA), Mikeletegi 57, Donostia-San Sebastian 20009, Spain

³Ikerkune A.I.E., San Antolin 3, 20870 Elgoibar, Spain



III.D.1.1 Context

Diego Montoya-Zapata, Carles Creus, Igor Ortiz, Piera Alvarez, Aitor Moreno, Jorge Posada, Oscar Ruiz-Salguero. Generation of 2.5D Deposition Strategies for LMD-based Additive Manufacturing. (2020). Procedia Computer Science. 180, p. 280-289. E-ISSN:1877-0509. International Conference on Industry 4.0 and Smart Manufacturing (ISM 2020). November 23-25, Hagenberg,

Austria. (Virtual attendance). URL: <https://www.sciencedirect.com/science/article/pii/S1877050921002052>. DOI: <https://doi.org/10.1016/j.procs.2021.01.165>

Indexing: SCOPUS, INSPEC

Abstract

Additive manufacturing is a key technology of Industry 4.0. In the context of Laser Metal Deposition (LMD), the problem of automating the generation of the layer-by-layer deposition strategies is relevant because the laser path pattern and the process parameters determine the mechanical quality of the resulting part and the efficiency of the process. Many of the existing approaches rely on path planning strategies created for subtractive manufacturing. However, these techniques generate path patterns not suitable for LMD. This manuscript presents deposition strategies which are specific for LMD processes, including the laser path and the process parameters at selected control points. This manuscript considers diverse infill patterns for general polygonal regions. This manuscript also reports the implementation of a 2D region avoidance algorithm, used to reposition the laser head between regions and between layers. These transitions are important because current hardware maintains the material feeding while the laser is OFF. Our implementation is validated by the fabrication and verification of actual metallic parts using our algorithms in an LMD process. Future work is required on optimization of material savings and overall process performance.

Keywords: additive manufacturing, path-planning, laser cladding, Industry 4.0.

Glossary

AM	Additive Manufacturing
LMD	Laser Metal Deposition
Laser	Source of the LMD system that provides the energy for the melting process
Nozzle	Spout component of the LMD system that deposits the metal powder onto the build area
2.5D LMD	Laser Metal Deposition process in which the machine effector is able to translate in three linear axes but can perform the melting process only in two axes
$\Omega \subset \mathbb{R}^2$	Polygonal region in \mathbb{R}^2 which constitutes a 2D slice of the work-piece
$\partial\Omega \subset \mathbb{R}^2$	Subset of \mathbb{R}^2 that represents the boundary of Ω
$\{L_i\}$	Family of equidistant parallel lines in \mathbb{R}^2 , $L_i \subset \mathbb{R}^2$, $i \in \mathbb{Z}$
$p_i \in \mathbb{R}^2$	Point that belongs to the line L_i
$\hat{u} \in \mathbb{R}^2$	Unitary vector that gives the direction of the family of lines $\{L_i\}$ (director vector)
$\hat{n} \in \mathbb{R}^2$	Unitary vector orthogonal to the family of lines $\{L_i\}$

$S_i \subset \mathbb{R}^2$	Set of segments that results from the intersection between the polygonal region Ω and the line L_i
$S \subset \mathbb{R}^2$	Set of segments that results from the intersection between the polygonal region Ω and the family of lines $\{L_i\}$
$\overline{P_1 P_2}$	Segment with endpoints P_1 and P_2

III.D.1.2 Introduction

The Industry 4.0 paradigm has revolutionized the industrial ecosystem by integrating smart systems in the production lines. Among all these new technologies, additive manufacturing (AM) has emerged as a crucial one, as it enables the fabrication of complex parts and the use of new materials [45, 145]. It also allows new production scenarios for personalized, lot-1 series, and a very high flexibility to produce quite different components with the same system. In particular, Laser Metal Deposition (LMD) plays a major role in the industry because of its applications in the reinforcement, reconditioning and repairing of high value components or the fabrication of industrial parts with complex and novel structures [62]. However, CAD-CAM design and other digital tools are still oriented to traditional manufacturing and do not match the fast-paced technical evolution of AM and LMD.

In this manuscript, we present a methodology for the generation of path planning for LMD in 2.5D, i.e. we consider that the machine effector translates in three linear axes but can execute the cladding process only in two axes. Particularly, due to typical hardware limitations in LMD real-world systems, we consider the case in which the metal dispensing through the nozzle is not interrupted at any time, while the other process parameters (e.g. process speed and laser power) can vary between metal melting stages. For this reason, we develop a 2D region avoidance algorithm to execute the transition movements, so that unmelted metal powder does not adhere on the surface of the part that is being built when the laser is OFF. The methodology is evaluated via physical experimentation using a fiber laser *IPG YLS-6000* and stainless steel *316L* as powder material.

We present in Section III.D.1.3 a systematic review of the related work. We describe the approach for the generation of path planning for 2.5D LMD and display the results of its implementation in Sections III.D.1.4 and III.D.1.5, respectively. Finally, we conclude the manuscript and make suggestions for further work in Section III.D.1.6.

III.D.1.3 Literature Review

III.D.1.3.1 Path Planning in Laser Metal Deposition

Path planning in LMD tackles two problems in the manufacturing process: 1) the generation of the trajectory that the laser must follow and 2) the determination of the process parameters (e.g. laser power, process speed, powder flow) at every point of the trajectory.

The temperature history has a significant impact in the mechanical and structural properties of the built parts manufactured by LMD. In this context, path planning plays a major role in LMD, since the temperature history is intrinsically linked to the tool trajectory and process parameters [77, 149].

Path planning strategies in AM are mainly based on the more mature path planning techniques used for subtractive manufacturing. It is often necessary to adapt these techniques, so that they are

suitable for AM [20, 46]. However, in the context of metal AM, previous research is mainly focused on Wire Arc Additive Manufacturing (WAAM) [46, 47, 95, 116] and few works address LMD [3, 20, 54].

III.D.1.3.1.1 2D Infill Geometries

Ding et al. [46] summarize the principal infill strategies used in the context of AM, namely raster, zig-zag, contour-offset and spiral. Related works propose variations of these four strategies that overcome some difficulties associated with each one. Flemmer et al. [61] propose a zig-zag infill that uses the medial axis of the 2D region instead of straight lines, which reduces the number of turning points. Xiong et al. [198] present a novel infill based on the level-set method that eliminates the voids that appear in traditional contour-offset infill. Ding et al. [46] and Jin et al. [81] consider a hybrid approach in which the contour-offset and zig-zag strategies are used together to reduce the geometrical inaccuracies that may appear when only zig-zag patterns are used.

Other works focus on the solution of particular problems related to the path-planning process. Liu et al. [95], Routhu et al. [155] and Xiong et al. [198] address the problem of material accumulation due to the sharp corners that appear on zig-zag or contour-offset patterns. Ding et al. [46] present a path-planning based on a divide-and-conquer approach by decomposing the polygonal zones in every slice into convex polygons which are simpler to fill. Michel et al. [116] show a solution in which the process parameters can vary in different zones of a continuous path. Thus, an experienced user can configure special process parameters in zones with a challenging geometry. However, far too little attention has been paid to process parameters configuration during path planning. Likewise, apart from Ding et al. [46], there is a general lack of research in the problem of connecting paths in the layer (intra-layer) and between layers (inter-layer).

III.D.1.3.2 Conclusions of the Literature Review

In our literature survey we have found that the path planning for AM is mainly based on subtractive manufacturing strategies. In general terms, subtractive manufacturing strategies are the core of path planning in LMD. However, it is also clear that these techniques should be adapted to meet the constraints of LMD.

We have found active research lines that tackle the particular issues (such as voids appearance and material accumulation in sharp corners) that arise from the direct use of subtractive manufacturing techniques in LMD. However, few studies consider the following two important needs properly: 1) continuous process parameters configuration during deposition and 2) the generation of intra- and inter-layer connections paths that fulfill the requirements of LMD. We present in this article a methodology that explicitly addresses both issues.

III.D.1.4 Methodology

III.D.1.4.1 Workflow of the Generation of Trajectories in 2.5D

In this work, we focus on the generation of the path planning for an LMD system restricted to 2.5D, i.e. the machine effector is able to translate in three linear axes but can perform the deposition process only in two axes. The procedure we follow is divided into four steps (see Fig. III.D.1.1):

1. **Polygon decomposition:** The polygonal domain $\Omega \subset \mathbb{R}^2$ defines the area to be filled. The polygonal domain Ω may contain holes, i.e. areas that should *not* be filled. We decompose Ω into simple polygons and organize them in a tree hierarchy. Fig. III.D.1.1b shows the resulting tree for the polygonal region in Fig. III.D.1.1a. Notice that each simple polygon in this tree can represent either a portion of material to be filled or a hole in its *parent* polygon. The strategy followed implies that in each particular slice (i.e. Z level) we hierarchically decompose the existing polygonal regions. This decomposition allows for the accommodation of polygons with holes that may exist inside other polygons (and so on). This tree-like representation also allows for the inclusion of orientation (clockwise or counter-clockwise) for external or internal polygon borders.
2. **2D infill generation:** The goal at this stage is to obtain a geometrical representation of the path lines in which material has to be deposited. Here, we process those polygons that represent areas to be filled. Fig. III.D.1.1c shows that, when generating the infill for these polygons, we also consider that their holes should be avoided. Further details for the infill pattern implemented in this work are given in Section III.D.1.4.2.
3. **Local 2D trajectory generation:** At this stage, the trajectory of every layer is generated (see Fig. III.D.1.1d). It is important to remark that a trajectory includes both geometrical and processing aspects: process speed, laser power, powder flow and all the other processing variables are defined at this stage. More details on the trajectory generation can be found in Section III.D.1.4.3.
4. **Global trajectory generation:** After the generation of the trajectory for each layer, it is still necessary to connect consecutive layers. Current available hardware maintains the material feeding when the laser is OFF. Unmelted powder particles on the surface of the previously deposited layers can affect the quality of the next layers. Thus, the inter-layer connection paths must avoid the previously deposited layers to prevent the deposition of metal powder on the surface of the building part. More details on how we generated valid connection paths are given in Section III.D.1.4.4. An example of a global trajectory is shown in Fig. III.D.1.1e.

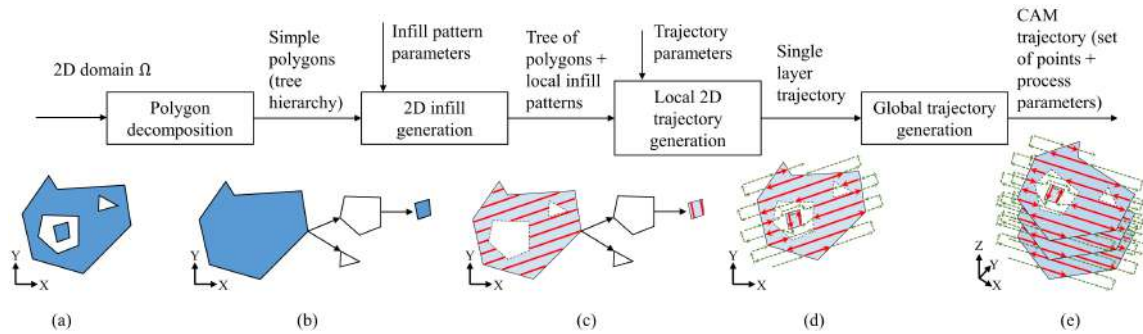


Figure III.D.1.1: Workflow for the path planning for prismatic parts in 2.5D.

III.D.1.4.2 2D Infill Generation

The infill generation marks the places in which the metal powder will be deposited and fused. It means that only *geometrical* considerations are considered at this stage. In this work, we implemented a pattern formed by uniformly separated parallel lines, that is suitable for raster and zig-zag trajectories.

In order to implement the parallel-lines infill pattern, we first solved the following problem: to find the intersection of a line with a 2D polygonal region. The problem was formalized using the traditional *Given-Goal* approach following the main idea in [190].

Given

1. 2D closed and bounded polygonal region $\Omega \subset \mathbb{R}^2$, that may contain holes.
2. A line L_i , with unitary director vector $\hat{u} \in \mathbb{R}^2$.
3. A point $p_i \in \mathbb{R}^2$ that belongs to L_i ($p_i \in L_i$).

Goal

To find the set of segments of L_i that lie inside or on the boundary of Ω , that is, to find the set S_i :

$$S_i = \{(s_0, s_f) : s_0 = p_i + \alpha_0 \hat{u} \in \partial\Omega, s_f = p_i + \alpha_f \hat{u} \in \partial\Omega, p_i + \alpha \hat{u} \in \Omega, \alpha_0 < \alpha < \alpha_f\}.$$

Our implemented pattern is formed by intersecting a family of parallel lines $\{L_j\}$ ($j \in \mathbb{Z}$) with the polygonal region Ω . The set $\{L_j\}$ can be uniquely defined with:

1. a unitary director vector \hat{u} which denotes the direction of the lines,
2. a point p_0 that belongs to L_0 ($p_0 \in L_0$),
3. a parameter $d > 0$ which denotes the separation between the lines.

The resulting set S of the intersection segments between the family of lines $\{L_j\}$ and the polygonal region Ω can be obtained by solving several times the formerly posed problem:

$$S = \bigcup_{j \in \mathbb{Z}} S_j,$$

where $p_j \in L_j$ are obtained using the following expression:

$$p_k = p_0 + (kd)\hat{n},$$

where \hat{n} is orthogonal to \hat{u} and $k \in \mathbb{Z}$. A graphical representation of the involved entities and the expected output is given in Fig. III.D.1.2(a).

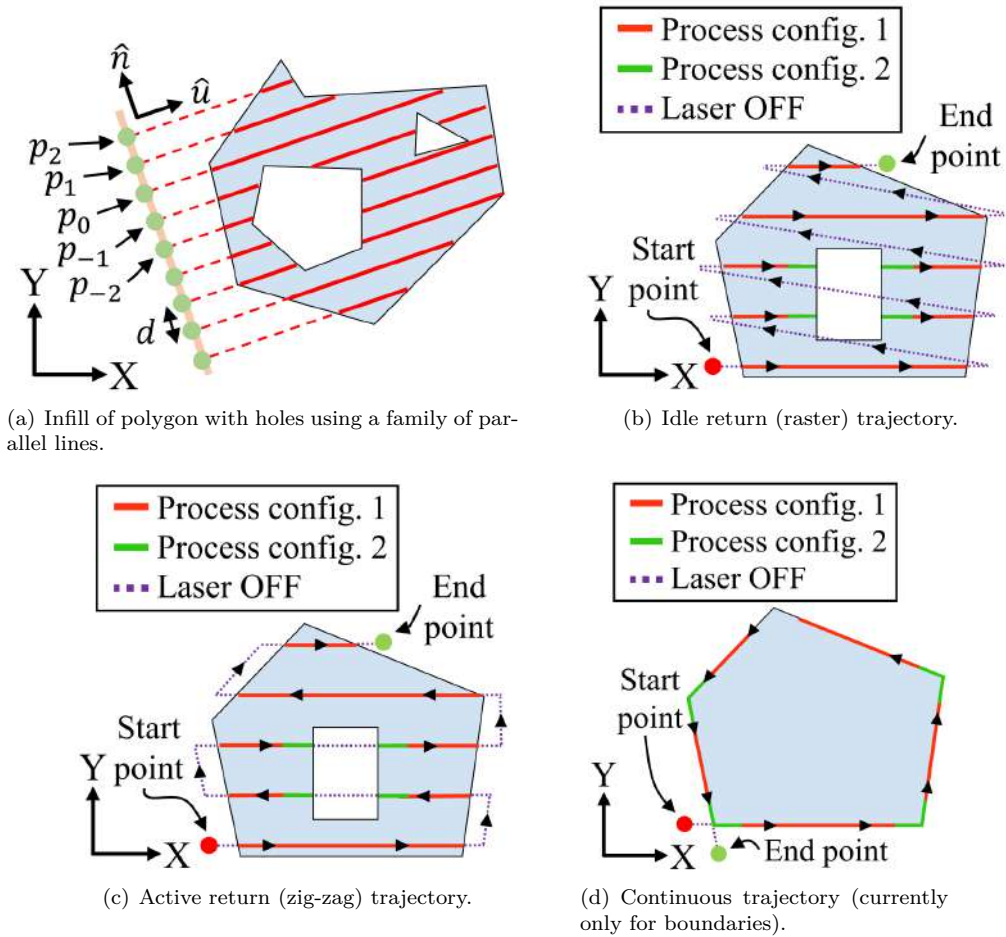


Figure III.D.1.2: Implemented methods for path planning in 2D. (a) Infill generation and (b)–(d) trajectory strategies.

III.D.1.4.3 CAM Trajectory Generation

The path planning encompasses two main aspects: the determination of the path that the tool follows and the process parameters at each point of the defined path. The geometrical aspects of the deposition path are determined in the previous stage of the workflow (infill generation). There are two questions that remain to be solved: 1) how to traverse the generated infill pattern and 2) how to connect the independent regions without affecting the quality of the workpiece.

In comparison with previous works, we dedicated special attention to the second issue, which refers to the movements of the laser head while it is OFF. Since current hardware maintains the material feeding along all the building process, it was important to prevent the deposition of powder particles on top of the surface of the workpiece with the laser OFF. Section III.D.1.4.4 describes our approach to generate them. We refer henceforth to these subsets of the trajectory as *idle* paths.

We implemented three types of trajectories to traverse the infill patterns: 1) raster or idle return, 2) zig-zag or active return, and 3) continuous (only implemented for polygon contours), which are shown in Fig. III.D.1.2. Figs. III.D.1.2(b)– III.D.1.2(d) exhibit red and green regions, which denote different process parameters configurations. The reader may observe that the green regions (*Process config. 2*) mark challenging zones where the deposition process must be adjusted (e.g. the presence of holes or corners). Although Figs. III.D.1.2(b)– III.D.1.2(d) show only two process configurations, the implemented software allows several configuration adjustments on a deposition segment.

III.D.1.4.4 Generation of Idle Paths

One of the main differences between LMD and subtractive manufacturing is in the generation of the idle trajectories. In contrast to subtractive manufacturing, the idle paths affect the quality of the final part. The main reason is that for many LMD systems, the powder is supplied during all the process, even when the laser is OFF. It is known that unmelted material can cause structural defects [146]. Therefore, we included the restriction to avoid the building piece when generating the idle paths.

We used a graph-based approach to deal with this problem. Fig. III.D.1.3(a) shows a geometric configuration in which the segment $\overline{P_1P_2}$ invades the building piece. In order to find a feasible solution, we construct an undirected weighted graph G using the bounding box of the building piece:

1. P_1, P_2 are added as nodes of the graph G (nodes 1 and 2 in Fig. III.D.1.3(c)).
2. The corners of the bounding box are added as nodes of the graph G (nodes 3–6 in Fig. III.D.1.3(c)).
3. Axis-aligned escape routes are found from P_1 and P_2 to reach the bounding box without invading the building piece. The points in the bounding box belonging to these escape routes are added as nodes of the graph G (nodes 7–14 in Fig. III.D.1.3(c)).
4. The edges that connect the nodes in the graph G are generated. Only axis-aligned edges are considered (see Fig. III.D.1.3(b)).
5. The distance between the nodes of the graph is assigned as the weight of each edge, except for those edges that invade the building piece. In that case, the weight is set to infinity. The resulting graph is shown in Fig. III.D.1.3(c), where $d_{i,j}$ denotes the Euclidean distance between nodes i and j .

We implemented Dijkstra’s algorithm to find the shortest path that connected P_1 and P_2 . It is important to remark that the resulting path given by the Dijkstra’s algorithm is the shortest path in the generated graph, which does not imply it is the shortest path in the geometric configuration. On the other hand, when only infinite-length paths exist, P_1 and P_2 are connected directly.

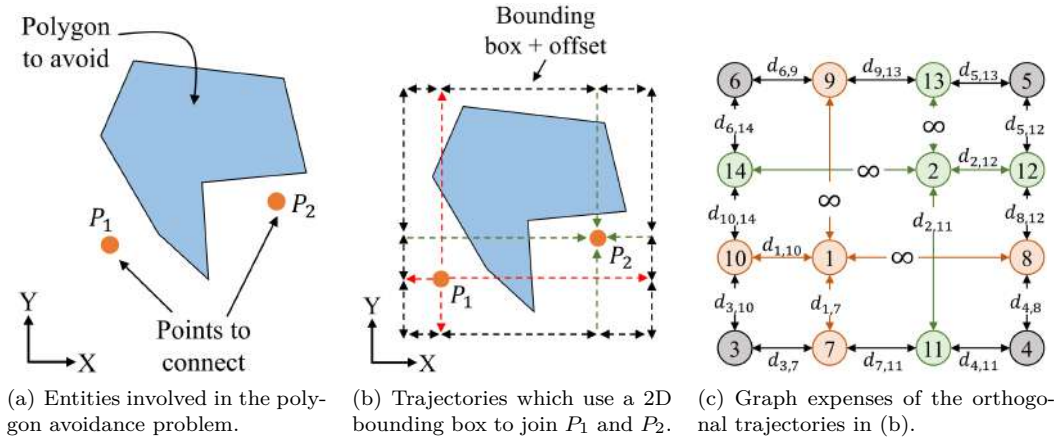


Figure III.D.1.3: Traversal strategy to reposition metal dispenser nozzle (while laser is OFF) between working stages.

III.D.1.5 Results

III.D.1.5.1 CAM Trajectory Generation

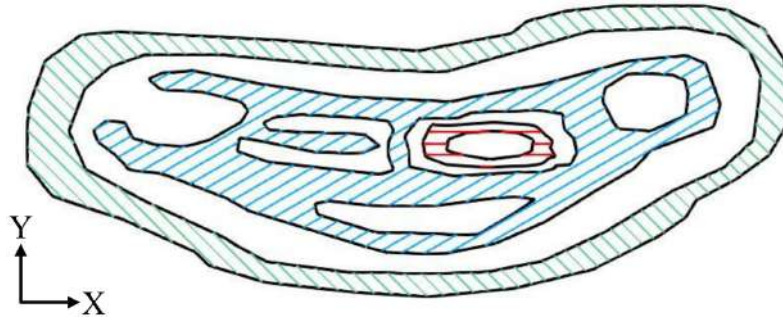
One of the keys of our proposed methodology is the decomposition of the polygonal region into simple polygons. Fig. III.D.1.4(a) shows a complex polygon region in which one can identify three disjoint zones where the material is to be deposited. The decomposition of this complex region into simpler polygons allows the generation of a custom infill for each polygon in a natural manner.

Figs. III.D.1.4(b)–III.D.1.5(a) present the path planning to build two solid (filled) parts and Fig. III.D.1.5(b) shows the path planning for a thin-wall structure. Fig. III.D.1.4(b) shows the resulting path to build a solid piece without holes. The path is generated using a zig-zag strategy and the laser head only moves upwards in layer-to-layer transitions (i.e. the X and Y coordinates of the end point of layer i coincide with the start point of layer $i + 1$).

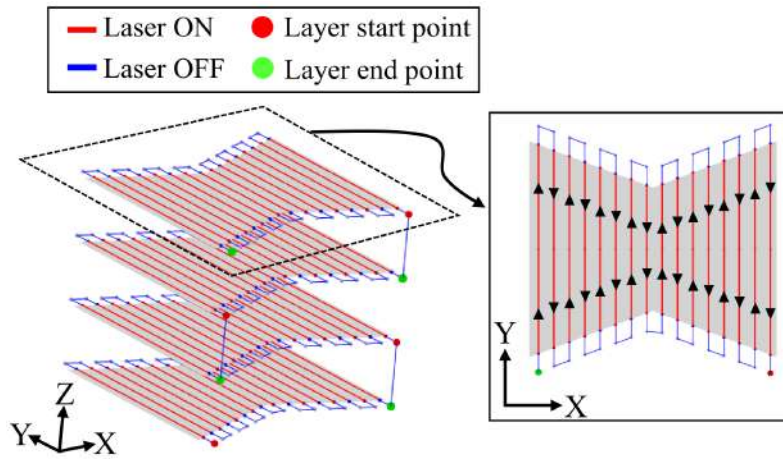
Figs. III.D.1.4(c) and III.D.1.5(a) show two trajectories to build a solid part with a hole. The deposition lines are traversed using the zig-zag trajectory. In contrast to the Fig. III.D.1.4(b), in this case the laser head must be repositioned in inter-layer transitions, since the start point of each layer is the same (X and Y coordinates). In Fig. III.D.1.4(c) is observed that the repositioning path line (green line) crosses the polygon. On the other hand, the repositioning path in Fig. III.D.1.5(a) goes around the polygon, preventing that unmelted powder material adheres to the surface of the building part. This path was obtained using the graph-based approach for polygon avoidance.

As mentioned in the methodology, another important aspect in our approach is to include transition points in the design of the trajectory so that the process parameters are adapted to enhance the quality of the final piece. In Figs. III.D.1.4(c) and III.D.1.5(a) it can be observed that when building solid pieces, transition points are added in the neighborhood of the hole. On the other hand, Fig. III.D.1.5(b) shows that transition points are added at the sharp corners (angles less than 90°) of the thin-wall pieces, since the material tends to accumulate at these zones. However, the location of the transition points as well as the value of the process parameters at these points

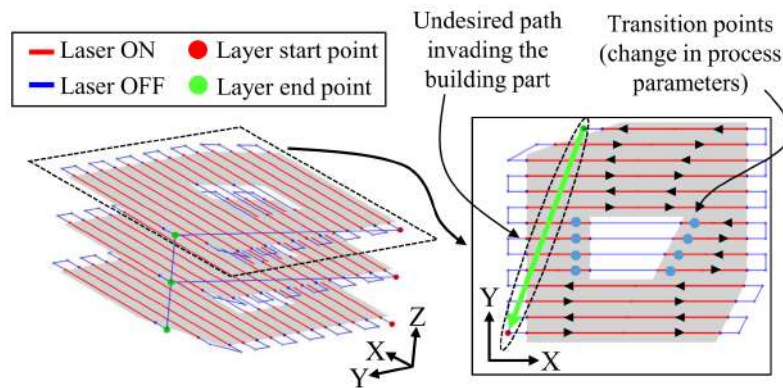
are still subjects of research.



(a) Tree-based hierarchical decomposition of 2D region, with diverse infill patterns.

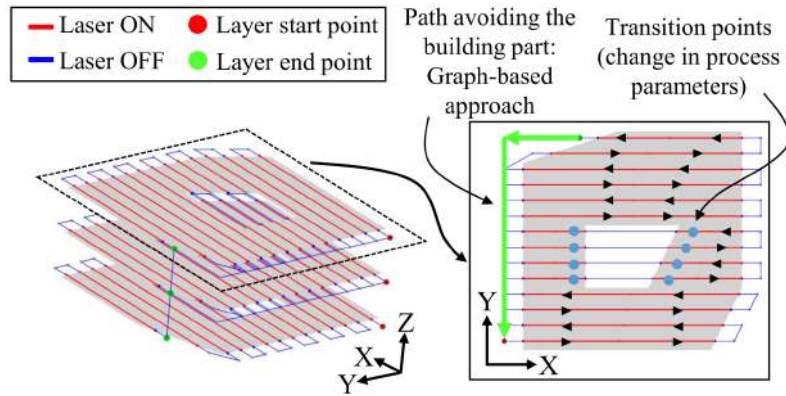


(b) Inter-layer positioning of nozzle using diverse transition (X, Y) resting points.

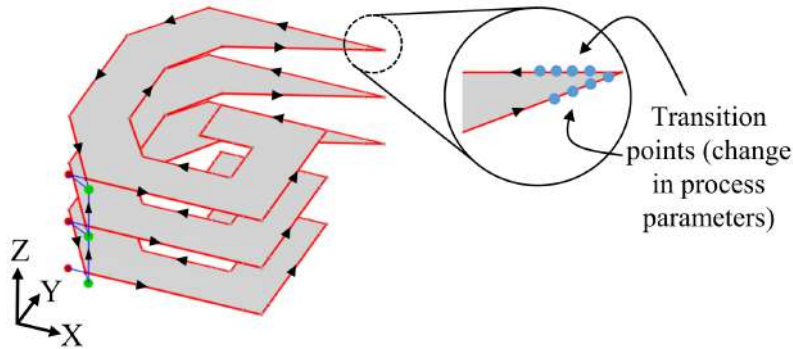


(c) Inter-layer positioning of nozzle using a constant transition (X, Y) resting point. Idle-laser trajectory crosses the workpiece slice.

Figure III.D.1.4: *Cont.*



(a) Inter-layer positioning of nozzle using a constant transition (X, Y) resting point. Idle-laser trajectory does not cross the recently executed workpiece slice by using the graph-based method for polygon avoidance.



(b) Process parameters control in boundary sharp corners due to redundant material delivery.

Figure III.D.1.5: Some resulting implementation features for LMD.

III.D.1.5.2 Experimental Validation

In order to validate the presented approach, we performed three tests using a powder-fed LMD machine. The powder material used for the experiments was *AM 316L (EN 1.4404)*, from Höganäs. The experiments were performed using a high power fiber laser (*IPG YLS-6000*), with wavelength of 1070 nm, and guided to the optical head by means of a 1000 μm core diameter optical fiber. The optical head was mounted in a 3 linear axis system.

Metallic powder particles were delivered to the process zone through a coaxial nozzle, using Nitrogen as carrier gas. Also, that gas was used to generate a protective atmosphere during the deposition process. A schematic layout of the used LMD system is shown in Fig. III.D.1.6(a). Table III.D.1.2 reports the LMD process parameters (consulted from Ref [3]) used in producing the actual workpieces in our experiments.

Table III.D.1.2: Process parameters used for the physical experiments [3].

Parameter	Value	Units
Process speed	13	mm/s
Laser power	2500	W
Powder flow	25	g/min
Overlap percentage	30%	N/A

The results of the experimental tests can be observed in Fig. III.D.1.6. The path planning for each test was calculated using the presented approach. We also automatically generated the instructions that served as input for the machine (in G-Code format). Figs. III.D.1.6(b) and III.D.1.6(c) show the resulting parts after using a zig-zag strategy to fill 2D areas with and without holes. The two tests were satisfactory, since the final pieces represent adequately the expected geometry. However, some height variations can be observed in the boundaries (internal and external), where the deposition starts or ends.

Fig. III.D.1.6(d) depicts a thin-wall structure produced using a continuous strategy. An excess of deposited material is present at the junctions of straight nozzle trajectories. The quantification, explanation and correction of such an effect is the matter of another manuscript by the research team.

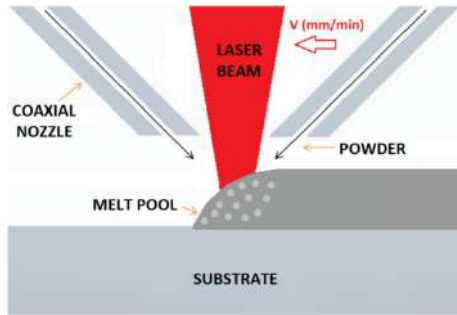
III.D.1.6 Conclusions

In this manuscript we presented a methodology for the generation of 2.5D path planning for LMD. The presented approach considered not only the geometrical aspects of the toolpath generation but also (1) incorporated a graph-based region avoidance algorithm to alleviate hardware limitations and (2) provided the user the control to use several process parameters in a single deposition segment.

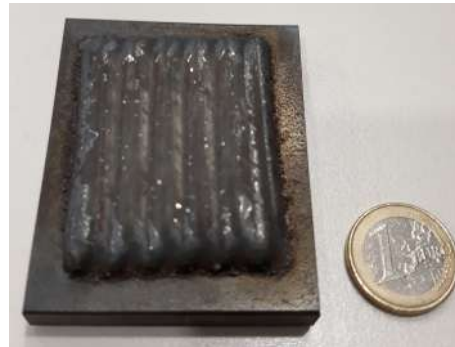
We implemented (1) the raster and zig-zag trajectories to fill a 2D polygonal zone that may contain holes and (2) a continuous trajectory to be used for thin-wall structures. These approaches were validated via physical experimentation using a powder-fed LMD system. The results of this study showed that subtractive manufacturing path planning methods can be used to LMD, even though it is necessary to adapt them to fulfill the particular constraints of LMD. Further work is needed to implement and validate additional infill strategies, such as spirals. It would also be interesting to seek approaches that minimize idle time and material waste.

Acknowledgements

This work has been partially funded by the Basque Government under ELKARTEK program (grants KK-2018/00115 (ADDISEND) and KK-2019/00006 (B4H)), and by the INZU Group (Talens Systems and Ikergune A.I.E.).



(a) Schematic layout of the coaxial laser cladding system [3].



(b) Polygonal region without holes filled with continuous-line hatching pattern.



(c) Polygonal region with holes filled with continuous-line hatching pattern.



(d) Thin-wall structures.

Figure III.D.1.6: Actual workpieces from powder-fed LMD hardware, using the software implemented and reported in this manuscript.

III.D.2

Cylindrical Transform Slicing of Revolute Parts with Overhangs for Laser Metal Deposition

Diego Montoya-Zapata^{1,2}, Aitor Moreno¹, Igor Ortiz³, Oscar Ruiz-Salguero² and Jorge Posada¹

¹Vicomtech Foundation, Basque Research and Technology Alliance (BRTA), Mikeletegi 57, Donostia-San Sebastian 20009, Spain

²Laboratory of CAD CAM CAE, Universidad EAFIT, Cra 49 no 7-sur-50, Medellín 050022, Colombia

³Ikerkune A.I.E., San Antolin 3, 20870 Elgoibar, Spain



III.D.2.1 Context

Diego Montoya-Zapata, Aitor Moreno, Igor Ortiz, Oscar Ruiz-Salguero and Jorge Posada. Cylindrical Transform Slicing of Revolute Parts with Overhangs for Laser Metal Deposition. XXXI Spanish Computer Graphics Conference (CEIG 2022). Vic, Spain. 5-8 July 2022. J. Posada and A. Serrano (Editors). Publisher: The Eurographics Association. ISBN: 978-3-03868-186-1. DOI: <https://doi.org/10.2312/ceig.20221141>. URL: <https://diglib.eg.org/handle/10.2312/ceig20221141>. Proceedings: <https://diglib.eg.org/handle/10.2312/2633203>.

Indexing: EUROGRAPHICS Digital Library

Abstract

In the context of Laser Metal Deposition (LMD), temporary support structures are needed to manufacture overhanging features. In order to limit the need for supports, multi-axis machines

intervene in the deposition by sequentially repositioning the part. Under multi-axis rotations and translations, slicing and toolpath generation represent significant challenges. Slicing has been partially addressed by authors in multi-axis LMD. However, tool-path generation in multi-axis LMD is rarely touched. One of the reasons is that the required slices for LMD may be strongly non-developable. This fact produces a significant mismatch between the tool-path speeds and other parameters in Parametric space vs. actual Euclidean space. For the particular case of developable slices present in workpieces with cylindrical kernel and overhanging neighborhoods, this manuscript presents a methodology for LMD tool path generation. Our algorithm takes advantage of existing cylindrical iso-radial slicing by generating a path in the (κ, z) parameter space and isometrically translating it into the \mathbb{R}^3 Euclidean space. The presented approach is advantageous because it allows the path-planning of complex structures by using the methods for conventional 2.5-axis AM. Our computer experiments show that the presented approach can be effectively used in manufacturing industrial/mechanical pieces (e.g., spur gears). Future work includes the generation of the machine g-code for actual LMD equipment.

Keywords

Applied computing → Computer-aided manufacturing

Computing methodologies → Modeling and simulation, Shape modeling

III.D.2.2 Introduction

Laser Metal Deposition (LMD) uses the power of a laser beam to melt a jet metal powder and add it to a workpiece. As opposed to other Additive Manufacturing (AM) processes, LMD does not allow the addition of support structures to build overhanging features. To answer this limitation, researchers are developing multi-axis LMD machines. However, 2.5-axis AM process planning does not apply for the multi-axis case.

III.D.2.2.1 Scope

The kernel, K , of a polygon Q is the convex subset of Q from which all the points in the boundary of Q are visible. This manuscript addresses 3D solid geometries B for which there is an axis $L \subset \mathbb{R}^3$ such that all cross-sections of B perpendicular to L : (i) are connected, (ii) have non-null kernel intersecting L , and (iii) have kernel containing a disk of radius $R > 0$ whose center is in L . These facts imply that L is a common rotation axis for the whole workpiece such that the material dispenser radial position and the angular position of the in-process workpiece can be synchronized so the dispenser is able to deliver the material in all points of the instantaneous periphery of the in-process cross-sections without hitting an already built portion of the workpiece.

Workpieces in which all cross-sections in one direction have kernel but there is no intersection of the projections of the kernels may still be manufactured, but an instantaneous mobile pivot point of the rotation axis will be needed (with its direction ray being constant). This requirement demands a multi-axis milling machine instead of a lathe and will not be considered in this manuscript. We also ignore workpieces for which there exists no vector $\mathbf{n} \in \mathbb{R}^3$ such that every workpiece cross-section (normal to \mathbf{n}) contains kernel.

III.D.2.3 Literature Review

In multi-axis AM, the 3D solid may be decomposed into a sequence of simpler workpieces, along with the rigid transformations which re-position the growing workpiece in the multi-axis machine. These 3D set partition algorithms use geometrical and optimization heuristics in order to reduce the usage of ancillary support structures. Refs. [156, 195] use 1D simplifications (skeletons) of the 3D solid to perform the decomposition. The branches in the skeleton define the sub-solids of the decomposition. Ref. [48] identifies the zones of higher surface curvature to segment the given solid. Refs. [66, 194] divide the solid with cutting planes. The placement of the cutting planes minimizes the area (or volume) of the overhanging geometry.

Multi-axis AM allows the deposition of non-planar layers. Ref. [39] discretizes the solid into voxels to compute synchronized 5-axis non-planar toolpaths that considerably reduce the need for support structures. Refs. [162, 199] define scalar fields (geodesic distance [162] and temperature [199]) over the volume of the 3D solid. The slices correspond to isolevel surfaces of these scalar fields. Ref. [53] presents support-minimizer slicing LMD method to fabricate gas exhaust manifolds. Refs. [49, 209] use cylindrical coordinate transforms to perform cylindrical-based slicing for revolute workpieces. The aforementioned publications do not present a discussion on the generation of tool paths.

III.D.2.3.1 Conclusions of the Literature Review

In the existing literature, several approaches aim to reduce the usage of support structures in AM by using multi-axis machines. Refs. [49, 209] use coordinate transforms to execute the slicing. The toolpath generation for these slicing methods is still an open research question. This manuscript presents a method to efficiently compute the slices and the toolpaths for 3D solids B with a rotation axis that allows radial access to all borders of B cross-sections. The toolpath generation method uses isometric (i.e., distance-preserving) parametrization along with conventional 2.5-axis toolpath generation [125, 128, 129] algorithms. This article shows that the presented algorithm can be used for the manufacturing of industrial workpieces, such as spur gears.

III.D.2.4 Methodology

Figure III.D.2.1 shows the procedure used to slice the B-Rep (skin) of the workpiece and to generate the tool paths to materialize the solid slices. The procedure applies to a workpiece having a revolution axis common to all its axial cuts' kernels. For slicing: (i) apply to the B-Rep a cylindrical transform which maps the revolute workpiece into a prismatic one (in the cylindrical coordinate system). (ii) slice with planes (in the cylindrical coordinate system) the prismatic B-Rep. For tool path generation in each iso-radial flat slice: (a) correct for length warping by computing (in this case) linear re-parametrization particular to each iso-radial slice, (b) apply the algorithms for flat slice tool-path planning, and (c) map tool paths in the cylindrical coordinate system back to Euclidean space iso-radial slices.

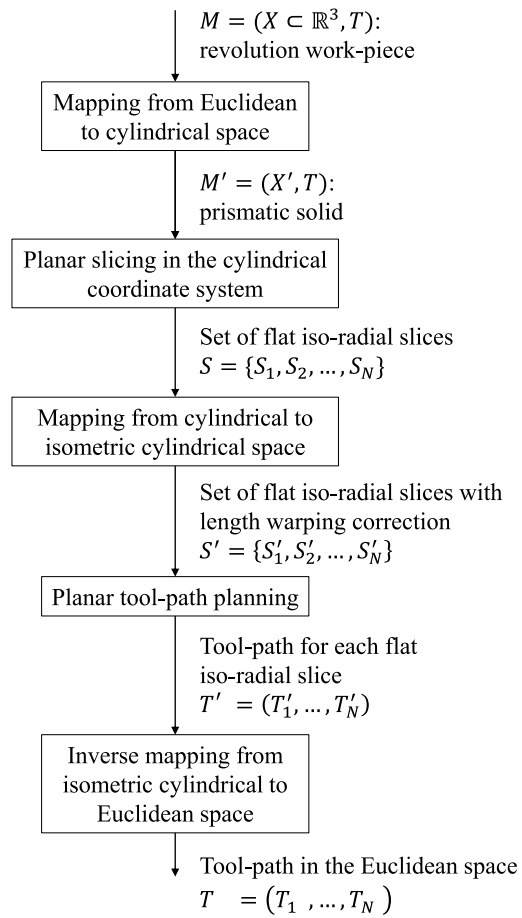


Figure III.D.2.1: Workflow for the slicing and toolpath generation.

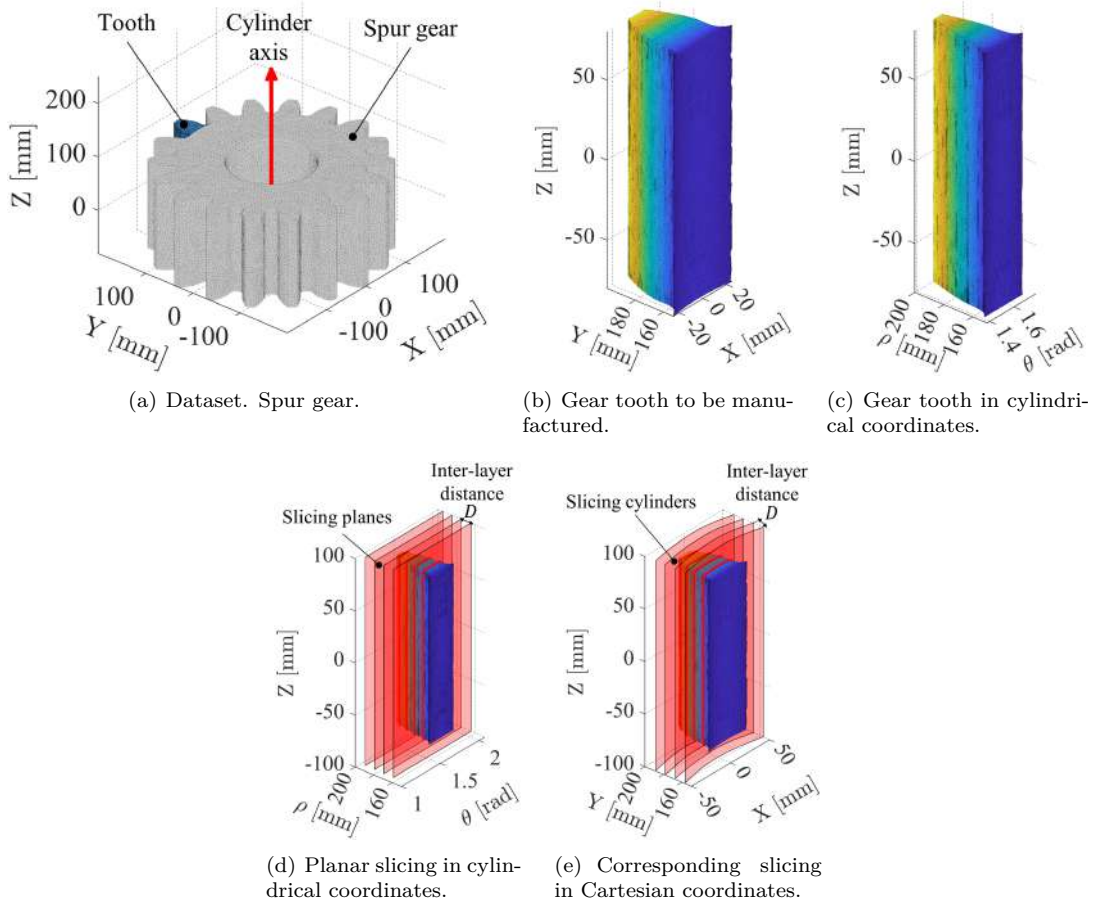


Figure III.D.2.2: Cylindrical-based slicing using coordinate transformation and planar slicing.

III.D.2.4.1 Cylindrical-Based Slicing for Overhanging Geometry

The map from cylindrical ($\theta \in (-\pi, \pi], \rho > 0, z$) to Cartesian coordinates (x, y, z) is given by:

$$f(\theta, \rho, z) = (x, y, z) = (\rho \cos(\theta), \rho \sin(\theta), z) \quad (\text{III.D.2.1})$$

The map from Cartesian to cylindrical coordinates is given by:

$$g(x, y, z) = (\theta, \rho, z) = \left(\text{atan2}(y, x), \sqrt{x^2 + y^2}, z \right); \quad (\text{III.D.2.2})$$

$$\text{atan2}(y, x) = \begin{cases} \arccos(x/\rho); & y \geq 0 \\ -\arccos(x/\rho); & y < 0 \end{cases} \quad (\text{III.D.2.3})$$

The representation of a cylinder of radius R , C_R , in Cartesian coordinates is:

$$C_R = \{(x, y, z) : x^2 + y^2 = R^2\}; \quad (\text{III.D.2.4})$$

which in cylindrical coordinates is the plane:

$$C_R = \{(\theta, \rho, z) : \rho = R\}. \quad (\text{III.D.2.5})$$

Therefore, a slice $\rho = R$ of the prismatic B-Rep in cylindrical coordinates amounts to a cylindrical slice in Cartesian coordinates.

III.D.2.4.2 Toolpath Generation Using Isometric Parametrization

The distance on a plane in cylindrical coordinates does not match the distance on a cylinder in Cartesian coordinates. Therefore, we transform the iso-radial slices in cylindrical coordinates onto the space (κ, R_i, z) which is isometric (i.e., distance-preserving) to the Euclidean space.

Given the slice S_i , which represents the intersection with the plane $\rho = R_i$ in cylindrical coordinates, we apply the following transformation to S_i , $w : S_i \rightarrow M_i \subset \mathbb{R}^3$, where M_i is a plane:

$$w(\theta, R_i, z) = (R_i\theta, R_i, z); \quad w^{-1}(\kappa, R_i, z) = (\kappa/R_i, R_i, z). \quad (\text{III.D.2.6})$$

This transformation stretches the θ -coordinate as given by the cylinder radius R_i . The map from coordinate (κ, z) to Cartesian coordinates is $h = f \circ w^{-1}$:

$$h(\kappa, R_i, z) = f(w^{-1}(\kappa, R_i, z)) \quad (\text{III.D.2.7})$$

$$= f(\kappa/R_i, R_i, z) \quad (\text{III.D.2.8})$$

$$= (R_i \cos(\kappa/R_i), R_i \sin(\kappa/R_i), z). \quad (\text{III.D.2.9})$$

Notice h maps planes in the coordinate system (κ, R_i, z) to cylinders of radius R_i in Cartesian coordinates (x, y, z) . The magnitude κ is the arc length measured on the cylinder surface.

Now, we show that the function h is an isometry (i.e., distance-preserving) and a bijection from planes onto cylinders. Let B_1 be the plane defined by the equation $y = R$. Consider the parametrization σ_1 for B_1 :

$$\sigma_1(u, v) = (u, R, v) \quad (\text{III.D.2.10})$$

Let B_2 be a cylinder of radius R centered at the origin with parametrization σ_2 :

$$\sigma_2(u, v) = (R \cos(u/R), R \sin(u/R), v) \quad (\text{III.D.2.11})$$

Consider the function $h : B_1 \rightarrow B_2$:

$$h(x, R, z) = (R \cos(x/R), R \sin(x/R), z) \quad (\text{III.D.2.12})$$

(i) $\sigma_2(u, v) = h(\sigma_1(u, v))$ and (ii) $I_1 = I_2$, where I_i is the first fundamental form of B_i . Therefore, h is an isometry.

(ii) follows from:

$$J_1 = \begin{bmatrix} 1 & 0 \\ 0 & 1 \\ 0 & 0 \end{bmatrix} \quad J_2 = \begin{bmatrix} -\sin(u/R) & 0 \\ \cos(u/R) & 0 \\ 0 & 1 \end{bmatrix}; \quad I_i = J_i^T J_i \quad (\text{III.D.2.13})$$

$$I_1 = \begin{bmatrix} 1 & 0 \\ 0 & 1 \end{bmatrix} = I_2 \quad (\text{III.D.2.14})$$

where J_1 and J_2 are the Jacobians of B_1 and B_2 , respectively.

Notice that we apply the same map h to the whole slice S_i in cylindrical coordinates, that is, no local mapping is necessary for each planar patch on S_i .

For all revolution workpieces, the approach in this manuscript cannot be applied when the rotation radius of the deposition spot nears zero. This limitation includes (but is not limited to) cylindrical and conical workpieces. In order to apply our approach, it is necessary to previously build, using traditional additive manufacturing, a cylindrical cob with a minimal finite radius. After this cob is available, our method may proceed. Notice that for cones, there is no finite radius different from 0 at the apex. This would be a theoretical limitation of our proposition. However, conical pieces with a sharp apex are discouraged at the level of mechanical or product design. It is common to introduce a bevel or spherical smoothing at the cone apex.

III.D.2.5 Results

To demonstrate the potential of our approach to manufacture industrial workpieces, we apply our method to the LMD path-planning of one tooth of a spur gear.

Fig. III.D.2.2(a) displays the geometry of the spur gear that we use for demonstration. Fig. III.D.2.2(b) shows the tooth to which we apply our slicing and tool-path planning its manufacturing via LMD.

Fig. III.D.2.2(c) shows the prismatic solid associated to the gear tooth in cylindrical coordinates. We apply conventional planar slicing over this prismatic solid in cylindrical coordinates.

Fig. III.D.2.2(d) displays the flat slices resulting from the planar slicing. We map the flat slices back to Cartesian coordinates using Eq. III.D.2.1 to show that each flat slice in cylindrical coordinates corresponds to a cylindrical slice in Cartesian coordinates.

Fig. III.D.2.2(e) shows the cylindrical slices in Cartesian coordinates. The distance D between the flat slices in Fig. III.D.2.2(d) is the same as the distance between the cylindrical slices in Fig. III.D.2.2(e).

Fig. III.D.2.3 presents the tool-path generation for one of the slices obtained at the previous stage. We use the function w (Eq. III.D.2.6) to map the flat slices obtained in cylindrical coordinates onto planar patches isometric to cylindrical patches in Cartesian coordinates. We use the spiral infill pattern for the tool-path planning, although other 2D infill patterns may be used. Finally, we map the obtained tool-path onto the cylinder surface in Cartesian coordinates using the function h (Eq. III.D.2.9).

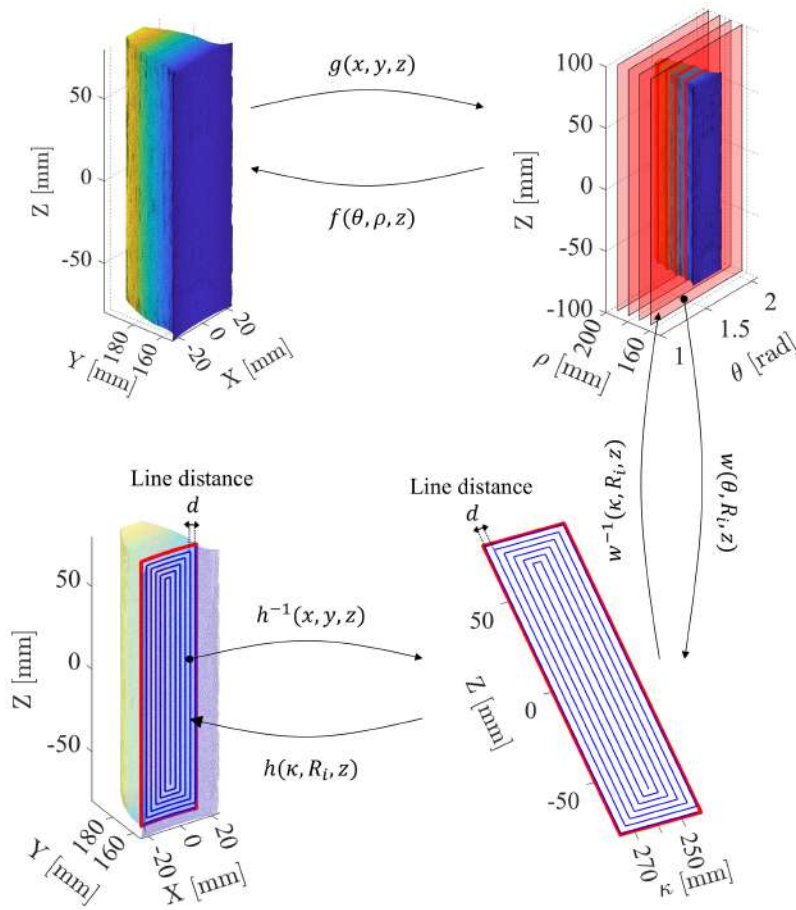


Figure III.D.2.3: Toolpath for cylindrical slice using isometric parametrization.

It is important to remark that the function h preserves the distance d between deposition lines. It is relevant because it allows the tool-path generation on a 2D planar polygonal region (where robust path planning algorithms already exist) instead of on a 3D curved surface. The reader may also notice that one must apply a different transformation to each slice since the function w depends on the cylinder radius R .

As stated in Section III.D.2.4, our method is suitable for a particular set of revolute workpieces with a cylindrical 3D core. In addition, to meet the condition of self-support, the sub-solids adhered to the cylindrical kernel cannot have prominent overhang features in the radial direction.

III.D.2.6 Conclusions

This manuscript presents a process planning method for Laser Metal Deposition (LMD) of revolute parts. These parts consist of a 3D (informally called cylindrical) kernel with overhanging features. Our method maps the B-Rep of the revolute workpiece to cylindrical coordinate space, producing a prismatic B-rep. This prismatic shape is sliced and its slices processed for LMD using 2D path planning tools. The tool paths are corrected for constant velocity and mapped back to Euclidean space thus producing the revolute part. This method is successful for generation of LMD tool paths for spur gear teeth. Future work addresses the actual gear manufacturing.

Funding

This work has been partially funded by the Basque Government under ELKARTEK program (grants KK-2018/00115 (ADDISEND) and KK-2018/00071 (LANGILEOK)), and by the INZU Group (Talens Systems and Ikerkune A.I.E.).

III.D.3

Computational Minimization of Over-deposition at Corners of Trajectories in Laser Metal Deposition

Diego Montoya-Zapata^{1,2}, Carles Creus¹, Aitor Moreno¹, Igor Ortiz³, Piera Alvarez³, Oscar Ruiz-Salguero², Jorge Posada¹

¹Vicomtech Foundation, Basque Research and Technology Alliance (BRTA), Mikeletegi 57, Donostia-San Sebastian 20009, Spain

²Laboratory of CAD CAM CAE, Universidad EAFIT, Cra 49 no 7-sur-50, Medellín 050022, Colombia

³Ikerkune A.I.E., San Antolin 3, 20870 Elgoibar, Spain



III.D.3.1 Context

Diego Montoya-Zapata , Carles Creus , Aitor Moreno , Igor Ortiz , Piera Alvarez , Oscar Ruiz-Salguero , Jorge Posada. Computational minimization of over-deposition at corners of trajectories in Laser Metal Deposition. Journal Manufacturing Letters, Elsevier, (ISSN 2213-8463), 2021, 29, 29-33; url= <https://www.sciencedirect.com/science/article/pii/S2213846321000225>, doi= <https://doi.org/10.1016/j.mfglet.2021.05.001>, Published online: 24 May 2021.

Indexing: SCOPUS(Q1), JCI(Q2), Publindex(A1)

Abstract

Avoidance of over-deposition at trajectory corners is relevant in Laser Metal Deposition (LMD) for Additive Manufacturing. Currently available LMD hardware only allows constant material feed (g/s). Therefore, gliding speed of the material dispenser is the remaining tuning variable for controlling metal over-deposition at corners. Existing literature reports trial-error physical experiments, addressing only particular corner angles. In response, this manuscript reports the implementation of a voxel-based simulator of the bead geometry, taking into consideration bead profile, dispenser velocity, material feed, and bead curve geometry. We use it to evaluate two constant-feed tailored-velocity strategies for minimizing material over-deposition at corners.

Keywords: additive manufacturing, laser cladding, optimization.

III.D.3.2 Introduction

Laser Metal Deposition (LMD) employs a laser beam to melt a jet of metal powder and to deliver it onto a workpiece. This promising Additive Manufacturing (AM) technique is used in workpiece coating, repairing and re-manufacturing [93, 125]. However, over-deposition of metal on curved or sharp-corner beads is a standing challenge for LMD.

In this manuscript, we present the implementation of a voxel-based simulator of the bead geometry, taking into consideration bead cross profile, nozzle velocity, variable material feed, and bead curve geometry. Our simulator allows for time-varying material feed (g/s), although this feature is an open research topic at the present time. We couple our bead geometry simulator with two variable speed strategies, used to minimize material over-deposition in corners.

III.D.3.3 Literature Review

AM uses Piecewise Linear (PL) trajectories. Two factors reinforce metal over deposition at corners: (a) overlapping deposition zone (Fig. III.D.3.1(a)) and (b) nozzle deceleration. The proposed methods in the literature to reduce over-deposition at the corners are (1) the control of the process parameters (e.g. speed, power and material flow) [193], (2) corner smoothing [58, 71, 140] and (3) a combination [32, 33] of (1) and (2). Corner smoothing is only acceptable if accuracy is not a priority. The authors [193] that aim only to control the process parameters (e.g. speed, power, material flow) do not use numerical methods to study the influence of the parameters in the corner deposition. Instead, they employ costly physical trial-error experimentation and limit their studies to right (90°) angles.

We identified two approaches to model computationally the bead geometry in LMD. The first assumes a pre-defined bead cross-section, namely circular [25, 55, 133, 135], elliptical [25, 210], parabolic [25, 133, 135, 186, 200], sinusoidal [25, 133, 135]. Other researchers [89, 193] model bead width and height as functions of process parameters.

In the second method, the bead geometry is not pre-defined but it is induced by the distribution of the delivered material which depends on the process parameters [6, 55, 178, 179]. We consider that, under conditions of full melting of the powder jet, the variation in nozzle velocity or material feed are more immediate factors to control over-deposition. Mainly two types of delivered material

functions have been studied: Gaussian [6, 55, 178, 179] and uniform [55]. Our simulator accepts any material distribution function $f : \mathbb{R}^2 \rightarrow \mathbb{R}$.

III.D.3.3.1 Conclusions of the Literature Review

In the existing literature, sharp corners deposition in LMD is addressed by smoothing the corner geometry and expensive trial-and-error experimentation. This manuscript presents an implementation of a material deposition geometric simulator which considers: bead geometry induced by model of delivered material distribution, PL trajectories, nozzle velocity (mm/s) and feed rate (g/s).

III.D.3.4 Methodology

III.D.3.4.1 Geometry Deposition Model

III.D.3.4.1.1 Powder Delivery Density

The function $I(x, y, t)$ (g/(s mm²)) reflects, given a time t , the metal particle density projected by the nozzle at the workpiece surface. Coordinate z is parallel to the jet. Eq. III.D.3.1 represents a Gaussian example of this distribution, with coordinates (x, y) already measured on the workpiece surface. Our simulator accepts any density function of (x, y) :

$$I(x, y, t) = \frac{2f(t)}{\pi R^2} \exp\left(\frac{-2\left((x - P_x(t))^2 + (y - P_y(t))^2\right)}{R^2}\right). \quad (\text{III.D.3.1})$$

f is the material feed rate (g/s), R is half of the nominal bead width (mm), $\mathbf{P}(t) = [P_x(t), P_y(t)]^T$ is the nozzle position (mm, mm) at time t .

Given the function I , the material density ρ and the total deposition time T , one can obtain the bead height H as:

$$H(x, y) = \frac{1}{\rho} \int_0^T I(x, y, \xi) d\xi. \quad (\text{III.D.3.2})$$

III.D.3.4.1.2 Nozzle Trajectory

$C = [p_0, \dots, p_N]$ is a PL approximation of the nozzle trajectory. f_k and v_k are the feed and velocity levels at point \mathbf{p}_k . Acceleration is assumed constant when velocity changes. Let t_k ($0 \leq k \leq N$) be the time at which the dispenser reaches point \mathbf{p}_k , with $t_0 = 0$ and $t_N = T$. Each t_k is a function of the speeds v_0, v_1, \dots, v_k . We numerically compute the bead height as per Eq. III.D.3.3:

$$H(x, y) = \frac{1}{\rho} \sum_{k=1}^N \int_{t_{k-1}}^{t_k} I(x, y, \xi) d\xi. \quad (\text{III.D.3.3})$$

III.D.3.4.2 Minimization of Material Overfill in Corners

We define an *ideal* corner as the one in which incoming and outgoing beads are free from over- and under-deposition. The ideal bead profile H_0 in Eq. III.D.3.4 corresponds to the steady state in a

linear nozzle trajectory. For the purpose of computing H_0 , we may consider this trajectory on the X axis and therefore $H_0(x, y) = H_0(y)$.

$$H_0(x, y) = \int_{-\infty}^{\infty} I(x, y, t) dt = \frac{\sqrt{2}f}{\rho\sqrt{\pi}Rv} \exp\left(\frac{-2y^2}{R^2}\right). \quad (\text{III.D.3.4})$$

The ideal or *goal* corner corresponds to an assembly of incoming and outgoing beads. They are completely symmetrical w.r.t. a plane bisecting the corner angle (Fig. III.D.3.1).

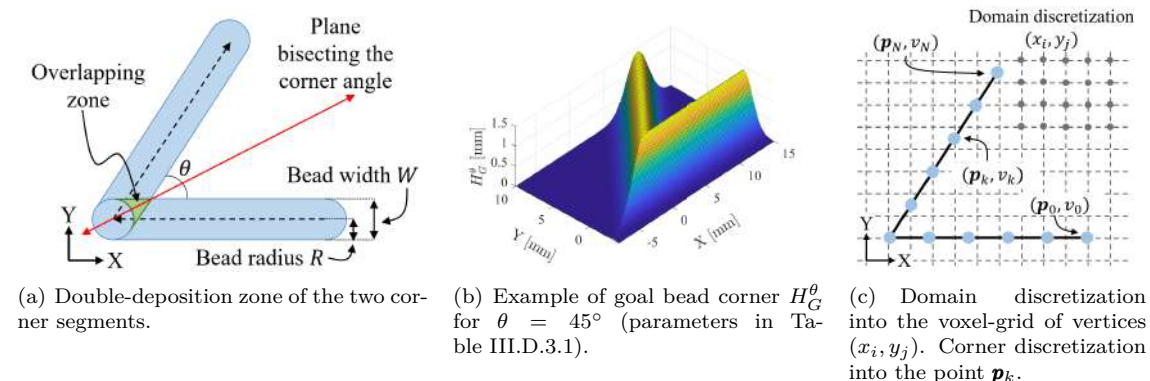


Figure III.D.3.1: Trajectory corner. Parameters, goal bead and discretization.

Considerations for corners in LMD are: (a) Over-deposition is reinforced by (i) overlapping zones in incoming and outgoing beads (Fig III.D.3.1), (ii) mandatory deceleration to reach null velocity at the corner itself. (b) Current LMD hardware is unable to produce variable feed (g/s) within the trajectory [7, 50, 193], leading to an overall constant feed. Because of these considerations, we proceed to use the nozzle cruise velocity as variable to minimize material over-deposition at corners.

The tuning variables for the over-deposition minimization are the nozzle speeds $V = (v_0, \dots, v_N)$ at each vertex \mathbf{p}_k of the corner discretization. We define the optimization problem assuming the domain is discretized into a rectangular grid G with vertices (x_i, y_j) , ($1 \leq i \leq G_1, 1 \leq j \leq G_2$), as shown in Fig. III.D.3.1(c). The optimization problem is stated as follows:

$$\begin{aligned} & \text{find } V = (v_0, \dots, v_N) \\ & \text{to minimize } E_k(V) = \frac{1}{G_1 G_2} \sum_{i=1}^{G_1} \sum_{j=1}^{G_2} e_k(x_i, y_j)^2 \\ & \text{subject to } 0 \leq v_i \leq v_{\max}, \quad i = 0, 1, \dots, N \\ & \quad \|\mathbf{a}(t)\| \leq a_{\max}, \quad t \in [0, T] \end{aligned} \quad (\text{III.D.3.5})$$

$\mathbf{a}(t) = [a_x(t), a_y(t)]^T$ is the nozzle acceleration. v_{\max} and a_{\max} are the maximal speed and acceleration permissible for the AM hardware or the process, respectively. $e_k : \mathbb{R}^2 \rightarrow \mathbb{R}$ is an error function that measures the deviation of the actual (given the speeds V) height w.r.t. the goal height. We consider two error functions:

1. Direct comparison between the actual and the goal height:

$$e_1(\mathbf{x}) = |H(\mathbf{x}) - H_G^\theta(\mathbf{x})| \quad (\text{III.D.3.6})$$

2. A more permissive function to diminish underfill due to nozzle acceleration:

$$e_2(\mathbf{x}) = \begin{cases} |H(\mathbf{x}) - H_G^\theta(\mathbf{x})|, & H(\mathbf{x}) < H_G^\theta(\mathbf{x}), \text{ i.e. underfill} \\ 0, & H_G^\theta(\mathbf{x}) \leq H(\mathbf{x}) \leq \max(H_G^\theta), \text{ i.e. permissible overfill} \\ H(\mathbf{x}) - \max(H_G^\theta), & H(\mathbf{x}) > \max(H_G^\theta), \text{ i.e. overfill} \end{cases} \quad (\text{III.D.3.7})$$

where $\max(H_G^\theta) = H_0(x, 0) = \frac{\sqrt{2}f}{\rho\sqrt{\pi}Rv}$.

III.D.3.5 Results

For the purpose of illustration, we produce the results of minimizing over-deposition with corner angles $\theta \in \{30^\circ, 60^\circ, 90^\circ\}$ and use the conditions of Table III.D.3.1. The material properties specific for LMD used in the simulation correspond to *AISI 316L* stainless steel in [3].

Table III.D.3.1: Simulation set-up. Parameters for the optimization of material overfill at the corners deposition. Values based on Refs. [3, 7, 142].

Parameter	Value
Material	<i>AISI 316L</i>
Density	$\rho = 7900 \text{ kg/m}^3$ [142]
Clad radius	$R = 2.3 \text{ mm}$
Nozzle cruising speed	$v_c = 13 \text{ mm/s}$
Material feed rate	$f = 0.42 \text{ g/s}$
Maximal speed	$v_{\max} = 2v_c = 26 \text{ mm/s}$
Maximal acceleration	$a_{\max} = 600 \text{ mm/s}^2$ [7]

Our model parametrizes the magnitude of the dispenser cruise speed in terms of the distance d from the corner tip. We approximate the optimal speed function V^O by a 4-stage PL function (see Table III.D.3.2). The stages of V^O are nonlinear functions of d . Given consecutive checkpoints (d_i, v_i) and (d_{i+1}, v_{i+1}) the velocity between them is given by:

$$V^O(d) = \sqrt{2a(d - d_i) + v_i^2}, \quad d \in [d_i, d_{i+1}], \quad (\text{III.D.3.8})$$

where a is the constant acceleration in the stage.

The minimization uses the exhaustive search method to find the optimal velocity histories for error accountancy methods e_1 and e_2 . This method is expensive in computing time. Therefore, this optimization is to be used at the stage of process-planning and not in real time during the manufacturing itself. The resulting speed profiles for each studied value of the corner angle θ are presented in Table III.D.3.2. For each angle, we found speed profiles $V_{e_1}^O$ and $V_{e_2}^O$ as per the error e_1 and e_2 functions in Eqs. III.D.3.6 and III.D.3.7.

The (decreasing) distance to the next corner presents velocity plots which occur in the negative horizontal axis. However, notice that the entry and exit velocity histories are, under the current assumptions, symmetrical with respect to the distance to the corner spot. These considerations lead to Table III.D.3.2 presenting the dispenser velocity at the *exit* from the corner and not in the *entry* phase. Both, $V_{e_1}^O$ and $V_{e_2}^O$ show similar behavior: (a) large acceleration near the corner, reaching the maximal value v_{\max} , (b) constant speed, and (c) deceleration to reach the cruise speed v_c . The sharper the corner, the smaller the angle θ and (as expected) the more abrupt the acceleration or deceleration near the corner spot. Error accountancy methods e_1 and e_2 call for the same acceleration (or deceleration) to depart from (or reach to) null velocity at the corner. However, the transition to cruise speed takes longer with method e_1 . Therefore, the average speed of $V_{e_1}^O$ is greater than the one of $V_{e_2}^O$.

Table III.D.3.2 shows the height functions for $\theta \in \{30^\circ, 60^\circ, 90^\circ\}$ associated to (1) the optimal speed functions $V_{e_i}^O$ ($i = 1, 2$) and (2) a simulation with a constant speed function V_{v_c} (which would require infinite acceleration/deceleration at the corner spot).

In Table III.D.3.2, (1) we can observe the material over-deposition at constant speed V_{v_c} is evident for all $\theta \in \{30^\circ, 60^\circ, 90^\circ\}$. Additionally, over-deposition increases when the angle decreases. (2) In the cross-section views for $\theta = 30^\circ$, we can note that $V_{e_1}^O$ produces more underfill than $V_{e_2}^O$. Since the average speed of $V_{e_1}^O$ is greater than the one of $V_{e_2}^O$, the amount of deposited material is lower.

The values of the objective functions (i.e. sum of squared errors in Eq. III.D.3.5) for the optimal velocity functions $V_{e_1}^O$ and $V_{e_2}^O$, and for the constant (uncontrolled) velocity function V_{v_c} are depicted in Fig III.D.3.2. The difference of the objective functions between the optimal ($V_{e_1}^O, V_{e_2}^O$) and uncontrolled (V_{v_c}) velocity functions is noticeable. The values under uncontrolled speed are at least 10 times greater than for the optimal solutions ($E_i(V_{v_c})/E_i(V_{e_i}^O) > 10, i = 1, 2$). We can also observe that, for every value of $\theta \in \{30^\circ, 60^\circ, 90^\circ\}$, the minimal value of E_1 is attained by $V_{e_1}^O$ (analogously for E_2 and $V_{e_2}^O$).

III.D.3.6 Conclusions

In this manuscript, we have presented the implementation of a voxel-based geometric simulator for Laser Metal Deposition (LMD). On this simulator, we have mounted and solved a minimization of the material over-deposition at corners in LMD. Results for the corner angle instances $\theta \in \{30^\circ, 60^\circ, 90^\circ\}$ show a reduction of over 90% of the over-deposition present at corners with no nozzle velocity control. An *exhaustive search* strategy is used for minimization. This strategy is expensive in computing time. Therefore, our method is to be used for the process planning stage. Further study of heuristics for cutting computing time expenditures are required for in-process applications.

Table III.D.3.2: Row 1: Optimal speed profiles $V_{e_1}^O, V_{e_2}^O$ for errors e_1 and e_2 . Corner angles $\theta \in \{30^\circ, 60^\circ, 90^\circ\}$. Rows 2-6: Resulting bead geometries. Row 2: no velocity control. Rows 3-4: Beads with optimal velocity, given errors e_1 and e_2 , respectively. Rows 5-6: Bead cross-section $Y = 0$ with optimal velocity, given errors e_1 and e_2 , respectively.

	$\theta = 30^\circ$	$\theta = 60^\circ$	$\theta = 90^\circ$
Optimal speed histories. Errors e_1 and e_2			
Bead geometry for constant velocity V_{v_c}			
Optimized bead geometry. Optimal velocity $V_{e_1}^O$			
Optimized bead geometry. Optimal velocity $V_{e_2}^O$			
Optimized bead cross-section $Y = 0$. Optimal velocity $V_{e_1}^O$			
Optimized bead cross-section $Y = 0$. Optimal velocity $V_{e_2}^O$			

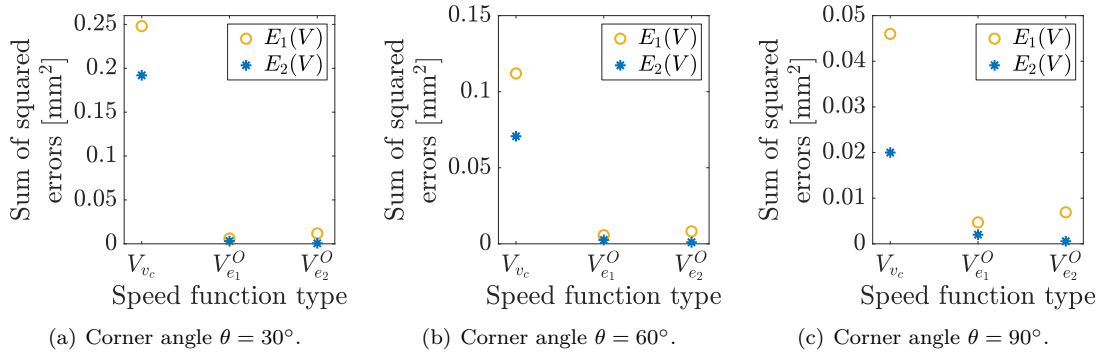


Figure III.D.3.2: Over-deposition consolidated estimators E_1 and E_2 (Eq. III.D.3.5) for velocity profiles $\{V_{v_c}, V_{e_1}^O, V_{e_2}^O\}$ and corner angles $\{30^\circ, 60^\circ, 90^\circ\}$. e_1 and e_2 : deposition punctual error methods (Eqs. III.D.3.6 and III.D.3.7, respectively).

Funding

This work has been partially funded by the Basque Government under ELKARTEK program (grants KK-2018/00115 (ADDISEND) and KK-2019/00006 (B4H)), and by the INZU Group (Talens Systems and Ikergune A.I.E.).

III.D.4

Experimental and Computational Assessment of Minimizing Overfill in Trajectory Corners by Laser Velocity Control of Laser Cladding

Diego Montoya-Zapata^{1,2}, Jorge Posada¹, Piera Alvarez³, Carles Creus¹, Aitor Moreno¹, Igor Ortiz³, Oscar Ruiz-Salguero²

¹Vicomtech Foundation, Basque Research and Technology Alliance (BRTA), Mikeletegi 57, Donostia-San Sebastian 20009, Spain

²Laboratory of CAD CAM CAE, Universidad EAFIT, Cra 49 no 7-sur-50, Medellín 050022, Colombia

³Ikerkune A.I.E., San Antolin 3, 20870 Elgoibar, Spain



The International Journal of
Advanced Manufacturing
Technology

III.D.4.1 Context

Diego Montoya-Zapata, Jorge Posada, Piera Alvarez, Carles Creus, Aitor Moreno, Igor Ortiz, Oscar Ruiz-Salguero. Experimental and computational assessment of minimizing overfill in trajectory corners by laser velocity control of laser cladding. *International Journal of Advanced Manufacturing Technology*, Springer, (eISSN 1433-3015, ISSN 0268-3768), 2022, 119, pp. 6393–6411. url= <https://link.springer.com/article/10.1007/s00170-021-08641-8>, doi= <https://doi.org/10.1007/s00170-021-08641-8>, Published online: 21 January 2022.

Indexing: SCOPUS(Q1), JCR(Q2), Publindex(A1)

Abstract

In the context of Laser Metal Deposition (LMD), the problem of avoiding unintentional material accumulation in bead corners or bends is central. Most of the existing approaches to limit such an accumulation are expensive trial-and-error ones. This manuscript presents the experimental verification of a recently reported computational method for minimizing material overfill in corners in LMD. The verification consisted in the deposition of single-layer corners with angle $\theta \in \{15^\circ, 30^\circ, 45^\circ, 60^\circ, 75^\circ\}$ with (i) constant and (ii) controlled (as dictated by the computational minimization) tool-head velocity. The term controlled velocity in this manuscript refers to the fact that the nozzle velocity can be adjusted in advance with predefined parameters resulting from the simulations of variable velocities. The comparison between the predicted and experimental bead topographies cannot be executed via standard registration methods because these methods minimize the distance between the registered datasets. In response to this limitation, this manuscript presents a registration method that avoids overall distance minimization. This registration method is based on the sequential matching of datums between the experimental and predicted datasets. The results of the experiments revealed that (i) the computational minimization strategy is effective for reducing material overfill in LMD and (ii) near 40% of the metal powder delivered by the nozzle is wasted. This powder loss is a constant feature across LMD implementations and is not caused by the minimization of metal overfill at corners. These facts show that (i) voxel-based modeling is an effective tool for bead topography and mass/area-based bead computations and (ii) LMD is useful for the cladding stage but not for the production of the bulk piece. Additional work is required to appraise the effective (i.e., not nominal) powder rate deposited at the bead. Future efforts will be dedicated to extend the material overfill minimization strategy to multi-layer deposition.

Keywords: Laser metal deposition, Additive manufacturing, Computational optimization, Mesh registration, Physical experiments, Trajectory corners, Bead geometry.

Glossary

AM	Additive Manufacturing.
CG	Center of gravity.
ICP	Iterative Closest Point.
LMD	Laser Metal Deposition.
XCT	X-ray Computer Tomography.
SO(3)	Special Orthogonal Group of dimension 3. A matrix \mathbf{R} ($n \times n$) is SO(n) (i.e. is a <i>rotation</i>) if $\mathbf{R}^T * \mathbf{R} = \mathbf{R} * \mathbf{R}^T = I$ and $\det(\mathbf{R}) = +1$.
$\mathcal{C}(u)$ [$C_x(u), C_y(u)$] ^T	= Planar parametric curve that represents the tool-path.
$\mathcal{C}^{PL}(\mathbf{c}_0, \dots, \mathbf{c}_N)$	Piecewise linear curve with vertices $\mathbf{c}_k \in \mathcal{C}$, ($k = 0, \dots, N$) that approximates $\mathcal{C}(u)$.
$I(x, y, t) : \mathbb{R}^2 \times \mathbb{R} \rightarrow \mathbb{R}$	Profile of powder delivery [$\text{kg}/(\text{s mm}^2)$] of a given nozzle at time t . (x, y) : local nozzle coordinates.

$H(x, y, t) : \mathbb{R}^2 \times \mathbb{R} \rightarrow \mathbb{R}$	Bead height [mm] at the point (x, y) of the substrate plate at time t .
$H_0(x, y) : \mathbb{R}^2 \rightarrow \mathbb{R}$	Bead height [mm] at plate point (x, y) under constant nozzle velocity direction and magnitude, and material flow rate.
$H_G^\theta(x, y) : \mathbb{R}^2 \rightarrow \mathbb{R}$	Bead height [mm] of an ideal (or goal) corner with angle θ .
$f(t) : \mathbb{R} \rightarrow \mathbb{R}$	Powder flow rate [kg/s] at nozzle exit.
f_{eff}	Powder flow rate [kg/s] integrated at the bead.
$\eta \in [0, 1]$	Material efficiency ratio f_{eff}/f .
$V(t) : \mathbb{R} \rightarrow \mathbb{R}$	Tool-head or nozzle velocity [mm/s] at time t .
$V(d) : \mathbb{R} \rightarrow \mathbb{R}$	Tool-head or nozzle velocity [mm/s] as a function of the signed distance d (measured in plant view along the bead) to the corner tip.
P	Laser power [W].
v_c	Tool-head cruise velocity [mm/s].
v_{max}	Maximal tool-head cruise velocity [mm/s].
W	Bead width [mm].
$R = W/2$	Half of the bead width [mm].
ρ	Density of the powder cladding material [kg/m ³].
$\mathbf{M} \in \mathbb{R}^4 \times \mathbb{R}^4$	Rigid transformation (rotation and translation) matrix resulting from the corner registration.
$[\mathbf{X}_w, \mathbf{Y}_w, \mathbf{Z}_w, \mathbf{O}_w]$	World coordinate system. Basis vectors $\{\mathbf{X}_w, \mathbf{Y}_w, \mathbf{Z}_w\}$ and origin $\mathbf{O}_w \in \mathbb{R}^3$.

III.D.4.2 Introduction

III.D.4.2.1 Research target

This manuscript reports the experimental validation of the method in Ref. [124] that minimizes the overfill of metal in trajectory corners in Laser Metal Deposition (LMD) by varying the cruise velocity of the metal dispenser nozzle. In assessing the deviation between experimental vs. predicted metal beads, the usual registration methods bias the appraisal. To avoid such a bias, this manuscript presents a datum-based sequential registration developed by the authors. This registration progressively matches reliable datums of the LMD (e.g. substrate plane, bead axes, etc.) between the experimental and predicted datasets. The results show that the variable nozzle velocity strategy significantly reduces the metal overfill at corners, thus approximating the ideal LMD beads.

III.D.4.2.2 Context

LMD is a manufacturing method that employs the power of a laser to manufacture medium to large-scale industrial parts. It is one of the Additive Manufacturing (AM) technologies with higher potential to be adopted at industrial scale due to its applications in repairing, coating, and manufacturing of high-value parts (Ref. [93]). One of the main challenges in LMD is the construction of sharp corners since they are prone to unwanted material accumulation.

The computational approach recently presented in Ref. [124] minimizes the material overfill at corners in LMD by adjusting the tool-head velocity at the process-planning stage. The present manuscript reports the experimental validation of this computational minimization method for single-layer trajectory corners of angle $\theta \in \{15^\circ, 30^\circ, 45^\circ, 60^\circ, 75^\circ\}$. For each angle, the method in Ref. [124] is used to find the tool-head velocity that minimizes the material overfill. The experiment consists in the deposition of single-layer corners at controlled (as dictated by the method in Ref. [124]) and constant tool-head velocity. The term controlled velocity in this manuscript refers to the fact that the nozzle velocity can be adjusted in advance with predefined parameters resulting from the simulations of variable velocities.

The resulting workpieces are optically scanned. The scanned data is aligned using a datum-based sequential registration developed by the authors. The results of the experiments show that the computational minimization method in Ref. [124] successfully produces tool-head velocity profiles that reduce the material overfill in trajectory corners in LMD. Side findings of the experiments show that around 40% of the powder material is wasted. This waste is inherent to the LMD, regardless of the existence or absence of bead corners. This manuscript does not intend to contribute to the prediction of material waste in LMD. The velocity variation strategy assessed in this manuscript will be integrated into the industrial AM Process Planning system previously reported in Ref. [125].

The remainder of this article is structured as follows: Section III.D.4.3 reviews the relevant existing literature. Section III.D.4.4 describes the methods and materials related to the experiment. Section III.D.4.5 displays and discusses the computational and experimental results. Section III.D.4.6 concludes the manuscript and suggests potential extensions of the work.

III.D.4.3 Literature review

III.D.4.3.1 Minimization of material overfill in trajectory corners

In the context of LMD, path planning algorithms generate piecewise linear tool-paths. Material overfill occurs at the tool-path corners due to the following facts: (i) the tool-head reduces its velocity in the vicinity of the corner and (ii) there is an overlap (or double deposition) zone which is larger for sharper corners. The proposed solutions in the literature focus on adjusting three process parameters: laser power, powder flow rate, and tool-head velocity.

The approaches in Refs. [124, 140, 193] vary the tool-head velocity in the vicinity of the corner. Ref. [140] executes several experimental trials to find adequate levels of smoothing of right-angle (90°) corners. The material overfill is limited because the smoothed corner is traversed at a higher speed. However, the smoothing compromises geometry accuracy. Ref. [193] fits a regression model to predict the bead height as a function of the tool-head velocity, laser power, and powder flow rate. This model is used to modify the tool-head velocity to build right-angled corners. The main drawback of both approaches (Refs. [140, 193]) is that they are limited to trial-and-error experimentation for 90° angles. Ref. [124] (precursor of the present one) presents a computational approach to minimize material overfill for several corner angles. This method solves a minimization problem to find a tool-head profile that limits material overfill at the corner. The results reported in Ref. [124] are purely computational, and the experimental validation is missing.

Ref. [10] presents an online controller to adjust the laser power during trajectory corners deposition. The reported experiments showed the capability of the system to reduce material overfill at corners. However, this approach changes the bead material properties. It also requires a more expensive Computer Vision hardware and software to sense the melt-pool during the deposition.

Ref. [7] presents a control system to regulate the material flow rate. The limitation of this method is the large response time of the powder flow systems. This delay impedes the synchronization of the powder rate decrement with the power or tool-head velocity and position near corners.

The problem of material deposition at corners is common in other AM technologies, such as fused filament fabrication. Refs. [32, 33] implement a computational fluid dynamics model to study the effects of corner smoothing, tool-head velocity, and material feed rate in fused filament fabrication. Numerical results show that synchronizing the feed rate with the tool-head velocity reduces the defects around the corner. However, current hardware limitations hinder the application of this approach in LMD.

Table III.D.4.1: Summary of the approaches to limit LMD-corner material overflow.

Reference	Tuning variable	Studied angle(s)	Advantages	Disadvantages
Ref. [124]	Tool-head velocity	30°, 60°, 90°	Avoids trial-and-error experimentation	No experimental validation Single-layer deposition
Ref. [140]	Tool-head velocity	90°	Multi-layer deposition: 50 layers, 25 mm height	Test only with 90° angle Corner smoothing Trial-and-error experimentation
Ref. [193]	Tool-head velocity	90°	Multi-layer deposition: 70 layers, 11.5 mm height	Test only with 90° angle Trial-and-error experimentation
Ref. [10]	Laser power	30°	Fast response time of laser power control hardware	Single-layer deposition Requires specialized vision hardware Test only with 30° angle Changes bead material properties
Ref. [7]	Powder feed rate	90°	Significant reduction of overflow	Slow response time of the powder rate controller Single-layer deposition Test only with 90° angle
This work	Tool-head velocity	15°, 30°, 45°, 60°, 75°	Avoids trial-and-error experimentation Several angles studied	Single-layer deposition May lead to underfill

III.D.4.3.2 Registration for dimensional inspection

The main techniques for non-destructive dimensional inspection in AM are contact-measurement machines, X-ray Computer Tomography (XCT), and 3D scanning (Ref. [27]).

Ref. [152] and Ref. [82] use contact-measurement machines to assess the geometrical accuracy in parts produced by powder bed fusion and fused filament fabrication, respectively. Contact-measurement machines are the most accurate devices for dimensional inspection in parts manufac-

tured by subtractive methods. However, the surface irregularities in the parts produced via AM disturb the measurements of these machines.

XCT is used in Ref. [83] to measure the porosity and in Ref. [185] to evaluate the internal features in AM-manufactured parts. However, the scanning time of XCT is very high (Ref. [83]). In addition, the voxel format of the XCT method requires additional processing to deliver surface measurement readings.

3D scanning is advantageous because it (i) provides detailed information of the workpiece surface, (ii) offers short data gathering time, and (iii) avoids having contact with the workpiece (Ref. [27]). Ref. [88] uses structured-light scanning to examine the surface roughness and thickness distribution in flat pieces built via Wire-and-Arc AM. Ref. [131] uses 3D scanning to estimate the volume and the surface roughness of thin plate-based structures also manufactured with Wire-and-Arc AM. Ref. [204] uses structured-light scanning to analyze the accuracy of dental models fabricated via several AM techniques such as, digital light processing, multi-jet printing, and stereolithography. Ref. [84] applies 3D laser scanning to reverse - engineer a metal impeller.

For the analysis of dimensional accuracy, the data acquired via 3D scanning must be registered (i.e., aligned) with a reference coordinate system. The standard registration approaches (e.g. Iterative Closest Point (ICP) and feature identification) statistically minimize the distance between the scanned data and a reference (target) model.

The ICP method iteratively applies rigid transformations over the scanned data. These rigid transformations minimize the overall distance between the scanned data and the target model (Ref. [212]). The feature identification method in Ref. [159] processes some particular entities (features) of the workpiece (e.g. planes, spheres, and cones). In this method, an experienced user selects the geometrical features to register between the scanned data and the target model. An overall distance minimization is then applied to simultaneously align all the selected features.

Both conventional and additive manufacturing employ distance-based registration. For example, Ref. [44] uses ICP to measure the deviation of workpieces built via fused filament fabrication, while Ref. [112] uses ICP for in-line dimensional inspection of warm forged workpieces. However, for the purpose of this work, overall distance-based registration methods cannot be used. The reason is that, when several datums are to be extracted from a point cloud sample, the overall registration moves the sampled points to an equidistant position to all the datums simultaneously. This even-handed approach dramatically biases the sampled data thus disabling any subsequent conclusions about deviation of individual features. In particular, in the scenario of LMD bead overfills, the assessment of a specific corner feature would be impossible. In particular, overall registrations would impede the evaluation of the strategy in Ref. [124] to minimize material overfill of bead corners in LMD.

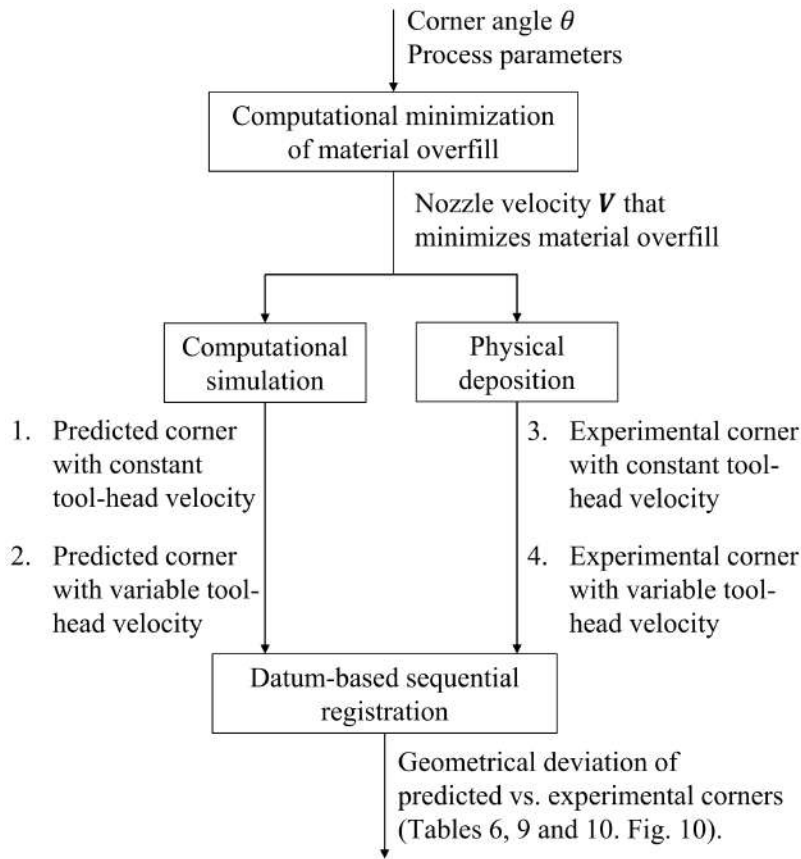


Figure III.D.4.1: Prediction vs. Experiment assessment. Minimization of bead corner overfill by using variable tool-head velocity (follow up from Ref. [124]).

III.D.4.3.3 Bead topography models

Existing literature shows two main trends in bead geometry modeling. In the first strategy, the bead cross-section is approximated by a predefined function. Refs. [25, 135] study the ability of parabolic, sinusoidal, and elliptical profiles to model the bead cross-section in LMD. Ref. [25] considers only single-track deposition. Ref. [135] considers multi-track and multi-layer deposition. In both studies (Refs. [25, 135]), the parabolic profile provides the best fit with respect to experimental data. Refs. [186, 200] use parabolic cross-section profile in the simulation of 2D finite element thermal [200] and thermo-fluid [186] models. Ref. [210] develops an analytical model to measure the laser power attenuation due to the interaction with the metal powder particles and uses an elliptical cross-section. All the previous approaches only model the bead cross-section. They do not address the spatial evolution of the bead geometry under instantaneous changes in the tool-head velocity or material flow rate.

In the second strategy, the distribution of the delivered material on the substrate surface governs the bead geometry. This approach links the bead geometry with instantaneous variations in the tool-head velocity and powder flow rate. Ref. [178] concludes that, for coaxial nozzles, the powder on

the substrate surface follows a Gaussian distribution. Ref. [55] shows that the Gaussian distribution induces good approximations at the bead centerline but not at the sides of the bead cross-section. Refs. [6, 179] use the Gaussian profile in the 3D finite element simulation of a thermo-fluid model. The model is used to estimate the evolution of the temperature of the melt-pool and the bead geometry.

As a conclusion, the literature survey indicates that, with the current LMD hardware, the tool-head velocity is a popular mean to diminish overfill in LMD bead corners. However, most of the works that attempt to tailor the tool-head velocity are based on trial-and-error experimentation, which is costly in time and materials. Ref. [124], a precursor of the present manuscript, reports a computational approach to adjust the tool-head velocity to reduce the material overfill at corners in LMD.

Table III.D.4.1 summarizes the existing approaches to limit material overfill in LMD trajectory corners.

The present work focuses on the experimental validation of the method presented in Ref. [124]. The experiment consists in the deposition of single-layer corners with angles $\theta \in \{15^\circ, 30^\circ, 45^\circ, 60^\circ, 75^\circ\}$ built with and without using the tool-head velocity variation in Ref. [124]. It must be remarked that such a validation entails the development and application of a datum-based sequential registration of LMD samples for dimensional inspection.

This manuscript does not intend to predict the portion of the metal powder that does not integrate into the bead. Notice that the powder loss occurs independently of the existence or absence of trajectory corners. Powder loss and bead overfill are both present at LMD trajectory corners. This manuscript addresses only the minimization of corner bead overfill.

III.D.4.4 Methodology

This manuscript reports the experimental validation of the computational method presented in Ref. [124]. Fig. III.D.4.1 shows the procedure followed in this work to assess the deposition of single-layer corners of angles $\theta \in \{15^\circ, 30^\circ, 45^\circ, 60^\circ, 75^\circ\}$. For each corner angle, four results are generated:

1. Corner predicted by simulating the deposition with constant nozzle velocity.
2. Corner predicted by simulating the deposition with variable nozzle velocity (Ref. [124]).
3. Corner physically built with constant nozzle velocity.
4. Corner physically built with the same nozzle velocity as in item (2) above (variable nozzle velocity provided by the method in Ref. [124]).

Observe that datasets (1), (2), (3) and (4) must be expressed in the same coordinate system in order to permit comparison. This conversion is called *registration* and it is implemented via a rigid transformation \mathbf{M} . \mathbf{M} is synthesized as the most plausible function that matches specific datums or features in those datasets.

The following sections discuss in detail how the predicted and the experimental corners are generated.

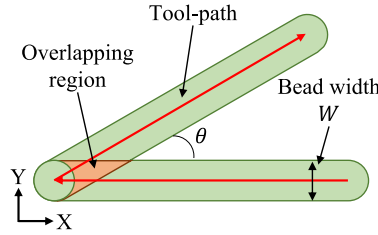


Figure III.D.4.2: Plant view of the overlapping region in the vicinity of the corner.

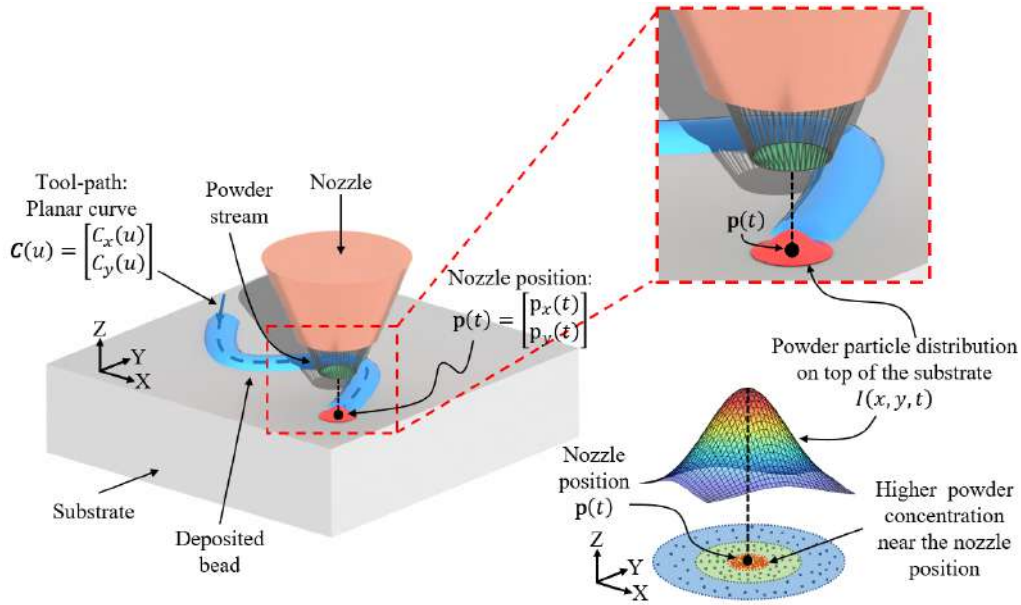


Figure III.D.4.3: Geometric simulation of material deposition. The function $I(x, y, t)$ represents the powder concentration $[\text{kg}/(\text{mm}^2 \text{ s})]$ at the substrate surface.

III.D.4.4.1 Material overfill in trajectory corners in LMD

In LMD of corners, the following circumstances are present to compound metal overfill:

1. Geometrical overlap: Fig. III.D.4.2 shows that material is redundantly deposited in the intersection region around the corner. Unwanted material accumulation in this overlapping region increases with sharper corner angles.
2. Tool-head deceleration: The tool-head must decelerate to draw the corner. Since the powder feed rate remains basically constant, this deceleration concentrates more material in the vicinity of the corner.
3. Hardware limitations: Current hardware does not offer real-time variation of the powder flow rate. Although the material feed rate can be adjusted, the response of the feed system is slow, rendering a basically constant rate (Refs. [10, 50, 193]).

4. Software limitations: Current software for process planning in AM does not consider material overflow at corners during the generation of the nozzle trajectory.

III.D.4.4.2 Geometry deposition simulator

This manuscript follows the procedure in Ref. [124] to simulate the deposited geometry in the LMD process. A description of this procedure follows.

Let the planar curve $\mathbf{C}(u) = [C_x(u), C_y(u)]^T$, $0 \leq u \leq 1$, be the tool-head path (see Fig. III.D.4.3). The function $I(x, y, t)$ denotes the powder concentration [kg/(mm²s)] at the substrate surface where the nozzle is depositing the powder. The function I describes variable powder feed rate [kg/s] and tool-head velocity [mm/s]. In this manuscript (as in Ref. [124]), I follows a Gaussian distribution:

$$I(x, y, t) = \frac{2f(t)}{\pi R^2} \exp\left(\frac{-2\left((x - p_x(t))^2 + (y - p_y(t))^2\right)}{R^2}\right), \quad (\text{III.D.4.1})$$

where $\mathbf{p}(t) = [p_x(t), p_y(t)] \in \mathbf{C}$ is the nozzle position, $f(t)$ [kg/s] is the powder flow rate and R [mm] is half of the bead width W [mm].

As an example of the physical meaning of the function I , assume the tool-head is at $\mathbf{p} = [0, 0]$ and it remains static. Also let the bead width be $W = 2$ mm ($R = 1$ mm) and the powder flow rate f be constant. The mass M [kg] deposited on a region $D \subset \mathbb{R}^2$ on the substrate surface is:

$$\begin{aligned} M &= \int_0^t \int_D I(x, y, t) dx dy dt \\ &= \frac{2f\Delta t}{\pi} \int_D e^{-2(x^2+y^2)} dx dy \end{aligned} \quad (\text{III.D.4.2})$$

where Δt [s] is the time span. The total mass delivered by the nozzle is $M_T = f \Delta t$.

Consider the two circular regions D_1 and D_2 on the substrate surface in Eqs. III.D.4.3 and III.D.4.4. The center of D_1 is at the same position as the tool-head. The center of D_2 is 0.8 mm away from the tool-head position. D_1 and D_2 have the same area.

$$D_1 = \{(x, y) : x^2 + y^2 \leq 0.1^2\} \quad (\text{III.D.4.3})$$

$$D_2 = \{(x, y) : (x - 0.8)^2 + y^2 \leq 0.1^2\} \quad (\text{III.D.4.4})$$

Recalling Eq. III.D.4.2, the mass deposited on D_1 is $M_1 \approx 0.02M_T$. The mass deposited on D_2 is $M_2 \approx 0.006M_T$. This result shows that, assuming a Gaussian I , the powder concentration is larger at the center point of the laser.

III.D.4.4.2.1 Computational simulation

Eq. III.D.4.1 implies that the bead height H at time t , with material density ρ [kg/m³], is:

$$H(x, y, t) = \frac{1}{\rho} \int_0^t I(x, y, \xi) d\xi. \quad (\text{III.D.4.5})$$

In order to numerically estimate the bead height H in Eq. III.D.4.5, the substrate surface is discretized into a rectangular grid (Fig. III.D.4.4) with vertices (x_i, y_j) . The tool-path curve \mathcal{C} is approximated by the piecewise linear curve $\mathcal{C}^{PL} = [\mathbf{c}_0, \mathbf{c}_1, \dots, \mathbf{c}_N], \mathbf{c}_k \in \mathcal{C}$. The tool-head velocity and the powder flow rate at $\mathbf{c}_k \in \mathcal{C}^{PL}$ are v_k and f_k , respectively.

Let t_k be the instant at which the nozzle is at \mathbf{c}_k . The height H_{ij} at the grid vertex (x_i, y_j) is approximated as in Ref. [124]:

$$H_{ij} = H(x_i, y_j) = \frac{1}{\rho} \sum_{k=1}^N \int_{t_{k-1}}^{t_k} I(x_i, y_i, \xi) d\xi \quad (\text{III.D.4.6})$$

The integral in Eq. III.D.4.6 is solved using numerical integration.

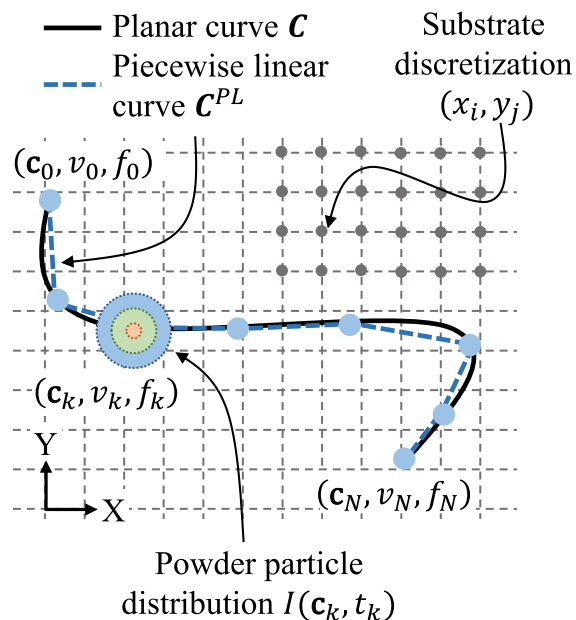


Figure III.D.4.4: Piecewise linear approximation of the tool-path. Voxel discretization of the substrate surface. The tool-path discretization is not constrained to the grid vertices.

III.D.4.4.3 Minimization of material overfill at corners in LMD

The present work follows Ref. [124] to minimize the metal overfill at trajectory corners in LMD. This optimization procedure finds the tool-head velocity function $V(t)$ that minimizes the material overfill at the corner.

Ref. [124] defines an ideal bead corner topography with no overfill. In it, the corner exit trajectory is defined as a rotation of the entry one. This rotation by the corner angle θ pivots at the corner tip.

Eq. III.D.4.7 (Ref. [124]) computes the bead height of an infinite linear trajectory along the X -

axis at steady conditions. v_c is the tool-head velocity [mm/s], and f is the powder flow rate [kg/s].

$$\begin{aligned} H_0(x, y) &= \int_{-\infty}^{\infty} I(x, y, t) dt \\ &= \frac{\sqrt{2}f}{\rho\sqrt{\pi}Rv_c} \exp\left(\frac{-2y^2}{R^2}\right). \end{aligned} \quad (\text{III.D.4.7})$$

The ideal corner for the angle θ , H_G^θ , is built by joining H_0 and its corresponding θ rotation. Fig. III.D.4.5 depicts the ideal corner H_G^θ for $\theta = 30^\circ$ for the process parameters in Table III.D.4.2.

Table III.D.4.2: Experimental set-up. Parameters used in the experiments.

Parameter	Value
Material	<i>Stellite 6</i>
Density	$\rho = 8400 \text{ kg/m}^3$
Nozzle cruising velocity	$v_c = 6.67 \text{ mm/s}$
Powder flow rate	$f = 0.12 \text{ g/s}$
Laser power	$P = 1200 \text{ W}$
Bead width	$W = 2R = 2.6 \text{ mm}$
Maximal velocity	$v_{\max} = 2v_c = 13.33 \text{ mm/s}$

Eqs. III.D.4.8 and III.D.4.9 pose the optimization problem presented in Ref. [124]. The problem is stated for a substrate surface discretized into a rectangular grid. N_{row} and N_{col} denote the number of rows and columns of the grid. The tuning variable, $V(t)$, is the tool-head velocity function that, for a given angle θ , produces the corner most similar to the ideal corner. The function $e(\mathbf{x})$ in Eq. III.D.4.9 (Ref. [124]) measures the discrepancy between the ideal corner and the corner achieved with the tuning tool-head velocity V .

$$\begin{aligned} &\text{find } V(t) \\ &\text{to minimize } E(V) = \\ &\quad \frac{1}{N_{\text{row}} \cdot N_{\text{col}}} \sum_{i=0}^{N_{\text{col}}} \sum_{j=0}^{N_{\text{row}}} e(x_i, y_j)^2 \end{aligned} \quad (\text{III.D.4.8})$$

$$\text{subject to } 0 < V(t) \leq v_{\max};$$

with

$$e(\mathbf{x}) = \begin{cases} |H(\mathbf{x}) - H_G^\theta(\mathbf{x})|, & \text{if } H(\mathbf{x}) < H_G^\theta(\mathbf{x}), \\ & \text{i.e. underfill} \\ 0, & \text{if } H_G^\theta(\mathbf{x}) \leq H(\mathbf{x}) \leq \max(H_G^\theta), \\ & \text{i.e. permissible overfill} \\ H(\mathbf{x}) - \max(H_G^\theta), & \text{if } H(\mathbf{x}) > \max(H_G^\theta), \\ & \text{i.e. overfill} \end{cases} \quad (\text{III.D.4.9})$$

In Eq. III.D.4.9, $\max(H_G^\theta) = \frac{\sqrt{2}f}{\rho\sqrt{\pi}Rv_c}$ is the maximum height of the ideal corner H_G^θ .

The present work (implemented in MATLAB) uses an exhaustive search to approximate solutions for this optimization problem. Table III.D.4.3 reports the parameters used in the numerical optimization. The corner entry and exit trajectories, bead topography and velocity V are assumed to be reflections of each other with respect to the plane that bisects the corner (Fig. III.D.4.5). Moreover, it is assumed that V is a piecewise linear (w.r.t. time) function with four stages.

Table III.D.4.3: Parameters used in the numerical optimization.

Parameter	Value
Optimization method	Exhaustive search
Length of the corner segment	20 mm
Voxel size	0.01 mm
Size of trajectory discretization	0.01 mm
Software	MATLAB

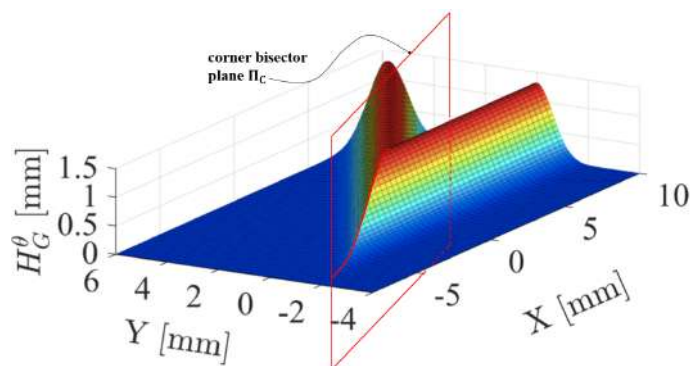


Figure III.D.4.5: Ideal corner H_G^θ for $\theta = 30^\circ$ (Eq. III.D.4.7) and corner bisector plane Π_C . Process parameters in Table III.D.4.2.

III.D.4.4.4 Materials for the experiments and the 3D scanning

The corner deposition experiments were executed with an *IPG Photonics YLS-6000* high-power fiber laser. The laser beam diameter was 2.5 mm. The optical head was placed in a 3-linear-axis machine. The metal powder was deposited through a coaxial nozzle with Nitrogen as carrier gas. The powder material used was *Stellite 6*, and the substrate was *S355* carbon steel. The powder flow rate, tool-head velocity, and laser power are listed in Table III.D.4.2.

The deposited corners were scanned with the *Gocator 3210* structured-light scanner. The maximum accuracy of the scanner is $35 \mu\text{m}$. The scanner light source is a blue LED emitted at wavelength 465 nm. To adequately capture the details of the workpieces, the scanner was integrated with the *Universal Robots UR10* 6-axis robot arm. Several captures of the workpieces were taken at different poses of the robot. The captures were then consolidated in the same coordinate system to obtain the corresponding 3D mesh of the workpiece.

III.D.4.4.5 Registration of the experimental corners

By definition, an overall standard registration would seek to minimize the distances between the predicted and the experimental plate - bead - corner data. This fact would bias the assessment of the effectiveness of the overfill minimization algorithm. Because of this reason, the present work uses instead a local probing datum-based sequential registration (Fig. III.D.4.6), implemented in MATLAB, that avoids such a bias.

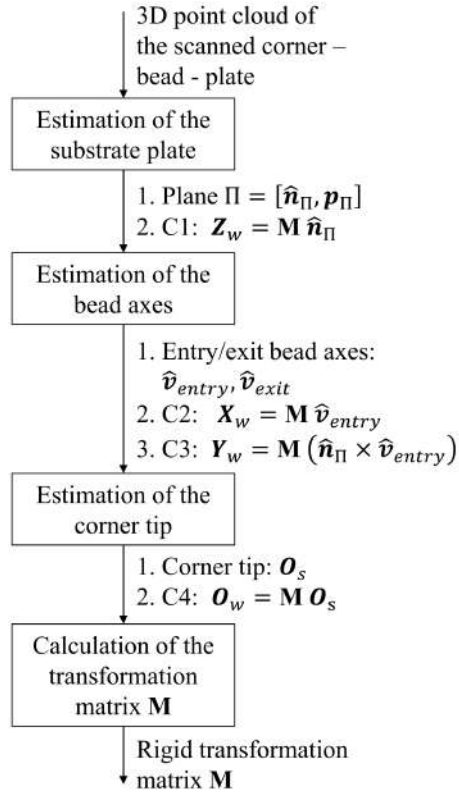


Figure III.D.4.6: Registration of the 3D point cloud of the experimental corner. Steps of the proposed datum-based sequential registration.

III.D.4.4.5.1 Problem statement

Given the 3D scanned data (point cloud) of the corner, $S_{\text{sample}} \subset \mathbb{R}^3$, one must find the rigid transformation

$$\mathbf{M} = \begin{bmatrix} \mathbf{R} & \mathbf{T} \\ \mathbf{0} & 1 \end{bmatrix}; \quad \mathbf{R} \in \text{SO}(3); \quad \mathbf{T} \in \mathbb{R}^3; \quad (\text{III.D.4.10})$$

from the local coordinate system to the World Coordinate System $[\mathbf{X}_w, \mathbf{Y}_w, \mathbf{Z}_w, \mathbf{O}_w]$, as shown in Fig. III.D.4.7. The matrix \mathbf{M} is different for each scanned corner.

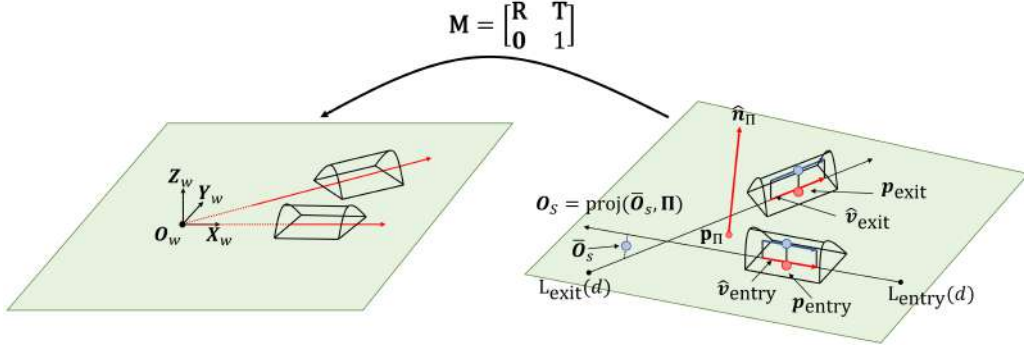


Figure III.D.4.7: Registration of the scanned data with the World Coordinate System. Estimation of the plane of the substrate plate surface and the lines of the bead axes.

III.D.4.4.5.2 Estimation of the substrate plate

The 3D point cloud S_{sample} is segmented into four subsets:

$$S_{\text{sample}} = S_{\text{plate}} \cup S_{\text{entry}} \cup S_{\text{exit}} \cup S_{\text{rest}}. \quad (\text{III.D.4.11})$$

S_{plate} contains the points on the substrate plate. S_{entry} and S_{exit} contain the points on the steady-state regions of the entry and exit beads. S_{rest} contains all the other points.

The substrate plate surface is represented by a plane $\Pi = (\hat{\mathbf{n}}_{\Pi}, \mathbf{p}_{\Pi})$. As usual, $\hat{\mathbf{n}}_{\Pi}$ = plate normal vector, \mathbf{p}_{Π} = any point on the plane. $\hat{\mathbf{n}}_{\Pi}$ is the direction of least variance of the point sample, and is determined via Principal Component Analysis. \mathbf{p}_{Π} is estimated as the center of gravity of S_{plate} (Eq. III.D.4.12):

$$\mathbf{p}_{\Pi} = \text{CG}(S_{\text{plate}}). \quad (\text{III.D.4.12})$$

The normal vector $\hat{\mathbf{n}}_{\Pi}$ sets the first constraint $C1$ needed to find \mathbf{M} :

$$C1 : \mathbf{Z}_w = \mathbf{M} \hat{\mathbf{n}}_{\Pi}. \quad (\text{III.D.4.13})$$

III.D.4.4.5.3 Estimation of the bead axes

Let $L_{\text{entry}} \subset \Pi$ be the line defining the axis of the entry bead:

$$L_{\text{entry}}(d) = \mathbf{p}_{\text{entry}} + d \hat{\mathbf{v}}_{\text{entry}}, \quad d \in \mathbb{R}. \quad (\text{III.D.4.14})$$

The definitions of $\hat{\mathbf{v}}_{\text{entry}}$ and $\mathbf{p}_{\text{entry}}$ follow. Let $\mathbf{v}_{\text{entry}}^*$ be the direction of maximum variability of the points in S_{entry} . This direction is estimated via Principal Component Analysis. The direction vector of L_{entry} , $\hat{\mathbf{v}}_{\text{entry}}$, is the projection of $\mathbf{v}_{\text{entry}}^*$ onto Π :

$$\hat{\mathbf{v}}_{\text{entry}} = \text{proj}(\mathbf{v}_{\text{entry}}^*, \Pi). \quad (\text{III.D.4.15})$$

$\mathbf{p}_{\text{entry}}$ can be estimated as the projection of the CG of S_{entry} onto Π :

$$\mathbf{p}_{\text{entry}} = \text{proj}(\text{CG}(S_{\text{entry}}), \Pi). \quad (\text{III.D.4.16})$$

An analogous procedure is used to find the axis of the exit bead $L_{\text{exit}} \subset \Pi$. Fig. III.D.4.7 shows a graphical representation of the entities involved in this process.

The direction vector of L_{entry} sets the second constraint $C2$ needed to find \mathbf{M} :

$$C2 : \mathbf{X}_w = \mathbf{M} \hat{\mathbf{v}}_{\text{entry}} \quad (\text{III.D.4.17})$$

Since \mathbf{M} represents a rigid transformation, the following constraint, $C3$, arises as a consequence of $C1$ and $C2$:

$$C3 : \mathbf{Y}_w = \mathbf{M} (\hat{\mathbf{n}}_{\Pi} \times \hat{\mathbf{v}}_{\text{entry}}) \quad (\text{III.D.4.18})$$

$C1$, $C2$ and $C3$ determine the $\text{SO}(3)$ vector triad of the coordinate system for the scanned data S_{sample} .

III.D.4.4.5.4 Estimation of the corner tip

The corner tip $\mathbf{O}_s \in \Pi$ is estimated as the intersection between L_{entry} and L_{exit} . \mathbf{O}_s is computed as per Eq. III.D.4.19:

$$\mathbf{O}_s = \text{proj}(\bar{\mathbf{O}}_s, \Pi) \quad (\text{III.D.4.19})$$

where $\bar{\mathbf{O}}_s$ is the midpoint of the shortest segment that joins L_{entry} and L_{exit} . The final constraint $C4$ needed to compute \mathbf{M} is:

$$C4 : \mathbf{O}_w = \mathbf{M} \mathbf{O}_s \quad (\text{III.D.4.20})$$

Recalling constraints $C1$, $C2$, $C3$ and $C4$, the following linear equation is obtained, with \mathbf{M} as the unknown variable:

$$\begin{bmatrix} \mathbf{Z}_w & \mathbf{X}_w & \mathbf{Y}_w & \mathbf{O}_w \\ 0 & 0 & 0 & 1 \end{bmatrix} = \mathbf{M} \begin{bmatrix} \hat{\mathbf{n}}_{\Pi} & \hat{\mathbf{v}}_{\text{entry}} & \hat{\mathbf{n}}_{\Pi} \times \hat{\mathbf{v}}_{\text{entry}} & \mathbf{O}_s \\ 0 & 0 & 0 & 1 \end{bmatrix} \quad (\text{III.D.4.21})$$

The rigid transformation matrix \mathbf{M} is then calculated as:

$$\mathbf{M} = \begin{bmatrix} \mathbf{Z}_w & \mathbf{X}_w & \mathbf{Y}_w & \mathbf{O}_w \\ 0 & 0 & 0 & 1 \end{bmatrix} \begin{bmatrix} \hat{\mathbf{n}}_{\Pi} & \hat{\mathbf{v}}_{\text{entry}} & \hat{\mathbf{n}}_{\Pi} \times \hat{\mathbf{v}}_{\text{entry}} & \mathbf{O}_s \\ 0 & 0 & 0 & 1 \end{bmatrix}^{-1} \quad (\text{III.D.4.22})$$

Notice that with the implemented method, the upper left (3×3) sub-matrix of \mathbf{M} (i.e. \mathbf{R} in Eq. III.D.4.10) is indeed Special Orthogonal $\text{SO}(3)$.

III.D.4.5 Results

III.D.4.5.1 Computational results

III.D.4.5.1.1 Tool-head velocity profiles

The optimization approach in Section III.D.4.4.3 is used to find tool-head velocity functions that locally minimize the overfill in corners. Computer runs were executed for angles $\theta \in \{15^\circ, 30^\circ, 45^\circ, 60^\circ, 75^\circ\}$.

Fig. III.D.4.8 shows, for each angle, the obtained velocity profile V as function of the signed distance d (measured in plant view along the bead) to the corner tip [mm]. As expected, (i) the velocity increases in the vicinity of the corner tip ($d = 0$) in all cases, and (ii) the velocity increment occurs sooner for smaller angles.

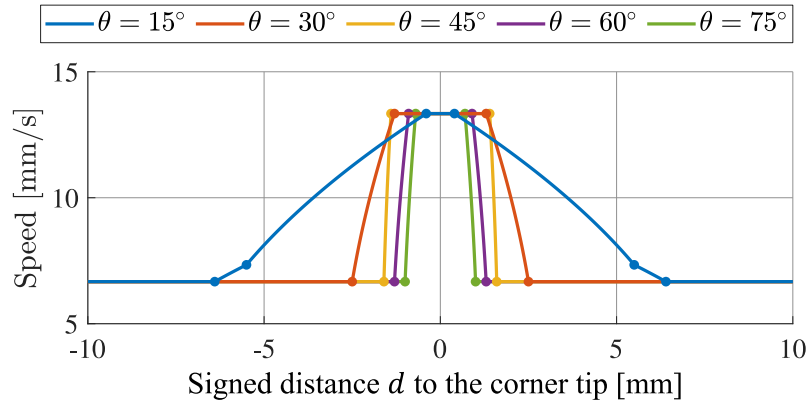


Figure III.D.4.8: Tool-head velocity profiles obtained via numerical optimization for $\theta \in \{15^\circ, 30^\circ, 45^\circ, 60^\circ, 75^\circ\}$. Process parameters in Table III.D.4.2. For entry stage, $d \leq 0$. For exit stage, $d \geq 0$.

Table III.D.4.4: Predicted bead geometry by the voxel-based simulator. Comparison of the corners simulated with constant and variable tool-head velocity.

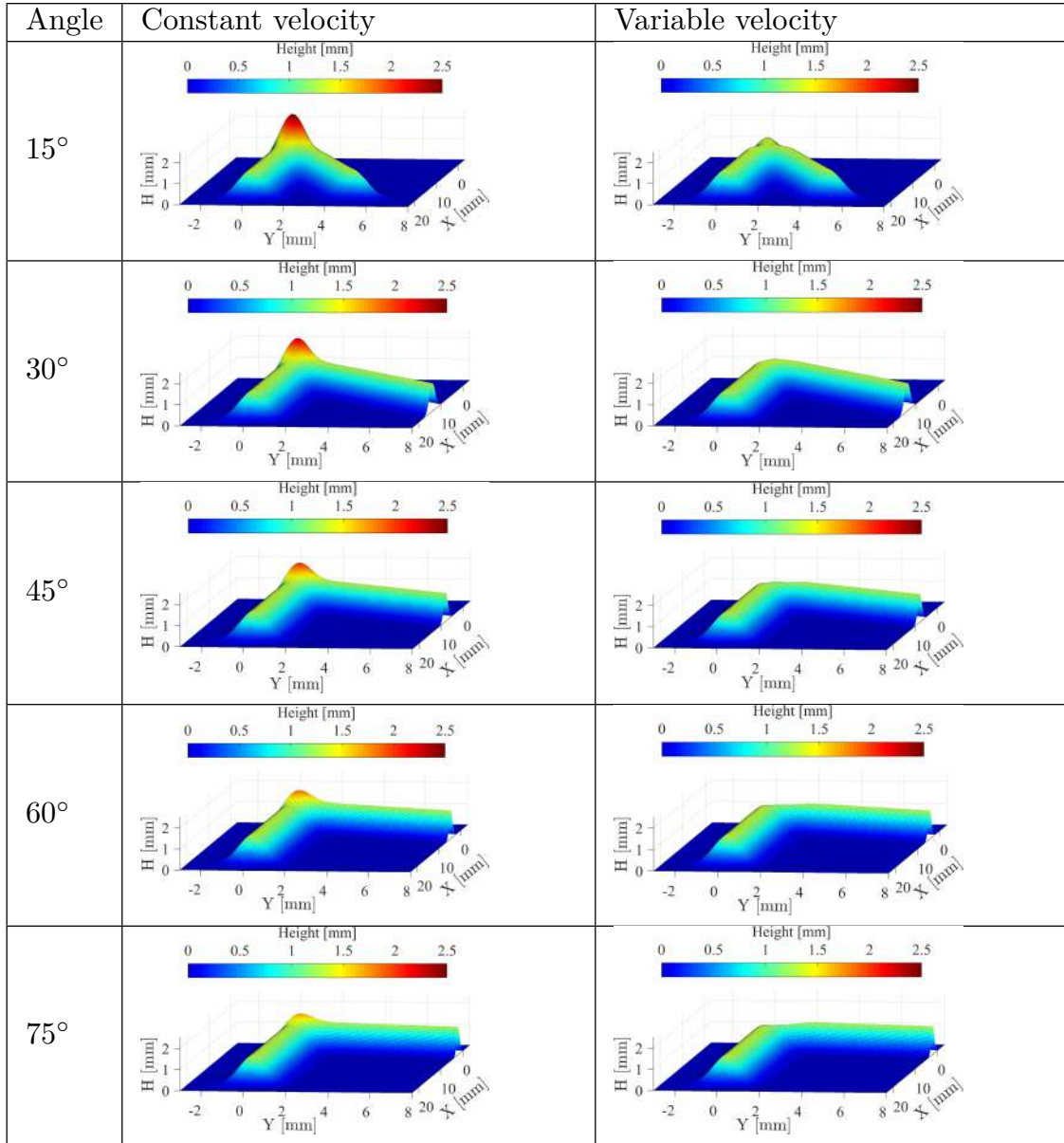


Table III.D.4.5: Experimental datasets. Deposited corners with constant and variable tool-head velocity.






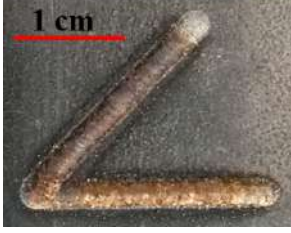




Angle	Uncontrolled velocity	Controlled velocity
15°	 A photograph of a 15-degree corner formed by a metal rod. The corner is relatively smooth. A red horizontal line with the text "1 cm" is positioned above the rod.	 A photograph of a 15-degree corner formed by a metal rod. The corner is smooth. A red horizontal line with the text "1 cm" is positioned above the rod.
30°	 A photograph of a 30-degree corner formed by a metal rod. The corner shows some surface irregularities. A red horizontal line with the text "1 cm" is positioned above the rod.	 A photograph of a 30-degree corner formed by a metal rod. The corner is smooth. A red horizontal line with the text "1 cm" is positioned above the rod.
45°	 A photograph of a 45-degree corner formed by a metal rod. The corner shows some surface irregularities. A red horizontal line with the text "1 cm" is positioned above the rod.	 A photograph of a 45-degree corner formed by a metal rod. The corner is smooth. A red horizontal line with the text "1 cm" is positioned above the rod.
60°	 A photograph of a 60-degree corner formed by a metal rod. The corner shows some surface irregularities. A red horizontal line with the text "1 cm" is positioned above the rod.	 A photograph of a 60-degree corner formed by a metal rod. The corner is smooth. A red horizontal line with the text "1 cm" is positioned above the rod.
75°	 A photograph of a 75-degree corner formed by a metal rod. The corner shows some surface irregularities. A red horizontal line with the text "1 cm" is positioned above the rod.	 A photograph of a 75-degree corner formed by a metal rod. The corner is smooth. A red horizontal line with the text "1 cm" is positioned above the rod.

Table III.D.4.6: Experimental validation. Columns 1-2: registered scanned data of the physical specimens in Table III.D.4.5. Column 3: bead height of variable vs. constant tool-head velocity at $Y = 0$.

Angle	Uncontrolled velocity	Controlled velocity	Controlled vs. uncontrolled velocity. Cross-section $Y = 0$
15°			
30°			
45°			
60°			
75°			

Table III.D.4.7: Bead height at the corner. Experimental corners. Constant vs. variable tool-head velocity.

Angle	Constant velocity		Variable velocity	
	Average height. Over-deposition zone	Deviation ⁱ	Average height. Over-deposition zone	Deviation ⁱ
$\theta = 15^\circ$	1.1 mm	0.32 mm (61%)	0.6 mm	-0.08 mm (-12%)
$\theta = 30^\circ$	1.0 mm	0.27 mm (47%)	0.6 mm	-0.08 mm (-12%)
$\theta = 45^\circ$	0.8 mm	0.12 mm (17%)	0.5 mm	-0.18 mm (-27%)
$\theta = 60^\circ$	0.9 mm	0.22 mm (32%)	0.6 mm	-0.08 mm (-12%)
$\theta = 75^\circ$	0.9 mm	0.22 mm (32%)	0.6 mm	-0.08 mm (-12%)

ⁱMeasured w.r.t. the average bead height in the steady zones: 0.68 mm.

III.D.4.5.1.2 Predicted corners with constant and variable tool-head velocity

Table III.D.4.4 shows the corners predicted by the geometrical simulator with variable (Fig. III.D.4.8) and constant tool-head velocity. Table III.D.4.4 shows significant material overfill at the corners simulated with constant tool-head velocity. The metal overfill is larger for sharper corners ($\theta \in \{15^\circ, 30^\circ\}$). As a result of the corner overfill minimization, the corners with variable tool-head velocity have a more uniform material distribution along the whole trajectory.

III.D.4.5.2 Experimental validation

Table III.D.4.5 presents the experimental corners resulting from constant and variable tool-head velocity. Table III.D.4.6 shows the registered scanned data corresponding to the physical corners depicted in Table III.D.4.5. The comparisons in Table III.D.4.6 demonstrate that the application of tool-head velocity variation significantly reduces material overfill at the corners. The height of the corners deposited with variable tool-head velocity is more uniform than the height of the corners built with constant velocity, such as previously observed in the simulated corners.

Table III.D.4.7 compares the bead height in the overfill zone for the corners resulting from constant and variable tool-head velocity. The average height of the 10 registered datasets at the steady-state region of the entry bead is 0.68 mm. Fig. III.D.4.9 shows the bead height deviation in the overfill zone for the experimental corners resulting from constant and variable tool-head velocity.

Constant tool-head velocity. (i) the average bead height in the overfill zone is, as expected, above the reference value (0.68 mm) and (ii) except for $\theta = 45^\circ$, the height deviation w.r.t. the reference value is above 30%. These two facts show that the material overfill at the corner is noticeable when the tool-head velocity is kept constant.

Variable tool-head velocity. The bead height deviation nears 10% (except for $\theta = 45^\circ$). It is a significant reduction when compared against the constant tool-head velocity case. The average height in the overfill zone is below the reference value for all the studied angles. It shows that the present approach tends to generate material underfill at the corner. This aspect is particularly apparent for $\theta = 45^\circ$, where the height deficit of the corner with variable tool-head velocity (27%) is higher than for the corner with constant tool-head velocity (17%).

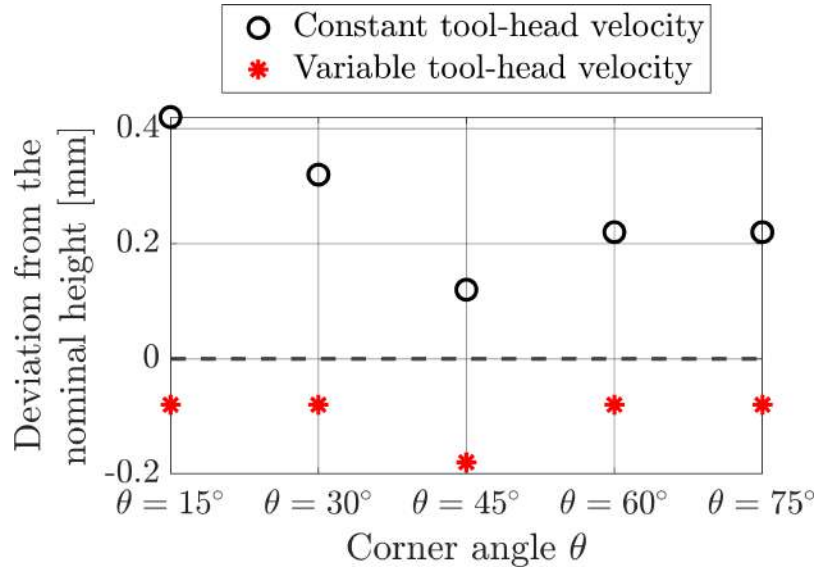


Figure III.D.4.9: Experimental corners. Constant vs. variable tool-head velocity. Bead height deviation (Table III.D.4.7) in the overfill zone.

Table III.D.4.8: Volume of the predicted and experimental corners.

Angle	Constant velocity		Variable velocity	
	Predicted corner	Experimental corner	Predicted corner	Experimental corner
$\theta = 15^\circ$	85.7 mm ³	51.3 mm ³	76.9 mm ³	43.7 mm ³
$\theta = 30^\circ$	85.7 mm ³	49.5 mm ³	81.2 mm ³	45.0 mm ³
$\theta = 45^\circ$	85.7 mm ³	49.3 mm ³	82.4 mm ³	46.3 mm ³
$\theta = 60^\circ$	85.7 mm ³	51.9 mm ³	83.2 mm ³	49.7 mm ³
$\theta = 75^\circ$	85.7 mm ³	55.1 mm ³	83.7 mm ³	51.4 mm ³

III.D.4.5.3 Comparison of the predicted vs. experimental corners

Table III.D.4.8 reports the volume of the predicted and experimental corners. The volume of the predicted corners is larger than the volume of the experimental corners. The predicted corners are

Table III.D.4.9: Corners built with constant tool-head velocity. Predicted ($\eta = 0.59$) vs. experimental data sets.

Angle	Predicted ($\eta = 0.59$)	Experimental	Predicted vs. experimental. Cross-section $Y = 0$
15°			
30°			
45°			
60°			
75°			

Table III.D.4.10: Corners built with variable tool-head velocity. Predicted ($\eta = 0.59$) vs. experimental data sets.

Angle	Predicted ($\eta = 0.59$)	Experimental	Predicted vs. experimental. Cross-section $Y = 0$
15°			
30°			
45°			
60°			
75°			

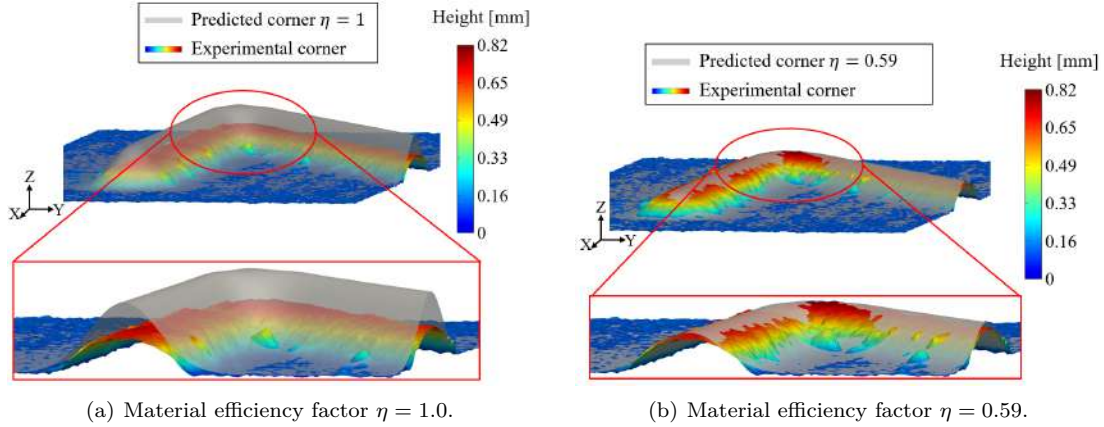


Figure III.D.4.10: Predicted vs. experimental datasets. Corners built with variable velocity. Corner angle $\theta = 30^\circ$.

simulated with the nominal powder flow rate f with the assumption that all the powder material is indeed melted and becomes part of the bead. However, it does not occur in the real LMD process, where an amount of the powder material is wasted (independently from corner existence). The effective powder flow rate f_{eff} , which models the amount of powder that effectively becomes part of the bead is:

$$f_{\text{eff}} = \eta * f, \quad (\eta \in [0, 1]) \quad (\text{III.D.4.23})$$

where $\eta \in [0, 1]$ is the material efficiency factor.

The value of η was approximated as the average ratio of the volume of the experimental vs. the predicted corners reported in Table III.D.4.8. The obtained value was $\eta \approx 0.59$. This value shows that, on average, 41% of the powder is wasted in the deposition of the 10 corners.

The predicted model for volume estimation in both constant and variable velocity differs from the measured volume, mainly due to material waste in the process (still difficult to adjust in the theoretical model). But a good experimental result is that the variable velocity approach indeed reduces sensibly the measured overflow at the corners, and that this reduction effect is more pronounced in sharper angles -columns 2 and 4 in Table III.D.4.8-. Thus, for the sharper angle of 15° the volume reduction is about 16% (43.7 vs. 51.3 mm³).

Tables III.D.4.9 and III.D.4.10 compare the bead height trend of the predicted vs. the experimental corners with constant and variable tool-head velocity, respectively. The bead height is compared at the cross-section $Y = 0$ because it corresponds to the zone of maximum height in the entry bead. In both Tables III.D.4.9 and III.D.4.10, the bead height of the predicted datasets was adjusted with the material efficiency factor $\eta = 0.59$.

Tables III.D.4.9 and III.D.4.10 show a good agreement between the predicted and the experimental datasets. In Table III.D.4.9, the cross-sectional data at $Y = 0$ for the corners with constant tool-head velocity show that the geometrical simulator overestimates the material overflow for the sharpest corners ($\theta \in \{15^\circ, 30^\circ, 45^\circ\}$). In the other cases, $\theta \in \{60^\circ, 75^\circ\}$, the approximation of the overflow is correct. For the corners with variable tool-head velocity, Table III.D.4.10 shows that the predicted corners provide valid estimations of the shape of the experimental corners in the cross-section $Y = 0$.

Fig. III.D.4.10 presents the corner of angle $\theta = 30^\circ$ built with variable velocity. The predicted corner in Fig. III.D.4.10(a) does not consider material loss, i.e. the material efficiency factor is $\eta = 1$. In Fig. III.D.4.10(a), the predicted corner is always above the experimental corner along the whole trajectory, not only at the corner.

Fig. III.D.4.10(b) compares the predicted vs. the experimental datasets considering the material loss for the simulation of the predicted corner. This figure supports the previous findings in Table III.D.4.10, which shows that the geometrical simulator estimates the deposited bead when the effective powder efficiency is known ($\eta = 0.59$).

The previous results show the capacity of the voxel-based simulator to approximate the topography of the bead in LMD trajectory corners and to optimize it for a given set of LMD settings. It is worth mentioning that the material efficiency does not affect the optimization process. The same optimal tool-head velocity profiles are obtained for different values of material efficiency $\eta \in (0, 1]$. On the other hand, the material efficiency η (usually known to the process engineer) is required to generate accurate predictions of the bead height with the voxel-based simulator.

III.D.4.5.4 Similarities and differences with other approaches

The LMD process settings (e.g. materials, tool-head velocity, laser power) for Refs. [7, 10, 124, 140, 193] differ from one reference to the other. The hardware used is also diverse. It is therefore unfeasible to establish numerical comparisons between these works. Hence, this section qualitatively compares this work and the other approaches in Table III.D.4.1 to limit overfill in LMD trajectory corners.

1. **Tuning process variable:** Tool-head velocity (Refs. [124, 140, 193]) prevails over the powder feed rate (Ref. [7]) and the laser power (Ref. [10]) as tuning variable. The main reasons are that (i) the response time of the kinematic system is faster than the one of the powder flux system, (ii) additional hardware is not required to modify the tool-head velocity and (iii) material waste additionally weakens the powder feed rate as a tuning variable.
2. **Trial-and-error vs. computational approaches:** Trial-and-error approaches (Refs. [140, 193]) are costly in time and materials and, therefore, few angles are studied. Computational approaches (e.g. this work and Ref. [124]) reduce experimentation costs and allow the study of several corner angles. In addition, computational approaches can simulate different conditions (e.g. corner angle or process parameters) without adding considerable costs. An advantage (at the present time) of the trial-and-error approaches in Refs. [140, 193] is that they admit multi-layer experiments.
3. **Corner smoothing:** This approach (Ref. [140]) rounds a 90 degree corner, lowers the tool-head velocity and variates the power delivered to the laser, thus depositing more or less material. The corner is rounded by affecting the *G502* instruction of the G-code and the *e* precision parameter (intervening the CNC controller). Ref. [140] does not present conclusions regarding the use of laser power as a tuning variable. The approach of the present manuscript is not to change the path geometry and therefore is not a competitor for Ref. [140].

III.D.4.6 Conclusions

This manuscript presents the experimental validation of the computational approach in Ref. [124] to use variable tool-head velocity in order to limit unintentional material accumulation in trajectory corners in Laser Metal Deposition (LMD). To validate the method in Ref. [124], single-layer corners with angles $\theta \in \{15^\circ, 30^\circ, 45^\circ, 60^\circ, 75^\circ\}$ are built with and without tool-head velocity variation. The results of the experiments show that:

1. The studied tool-head velocity variation effectively limits material overfill for the trajectory corners with angles $\theta \in \{15^\circ, 30^\circ, 60^\circ, 75^\circ\}$. After applying the tool-head velocity variation, the maximum height deviation reduces from 61% to 12% and from 32% to 12% for the angles $\theta = 15^\circ$ and $\theta = 75^\circ$, respectively. This result shows that the benefit of the tool-head velocity strategy is greater for smaller angles.
2. A significant underfill of 27% around the corner tip is observed for $\theta = 45^\circ$ when the tool-head velocity variation is applied.
3. Metal powder waste is an important aspect to consider in LMD. In the experiments reported in this manuscript, a considerable amount (near 40%) of metal powder dispensed by the nozzle is wasted. This material loss is present along the whole trajectory and it is independent of the presence of corners in the trajectory.
4. The manufacturing engineer plans the LMD process, using the nominal material feed [kg/s], the nozzle trajectories, material efficiency η , etc. Observe that the material efficiency for a particular process/machine is generally known to the process engineer, and is present regardless of the presence/absence of trajectory corners. The presented strategy for minimizing the metal overfill prescribes velocity profiles at the trajectory corners. When the LMD (with these velocity profiles) is executed, the engineer finds that the corners significantly improve, as compared against the constant velocity counterparts. On the other hand, the overall multi-layer deposition progresses according to the process/machine material waste (approx. 40%). As a consequence, the number of layers required to clad the workpiece increases. However, the focus of this manuscript (i.e. the metal overfill minimization at corners) is substantially achieved.

Additional work is necessary over the computational approach to control the effect (2) above. Future work will also be devoted to extending the current overfill minimization strategy to multi-layer situations.

Context of application

This manuscript reports the extension of the capabilities of Process Planning in Additive Manufacturing (Refs. [110, 125]). The manuscript reports the experimental validation of a method to limit unwanted metal overfill. This computational method is to be integrated into a larger LMD planning tool (Ref. [125]).

Declarations

Funding

This work has been partially funded by the Basque Government under ELKARTEK program (grants KK-2018/00115 (ADDISEND) and KK-2018/00071 (LANGILEOK)), and by the INZU Group (Talens Systems and Ikerguna A.I.E.).

Conflicts of interest

The authors declare that they have no conflicts of interest.

Data availability

The data in this study is not available due to industrial confidentiality restrictions.

Code availability

The code in this study is not available due to industrial confidentiality restrictions.

Ethics approval

Not applicable.

Consent to participate

Not applicable.

Consent for publication

The authors and their affiliation institutions have given permission to publish this manuscript.

Authors' contributions

Conceptualization: Diego Montoya Zapata, Jorge Posada, Aitor Moreno, Oscar Ruiz-Salguero; Methodology: all the authors; Formal analysis and investigation: all the authors; Writing: Diego Montoya-Zapata, Jorge Posada, Carles Creus, Aitor Moreno, Oscar Ruiz-Salguero; Supervision: Oscar Ruiz-Salguero, Jorge Posada, Aitor Moreno; Software: Diego Montoya-Zapata, Aitor Moreno.

III.D.5

Synthesis of Reeb Graph and Morse Operators from Level Sets of a Boundary Representation

Juan Pareja-Corcho^{1,2}, Diego Montoya-Zapata^{1,2}, Carlos Cadavid³, Aitor Moreno², Jorge Posada², Ketzare Arenas-Tobon¹ and Oscar Ruiz-Salguero¹

¹Laboratory of CAD CAM CAE, Universidad EAFIT, Cra 49 no 7-sur-50, Medellín 050022, Colombia

²Vicomtech Foundation, Basque Research and Technology Alliance (BRTA), Mikeletegi 57, Donostia-San Sebastian 20009, Spain

³Mathematics and Applications, Universidad EAFIT, Cra 49 no 7-sur-50, Medellín 050022, Colombia



III.D.5.1 Context

Juan Pareja-Corcho, Diego Montoya-Zapata, Carlos Cadavid, Aitor Moreno, Jorge Posada, Ketzare Arenas-Tobon and Oscar Ruiz-Salguero. Synthesis of Reeb Graph and Morse Operators from Level Sets of a Boundary Representation. XXXI Spanish Computer Graphics Conference (CEIG 2022). Vic, Spain. 5-8 July 2022. J. Posada and A. Serrano (Editors). Publisher: The Eurographics Association. ISBN: 978-3-03868-186-1. DOI: <https://doi.org/10.2312/ceig.20221140>. URL: <https://diglib.eg.org/handle/10.2312/ceig20221140>. Proceedings: <https://diglib.eg.org/handle/10.2312/2633203>.

Indexing: EUROGRAPHICS Digital Library

Abstract

In the context of Industrie 4.0, it is necessary for several applications, to encode characteristics of a Boundary Representation of a manifold \mathcal{M} in an economical manner. Two related characterizations of closed B-Reps (and the solid they represent) are (1) medial axis and (2) Reeb Graph. The medial axis of a solid region is a non-manifold mixture of 1-simplices and 2-simplices and it is expensive to extract. Because of this reason, this manuscript concentrates in the work-flow necessary to extract the Reeb Graph of the B-Rep. The extraction relies on (a) tests of geometric similarities among slices of \mathcal{M} and (b) characterization of the topological transitions in the slice sequence of \mathcal{M} . The process roughly includes: (1) tilt of the B-Rep to obtain an unambiguous representation of the level sets of \mathcal{M} , (2) identification and classification of the topological transitions that arise between consecutive level sets, (3) sample of Reeb graph vertices inside the material regions defined by the level sets, (4) creation of Reeb graph edges based on the type of topological transition and the 2D similarity among material regions of consecutive levels. Although the Reeb Graph is a topological construct, geometrical processing is central in its synthesis and compliance with the Nyquist-Shannon sampling interval is crucial for its construction. Future work is needed on the extension of our methodology to account for manifolds with internal voids or nested solids.

Keywords

Computing methodologies → Computer graphics, Shape analysis, Volumetric models

III.D.5.2 Introduction

The encoding of geometry and topology characteristics of a Boundary Representation (B-Rep) in a computationally economical manner is a useful process in several fields such as medical imaging, computer graphics and computational mechanics[69]. Two of the most commonly used characterizations of a closed manifold are (1) medial axis and (2) Reeb Graph. The Reeb Graph in particular is used in the analysis of large data sets, such as: the efficient classification and segmentation of large point clouds [191], mesh segmentation oriented towards topological optimization [104], CAD model segmentation [75, 175], shape similarity and matching [118] and data abstraction from large data sets [132]. For a detailed description of applications of Reeb Graphs in computer graphics see [17].

The goal of this manuscript is to introduce the necessary steps to synthesize the Reeb Graph from the Boundary Representation of a closed manifold \mathcal{M} . The proposed methodology relies on (a) the identification of the critical points of the slice-driven Morse function defined on \mathcal{M} and (b) the synthesis of connectivity between critical points based on tests of geometric similarities between slices of \mathcal{M} and the type of topological transitions.

The *Medial Axis* of a compact 3D region $\Omega \subset \mathbb{R}^3$ is defined as the set of all points $p \in \Omega$ such that the closest point in the boundary $\partial\Omega$ is not unique. The medial axis is a non-manifold mixture of 1-simplices and 2-simplices. The extraction of the medial axis of a closed manifold is computationally expensive and therefore unsuitable for applications that require real time interaction.

The *Reeb Graph* [150] is a way to encode the topological characteristics of a closed manifold in an efficient manner. The Reeb graph depends on the characteristics of the level sets determined by a slicing-driven function on a closed manifold \mathcal{M} . Slicing a closed 2- or 3-manifold mesh is to

compute level sets of a height function $f : \mathcal{M} \rightarrow \mathbb{R}$ with $f(x, y, z) = z$. The preimage f^{-1} of such function at a point c is known as a level set of f .

The topological characteristics of manifold \mathcal{M} are determined by the critical points of the function f defined on \mathcal{M} . To avoid ambiguity in the level sets, the height function f defined on \mathcal{M} must be a *Morse* function. A *Morse* function is characterized by its critical points. A critical point of f is a point $p \in \mathcal{M}$ such that its tangent gradient $\nabla_{\mathcal{M}}f(p)$ is zero. A critical point is degenerate if its tangent Hessian matrix $\mathbf{H}_{\mathcal{M}}f(p)$ is degenerate, that is, if its matrix determinant is zero.

Morse Function: Let \mathcal{M} be a closed and oriented 2- or 3-manifold without inner cavities embedded in \mathbb{R}^3 , and consider a twice differentiable function $f: \mathcal{M} \rightarrow \mathbb{R}$. The function f is a *Morse function* if all critical points of f are non-degenerate:

$$\forall p \in \mathcal{M} : \nabla_{\mathcal{M}}f(p) = 0 \rightarrow \det(\mathbf{H}_{\mathcal{M}}f(p)) \neq 0 \quad (\text{III.D.5.1})$$

Given a *Morse* function f defined on manifold \mathcal{M} , it is then possible to define the Reeb Graph of f , denoted as $R(f)$.

Reeb Graph: Let $f : \mathcal{M} \rightarrow \mathbb{R}$ be continuous and call a component of a level set a contour. Two points $p, q \in \mathcal{M}$ are equivalent if they belong to the same connected component of $f^{-1}(c)$ with $c = f(p) = f(q)$. The Reeb Graph of f , $R(f) = \mathbb{X}_{\sim}$, is the quotient space defined by this equivalence relation.

There is a continuous map $\psi : \mathcal{M} \rightarrow R(f)$. Point $u \in R(f)$ is a *node* if $\psi^{-1}(u)$ contains a critical point, that is, if u is the image of a critical point of f under ψ .

The rest of the manuscript is structured as follows: Section III.D.5.3 presents the literature review regarding the Reeb Graph extraction on manifolds, Section III.D.5.4 presents our proposed methodology, Section III.D.5.5 shows the application of the proposed methodology to example data sets and Section III.D.5.6 concludes the manuscript.

III.D.5.3 Literature Review

Two of the most commonly used characterizations of a closed manifold are (1) medial axis and (2) Reeb Graph. The calculation of the medial axis of a 3D region is a computationally expensive problem [40, 148], making it unsuitable for applications that require real time interaction. The Reeb Graph was introduced to graphics applications by Shinagawa et al. [164].

Available methods for the extraction of Reeb Graph can be classified according to the choice of the Morse function $f : \mathcal{M} \rightarrow \mathbb{R}$ that encodes the topological information of the manifold [19]. Some functions used include the height function [17, 111], the geodesic distance from a seed vertex [74] and distance from center of mass [18]. The height function approach imposes the lowest computational cost of all three options but requires an adequate definition of the slicing that defines the function f . The main advantage of such a function is the independence from translations and uniform scaling. However, the height function is not independent from rotations. The approaches based on distance from barycenter and geodesic distance from a seed vertex impose greater computational cost than the height function method [18], but with the advantage of independence with respect to rotations. Given a slicing-driven height function, available methods differ on how to find the connectivity of the Reeb Graph. Standard methods rely solely on proximity between level sets and handle classification, such as the ones in [76, 164]. Other authors have proposed to use heat-based mesh segmentation [74] or triangular mesh collapse [76] to link together the nodes of the Reeb Graph. Sweep algorithms are also used to find the connectivity of the Reeb Graph, such as the one in

[31]. Some authors have explored the 2D shape similarity analysis between the polygonal regions denoted by a connected component of a level set as a filter to establish connectivity between slices [157, 158] in the surface reconstruction context. The proximity-only solutions are unreliable to produce correct results in complex topological transitions [164]. The addition of a shape similarity filter increases the reliability of the connectivity extraction by ensuring the correctness of each ancestor-descendant relationship between level sets. Other approaches, such as the one in [176], are heavily dependant on the mesh representation of the manifold, entailing problems regarding the mesh density and the computational cost of mesh segmentation. Other works have focused on the definition and extraction of discrete Reeb Graphs on voxelized domains [16] or the reduction of the topological complexity of the extracted graphs [41].

The Reeb Graph is able to adequately reflect the topological structure only of manifolds with no inner voids. When inner voids are present, the Reeb Graph fails to univocally capture the topological structure of the manifold [51, 174]. The reason for this is that the Reeb Graph is sensible only to topological changes that affect the number of connected components in the level set (i.e. in the cross section). The introduction of inner contours does not change the number of connected components in a level set.

III.D.5.3.1 Conclusion of Literature Review

Reeb Graph extraction methods can be classified according to the nature of the function $f : \mathcal{M} \rightarrow \mathbb{R}$ that encodes the topological characteristics of the manifold. The most commonly used function is the height function. It allows for easy implementation and low computational cost at the setback of being dependant on the orientation of the manifold in 3D space.

The synthesis of the edges of the Reeb Graph is also approached using different methods. Proximity-only solutions are unreliable for automatic extraction of the edges and other approaches entail high computational costs. Some authors have explored 2D shape similarity as an additional filter to improve reliability of level set connectivity in other contexts such as surface reconstruction. The Reeb Graph is limited to 2-manifolds or 3-manifolds without inner cavities, since it is only sensible to topological changes that affect the number of connected components.

To encode 3D shape, the medial axis computation is extremely expensive if directly addressed. On the other hand, the Reeb Graph by itself presents the aforementioned limitations. Because of this reason, this manuscript presents the first steps in supplementing the Reeb Graph with geometrical information, thus allowing in the future a reasonable encoding of 3D shape with inner voids characteristics.

III.D.5.4 Methodology

We propose a methodology to extract the Reeb Graph of a given Boundary Representation of a 2- or 3-manifold without inner cavities \mathcal{M} embedded in \mathbb{R}^3 . Our algorithm can be summarized in the following steps:

1. *Level set extraction:* Tilt of the B-Rep to obtain an unambiguous representation of the level sets of \mathcal{M} .
2. *Nodes definition:* Sampling of the material regions denoted by the obtained level sets of \mathcal{M} to obtain the nodes of the Reeb Graph.

3. *Edges definition:* Synthesis of the connectivity (edges) of the Reeb Graph according to the criteria of shape similarity and the type of topological transition.

III.D.5.4.1 Level sets extraction

Given a Boundary Representation of a 2- or 3-manifold without inner cavities \mathcal{M} embedded in \mathbb{R}^3 (Fig. III.D.5.1), a height function $f : \mathcal{M} \rightarrow \mathbb{R}$ is defined on the manifold driven by a planar slicing with a set of planar surfaces Π parallel to the $x - y$ plane. The orientation of the manifold \mathcal{M} in \mathbb{R}^3 must be one in which the function induced by the planar slicing is a *Morse* function (see Eq. III.D.5.1). The fact that the function f defined on \mathcal{M} is Morse ensures the unambiguity of the level sets of \mathcal{M} retrieved from such a mapping.

A level set $\Pi_c : f^{-1}(c)$ defined by the preimage of the Morse function f can contain one or more contours (connected components). For example, in Fig. III.D.5.1, the level set Π_{c_i} has one contour and the level set Π_{c_j} has two contours. The contour population between level sets evolve as a result of changes in the cross-section composition of \mathcal{M} .

The distance between the slices is subjected to compliance with the Nyquist-Shannon principle in all directions. The technician must decide which level of geometric detail d is to be captured. The sampling distance should be less than $d/2$ (in all directions). Therefore, there is no universal sampling rate. For example, if the designer wants to preserve very close cavities as separate ones, the sampling distance (in all directions) must be set up as half of the minimal separation among holes, or less

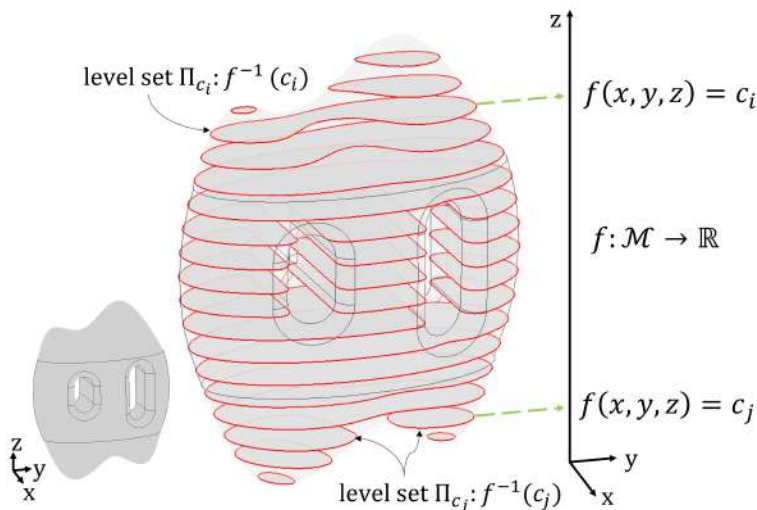


Figure III.D.5.1: Definition of Morse function $f : \mathcal{M} \rightarrow \mathbb{R}$ on \mathcal{M} . Level sets are obtained by the preimage of f .

III.D.5.4.2 Nodes definition

A set \mathcal{P} of material points is obtained by sampling each polygonal region denoted by the contours of each level set. Each point $p \in \mathcal{P}$ represents a polygonal region (connected component) inscribed

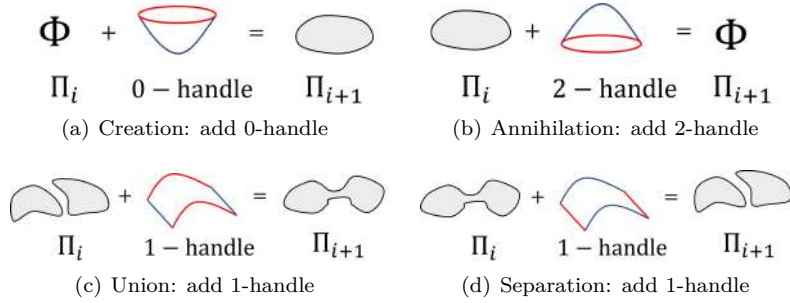


Figure III.D.5.2: Effect of Morse operators (handles) on the contour population between level sets Π_i and Π_{i+1} .

within one or more contours. As stated before (see Section 1), the vertices V of the Reeb graph $R(f) = (V, E)$ are the points in \mathcal{P} such that they are critical points (i.e. they belong to a critical level set).

III.D.5.4.3 Edges definition

Before establishing a connectivity between the nodes of the Reeb Graph, the topological changes in the level set sequence must be identified and classified. A set of Morse operators known as *handles* govern the evolution of the contour population. Each *handle* represents a topological change in the manifold \mathcal{M} and a change in the number of contours (connected components) between level sets. The application of handle operators can be classified as follows (Fig. III.D.5.2): (a) a 0-handle creates a new contour from the empty set, (b) a 2-handle annihilates a contour and (c) a 1-handle either separates a contour into two different contours or unites two contours into a single contour. The occurrence of handles in the level set sequence dictates whether a level set is critical or not. A level set is critical if there is a change in the contour population with respect to the previous or the next level set in the sequence. Fig. III.D.5.3 shows the critical level sets in the sequence for manifold \mathcal{M} and the type of handle operator that acts upon the level set sequence in each step.

Even though the slicing provides the vertices of the Reeb graph, the connectivity of the Reeb graph does not unequivocally follows from the slicing. We propose an heuristic to find the edges E of Reeb graph $R(f) = (V, E)$ by following the level set sequence and connecting two vertices in neighboring level sets according to (a) the handle operator that acts on the contour population between the neighboring level sets and (b) shape similarity between polygonal regions. In this heuristic, the non-critical level sets are necessary to synthesize the connectivity of the Reeb graph.

For example, in Fig. III.D.5.4, to obtain the connectivity between vertices v_5 and v_8 it is necessary to take into account noncritical points p_6 and p_7 (edges $e_{5-6}, e_{6-7}, e_{7-8}$). Each edge is labeled with a handle operation according to the contour population evolution. Edges e_{3-5} and e_{4-5} are 1-handle edges since they connect a level set with two contours (represented by vertices v_3 and v_4) with a level set with only one contour (represented by vertex v_5).

Once all vertices and edges are obtained, the Reeb graph $R(f)$ for a Morse function $f : \mathcal{M} \rightarrow \mathbb{R}$ encodes the characteristics of the Boundary Representation of the manifold \mathcal{M} , as seen in Fig. III.D.5.5.

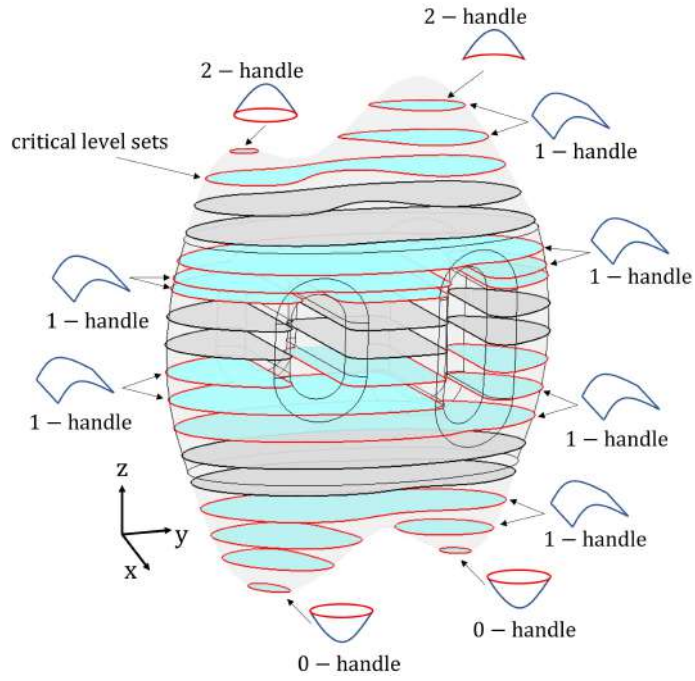


Figure III.D.5.3: Critical level sets on manifold M with handles.

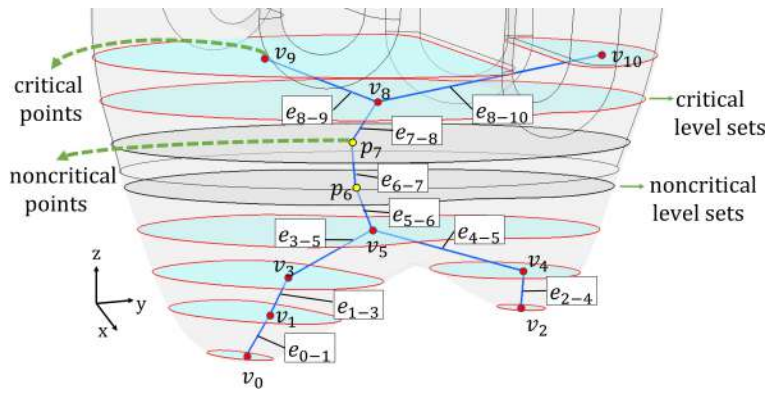


Figure III.D.5.4: Connectivity between level sets to synthesize Reeb graph $R(f) = (V, E)$.

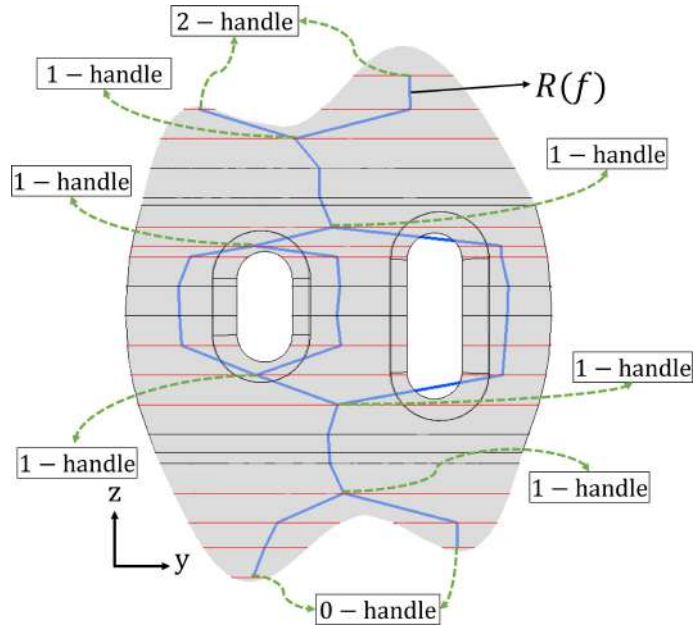


Figure III.D.5.5: Reeb graph $R(f)$ for the example manifold \mathcal{M} .

III.D.5.5 Results

Figure III.D.5.6 shows the Reeb Graph synthesized for two example data sets. Figures III.D.5.6(a) and III.D.5.6(b) shows the Reeb Graph for the *hands* dataset. Figures III.D.5.6(c) and III.D.5.6(d) shows the Reeb Graph for the *elephant* dataset. In both examples the synthesized Reeb Graph correctly captures the topological transitions that occur through the Boundary Representation. Notice that, since our methodology is geometrically-driven, the Reeb graph resembles the geometry of the manifold \mathcal{M} .

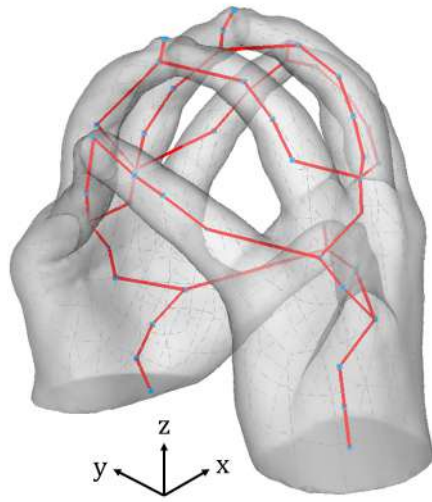
Even though there is not a preferred way of drawing the Reeb Graph (connections between nodes could take any shape), the fact that the connections resemble the geometry of the manifold \mathcal{M} is useful towards the use of the Reeb Graph for the computation of the medial axis of the manifold \mathcal{M} .

III.D.5.6 Conclusions

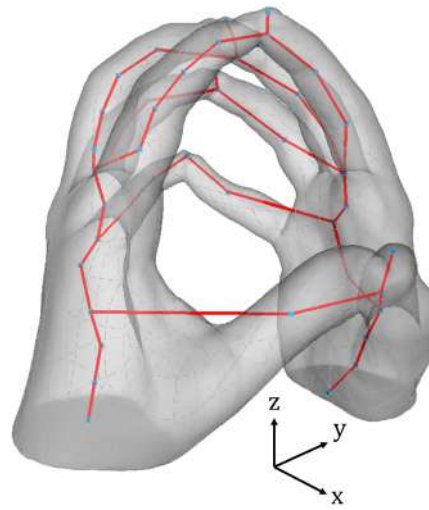
This manuscript presents a workflow for the synthesis of a Reeb Graph encoding for a solid region in \mathbb{R}^3 denoted by its Boundary Representation \mathcal{M} . The Reeb Graph for \mathcal{M} is a well known topological entity. However, its geometrical realization presents challenges and variations. Our approach starts with the rotation of \mathcal{M} to obtain a Morse function $f : \mathcal{M} \rightarrow \mathbb{R}$ on the manifold, with $f(x, y, z) = z$ for point (x, y, z) in \mathcal{M} . Morse-compliance guarantees that level sets of f unambiguously determine the material regions of \mathcal{M} on each slice. The nodes of the Reeb Graph (non-degenerate critical points of f) are detected by registering the topological changes (i.e. classifying the Morse handles)

in the level sets of a Nyquist-Shannon equispaced slicing of \mathcal{M} . The Reeb Graph admits several edges for each pair of nodes. Detection and per-slice-tracing of these edges is achieved by using the handle classification and 2D shape similarity among level sets.

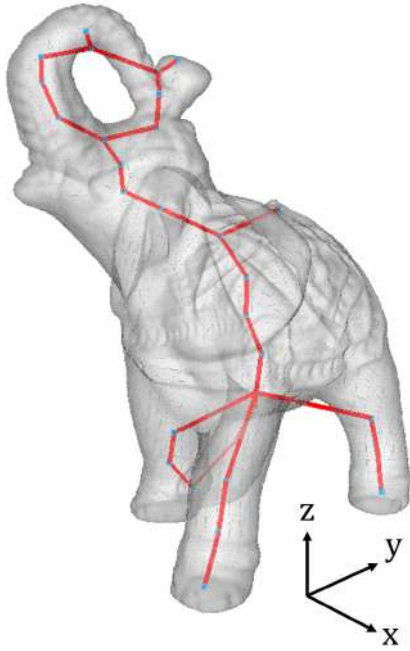
This geometry-driven methodology correctly synthesizes the Reeb Graph of the example B-Reps. It results in Reeb Graph representations faithful to the geometrical characteristics of \mathcal{M} , and not only to its topological features. Future work is needed in: (a) the extension of the methodology to obtain a topological representation of manifolds in \mathbb{R}^3 with inner cavities and (b) trying to achieve independence of the slicing with respect to the orientation of the manifold in \mathbb{R}^3 .



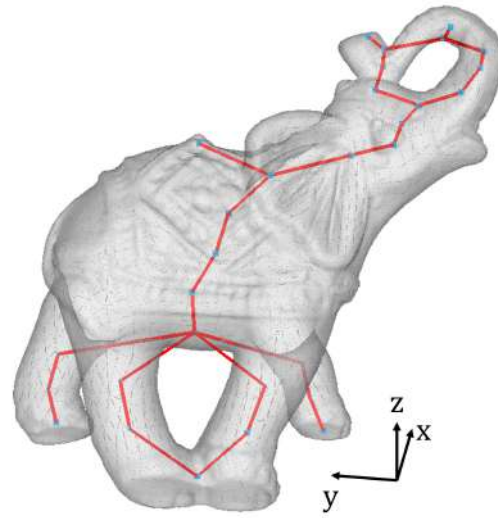
(a) Reeb Graph on *hands* dataset. Viewpoint 1.



(b) Reeb Graph on *hands* dataset. Viewpoint 2.



(c) Reeb Graph on *elephant* dataset. Viewpoint 1.



(d) Reeb Graph on *elephant* dataset. Viewpoint 2.

Figure III.D.5.6: Synthesis of the Reeb Graph representation on example manifolds.

Part IV

General Conclusions

IV.A

Contributions

This thesis presents the following contributions of Computational Geometry Applied to Additive Manufacturing:

In the domain of **Shape Optimization in Lattice Structures**, this thesis presents:

- (a) The implementation and sensitivity analysis of the SIMP (Solid Isotropic Material with Penalization) topology optimization strategy. The sensitivity analysis shows that extreme values of the SIMP parameters affect the manufacturability and mechanical performance of the final designs (see Section III.B.1).
- (b) A method to transform density maps (e.g. resulting from topology optimization) into surface lattice structures. The lattice structures generated by this method (i) resemble the given density distribution and (ii) are fabricated via metal Additive Manufacturing, specifically with the processes of selective laser melting and binder jetting (see Section III.B.2).
- (c) A procedure to integrate material homogenization and Design of Experiments (DOE) to estimate the stress/strain response of large surface lattice domains. The procedure significantly reduces the computational cost with respect to direct Finite Element Simulation. Material homogenization efficiently approximates the displacements on the lattice domains and DOE produces simple mathematical expressions to express the stresses in the lattice as functions of the displacements obtained through homogenization. Results show that the proposed methodology is an efficient tool with potential applications in the coarse estimation of the von Mises stress in large lattice domains (see Section III.B.3).

In the domain of **Simulation of Laser Metal Deposition**, this thesis presents:

- (a) The Finite Element Method implementation of a 2D linear transient thermal model for a metal substrate that is heated by the action of a laser. The analysis of the influence of the laser intensity distribution and the laser spot radius showed that these two parameters strongly affect the shape (width and depth) of the heat affected zone and the maximum temperature on the metal substrate. A comparison with a nonlinear model shows that the linear model is a good option for digital twin designs, due to their simplicity and reasonable accuracy (see Section III.C.1).
- (b) The Finite Element Method implementation of a 2D nonlinear thermal model of the Laser Metal Deposition (LMD) process. This implementation considers the following nonlinear phenomena: (i) temperature-dependent material properties, (ii) phase change, and (iii) radiation. The energy of the laser is represented as an energy flux boundary condition. The material deposition model is dictated by the delivery rate of powder (feed rate [kg/s]) and its associated Gaussian function of the radii from the nozzle axis. The model does not assume a particular geometry (parabolic, circular, sinusoidal, etc.) for the bead cross-section, as some

previous works do. The results of the simulations show reasonable accuracy to predict the bead geometry (width error 15%, height error 22%) (see Section III.C.2).

In the context of **Process Planning for Laser Metal Deposition**, I had the opportunity to work on a project funded by a private industrial company. The goal of the project was to develop a software that provided CAD/CAM support for the path-planning and process-planning of LMD. In view of this, this thesis presents the following scientific and industrial contributions:

- (a) The implementation of a 2.5D path planning method for Laser Metal Deposition which (i) considers the geometrical aspects of the toolpath generation, and (ii) incorporates a graph-based region avoidance algorithm to alleviate hardware limitations. The physical experiments, using a powder-fed LMD system, show that the path planning methods for subtractive manufacturing must be adapted to fulfill the particular constraints of the LMD process. This computational method is integrated into an industrial LMD process planning tool (see Section III.D.1).
- (b) The implementation of a 3D (non-planar) path planning method for Laser Metal Deposition (LMD). The method allows the manufacturing, via LMD, of overhanging features of revolution workpieces with a cylindrical 3D kernel. The algorithm slices the geometry into cylindrical layers using coordinate transformation and planar slicing. The algorithm generates the tool-path for each cylindrical slice using isometric parametrization and planar toolpath-planning methods. The results of the simulations show that this algorithm allows the LMD manufacturing of industrial workpieces, such as gear teeth and cam lobes. This strategy for cylindrical slicing is also integrated into an industrial LMD process planning tool (see Section III.D.2).
- (c) The implementation of a voxel-based geometric simulator for Laser Metal Deposition (LMD) and a tool for the minimization of the material over-deposition at corners in LMD. The method controls tool-head velocity near the corner tip. Results for the corner angle instances $\theta \in \{30^\circ, 60^\circ, 90^\circ\}$ show a reduction of over 90% of the over-deposition present at corners without nozzle velocity control (see Section III.D.3).
- (d) The experimental validation of the computational minimization approach in (c). The experiments consider single-layer corners with angles $\theta \in \{15^\circ, 30^\circ, 45^\circ, 60^\circ, 75^\circ\}$ built with and without tool-head velocity control. The results of the experiments show that this method limits material overfill for trajectory corners in LMD. The benefit of the method is greater for smaller angles (see Section III.D.4).
- (e) A workflow for the synthesis of the Reeb Graph for a solid region in \mathbb{R}^3 denoted by its Boundary Representation (B-Rep) \mathcal{M} . The workflow starts by rotating \mathcal{M} so that the function $f(x, y, z) = z$ becomes a Morse function. The nodes of the Reeb Graph (non-degenerate critical points of f) are detected by classifying the Morse handles of the equispaced level sets (slices) of \mathcal{M} . The edges of the Reeb Graph are achieved by using the handle classification and 2D shape similarity among level sets. The results show that this geometry-driven methodology correctly synthesizes the Reeb Graph of the example B-Reps (see Section III.D.5).

IV.B

Future Directions and Opportunities

The development and advance in (Metal) Additive Manufacturing depend on multidisciplinary efforts. It requires simulation, experimentation, and the interaction and integration of physics, geometry, materials science, robotics, and software development. This thesis has contributed to the development of Computational Geometry and its integration into industrial software for the Laser Metal Deposition process. In this section, I describe some potential directions that this work leaves open for future investigations.

In the domain of **Shape Optimization in Lattice Structures**, further work is required on the following:

- (a) The transformation of density maps into lattice structures. This thesis presented a solution to this problem in Section III.B.2 using a single family of lattices, namely the Schwarz cell. An interesting direction to explore is the use of two or more families of lattice cells at the same time. In this manner, one could exploit the mechanical advantages of different lattice families on the same workpiece. One of the challenging problems would be to achieve smooth transitions in the connections between lattice cells of different families.
- (b) The efficient simulation of the thermo-fluid-mechanical response of large lattice domains under working loads. The simulations should also account for arbitrary topology and geometry of the workpiece filled with lattice cells. In Section III.B.3, this thesis presented a multiscale model based on homogenization and DOE that points in this direction. However, further efforts are required to improve its accuracy by, for example, fitting of more robust meta-models that use more information from the displacements field obtained via homogenization.

In the domain of **Simulation of Laser Metal Deposition**, further work is required on the following:

- (a) The physical-based simulation of the Laser Metal Deposition regarding its efficiency and accuracy. Particularly, for the 2D nonlinear thermal model presented in Section III.C.2, further investigation is required to calibrate the absorption coefficient, which expresses the portion of the laser power that indeed inputs to the bead-substrate. It is affected by phenomena not yet understood or even identified. Future work is also needed to account for the particle (thermal) dynamics over the substrate, which is responsible for significant material and energy waste.
- (b) The inclusion of stochastic conditions during the simulation. For example, the material feed rate is not constant but suffers perturbations that non-stochastic models do not consider. Although stochastic considerations generally come at a sacrifice of efficiency, I think this could be a valuable path to explore for addressing repeatability issues sometimes associated to LMD and Additive Manufacturing in general.

As mentioned above, the contributions to **Process Planning for Laser Metal Deposition** were achieved in the framework of a project funded by a private industrial company. This industrial

collaboration is still ongoing. Our ultimate goal in this regard is to develop and apply Computational Geometry techniques and translate them into CAD/CAM software solutions that contribute to the industrial adoption of LMD. In other words, we aim to contribute to the increase of LMD's Technology Readiness Level (TRL). In light of this, future work will be devoted to the following:

- (a) The implementation and validation of additional deposition strategies for LMD, apart from those described in Section III.D.1. The process planning for LMD should consider the whole manufacturing process, including the postprocessing (e.g. machining) to which the LMD-manufactured workpieces are subjected to.
- (b) The use of the 3D cylindrical slicing presented in Section III.D.2 for the LMD-manufacturing of industrial gears whose pitch surface is a cylinder (e.g. spur and helical gears). The upcoming stages of this project will be: (i) the experimental validation of the proposed approach and (ii) the development of the inverse kinematics to translate the 3D trajectory into the movements of a 6-axis robot. Another direction for future research is the extension of the mathematical model to consider industrial gears whose pitch surface is a cone (e.g. bevel gears).
- (c) The tool for the minimization of the material over-deposition at corners in LMD presented in Sections III.D.3 and III.D.4 currently uses an exhaustive search strategy. This strategy is expensive in computing time. Further study of other optimization techniques (e.g. branch and bounding) and heuristics for cutting computing time expenditures are required for in-process applications. Future work will also be devoted to extending the current overfill minimization strategy to multilayer situations.
- (d) The workflow for synthesizing the Reeb Graph for a solid region presented in Section III.D.5 does not account for 3-manifolds with inner cavities. Further efforts will be devoted to addressing this problem. Future work is also needed to explore the potential of the Reeb Graph to serve for the decomposition of solids in the context of desynchronized multi-axis (3+1 or 3+2 axis) additive manufacturing.

The aforementioned contributions are the product of the joint collaboration between the Universidad EAFIT and Vicomtech Research Center, Laboratory of CAD CAM CAE (Universidad EAFIT), Department of Industry and Advanced Manufacturing (Vicomtech), and all the doctoral research team. These contributions have been screened, revised and accepted by the international scientific community, achieving publication in indexed International Journals and Conferences. Some of these contributions have been approved and integrated into industrial software, and are being commercially exploited by IkerGune A.I.E. and Talens Systems, part of the INZU Group.

Bibliography

- [1] M. Afshar, A. Pourkamali Anaraki, H. Montazerian, and J. Kadkhodapour. Additive manufacturing and mechanical characterization of graded porosity scaffolds designed based on triply periodic minimal surface architectures. Journal of the Mechanical Behavior of Biomedical Materials, 62:481 – 494, 2016. doi:10.1016/j.jmbbm.2016.05.027.
- [2] James Ahrens, Berk Geveci, and Charles Law. ParaView: An end-user tool for large-data visualization. In Charles D. Hansen and Chris R. Johnson, editors, Visualization Handbook, pages 717 – 731. Butterworth-Heinemann, Burlington, 2005. URL: <http://www.sciencedirect.com/science/article/pii/B9780123875822500381>, doi:10.1016/B978-012387582-2/50038-1.
- [3] Piera Alvarez, M. Ángeles Montealegre, Jose F. Pulido-Jiménez, and Jon Iñaki Arrizubieta. Analysis of the process parameter influence in laser cladding of 316L stainless steel. Journal of Manufacturing and Materials Processing, 2(3):55, 2018. doi:10.3390/jmmp2030055.
- [4] Mahmoud Alzahrani, Seung-Kyum Choi, and David W. Rosen. Design of truss-like cellular structures using relative density mapping method. Materials & Design, 85:349 – 360, 2015. doi:10.1016/j.matdes.2015.06.180.
- [5] A Aremu, I Ashcroft, R Hague, R Wildman, and C Tuck. Suitability of SIMP and BESO topology optimization algorithms for additive manufacture. In 21st Annual International Solid Freeform Fabrication Symposium (SFF)—An Additive Manufacturing Conference, pages 679–692, 2010.
- [6] Jon Iñaki Arrizubieta, Aitzol Lamikiz, Fritz Klocke, Silvia Martínez, Kristian Arntz, and Eneko Ukar. Evaluation of the relevance of melt pool dynamics in laser material deposition process modeling. International Journal of Heat and Mass Transfer, 115:80 – 91, 2017. doi:10.1016/j.ijheatmasstransfer.2017.07.011.
- [7] Jon Iñaki Arrizubieta, Silvia Martínez, Aitzol Lamikiz, Eneko Ukar, Kristian Arntz, and Fritz Klocke. Instantaneous powder flux regulation system for laser metal deposition. Journal of Manufacturing Processes, 29:242 – 251, 2017. doi:10.1016/j.jmapro.2017.07.018.
- [8] Arash Ataei, Yuncang Li, Darren Fraser, Guangsheng Song, and Cuie Wen. Anisotropic Ti-6Al-4V gyroid scaffolds manufactured by electron beam melting (EBM) for bone implant applications. Materials & Design, 137:345 – 354, 2018. doi:10.1016/j.matdes.2017.10.040.

- [9] Shashwat Bakhshi. Numerical analysis to study the effect of sag and non-circular whirl orbits on the damping performance of a squeeze film damper. Master’s thesis, University of Cincinnati, Cincinnati, USA, 2018.
- [10] Stefano Baraldo, Ambra Vandone, Anna Valente, and Emanuele Carpanzano. Closed-loop control by laser power modulation in direct energy deposition additive manufacturing. In Lihui Wang, Vidosav D. Majstorovic, Dimitris Mourtzis, Emanuele Carpanzano, Giovanni Moroni, and Luigi Maria Galantucci, editors, Proceedings of 5th International Conference on the Industry 4.0 Model for Advanced Manufacturing, pages 129–143, Cham, 2020. Springer International Publishing. doi:https://doi.org/10.1007/978-3-030-46212-3_9.
- [11] Mohamad Bayat, Venkata K. Nadimpalli, Francesco G. Biondani, Sina Jafarzadeh, Jesper Thorborg, Niels S. Tiedje, Giuliano Bissacco, David B. Pedersen, and Jesper H. Hattel. On the role of the powder stream on the heat and fluid flow conditions during Directed Energy Deposition of maraging steel—Multiphysics modeling and experimental validation. Additive Manufacturing, 43:102021, 2021. URL: <https://www.sciencedirect.com/science/article/pii/S221486042100186X>, doi:<https://doi.org/10.1016/j.addma.2021.102021>.
- [12] M. P. Bendsøe. Optimal shape design as a material distribution problem. Structural optimization, 1(4):193–202, Dec 1989. doi:10.1007/BF01650949.
- [13] Martin P. Bendsøe. The homogenization approach to topology design, pages 5–77. Springer Berlin Heidelberg, Berlin, Heidelberg, 1995. doi:10.1007/978-3-662-03115-5_2.
- [14] Martin P. Bendsøe and Ole Sigmund. Topology optimization by distribution of isotropic material, pages 1–69. Springer Berlin Heidelberg, Berlin, Heidelberg, 2004. doi:10.1007/978-3-662-05086-6_1.
- [15] J.-M. Bergheau and R. Fortunier. Non-linearities. In Finite Element Simulation of Heat Transfer, chapter 5, pages 143–167. John Wiley & Sons, Ltd, 2008. doi:10.1002/9780470611418.ch5.
- [16] Piyush Kanti Bhunre and Partha Bhowmick. Topological analysis of voxelized objects by discrete geodesic Reeb graph. Journal of Computer and System Sciences, 95:151–164, 2018. doi:<https://doi.org/10.1016/j.jcss.2017.09.002>.
- [17] S. Biasotti, D. Giorgi, M. Spagnuolo, and B. Falcidieno. Reeb graphs for shape analysis and applications. Theoretical Computer Science, 392(1):5–22, 2008. Computational Algebraic Geometry and Applications. doi:<https://doi.org/10.1016/j.tcs.2007.10.018>.
- [18] S. Biasotti, S. Marini, M. Mortara, and G. Patane. An overview on properties and efficacy of topological skeletons in shape modeling. In 2003 Shape Modeling International., pages 245–254. IEEE Computer Society, 2003. doi:<https://doi.org/10.1109/SMI.2003.1199624>.
- [19] Silvia Biasotti. Reeb graph representation of surfaces with boundary. In Proceedings Shape Modeling Applications, 2004., pages 371–374. IEEE, 2004. doi:<https://doi.org/10.1109/SMI.2004.1314530>.

- [20] Max Biegler, Jiahan Wang, Lukas Kaiser, and Michael Rethmeier. Automated tool-path generation for rapid manufacturing of additive manufacturing directed energy deposition geometries. Steel Research International, page 2000017, 2020. doi:10.1002/srin.202000017.
- [21] Colin Bonatti and Dirk Mohr. Mechanical performance of additively-manufactured anisotropic and isotropic smooth shell-lattice materials: Simulations & experiments. Journal of the Mechanics and Physics of Solids, 122:1 – 26, 2019. doi:10.1016/j.jmps.2018.08.022.
- [22] George E. P. Box, J. Stuart Hunter, and William G. Hunter. Statistics for experimenters: design, discovery, and innovation. Wiley Series in Probability and Statistics. Wiley, 2nd edition, 2005.
- [23] BQ. PLA filament: technical datasheet, 2018. <https://www.bq.com/en/support/pla-premium/support-sheet>. URL: <https://www.bq.com/en/support/pla-premium/support-sheet>.
- [24] D Brackett, I Ashcroft, and R Hague. Topology optimization for additive manufacturing. In Proceedings of the solid freeform fabrication symposium, volume 1, pages 348–362, 2011.
- [25] Fabrizia Caiazzo and Vittorio Alfieri. Simulation of laser-assisted directed energy deposition of Aluminum powder: Prediction of geometry and temperature evolution. Materials, 12(13):2100, 2019. doi:10.3390/ma12132100.
- [26] J. M. Carbonell, J. M. Rodríguez, and E. Oñate. Modelling 3D metal cutting problems with the particle finite element method. Computational Mechanics, 66(3):603–624, 2020. doi:10.1007/s00466-020-01867-5.
- [27] Paschalis Charalampous, Ioannis Kostavelis, and Dimitrios Tzovaras. Non-destructive quality control methods in additive manufacturing: a survey. Rapid Prototyping Journal, 26(4):777–790, 2020. URL: <https://doi.org/10.1108/RPJ-08-2019-0224>, doi:10.1108/rpj-08-2019-0224.
- [28] Bo Cheng, Subin Shrestha, and Kevin Chou. Stress and deformation evaluations of scanning strategy effect in selective laser melting. Additive Manufacturing, 12:240 – 251, 2016. doi:10.1016/j.addma.2016.05.007.
- [29] Lin Cheng, Pu Zhang, Emre Biyikli, Jiayi Bai, Joshua Robbins, and Albert To. Efficient design optimization of variable-density cellular structures for additive manufacturing: theory and experimental validation. Rapid Prototyping Journal, 23(4):660–677, 2017. doi:10.1108/RPJ-04-2016-0069.
- [30] Zhong Yang Chua, Il Hyuk Ahn, and Seung Ki Moon. Process monitoring and inspection systems in metal additive manufacturing: Status and applications. International Journal of Precision Engineering and Manufacturing-Green Technology, 4(2):235–245, 2017. URL: <https://doi.org/10.1007/s40684-017-0029-7>, doi:10.1007/s40684-017-0029-7.
- [31] Kree Cole-McLaughlin, Herbert Edelsbrunner, John Harer, Vijay Natarajan, and Valerio Pascucci. Loops in Reeb graphs of 2-manifolds. Discrete & Computational Geometry, 32(2):231–244, 2004. doi:<https://doi.org/10.1007/s00454-004-1122-6>.

- [32] Raphaël Comminal, Marcin P. Serdeczny, David B. Pedersen, and Jon Spangenberg. Numerical modeling of the material deposition and contouring precision in fused deposition modeling. In Proceedings of the 29th Annual International Solid Freeform Fabrication Symposium 2018: An Additive Manufacturing Conference, pages 1855–1864. Laboratory for Freeform Fabrication, 2018.
- [33] Raphaël Comminal, Marcin P. Serdeczny, David B. Pedersen, and Jon Spangenberg. Motion planning and numerical simulation of material deposition at corners in extrusion additive manufacturing. Additive Manufacturing, 29:100753, 2019. doi:10.1016/j.addma.2019.06.005.
- [34] David J. Corbin, Abdalla R. Nassar, Edward W. Reutzler, Allison M. Beese, and Nathan A. Kistler. Effect of directed energy deposition processing parameters on laser deposited Inconel® 718: External morphology. Journal of Laser Applications, 29(2):022001, May 2017. doi:10.2351/1.4977476.
- [35] F. Cordovilla, P. Álvarez, A. García-Beltrán, M. A. Montealegre, and J.L. Ocaña. Non-linear thermal model of the direct laser melting process considering the adhesion of the consolidated material to the substrate using a domain with discontinuous material properties. In Proceedings of Lasers in Manufacturing, 2019.
- [36] Camilo Cortés, Maria Osorno, David Uribe, Holger Steeb, Oscar Ruiz-Salguero, Iñigo Barandiaran, and Julián Flórez. Geometry simplification of open-cell porous materials for elastic deformation FEA. Engineering with Computers, 35(1):257–276, 2019. doi:10.1007/s00366-018-0597-3.
- [37] L. Costa, T. Reti, A.M. Deus, and R. Vilar. Simulation of layer overlap tempering kinetics in steel parts deposited by laser cladding. In Proceedings of International Conference on Metal Powder Deposition for Rapid Manufacturing, pages 172–176. MPIF, Princeton, NJ, 2002.
- [38] A. Dadalau, A. Hafla, and A. Verl. A new adaptive penalization scheme for topology optimization. Production Engineering, 3(4):427, 2009. doi:10.1007/s11740-009-0187-8.
- [39] Chengkai Dai, Charlie C. L. Wang, Chenming Wu, Sylvain Lefebvre, Guoxin Fang, and Yong-Jin Liu. Support-free volume printing by multi-axis motion. ACM Trans. Graph., 37(4):134, 2018. doi:10.1145/3197517.3201342.
- [40] Francisco de Moura Pinto and Carla Maria Dal Sasso Freitas. Fast medial axis transform for planar domains with general boundaries. In 2009 XXII Brazilian Symposium on Computer Graphics and Image Processing, pages 96–103. IEEE, 2009. doi:https://doi.org/10.1109/SIBGRAPI.2009.21.
- [41] Vin De Silva, Elizabeth Munch, and Amit Patel. Categorized Reeb graphs. Discrete & Computational Geometry, 55(4):854–906, 2016. doi:https://doi.org/10.1007/s00454-016-9763-9.
- [42] Joshua D. Deaton and Ramana V. Grandhi. A survey of structural and multidisciplinary continuum topology optimization: post 2000. Structural and Multidisciplinary Optimization, 49(1):1–38, Jan 2014. doi:10.1007/s00158-013-0956-z.

- [43] T. DebRoy, W. Zhang, J. Turner, and S.S. Babu. Building digital twins of 3D printing machines. Scripta Materialia, 135:119 – 124, 2017. doi:[10.1016/j.scriptamat.2016.12.005](https://doi.org/10.1016/j.scriptamat.2016.12.005).
- [44] Nathan Decker, Yuanxiang Wang, and Qiang Huang. Efficiently registering scan point clouds of 3D printed parts for shape accuracy assessment and modeling. Journal of Manufacturing Systems, 56:587–597, 2020. doi:<https://doi.org/10.1016/j.jmsy.2020.04.001>.
- [45] Ugur M. Dilberoglu, Bahar Gharehpapagh, Ulas Yaman, and Melik Dolen. The role of additive manufacturing in the era of Industry 4.0. Procedia Manufacturing, 11:545 – 554, 2017. 27th International Conference on Flexible Automation and Intelligent Manufacturing, FAIM2017, 27-30 June 2017, Modena, Italy. doi:[10.1016/j.promfg.2017.07.148](https://doi.org/10.1016/j.promfg.2017.07.148).
- [46] Donghong Ding, Zengxi Pan, Dominic Cuiuri, and Huijun Li. A tool-path generation strategy for wire and arc additive manufacturing. The International Journal of Advanced Manufacturing Technology, 73(1-4):173–183, 2014. doi:[10.1007/s00170-014-5808-5](https://doi.org/10.1007/s00170-014-5808-5).
- [47] Donghong Ding, Zengxi Pan, Dominic Cuiuri, and Huijun Li. A practical path planning methodology for wire and arc additive manufacturing of thin-walled structures. Robotics and Computer-Integrated Manufacturing, 34:8 – 19, 2015. doi:[10.1016/j.rcim.2015.01.003](https://doi.org/10.1016/j.rcim.2015.01.003).
- [48] Donghong Ding, Zengxi Pan, Dominic Cuiuri, Huijun Li, Nathan Larkin, and Stephen van Duin. Automatic multi-direction slicing algorithms for wire based additive manufacturing. Robotics and Computer-Integrated Manufacturing, 37:139–150, 2016. URL: <https://www.sciencedirect.com/science/article/pii/S0736584515000873>, doi:doi.org/10.1016/j.rcim.2015.09.002.
- [49] Yaoyu Ding, Rajeev Dwivedi, and Radovan Kovacevic. Process planning for 8-axis robotized laser-based direct metal deposition system: A case on building revolved part. Robotics and Computer-Integrated Manufacturing, 44:67–76, 2017. URL: <https://www.sciencedirect.com/science/article/pii/S0736584515300326>, doi:[10.1016/j.rcim.2016.08.008](https://doi.org/10.1016/j.rcim.2016.08.008).
- [50] Yaoyu Ding, James Warton, and Radovan Kovacevic. Development of sensing and control system for robotized laser-based direct metal addition system. Additive Manufacturing, 10:24–35, 2016. doi:[10.1016/j.addma.2016.01.002](https://doi.org/10.1016/j.addma.2016.01.002).
- [51] Herbert Edelsbrunner, John Harer, and Amit K. Patel. Reeb spaces of piecewise linear mappings. In Proceedings of the Twenty-Fourth Annual Symposium on Computational Geometry, pages 242–250, New York, NY, USA, 2008. Association for Computing Machinery. doi:<https://doi.org/10.1145/1377676.1377720>.
- [52] C. S. Edwards, H. A. Kim, and C. J. Budd. An evaluative study on ESO and SIMP for optimising a cantilever tie—beam. Structural and Multidisciplinary Optimization, 34(5):403–414, 2007. doi:[10.1007/s00158-007-0102-x](https://doi.org/10.1007/s00158-007-0102-x).
- [53] Daniel Eisenbarth, Alessandro Menichelli, Fabian Soffel, and Konrad Wegener. Adaptive slicing and process optimization for direct metal deposition to fabricate exhaust manifolds. In Mirko Meboldt and Christoph Klahn, editors, Industrializing Additive Manufacturing, pages 160–173, Cham, 2021. Springer International Publishing. doi:[10.1007/978-3-030-54334-1_12](https://doi.org/10.1007/978-3-030-54334-1_12).

- [54] Daniel Eisenbarth, Florian Wirth, Kevin Spieldiener, and Konrad Wegener. Enhanced toolpath generation for direct metal deposition by using distinctive CAD data. In Industrializing Additive Manufacturing - Proceedings of Additive Manufacturing in Products and Applications - AMPA2017, pages 152–161. Springer International Publishing, 2017. doi:10.1007/978-3-319-66866-6_15.
- [55] Hussam El Cheikh, Bruno Courant, Samuel Branchu, Jean-Yves Hascoët, and Ronald Guillén. Analysis and prediction of single laser tracks geometrical characteristics in coaxial laser cladding process. Optics and Lasers in Engineering, 50(3):413 – 422, 2012. doi:10.1016/j.optlaseng.2011.10.014.
- [56] Waiel Elmadih, Wahyudin P. Syam, Ian Maskery, Dimitrios Chronopoulos, and Richard Leach. Mechanical vibration bandgaps in surface-based lattices. Additive Manufacturing, 25:421 – 429, 2019. doi:10.1016/j.addma.2018.11.011.
- [57] Darren Engwirda. Locally optimal Delaunay-refinement and optimisation-based mesh generation. PhD thesis, University of Sydney, 2014. URL: <http://hdl.handle.net/2123/13148>.
- [58] Deniz Sera Ertay, Alexander Yuen, and Yusuf Altintas. Synchronized material deposition rate control with path velocity on fused filament fabrication machines. Additive Manufacturing, 19:205 – 213, 2018. doi:10.1016/j.addma.2017.05.011.
- [59] Shady Farah, Daniel G. Anderson, and Robert Langer. Physical and mechanical properties of PLA, and their functions in widespread applications—a comprehensive review. Advanced Drug Delivery Reviews, 107:367 – 392, 2016. doi:10.1016/j.addr.2016.06.012.
- [60] Parisa Farahmand and Radovan Kovacevic. An experimental–numerical investigation of heat distribution and stress field in single- and multi-track laser cladding by a high-power direct diode laser. Optics & Laser Technology, 63:154–168, 2014. URL: <https://www.sciencedirect.com/science/article/pii/S0030399214001066>, doi:<https://doi.org/10.1016/j.optlastec.2014.04.016>.
- [61] John Flemmer, Norbert Pirch, and Fabian Drinck. LMDCAM2: Software Tool for Near-Net Repair, Cladding and Built-Up by Laser Metal Deposition. In Proceedings of the ASME 2015 International Manufacturing Science and Engineering Conference. Volume 1: Processing, volume Volume 1: Processing of International Manufacturing Science and Engineering Conference, page V001T02A015, June 2015. doi:10.1115/MSEC2015-9243.
- [62] Simon Ford and Mélanie Despeisse. Additive manufacturing and sustainability: an exploratory study of the advantages and challenges. Journal of Cleaner Production, 137:1573 – 1587, 2016. doi:10.1016/j.jclepro.2016.04.150.
- [63] Junjian Fu, Hao Li, Liang Gao, and Mi Xiao. Design of shell-infill structures by a multiscale level set topology optimization method. Computers & Structures, 212:162 – 172, 2019. doi:10.1016/j.compstruc.2018.10.006.
- [64] Aniruddha Gaikwad, Reza Yavari, Mohammad Montazeri, Kevin Cole, Linkan Bian, and Prahalada Rao. Toward the digital twin of additive manufacturing: Integrating thermal simulations, sensing, and analytics to detect process faults. IISE Transactions, 52(11):1204–1217, 2020. doi:10.1080/24725854.2019.1701753.

- [65] Wei Gao, Yunbo Zhang, Devarajan Ramanujan, Karthik Ramani, Yong Chen, Christopher B. Williams, Charlie C.L. Wang, Yung C. Shin, Song Zhang, and Pablo D. Zavattieri. The status, challenges, and future of additive manufacturing in engineering. Computer-Aided Design, 69:65 – 89, 2015. doi:10.1016/j.cad.2015.04.001.
- [66] Yisong Gao, Lifang Wu, Dong-Ming Yan, and Liangliang Nan. Near support-free multi-directional 3D printing via global-optimal decomposition. Graphical Models, 104:101034, 2019. URL: <https://www.sciencedirect.com/science/article/pii/S1524070319300256>, doi:10.1016/j.gmod.2019.101034.
- [67] Alain Garaigordobil, Ruben Ansola, and Estrella Veguería. Study of topology optimization parameters and scaffold structures in additive manufacturing. In Proceedings of the VII European Congress on Computational Methods in Applied Sciences and Engineering, pages 3700–3710. National Technical University of Athens, 2016. doi:10.7712/100016.2066.6404.
- [68] Marco Garetti, Paolo Rosa, and Sergio Terzi. Life cycle simulation for the design of product-service systems. Computers in Industry, 63(4):361 – 369, 2012. Product Service System Engineering: From Theory to Industrial Applications. doi:10.1016/j.compind.2012.02.007.
- [69] Xiaoyin Ge, Issam Safa, Mikhail Belkin, and Yusu Wang. Data skeletonization via Reeb graphs. In Proceedings of the 24th International Conference on Neural Information Processing Systems, page 837–845, Red Hook, NY, USA, 2011. Curran Associates Inc.
- [70] Hailu Shimels Gebremedhen, Dereje Engida Woldemichael, and Fakhruddin Mohd Hashim. Effect of modeling parameters in SIMP based stress constrained structural topology optimization. International Journal of Mechanical and Mechatronics Engineering, 17(6):32–39, 2017.
- [71] Hermes Giberti, Luca Sbaglia, and Marcello Urgo. A path planning algorithm for industrial processes under velocity constraints with an application to additive manufacturing. Journal of Manufacturing Systems, 43:160 – 167, 2017. doi:10.1016/j.jmsy.2017.03.003.
- [72] Dara Moazami Goodarzi, Joonas Pekkarinen, and Antti Salminen. Effect of process parameters in laser cladding on substrate melted areas and the substrate melted shape. Journal of Laser Applications, 27(S2):S29201, Feb. 2015. doi:10.2351/1.4906376.
- [73] Heng Gu and Lin Li. Computational fluid dynamic simulation of gravity and pressure effects in laser metal deposition for potential additive manufacturing in space. International Journal of Heat and Mass Transfer, 140:51–65, 2019. URL: <https://www.sciencedirect.com/science/article/pii/S0017931018339188>, doi:<https://doi.org/10.1016/j.ijheatmasstransfer.2019.05.081>.
- [74] M. Hachani, A. Ouled Zaid, and W. Puech. Kinematic reeb graph extraction based on heat diffusion. In 2014 22nd International Conference on Pattern Recognition, pages 3981–3986, 2014. doi:<https://doi.org/10.1109/ICPR.2014.682>.
- [75] Mustafa Hajij and Paul Rosen. An efficient data retrieval parallel Reeb graph algorithm. Algorithms, 13(10):258, 2020. doi:<https://doi.org/10.3390/a13100258>.

- [76] William Harvey, Yusu Wang, and Rephael Wenger. A randomized $O(m \log m)$ time algorithm for computing Reeb graphs of arbitrary simplicial complexes. In *Proceedings of the Twenty-Sixth Annual Symposium on Computational Geometry*, page 267–276, New York, NY, USA, 2010. Association for Computing Machinery. doi:<https://doi.org/10.1145/1810959.1811005>.
- [77] J.C. Heigel, P. Michaleris, and T.A. Palmer. In situ monitoring and characterization of distortion during laser cladding of Inconel® 625. *Journal of Materials Processing Technology*, 220:135 – 145, 2015. doi:[10.1016/j.jmatprotec.2014.12.029](https://doi.org/10.1016/j.jmatprotec.2014.12.029).
- [78] Mark Helou and Sami Kara. Design, analysis and manufacturing of lattice structures: an overview. *International Journal of Computer Integrated Manufacturing*, 31(3):243–261, 2018. doi:[10.1080/0951192X.2017.1407456](https://doi.org/10.1080/0951192X.2017.1407456).
- [79] Wenbin Hou, Xing Yang, Wei Zhang, and Yang Xia. Design of energy-dissipating structure with functionally graded auxetic cellular material. *International Journal of Crashworthiness*, 23(4):366–376, 2018. doi:[10.1080/13588265.2017.1328764](https://doi.org/10.1080/13588265.2017.1328764).
- [80] Adnan Ibrahimbegovic. *Nonlinear solid mechanics: Theoretical formulations and finite element solution methods*, volume 160. Springer Science & Business Media, 2009.
- [81] G.Q. Jin, W.D. Li, and L. Gao. An adaptive process planning approach of rapid prototyping and manufacturing. *Robotics and Computer-Integrated Manufacturing*, 29(1):23 – 38, 2013. doi:[10.1016/j.rcim.2012.07.001](https://doi.org/10.1016/j.rcim.2012.07.001).
- [82] J. Kacmarcik, D. Spahic, K. Varda, E. Porca, and N. Zaimovic-Uzunovic. An investigation of geometrical accuracy of desktop 3D printers using CMM. *IOP Conference Series: Materials Science and Engineering*, 393:012085, 2018. doi:<https://doi.org/10.1088/1757-899x/393/1/012085>.
- [83] Mohammad Reza Khosravani and Tamara Reinicke. On the use of X-ray computed tomography in assessment of 3D-printed components. *Journal of Nondestructive Evaluation*, 39(4), 2020. doi:<https://doi.org/10.1007/s10921-020-00721-1>.
- [84] N. Kladovasilakis, T. Kontodina, P. Charalampous, I. Kostavelis, D. Tzetzis, and D. Tzouvaras. A case study on 3D scanning, digital reparation and rapid metal additive manufacturing of a centrifugal impeller. *IOP Conference Series: Materials Science and Engineering*, 1037(1):012018, 2021. doi:[10.1088/1757-899x/1037/1/012018](https://doi.org/10.1088/1757-899x/1037/1/012018).
- [85] G.L. Knapp, T. Mukherjee, J.S. Zuback, H.L. Wei, T.A. Palmer, A. De, and T. DebRoy. Building blocks for a digital twin of additive manufacturing. *Acta Materialia*, 135:390 – 399, 2017. doi:[10.1016/j.actamat.2017.06.039](https://doi.org/10.1016/j.actamat.2017.06.039).
- [86] Andrejs Kovalovs, Andris Chate, Sergejs Gaidukovs, and Arturs Medvids. Finite element simulation of indentation experiment on branched epoxy novolac resin. *IOP Conference Series: Materials Science and Engineering*, 500:012006, 2019. doi:[10.1088/1757-899x/500/1/012006](https://doi.org/10.1088/1757-899x/500/1/012006).
- [87] Sebastian Kreissl, Georg Pinggen, Anton Evgrafov, and Kurt Maute. Topology optimization of flexible micro-fluidic devices. *Structural and Multidisciplinary Optimization*, 42(4):495–516, Oct 2010. doi:[10.1007/s00158-010-0526-6](https://doi.org/10.1007/s00158-010-0526-6).

- [88] Vittoria Laghi, Michele Palermo, Giada Gasparini, Valentina Alena Girelli, and Tomaso Trombetti. On the influence of the geometrical irregularities in the mechanical response of wire-and-arc additively manufactured planar elements. Journal of Constructional Steel Research, 178:106490, 2021. doi:<https://doi.org/10.1016/j.jcsr.2020.106490>.
- [89] C. Lalas, K. Tsirbas, K. Salonitis, and G. Chryssolouris. An analytical model of the laser clad geometry. The International Journal of Advanced Manufacturing Technology, 32(1-2):34–41, 2006. doi:10.1007/s00170-005-0318-0.
- [90] Matthijs Langelaar. Topology optimization of 3D self-supporting structures for additive manufacturing. Additive Manufacturing, 12:60–70, 2016. doi:10.1016/j.addma.2016.06.010.
- [91] Dong-Wook Lee, Kamran A. Khan, and Rashid K. Abu Al-Rub. Stiffness and yield strength of architected foams based on the Schwarz Primitive triply periodic minimal surface. International Journal of Plasticity, 95:1 – 20, 2017. doi:10.1016/j.ijplas.2017.03.005.
- [92] Hongshuai Lei, Chuanlei Li, Jinxin Meng, Hao Zhou, Yabo Liu, Xiaoyu Zhang, Panding Wang, and Daining Fang. Evaluation of compressive properties of SLM-fabricated multi-layer lattice structures by experimental test and μ -CT-based finite element analysis. Materials & Design, 169:107685, 2019. doi:10.1016/j.matdes.2019.107685.
- [93] Maija Leino, Joonas Pekkarinen, and Risto Soukka. The role of laser additive manufacturing methods of metals in repair, refurbishment and remanufacturing –enabling circular economy. Physics Procedia, 83:752 – 760, 2016. doi:10.1016/j.phpro.2016.08.077.
- [94] Dawei Li, Wenhe Liao, Ning Dai, Guoying Dong, Yunlong Tang, and Yi Min Xie. Optimal design and modeling of gyroid-based functionally graded cellular structures for additive manufacturing. Computer-Aided Design, 104:87 – 99, 2018. doi:10.1016/j.cad.2018.06.003.
- [95] H. H. Liu, T. Zhao, L. Y. Li, W. J. Liu, T. Q. Wang, and J. F. Yue. A path planning and sharp corner correction strategy for wire and arc additive manufacturing of solid components with polygonal cross-sections. The International Journal of Advanced Manufacturing Technology, 106(11-12):4879–4889, jan 2020. doi:10.1007/s00170-020-04960-4.
- [96] Huaming Liu, Xunpeng Qin, Song Huang, Zeqi Hu, and Mao Ni. Geometry modeling of single track cladding deposited by high power diode laser with rectangular beam spot. Optics and Lasers in Engineering, 100:38 – 46, 2018. doi:10.1016/j.optlaseng.2017.07.008.
- [97] Jikai Liu, Andrew T. Gaynor, Shikui Chen, Zhan Kang, Krishnan Suresh, Akihiro Takezawa, Lei Li, Junji Kato, Jinyuan Tang, Charlie C. L. Wang, Lin Cheng, Xuan Liang, and Albert. C. To. Current and future trends in topology optimization for additive manufacturing. Structural and Multidisciplinary Optimization, 57(6):2457–2483, 2018. doi:10.1007/s00158-018-1994-3.
- [98] Jikai Liu and Yongsheng Ma. A survey of manufacturing oriented topology optimization methods. Advances in Engineering Software, 100:161 – 175, 2016. doi:10.1016/j.advengsoft.2016.07.017.

- [99] Jikai Liu, Huangchao Yu, and Albert C. To. Porous structure design through Blinn transformation-based level set method. *Structural and Multidisciplinary Optimization*, 57(2):849–864, 2018. doi:10.1007/s00158-017-1786-1.
- [100] Kai Liu and Andrés Tovar. An efficient 3D topology optimization code written in Matlab. *Structural and Multidisciplinary Optimization*, 50(6):1175–1196, 2014. doi:10.1007/s00158-014-1107-x.
- [101] Lu Liu, Paul Kamm, Francisco García-Moreno, John Banhart, and Damiano Pasini. Elastic and failure response of imperfect three-dimensional metallic lattices: the role of geometric defects induced by Selective Laser Melting. *Journal of the Mechanics and Physics of Solids*, 107:160 – 184, 2017. doi:10.1016/j.jmps.2017.07.003.
- [102] Xingchen Liu and Vadim Shapiro. Sample-based design of functionally graded material structures. In *ASME 2016 International Design Engineering Technical Conferences and Computers and Information in Engineering Conference*, page V02AT03A035. ASME, 2016. doi:10.1115/DETC2016-60431.
- [103] Bill Lozanovski, David Downing, Phuong Tran, Darpan Shidid, Ma Qian, Peter Choong, Milan Brandt, and Martin Leary. A monte carlo simulation-based approach to realistic modelling of additively manufactured lattice structures. *Additive Manufacturing*, 32:101092, 2020. doi:10.1016/j.addma.2020.101092.
- [104] Chao Ma and Yunkai Gao. Study on mesh segmentation of topology optimization results using Reeb graph. In *2021 International Conference on Artificial Intelligence and Electromechanical Automation (AIEA)*, pages 277–280. IEEE, 2021. doi:https://doi.org/10.1109/AIEA53260.2021.00065.
- [105] Kevin J. Maloney, Kathryn D. Fink, Tobias A. Schaedler, Joanna A. Kolodziejska, Alan J. Jacobsen, and Christopher S. Roper. Multifunctional heat exchangers derived from three-dimensional micro-lattice structures. *International Journal of Heat and Mass Transfer*, 55(9):2486 – 2493, 2012. doi:10.1016/j.ijheatmasstransfer.2012.01.011.
- [106] V. Manvatkar, A. De, and T. DebRoy. Spatial variation of melt pool geometry, peak temperature and solidification parameters during laser assisted additive manufacturing process. *Materials Science and Technology*, 31(8):924–930, 2015. doi:10.1179/1743284714Y.0000000701.
- [107] Jonàs Martínez, Samuel Hornus, Haichuan Song, and Sylvain Lefebvre. Polyhedral voronoi diagrams for additive manufacturing. *ACM Trans. Graph.*, 37(4):129:1–129:15, 2018. doi:10.1145/3197517.3201343.
- [108] I. Maskery, L. Sturm, A.O. Aremu, A. Panesar, C.B. Williams, C.J. Tuck, R.D. Wildman, I.A. Ashcroft, and R.J.M. Hague. Insights into the mechanical properties of several triply periodic minimal surface lattice structures made by polymer additive manufacturing. *Polymer*, 152:62 – 71, 2018. doi:10.1016/j.polymer.2017.11.049.
- [109] Y A Mayi, M Dal, P Peyre, M Bellet, C Metton, C Moriconi, and R Fabbro. Laser-induced plume investigated by finite element modelling and scaling of particle entrainment in laser powder bed fusion. *Journal of Physics D: Applied Physics*, 53(7):075306, 2020. doi:10.1088/1361-6463/ab5900.

- [110] Daniel Mejia, Aitor Moreno, Ander Arbelaiz, Jorge Posada, Oscar Ruiz-Salguero, and Raúl Chopitea. Accelerated thermal simulation for three-dimensional interactive optimization of computer numeric control sheet metal laser cutting. Journal of Manufacturing Science and Engineering, 140(3), dec 2017. doi:10.1115/1.4038207.
- [111] Daniel Mejia-Parra, Oscar Ruiz-Salguero, Carlos Cadavid, Aitor Moreno, and Jorge Posada. Level sets of weak-Morse functions for triangular mesh slicing. Mathematics, 8(9):1624, 2020. doi:https://doi.org/10.3390/math8091624.
- [112] Daniel Mejia-Parra, Jairo R. Sánchez, Oscar Ruiz-Salguero, Marcos Alonso, Alberto Izaguirre, Erik Gil, Jorge Palomar, and Jorge Posada. In-line dimensional inspection of warm-die forged revolution workpieces using 3D mesh reconstruction. Applied Sciences, 9(6):1069, 2019. doi:https://doi.org/10.3390/app9061069.
- [113] Ferry P.W. Melchels, Katia Bertoldi, Ruggero Gabbrielli, Aldrik H. Velders, Jan Feijen, and Dirk W. Grijpma. Mathematically defined tissue engineering scaffold architectures prepared by stereolithography. Biomaterials, 31(27):6909 – 6916, 2010. doi:10.1016/j.biomaterials.2010.05.068.
- [114] William M. Mendenhall and Terry L. Sincich. Statistics for Engineering and the Sciences. CRC Press, 6th edition, 2016.
- [115] Panagiotis Michaleris. Modeling metal deposition in heat transfer analyses of additive manufacturing processes. Finite Elements in Analysis and Design, 86:51 – 60, 2014. doi:10.1016/j.finel.2014.04.003.
- [116] Florent Michel, Helen Lockett, Jialuo Ding, Filomeno Martina, Gianrocco Marinelli, and Stewart Williams. A modular path planning solution for wire + arc additive manufacturing. Robotics and Computer-Integrated Manufacturing, 60:1 – 11, 2019. doi:10.1016/j.rcim.2019.05.009.
- [117] Kenneth C Mills. Fe pure iron. In Kenneth C Mills, editor, Recommended Values of Thermophysical Properties for Selected Commercial Alloys, Woodhead Publishing Series in Metals and Surface Engineering, pages 105–112. Woodhead Publishing, 2002. doi:10.1533/9781845690144.105.
- [118] Waleed Mohamed and A Ben Hamza. Reeb graph path dissimilarity for 3D object matching and retrieval. The Visual Computer, 28(3):305–318, 2012. doi:https://doi.org/10.1007/s00371-011-0640-5.
- [119] Diego Montoya-Zapata, Diego A. Acosta, Camilo Cortés, Juan Pareja-Corcho, Aitor Moreno, Jorge Posada, and Oscar Ruiz-Salguero. Meta-modeling of lattice mechanical responses via design of experiments. In 2020 International Conference on Mathematics and Computers in Science and Engineering (MACISE), pages 308–317, 2020. doi:10.1109/MACISE49704.2020.00065.
- [120] Diego Montoya-Zapata, Diego A. Acosta, Camilo Cortés, Juan Pareja-Corcho, Aitor Moreno, Jorge Posada, and Oscar Ruiz-Salguero. Approximation of the mechanical response of large lattice domains using homogenization and design of experiments. Applied Sciences, 10(11):3858, 2020. URL: https://www.mdpi.com/2076-3417/10/11/3858, doi:10.3390/app10113858.

- [121] Diego Montoya-Zapata, Diego A. Acosta, Aitor Moreno, Jorge Posada, and Oscar Ruiz-Salguero. Sensitivity analysis in shape optimization using voxel density penalization. In Dan Casas and Adrián Jarabo, editors, Spanish Computer Graphics Conference (CEIG). The Eurographics Association, 2019. doi:10.2312/ceig.20191201.
- [122] Diego Montoya-Zapata, Diego A. Acosta, Oscar Ruiz-Salguero, Jorge Posada, and David Sanchez-Londono. A general meta-graph strategy for shape evolution under mechanical stress. Cybernetics and Systems, 50(1):3–24, 2019. doi:10.1080/01969722.2018.1558011.
- [123] Diego Montoya-Zapata, Camilo Cortés, and Oscar Ruiz-Salguero. FE-simulations with a simplified model for open-cell porous materials: A Kelvin cell approach. Journal of Computational Methods in Sciences and Engineering, 19:989 – 1000, 2019. doi:10.3233/JCM-193669.
- [124] Diego Montoya-Zapata, Carles Creus, Aitor Moreno, Igor Ortiz, Piera Alvarez, Oscar Ruiz-Salguero, and Jorge Posada. Computational minimization of over-deposition at corners of trajectories in Laser Metal Deposition. Manufacturing Letters, 29:29–33, 2021. doi:https://doi.org/10.1016/j.mfglet.2021.05.001.
- [125] Diego Montoya-Zapata, Carles Creus, Igor Ortiz, Piera Alvarez, Aitor Moreno, Jorge Posada, and Oscar Ruiz-Salguero. Generation of 2.5D deposition strategies for LMD-based additive manufacturing. Procedia Computer Science, 180:280–289, 2021. doi:https://doi.org/10.1016/j.procs.2021.01.165.
- [126] Diego Montoya-Zapata, Aitor Moreno, Igor Ortiz, Oscar Ruiz-Salguero, and Jorge Posada. Cylindrical transform slicing of revolute parts with overhangs for laser metal deposition. In Jorge Posada and Ana Serrano, editors, Spanish Computer Graphics Conference (CEIG). The Eurographics Association, 2022. doi:10.2312/ceig.20221141.
- [127] Diego Montoya-Zapata, Aitor Moreno, Juan Pareja-Corcho, Jorge Posada, and Oscar Ruiz-Salguero. Density-sensitive implicit functions using sub-voxel sampling in additive manufacturing. Metals, 9(12):1293, 2019. URL: https://www.mdpi.com/2075-4701/9/12/1293, doi:10.3390/met9121293.
- [128] Diego Montoya-Zapata, Jorge Posada, Piera Alvarez, Carles Creus, Aitor Moreno, Igor Ortiz, and Oscar Ruiz-Salguero. Experimental and computational assessment of minimizing overfill in trajectory corners by laser velocity control of laser cladding. The International Journal of Advanced Manufacturing Technology, 119(9):6393–6411, 2022. doi:10.1007/s00170-021-08641-8.
- [129] Diego Montoya-Zapata, Juan M. Rodríguez, Aitor Moreno, Oscar Ruiz-Salguero, and Jorge Posada. Nonlinear thermal simulation of laser metal deposition. Australian Journal of Mechanical Engineering, 19(5):653–668, 2021. doi:10.1080/14484846.2021.1988435.
- [130] Montoya-Zapata, Diego, Rodríguez, Juan M., Moreno, Aitor, Posada, Jorge, and Ruiz-Salguero, Oscar. 2D linear finite element simulation of laser metal heating for digital twins. Int. J. Simul. Multidisci. Des. Optim., 12:11, 2021. doi:10.1051/smdo/2021011.
- [131] Jonas Näsström, Frank Brueckner, and Alexander F. H. Kaplan. Laser enhancement of wire arc additive manufacturing. Journal of Laser Applications, 31(2):022307, 2019. doi:10.2351/1.5096111.

- [132] Mattia Natali, Silvia Biasotti, Giuseppe Patanè, and Bianca Falcidieno. Graph-based representations of point clouds. Graphical Models, 73(5):151–164, 2011. doi:<https://doi.org/10.1016/j.gmod.2011.03.002>.
- [133] Ondřej Nenadl, Václav Ocelík, Armin Palavra, and Jeff Th.M. De Hosson. The prediction of coating geometry from main processing parameters in laser cladding. Physics Procedia, 56:220 – 227, 2014. 8th International Conference on Laser Assisted Net Shape Engineering LANE 2014. doi:[10.1016/j.phpro.2014.08.166](https://doi.org/10.1016/j.phpro.2014.08.166).
- [134] NIST/SEMATECH. e-Handbook of Statistical Methods. <http://www.itl.nist.gov/div898/handbook/>. Accessed: 2019–12–04. URL: <http://www.itl.nist.gov/div898/handbook/>.
- [135] V. Ocelík, O. Nenadl, A. Palavra, and J.Th.M. De Hosson. On the geometry of coating layers formed by overlap. Surface and Coatings Technology, 242:54 – 61, 2014. doi:[10.1016/j.surfcoat.2014.01.018](https://doi.org/10.1016/j.surfcoat.2014.01.018).
- [136] Livia Á. Oliveira, Júlio C. Santos, Túlio H. Panzera, Rodrigo T.S. Freire, Luciano M.G. Vieira, and Fabrizio Scarpa. Evaluation of hybrid-short-coir-fibre-reinforced composites via full factorial design. Composite Structures, 202:313 – 323, 2018. doi:[10.1016/j.compstruct.2018.01.088](https://doi.org/10.1016/j.compstruct.2018.01.088).
- [137] Ajit Panesar, Meisam Abdi, Duncan Hickman, and Ian Ashcroft. Strategies for functionally graded lattice structures derived using topology optimisation for Additive Manufacturing. Additive Manufacturing, 19:81–94, 2018. doi:[10.1016/j.addma.2017.11.008](https://doi.org/10.1016/j.addma.2017.11.008).
- [138] Juan Pareja-Corcho, Diego Montoya-Zapata, Carlos Cadavid, Aitor Moreno, Jorge Posada, Ketzare Arenas-Tobon, and Oscar Ruiz-Salguero. Synthesis of Reeb graph and Morse operators from level sets of a boundary representation. In Jorge Posada and Ana Serrano, editors, Spanish Computer Graphics Conference (CEIG). The Eurographics Association, 2022. doi:[10.2312/ceig.20221140](https://doi.org/10.2312/ceig.20221140).
- [139] Sang-In Park and David W. Rosen. Homogenization of Mechanical Properties for Material Extrusion Periodic Lattice Structures Considering Joint Stiffening Effects. Journal of Mechanical Design, 140(11), 09 2018. 111414. doi:[10.1115/1.4040704](https://doi.org/10.1115/1.4040704).
- [140] Juan Carlos Pereira, Herman Borovkov, Fidel Zubiri, Mari Carmen Guerra, and Josu Caminos. Optimization of thin walls with sharp corners in SS316L and IN718 alloys manufactured with laser metal deposition. Journal of Manufacturing and Materials Processing, 5(1):5, 2021. doi:[10.3390/jmmp5010005](https://doi.org/10.3390/jmmp5010005).
- [141] Suwattnarwong Phanphet, Surangsee Dechjarern, and Sermkiat Jomjanyong. Above-knee prosthesis design based on fatigue life using finite element method and design of experiment. Medical Engineering & Physics, 43:86 – 91, 2017. doi:[10.1016/j.medengphy.2017.01.001](https://doi.org/10.1016/j.medengphy.2017.01.001).
- [142] Peter Pichler, Brian J. Simonds, Jeffrey W. Sowards, and Gernot Pottlacher. Measurements of thermophysical properties of solid and liquid NIST SRM 316L stainless steel. Journal of Materials Science, 55(9):4081–4093, dec 2019. doi:[10.1007/s10853-019-04261-6](https://doi.org/10.1007/s10853-019-04261-6).
- [143] Andrew J. Pinkerton. Advances in the modeling of laser direct metal deposition. Journal of Laser Applications, 27(S1):S15001, 2015. doi:[10.2351/1.4815992](https://doi.org/10.2351/1.4815992).

- [144] V. Pomezanski, O.M. Querin, and G.I.N. Rozvany. CO-SIMP: extended SIMP algorithm with direct CORner CONTACT CONTROL. Structural and Multidisciplinary Optimization, 30(2):164–168, Aug 2005. doi:10.1007/s00158-005-0514-4.
- [145] J. Posada, C. Toro, I. Barandiaran, D. Oyarzun, D. Stricker, R. de Amicis, E. B. Pinto, P. Eisert, J. Döllner, and I. Vallarino. Visual Computing as a Key Enabling Technology for Industrie 4.0 and Industrial Internet. IEEE Computer Graphics and Applications, 35(2):26–40, 2015. doi:10.1109/MCG.2015.45.
- [146] A. W. Prabhu, T. Vincent, A. Chaudhary, W. Zhang, and S. S. Babu. Effect of microstructure and defects on fatigue behaviour of directed energy deposited Ti-6Al-4V. Science and Technology of Welding and Joining, 20(8):659–669, 2015. doi:10.1179/1362171815Y.0000000050.
- [147] R Core Team. R: A Language and Environment for Statistical Computing. R Foundation for Statistical Computing, Vienna, Austria, 2019. URL: <https://www.R-project.org/>.
- [148] M Ramanathan and Balan Gurumoorthy. Constructing medial axis transform of planar domains with curved boundaries. Computer-Aided Design, 35(7):619–632, 2003. doi:[https://doi.org/10.1016/S0010-4485\(02\)00085-4](https://doi.org/10.1016/S0010-4485(02)00085-4).
- [149] G.A. Ravi, X.J. Hao, N. Wain, X. Wu, and M.M. Attallah. Direct laser fabrication of three dimensional components using SC420 stainless steel. Materials & Design, 47:731 – 736, 2013. doi:10.1016/j.matdes.2012.12.062.
- [150] Georges Reeb. Sur les points singuliers d’une forme de Pfaff complètement integrable ou d’une fonction numérique [on the singular points of a completely integrable Pfaff form or of a numerical function]. Comptes Rendus Acad. Sciences Paris, 222:847–849, 1946.
- [151] X. Ren, L. Xiao, and Z. Hao. Multi-property cellular material design approach based on the mechanical behaviour analysis of the reinforced lattice structure. Materials & Design, 174:107785, 2019. doi:10.1016/j.matdes.2019.107785.
- [152] Vicente M. Rivas Santos, Adam Thompson, Danny Sims-Waterhouse, Ian Maskery, Peter Woolliams, and Richard Leach. Design and characterisation of an additive manufacturing benchmarking artefact following a design-for-metrology approach. Additive Manufacturing, 32:100964, 2020. doi:<https://doi.org/10.1016/j.addma.2019.100964>.
- [153] J.P. Rizzuto. Experimental investigation of reciprocally supported element (rse) lattice honeycomb domes structural behaviour. Engineering Structures, 166:496 – 510, 2018. doi:10.1016/j.engstruct.2018.03.094.
- [154] J. M. Rodriguez, J. M. Carbonell, J. C. Cante, and J. Oliver. The particle finite element method (PFEM) in thermo-mechanical problems. International Journal for Numerical Methods in Engineering, 107(9):733–785, 2016. doi:10.1002/nme.5186.
- [155] Swathi Routhu, Divya Kanakanala, Jianzhong Ruan, Xiaoqing Frank Liu, and Frank Liou. 2-D Path Planning for Direct Laser Deposition Process. In Proceedings of the ASME 2010 International Design Engineering Technical Conferences and Computers and Information in Engineering Conference. Volume 1: 36th Design Automation Conference, Parts A and B,

- volume Volume 1: 36th Design Automation Conference, Parts A and B of International Design Engineering Technical Conferences and Computers and Information in Engineering Conference, pages 415–423, August 2010. doi:10.1115/DETC2010-28440.
- [156] Jianzhong Ruan, Kunyayut Eiamsa-ard, and F. W. Liou. Automatic multi-axis slicing based on centroidal axis computation. In International Design Engineering Technical Conferences and Computers and Information in Engineering Conference. Volume 3: 25th Computers and Information in Engineering Conference, Parts A and B, pages 383–393, Long Beach, CA, USA, 2005. doi:10.1115/DETC2005-85261.
- [157] Óscar E Ruíz and Carlos A Cadavid. Boolean 2D shape similarity for surface reconstruction. In M. H. Hamza, editor, Proceedings of the IASTED International Conference on Visualization, Imaging and Image Processing (VIIP 2001), pages 245–249. ACTA Press, 2001.
- [158] Oscar E Ruiz, Carlos A Cadavid, Miguel Granados, Sebastián Peña, and Eliana Vásquez. 2D shape similarity as a complement for Voronoi-Delone methods in shape reconstruction. Computers & Graphics, 29(1):81–94, 2005. doi:https://doi.org/10.1016/j.cag.2004.11.009.
- [159] Jairo R. Sánchez, Álvaro Segura, and Iñigo Barandiaran. Fast and accurate mesh registration applied to in-line dimensional inspection processes. International Journal on Interactive Design and Manufacturing (IJIDeM), 12(3):877–887, 2017. doi:https://doi.org/10.1007/s12008-017-0449-1.
- [160] Gianpaolo Savio, Roberto Meneghello, and Gianmaria Concheri. Design of variable thickness triply periodic surfaces for additive manufacturing. Progress in Additive Manufacturing, 2019. doi:10.1007/s40964-019-00073-x.
- [161] Christina Schäfer and Eckhard Finke. Shape optimisation by design of experiments and finite element methods—an application of steel wheels. Structural and Multidisciplinary Optimization, 36(5):477–491, 2008. doi:10.1007/s00158-007-0183-6.
- [162] Yujie Shan, Dongming Gan, and Huachao Mao. Curved layer slicing based on isothermal surface. Procedia Manufacturing, 53:484–491, 2021. URL: https://www.sciencedirect.com/science/article/pii/S2351978921001025, doi:10.1016/j.promfg.2021.06.081.
- [163] Jonathan Richard Shewchuk. Triangle: Engineering a 2D quality mesh generator and Delaunay triangulator. In Ming C. Lin and Dinesh Manocha, editors, Applied Computational Geometry Towards Geometric Engineering, pages 203–222, Berlin, Heidelberg, 1996. Springer Berlin Heidelberg.
- [164] Yoshihisa Shinagawa and Toshiyasu L Kunii. Constructing a Reeb graph automatically from cross sections. IEEE Computer Graphics and Applications, 11(6):44–51, 1991. doi:https://doi.org/10.1109/38.103393.
- [165] O. Sigmund. A 99 line topology optimization code written in Matlab. Structural and Multidisciplinary Optimization, 21(2):120–127, 2001. doi:10.1007/s001580050176.
- [166] Ole Sigmund and Kurt Maute. Topology optimization approaches. Structural and Multidisciplinary Optimization, 48(6):1031–1055, 2013. doi:10.1007/s00158-013-0978-6.

- [167] Boxue Song, Tianbiao Yu, Xingyu Jiang, Wenchao Xi, and Xiaoli Lin. Effect of laser power on molten pool evolution and convection. Numerical Heat Transfer, Part A: Applications, 78(2):48–59, 2020. doi:10.1080/10407782.2020.1777795.
- [168] Guo-Hua Song, Shi-Kai Jing, Fang-Lei Zhao, Ye-Dong Wang, Hao Xing, and Jing-Tao Zhou. Design optimization of irregular cellular structure for additive manufacturing. Chinese Journal of Mechanical Engineering, 30(5):1184–1192, 2017. doi:10.1007/s10033-017-0168-3.
- [169] O. Sorkine, D. Cohen-Or, Y. Lipman, M. Alexa, C. Rössl, and H.-P. Seidel. Laplacian surface editing. In Proceedings of the 2004 Eurographics/ACM SIGGRAPH Symposium on Geometry Processing, SGP '04, page 175–184, New York, NY, USA, 2004. Association for Computing Machinery. doi:10.1145/1057432.1057456.
- [170] Bret Stanford and Philip Beran. Conceptual design of compliant mechanisms for flapping wings with topology optimization. AIAA Journal, 49(4):855–867, 2011. doi:10.2514/1.J050940.
- [171] Michael E. Stender, Lauren L. Beghini, Joshua D. Sugar, Michael G. Veilleux, Samuel R. Subia, Thale R. Smith, Christopher W. San Marchi, Arthur A. Brown, and Daryl J. Dagle. A thermal-mechanical finite element workflow for directed energy deposition additive manufacturing process modeling. Additive Manufacturing, 21:556 – 566, 2018. URL: <http://www.sciencedirect.com/science/article/pii/S2214860418301246>, doi:https://doi.org/10.1016/j.addma.2018.04.012.
- [172] Grant P. Steven. Homogenization of multicomponent composite orthotropic materials using fea. Communications in Numerical Methods in Engineering, 13(7):517–531, 1997. doi:10.1002/(SICI)1099-0887(199707)13:7<517::AID-CNM74>3.0.CO;2-L.
- [173] G. Strano, L. Hao, R. M. Everson, and K. E. Evans. A new approach to the design and optimization of support structures in additive manufacturing. The International Journal of Advanced Manufacturing Technology, 66(9):1247–1254, 2013. doi:10.1007/s00170-012-4403-x.
- [174] Birgit Strodthoff and Bert Jüttler. Layered Reeb graphs for three-dimensional manifolds in boundary representation. Computers & Graphics, 46:186–197, 2015. doi:https://doi.org/10.1016/j.cag.2014.09.026.
- [175] Birgit Strodthoff and Bert Jüttler. Automatic decomposition of 3D solids into contractible pieces using Reeb graphs. Computer-Aided Design, 90:157–167, 2017. doi:https://doi.org/10.1016/j.cad.2017.05.006.
- [176] Birgit Strodthoff, Martin Schifko, and Bert Juettler. Horizontal decomposition of triangulated solids for the simulation of dip-coating processes. Computer-Aided Design, 43(12):1891–1901, 2011. doi:https://doi.org/10.1016/j.cad.2011.06.013.
- [177] Alok Sutradhar, Glaucio H. Paulino, Michael J. Miller, and Tam H. Nguyen. Topological optimization for designing patient-specific large craniofacial segmental bone replacements. Proceedings of the National Academy of Sciences, 107(30):13222–13227, 2010. doi:10.1073/pnas.1001208107.

- [178] I. Tabernero, A. Lamikiz, E. Ukar, L.N. López de Lacalle, C. Angulo, and G. Urbikain. Numerical simulation and experimental validation of powder flux distribution in coaxial laser cladding. Journal of Materials Processing Technology, 210(15):2125 – 2134, 2010. doi:10.1016/j.jmatprotec.2010.07.036.
- [179] I. Tabernero, A. Lamikiz, E. Ukar, S. Martínez, and A. Celaya. Modeling of the geometry built-up by coaxial laser material deposition process. The International Journal of Advanced Manufacturing Technology, 70(5):843–851, 2013. doi:10.1007/s00170-013-5284-3.
- [180] Nusrat Tamanna, Roger Crouch, and Sumsun Naher. Progress in numerical simulation of the laser cladding process. Optics and Lasers in Engineering, 122:151–163, 2019. doi:10.1016/j.optlaseng.2019.05.026.
- [181] Y. Tang, G. Dong, Q. Zhou, and Y. F. Zhao. Lattice structure design and optimization with additive manufacturing constraints. IEEE Transactions on Automation Science and Engineering, 15(4):1546–1562, 2018. doi:10.1109/TASE.2017.2685643.
- [182] Yunlong Tang, Aidan Kurtz, and Yaoyao Fiona Zhao. Bidirectional Evolutionary Structural Optimization (BESO) based design method for lattice structure to be fabricated by additive manufacturing. Computer-Aided Design, 69:91–101, 2015. doi:10.1016/j.cad.2015.06.001.
- [183] Zi-jue Tang, Wei-wei Liu, Yi-wen Wang, Kaze Mojtaba Saleheen, Zhi-chao Liu, Shi-tong Peng, Zhao Zhang, and Hong-chao Zhang. A review on in situ monitoring technology for directed energy deposition of metals. The International Journal of Advanced Manufacturing Technology, 108(11-12):3437–3463, 2020. URL: <https://doi.org/10.1007%2Fs00170-020-05569-3>, doi:10.1007/s00170-020-05569-3.
- [184] Patrick Terriault and Vladimir Brailovski. Modeling and simulation of large, conformal, porosity-graded and lightweight lattice structures made by additive manufacturing. Finite Elements in Analysis and Design, 138:1 – 11, 2018. doi:10.1016/j.finel.2017.09.005.
- [185] A. Thompson, I. Maskery, and R. K. Leach. X-ray computed tomography for additive manufacturing: a review. Measurement Science and Technology, 27(7):072001, 2016. doi:<https://doi.org/10.1088/0957-0233/27/7/072001>.
- [186] Hucheng Tian, Xiangdong Chen, Zhaohua Yan, Xinlei Zhi, Qi Yang, and Zijun Yuan. Finite-element simulation of melt pool geometry and dilution ratio during laser cladding. Applied Physics A, 125(7), 2019. doi:10.1007/s00339-019-2772-9.
- [187] Tore Tryland, Odd S. Hopperstad, and Magnus Langseth. Design of experiments to identify material properties. Materials & Design, 21(5):477 – 492, 2000. doi:10.1016/S0261-3069(00)00035-2.
- [188] J. Vanek, J. A. G. Galicia, and B. Benes. Clever Support: Efficient support structure generation for digital fabrication. Computer Graphics Forum, 33(5):117–125, 2014. doi:10.1111/cgf.12437.
- [189] Gieljan Vantighem, Veerle Boel, Marijke Steeman, and Wouter De Corte. Multi-material topology optimization involving simultaneous structural and thermal analyses. Structural and Multidisciplinary Optimization, 2018. doi:10.1007/s00158-018-2095-z.

- [190] Bala R. Vatti. A generic solution to polygon clipping. *Commun. ACM*, 35(7):56–63, July 1992. doi:10.1145/129902.129906.
- [191] Weiming Wang, Yang You, Wenhai Liu, and Cewu Lu. Point cloud classification with deep normalized Reeb graph convolution. *Image and Vision Computing*, 106:104092, 2021. doi:https://doi.org/10.1016/j.imavis.2020.104092.
- [192] Meinhard Wohlgemuth, Nataliya Yufa, James Hoffman, and Edwin L. Thomas. Triply periodic bicontinuous cubic microdomain morphologies by symmetries. *Macromolecules*, 34(17):6083–6089, 2001. doi:10.1021/ma0019499.
- [193] Young-Yun Woo, Sang-Wook Han, Il-Yeong Oh, Young-Hoon Moon, and Won Ha. Control of directed energy deposition process to obtain equal-height rectangular corner. *International Journal of Precision Engineering and Manufacturing*, 20(12):2129–2139, 2019. doi:10.1007/s12541-019-00226-6.
- [194] Chenming Wu, Chengkai Dai, Guoxin Fang, Yong-Jin Liu, and Charlie C. L. Wang. General support-effective decomposition for multi-directional 3-D printing. *IEEE Transactions on Automation Science and Engineering*, 17(2):599–610, 2020. doi:10.1109/TASE.2019.2938219.
- [195] Chenming Wu, Chengkai Dai, Guoxin Fang, Yong-Jin Liu, and Charlie C.L. Wang. RoboFDM: A robotic system for support-free fabrication using FDM. In *2017 IEEE International Conference on Robotics and Automation (ICRA)*, pages 1175–1180, 2017. doi:10.1109/ICRA.2017.7989140.
- [196] Jun Wu, Charlie C.L. Wang, Xiaoting Zhang, and Rüdiger Westermann. Self-supporting rhombic infill structures for additive manufacturing. *Computer-Aided Design*, 80:32–42, 2016. doi:10.1016/j.cad.2016.07.006.
- [197] Jun Wu, Weiming Wang, and Xifeng Gao. Design and optimization of conforming lattice structures. *IEEE Transactions on Visualization and Computer Graphics*, pages 1–1, 2019. doi:10.1109/TVCG.2019.2938946.
- [198] Yi Xiong, Sang-In Park, Suhasini Padmanathan, Audelia Gumarus Dharmawan, Shaohui Foong, David William Rosen, and Gim Song Soh. Process planning for adaptive contour parallel toolpath in additive manufacturing with variable bead width. *The International Journal of Advanced Manufacturing Technology*, 105(10):4159–4170, 2019. doi:10.1007/s00170-019-03954-1.
- [199] Ke Xu, Yingguang Li, Lufeng Chen, and Kai Tang. Curved layer based process planning for multi-axis volume printing of freeform parts. *Computer-Aided Design*, 114:51–63, 2019. URL: https://www.sciencedirect.com/science/article/pii/S0010448518305384, doi:10.1016/j.cad.2019.05.007.
- [200] Wei Ya, B. Pathiraj, and Shaojie Liu. 2D modelling of clad geometry and resulting thermal cycles during laser cladding. *Journal of Materials Processing Technology*, 230:217 – 232, 2016. doi:10.1016/j.jmatprotec.2015.11.012.

- [201] Chunze Yan, Liang Hao, Ahmed Hussein, and David Raymont. Evaluations of cellular lattice structures manufactured using selective laser melting. International Journal of Machine Tools and Manufacture, 62:32 – 38, 2012. doi:10.1016/j.ijmachtools.2012.06.002.
- [202] Zhuo Yang, Douglas Eddy, Sundar Krishnamurty, Ian Grosse, Peter Denno, Yan Lu, and Paul Witherell. Investigating grey-box modeling for predictive analytics in smart manufacturing. In Volume 2B: 43rd Design Automation Conference. American Society of Mechanical Engineers, aug 2017. doi:10.1115/detc2017-67794.
- [203] Sha Yin, Linzhi Wu, Jinshui Yang, Li Ma, and Steven Nutt. Damping and low-velocity impact behavior of filled composite pyramidal lattice structures. Journal of Composite Materials, 48(15):1789–1800, 2014. doi:10.1177/0021998313490582.
- [204] Soo-Yeon Yoo, Seong-Kyun Kim, Seong-Joo Heo, Jai-Young Koak, and Joung-Gyu Kim. Dimensional accuracy of dental models for three-unit prostheses fabricated by various 3D printing technologies. Materials, 14(6):1550, 2021. doi:https://doi.org/10.3390/ma14061550.
- [205] Huangchao Yu, Jiaqi Huang, Bin Zou, Wen Shao, and Jikai Liu. Stress-constrained shell-lattice infill structural optimisation for additive manufacturing. Virtual and Physical Prototyping, 15(1):35–48, 2020. doi:10.1080/17452759.2019.1647488.
- [206] Kaiqing Zhang, Gengdong Cheng, and Liang Xu. Topology optimization considering overhang constraint in additive manufacturing. Computers & Structures, 212:86 – 100, 2019. doi:10.1016/j.compstruc.2018.10.011.
- [207] Li Zhang, Xiaoqi Chen, Wei Zhou, Taobo Cheng, Lijia Chen, Zhen Guo, Bing Han, and Longxing Lu. Digital twins for additive manufacturing: A state-of-the-art review. Applied Sciences, 10(23), 2020. doi:10.3390/app10238350.
- [208] Pu Zhang, Jakub Toman, Yiqi Yu, Emre Biyikli, Mesut Kirca, Markus Chmielus, and Albert C. To. Efficient design-optimization of variable-density hexagonal cellular structure by additive manufacturing: Theory and validation. Journal of Manufacturing Science and Engineering, 137:021004 – 021004–8, 2015. doi:10.1115/1.4028724.
- [209] Gang Zhao, Guocai Ma, Jiangwei Feng, and Wenlei Xiao. Nonplanar slicing and path generation methods for robotic additive manufacturing. The International Journal of Advanced Manufacturing Technology, 96(9-12):3149–3159, 2018. doi:10.1007/s00170-018-1772-9.
- [210] Shengfeng Zhou, Xiaoqin Dai, and Haizhong Zheng. Analytical modeling and experimental investigation of laser induction hybrid rapid cladding for Ni-based WC composite coatings. Optics & Laser Technology, 43(3):613 – 621, 2011. doi:10.1016/j.optlastec.2010.09.001.
- [211] J. Zhu, M. Khurshid, and Z. Barsoum. Accuracy of computational welding mechanics methods for estimation of angular distortion and residual stresses. Welding in the World, 63(5):1391–1405, 2019. doi:10.1007/s40194-019-00746-9.
- [212] Liang Zhu, Jacob Barhak, Vijay Srivatsan, and Reuven Katz. Efficient registration for precision inspection of free-form surfaces. The International Journal of Advanced Manufacturing Technology, 32(5-6):505–515, 2006. doi:https://doi.org/10.1007/s00170-005-0370-9.